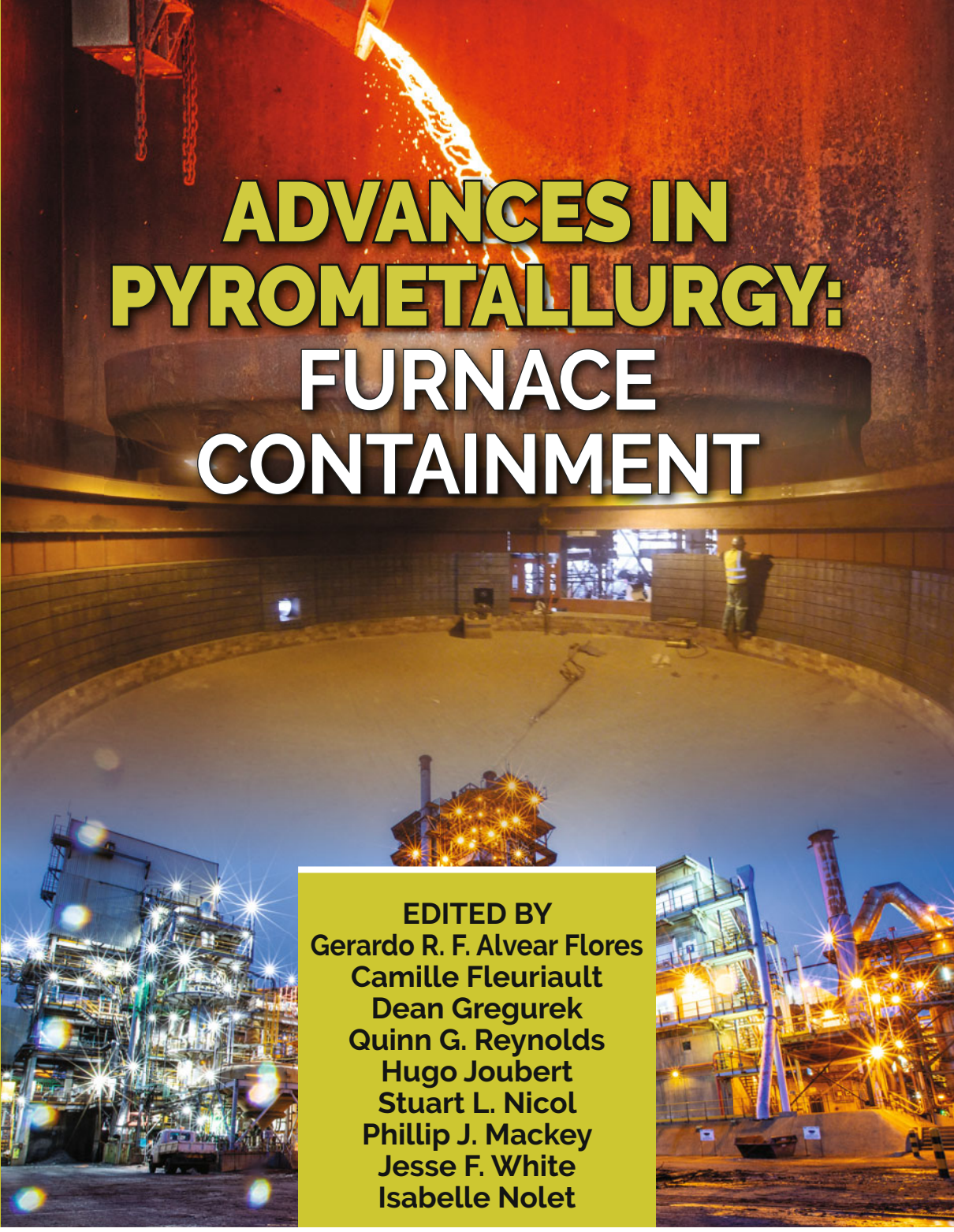

ADVANCES IN PYROMETALLURGY: FURNACE CONTAINMENT

EDITED BY
Gerardo R. F. Alvear Flores
Camille Fleuriault
Dean Gregurek
Quinn G. Reynolds
Hugo Joubert
Stuart L. Nicol
Phillip J. Mackey
Jesse F. White
Isabelle Nolet

TMS

Springer

The Minerals, Metals & Materials Series

Gerardo R. F. Alvear Flores · Camille Fleuriault ·
Dean Gregurek · Quinn G. Reynolds ·
Hugo Joubert · Stuart L. Nicol · Phillip J. Mackey ·
Jesse F. White · Isabelle Nolet
Editors

Advances in Pyrometallurgy

Furnace Containment

TMS

Springer

Editors
Gerardo R. F. Alvear Flores
CaEng Associates
Toronto, ON, Canada

Dean Gregurek
RHI Magnesita Technology Center
Leoben, Austria

Hugo Joubert
Tenova Pyromet
Johannesburg, South Africa

Phillip J. Mackey
P. J. Mackey Technology, Inc.
Kirkland, QC, Canada

Isabelle Nolet
Hatch
Johannesburg, South Africa

Camille Fleuriault
Eramet Norway
Sauda, Norway

Quinn G. Reynolds
Mintek
Johannesburg, South Africa

Stuart L. Nicol
Glencore Technology
Brisbane, QLD, Australia

Jesse F. White
Kanthal AB
Hallstahammar, Sweden

ISSN 2367-1181 ISSN 2367-1696 (electronic)
The Minerals, Metals & Materials Series
ISBN 978-3-031-50175-3 ISBN 978-3-031-50176-0 (eBook)
https://doi.org/10.1007/978-3-031-50176-0

© The Minerals, Metals & Materials Society 2024

This work is subject to copyright. All rights are solely and exclusively licensed by the Publisher, whether the whole or part of the material is concerned, specifically the rights of translation, reprinting, reuse of illustrations, recitation, broadcasting, reproduction on microfilms or in any other physical way, and transmission or information storage and retrieval, electronic adaptation, computer software, or by similar or dissimilar methodology now known or hereafter developed.
The use of general descriptive names, registered names, trademarks, service marks, etc. in this publication does not imply, even in the absence of a specific statement, that such names are exempt from the relevant protective laws and regulations and therefore free for general use.
The publisher, the authors, and the editors are safe to assume that the advice and information in this book are believed to be true and accurate at the date of publication. Neither the publisher nor the authors or the editors give a warranty, expressed or implied, with respect to the material contained herein or for any errors or omissions that may have been made. The publisher remains neutral with regard to jurisdictional claims in published maps and institutional affiliations.

This Springer imprint is published by the registered company Springer Nature Switzerland AG
The registered company address is: Gewerbestrasse 11, 6330 Cham, Switzerland

Paper in this product is recyclable.

Preface

The Pyrometallurgy Committee of the Extraction and Processing Division (EPD) of TMS aims to promote the development and exchange of fundamental and applied research, as well as industrial practices, to support the transition to more sustainable metallurgical processes.

Aligned with the above-mentioned objective, special attention has been given to support more sustainable operating practices (Furnace Tapping 2022), and developing low carbon pathways with a focus on the use of hydrogen (Advances in Pyrometallurgy 2023). Following the same trend, Advances in Pyrometallurgy 2024 focuses on reactor design from the perspective of material containment.

In addition to a proper metallurgical concept developed on solid thermodynamic and kinetic knowledge, a robust pyrometallurgical process requires a safe and reliable system to contain the melt. Proper attention to the design of the furnace containment system is therefore an integral part of the overall reactor design, allowing durable containment of the high temperature product streams and the energy associated with pyrometallurgical processes.

Containing corrosive and abrasive materials at extreme temperatures requires attention to topics such as:

- Furnace lining design philosophies
- Furnace design configurations and other design considerations
- Fundamentals of materials design and cooling systems
- Challenges during construction and commissioning
- Safe operation

In addition, following successful design, fabrication, erection, and commissioning of suitable pyrometallurgical reactors, ongoing attention is required on the following aspects to ensure robust, successful, and safe metallurgical operations:

- Monitoring and preventative maintenance,
- Slag engineering

- Process control through strategies implemented though advanced process and equipment control
- Best industrial operating practices

The intention of this symposium has been to create a platform for the exchange of ideas on the challenges, solutions, failures, and successes in furnace containment designs and applications. It brings together the perspectives from industry, design houses, and research institutions.

On behalf of the Advances in Pyrometallurgy Organizing Committee,
Prof. Dr. Gerardo R. F. Alvear Flores

Contents

About the Editors

Gerardo R. F. Alvear Flores is an industry leader in the non-ferrous industry with over 30 years of work experience. Dr. Alvear graduated as a chemical engineer in 1986 and pursued post-graduated education in Japan to grow not only professionally, but also personally, by developing a new way of thinking to approach personal and professional challenges.

During his professional career working in Japan, Chile, Australia, Germany, Singapore, and Canada, he has been able to build experience in operations, management, engineering design, research, development, and technology innovation in the base metals industry.

Dr. Alvear is the author of more than 50 technical papers and co-author of *Extractive Metallurgy of Copper*, 6th Edition. He is currently President of Canadian Engineering Associates, Industrial Advisor of TMS EPD Council, and Adjunct Professor at the University of Queensland. He is also Co-chairman for Copper 2025.

Camille Fleuriault is senior project manager at Eramet Norway AS in Sauda, Norway. Her work focuses on identifying and enabling zero carbon strategies for the production of manganese alloys. She previously worked on developing innovative and environmentally friendly recycling processes for the secondary metals industry. She holds a B.S. in Geological Engineering and an M.Eng. in Mineral Engineering from the National School of Geological Engineering in Nancy, France, and a M.Sc. in Metallurgical Engineering from Colorado School of Mines, USA. She is chair of the TMS Pyrometallurgy Committee and a former *JOM* advisor for the same committee.

Dean Gregurek has been a senior mineralogist in the RHI Magnesita Technology Center in Leoben, Austria since 2001. Dr. Gregurek received his M.Sc. degree at the University of Graz in 1995, his doctorate degree from the University of Leoben in 1999, and degree of assoc. prof. in 2019. Prior to RHI Magnesita, he worked for two years for Luzenac Europe in talc business. His current research interests and technical expertise are focused on chemical and mineralogical studies related to interactions between refractories, molten metals, and slags from pyrometallurgical furnaces. Dr. Gregurek has been a TMS member since 2012, *JOM* advisor (2014–2017), chair of the Pyrometallurgy Committee (2018–2020), EPD programming representative (2021–2024), and co-organizer for 7th–12th International Symposium on High-Temperature Metallurgical Processing (TMS Annual Meetings 2016–2021), Furnace Tapping (TMS Annual Meeting 2022), Advances in Pyrometallurgy (TMS Annual Meetings 2023–2024) and Measurement and Control of High-Temperature Processes (TMS Annual Meeting 2024).

Quinn G. Reynolds holds an undergraduate degree in Chemical Engineering from the University of Kwazulu-Natal, a Masters in Engineering from the University of the Witwatersrand, and a Ph.D. in Applied Mathematics from the University of Cape Town. He has worked in the Pyrometallurgy Division at Mintek for the past 25 years. Mintek is a research institute conducting applied research and development to serve the extensive mineral processing and metallurgical industry in South Africa and worldwide. Dr. Reynolds' expertise includes mathematical and computational modelling of complex coupled phenomena in high temperature processes and in particular the application of high-performance computing and open-source modelling software to pyrometallurgy. His current areas of research include magnetohydrodynamic modelling of electric arcs, multiphysics fluid flow problems in furnace tapping and phase separation, combustion modelling for metallurgical processing, and discrete element modelling for particle flow problems. He has also performed extensive work in the characterization of the dynamic behavior of direct-current plasma arcs using high-speed photography and electrical measurement techniques.

Hugo Joubert is a Mechanical Engineer with 30-years of furnace and smelter design experience. Working in numerous roles in production, technical development, business development and management, he specializes in furnace equipment design and solution development. He started his career as a plant engineer on iron blast furnaces in South Africa and completed his Master's degree part time on furnace lining/cooling system design. He first joined Tenova Pyromet in 1998 as a Design Engineer. His experience includes electric furnace as well as top submerged lance furnace technology. He is currently the General Manager responsible for Base Metals at Tenova Pyromet.

Stuart L. Nicol (RPEQ) has a BE and PhD in chemical and metallurgical engineering from the University of Queensland. He is an expert in base metal smelting, with experience in the operation, design and fundamentals of smelters gained from experience working in both Australia and the United States. Currently, he is working on a number of international projects which involve recovering critical metals from end-of-life consumer materials.

Phillip J. Mackey a member of the Canadian Mining Hall of Fame, is one of the few Canadians to have advanced the development of not one but two significant copper smelting technologies that have benefited copper metallurgical plants around the world. He co-developed the Noranda Reactor Process, a major non-ferrous smelting technology and co-invented the Noranda Converting Process, which has produced more than 4 million tonnes of copper since the late 1990s.

Mackey obtained a BSc (Honors) from the School of Metallurgy at the University of New South Wales, Australia, in 1963, and completed his doctorate there in 1969. He then moved to Montreal, Canada to join Noranda Research Centre, which was then striving to develop in Canada a new autogenous process to smelt copper concentrates. The process also achieved early success in the United States, Australia, and China. He was involved with other initiatives during his career with Noranda (and related entities such as Falconbridge and Xstrata), in particular, new developments for processing lateritic nickel ore and is an Advisor to Horizonte Minerals plc, who is at present constructing a new nickel smelter in Brazil.

Phillip Mackey is a co-founder of the Copper-Cobre conferences, which expanded from a joint Canadian-Chilean enterprise to embrace the entire global industry. He is a Past President of the Metallurgical Society of the Canadian Institute of Mining and Metallurgy (CIM), a Fellow of CIM and of The Minerals, Metals & Material Society (TMS) in the USA, Mackey has authored or co-authored more than 100 technical papers covering diverse aspects of non-ferrous metallurgy. His CIM

Awards include the Silver Medal (2006), a Special Medal of Honour (2007), the Selwyn G Blaylock Medal (2010), and the prestigious Airey Award (2012) for "outstanding contributions" to the field of extractive metallurgy. Mackey is also on the Board of Hazen Research of Denver, USA.

The Phillip Mackey Symposium was held in honor of Dr. Mackey at the 2019 Copper Conference in Vancouver, Canada. He presented the Extraction & Processing Division Distinguished Lecture at the TMS 2020 Annual Meeting & Exhibition, received the John Elliott Lectureship Award of the Association for Iron and Steel Technology for 2021–2022, and was a Distinguished Lecturer of CIM in 2022–2023.

Jesse F. White holds a Ph.D. in Materials Science and Engineering from the KTH Royal Institute of Technology, an M.Sc. in Metallurgical and Materials Engineering from the Colorado School of Mines, and a B.S. in Metallurgical Engineering from the South Dakota School of Mines and Technology. He has 27 years of industrial and R&D experience in the aluminum, photovoltaic silicon, ferrosilicon, and carbon materials industries. Currently he is the Strategic Area Manager for Steelmaking at Kanthal, AB in Hallstahammar, Sweden. In parallel, Dr. White is also Faculty Affiliate at the Materials Science and Engineering Department at the KTH Royal Institute of Technology in Stockholm, Sweden.

Isabelle Nolet holds a B. Eng. in chemical engineering from Ecole Polytechnique de Montreal. She has 20 years of experience in metallurgical processing, particularly in the field of pyrometallurgy. She has strong practical and technical knowledge on smelting furnaces, converters, process modelling, process optimization, equipment upgrades, and commissioning. Isabelle is passionate about developing technologies that move the world forward. She has gained experience working in Canada, Australia, South Africa, New Caledonia, and Germany. Isabelle is currently the Global Director for Process Technology Development at Hatch.

Part I
Furnace Design and Operations

Designing Smelting Furnaces to Meet Process Requirements

Allan MacRae

Abstract Pyrometallurgical furnaces are not conventional structures that fall directly under a single design code. Engineering companies attempt to apply appropriate safety factors for stresses and temperatures to vessel shells, refractory, and cooling elements. The furnace components must be designed to function together to avoid plastic deformation, erosion, corrosion, and fracture. Thermal cycling, intense heat loads, and required design loads are not typically found in design handbooks or codes. The loads can vary significantly as the refractory lining wears. Historical analysis of vessel performance under similar operating conditions and processes are key for developing design loads and limits for heat, stress, corrosion, and movement. Advancements made in furnace design over the past several decades are highlighted.

Keywords Furnace · Design · Analysis · Inspection

Introduction

The furnace steel shell, refractory lining, and cooling elements (if present) work together as an integrated system. The steel shell must contain the refractory lining and cooling elements from startup to normal operating conditions and back to cool down for maintenance. The design must provide for a safe and reliable operation, as well as ease of assembly and maintenance.

Engineers have worked to reduce the frequency of leaks and breakouts by improvements in material selection, analytical techniques, and design detail. Suppliers have also taken steps to improve material quality and inspection techniques.

Thermal analysis, furnace binding forces, differential pressure between refractory and the confining steel structure, expansion allowance for thermal growth of refractory, and cooling elements are well established. The focus here will be on thermal and mechanical design aspects.

A. MacRae (✉)
MacRae Technologies, Inc., 1000 Silver Maple Ln, Hayward, CA 94544, USA
e-mail: amacrae@macraet.com

© The Minerals, Metals & Materials Society 2024

G. Alvear et al. (eds.), *Advances in Pyrometallurgy*, The Minerals, Metals & Materials Series, https://doi.org/10.1007/978-3-031-50176-0_1

Refractory

Significant improvements have been made in refractory production in terms of quality and dimensional tolerances on shapes. Due to leaks from cooling blocks, there has been a trend to replace magnesia with alumina refractory, particularly in the hearth below the blocks. The use of Kieserite (magnesium sulfate monohydrate) coatings has proven to be effective in reducing low-temperature hydration of magnesia brick stored in hot, damp locations (e.g., over 40 °C).

Wall thicknesses were often increased at tapholes to counter local corrosion and wear. Refractory brick linings laid dry can transfer compressive but not tensile forces, as the bricks are neither bonded to themselves nor to other structures. An exception would include graphite bricks which can be installed with a strong adhesive on the hot face of staves.

Due to the thermal gradient across a brick course in a wall, it will expand more on the hot face than the cold face. Compression at the hot face cannot be just at the edges. For the ring brick in Fig. 1, there needs to be some local crushing, plastic, or elastic deformation on the hot face so there is a contact area for compressive load transfer. For an assumed length of contact along about 25% of the brick length, the load path for the force components (line of thrust) would be about 1/3 along the length of the contact area. For a rectangular furnace, bowing of wall brick must be prevented; hence, the refractory would normally exhibit little pressure against the wall. Fluid pressure from molten material inside the furnace would generate pressure against the hearth and walls.

For the course of brick shown in Fig. 2, the line of thrust is outside the brickwork. At the same location, there will be a force component into the furnace due to the angle change to the line of thrust. The force, combination of shapes, and large step sizes can lead to shifting of bricks and significant melt penetration.

The vertical line of thrust will be further back in the walls if the brick is permitted to rotate (refer to Fig. 3). The horizontal steps from bottom to top were reduced from a full brick thickness to one half a brick thickness to reduce cracking of brick at the hot face, and improved flow of charge from top to bottom.

The remaining wall thickness at the end of a campaign must be stable to prevent mechanical collapse. Severe undercutting of a wall can lead to premature failure.

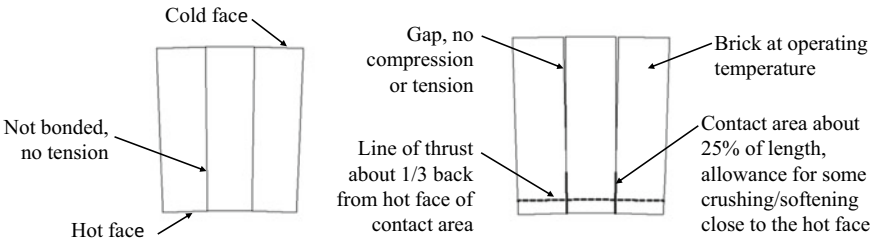

Fig. 1 Approximate contact areas to allow for thermal distortion of brick

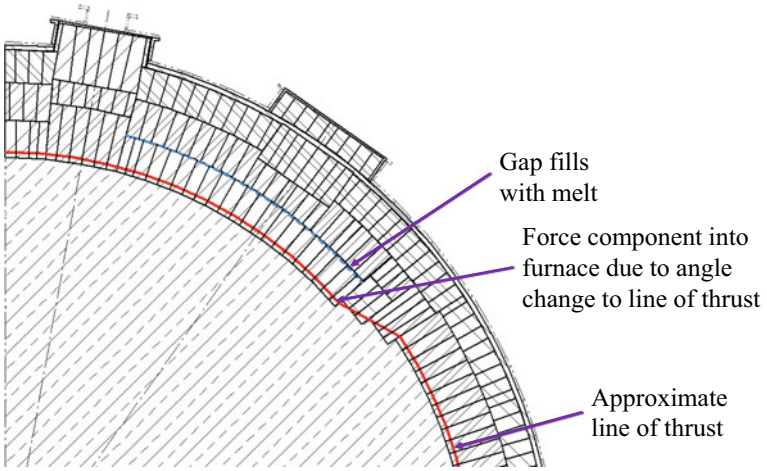

Fig. 2 Local thickening of refractory lining at metal and slag tapholes

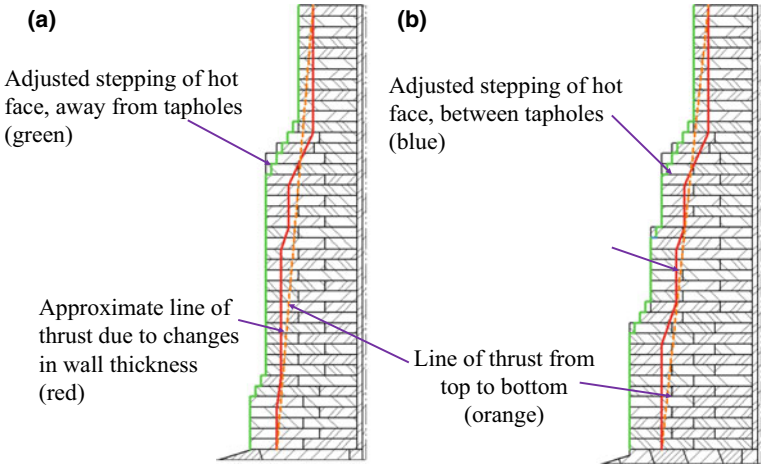

Fig. 3 Common sidewall thickness variations, **a** away from and **b** near tapholes

Providing a thick wall with an allowance for wear at a projected rate is a historical approach. This was based on known rates of material loss for a particular process. If cooling blocks are used to arrest refractory loss, then they must be spaced close enough to ensure that the system is stable. As shown in Fig. 4, if the coolers were to be spaced further apart, then the residual wall thickness may be too thin for the expected operating conditions.

Fig. 4 Worn refractory wall with horizontal plate coolers to arrest wear [1]

Furnace Structural Steel

Furnaces with a horizontal cylindrical shell must accommodate (a) differential thermal expansion between the shell and the brick, (b) differential expansion between the shell and the riding rings, (c) thermal expansion of the shell, (d) gravity loads, (e) torque from the drive system, and (f) axial load due to friction and binding. The stress solution for a converter is included in Fig. 5 for the applied loads, and differential thermal expansion between the brick and the shell and between the riding rings and the shell. All the loads listed must be included in the stress analysis at the same time to obtain the combined stresses and displacements. All cold gaps and member releases must be included to avoid over restraining the model.

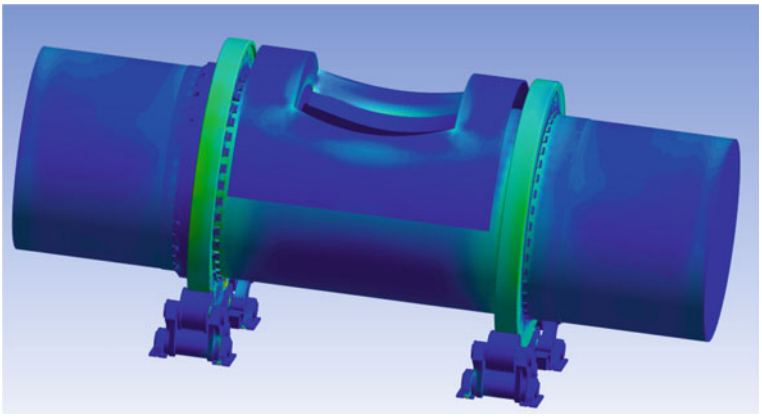

Fig. 5 Equivalent stresses for combination of all loads

A vertically orientated cylindrical furnace would also need to be analyzed both for temperatures and stresses. The shells are normally rigid. The hearth typically expands below the nearly stationary wall, exerting high local pressure against the shell. Thermal expansion of the hearth must be accommodated with a combination of expansion allowance material or mortar between brick joints. Some compressible material between the outer perimeter of the hearth and the steel shell is needed to avoid overstressing the shell. The compressible material (e.g., refractory board, carbon paste) should be monitored for deformation, to determine when it needs to be changed during a cold shutdown.

Rectangular furnaces with spring systems can be designed to accommodate thermal expansion of the refractory, and to apply forces to shift it back during a cooling cycle.

Although furnace steel is not a building structure, design limits from structural building codes are often used for evaluation. Codes include a greater factor of safety against sudden forms of failure such as shear. Gradual plastic deformation of furnace steel is a common occurrence, but rarely leads to a breakout if corrected in time. A sudden mode failure such as loss of a tie rod or shear failure of a taphole block restraint could result in the sudden loss of binding and furnace failure.

As a furnace deforms load redistribution can occur. Shell distortion can lead to uneven loading and failure of bolts or welds.

Stress concentrations are common at shell openings. It is good practice to have full strength welds at taphole openings, and to X-ray the joints both at initial installation and for repairs. Reliability and safety are maximized by close examination prior to operation.

Components which may be expected to be removed and then reattached during a shutdown should have fasteners and connections for ease of removal and manipulation.

Thermal Modelling

Design companies often maintain historical data for various types of processes and conditions. For an operating vessel, energy gains from cooling fluids are used to establish heat fluxes. Heat flux often varies with time, height of the furnace walls, through tapping channels, around burner ports, the roof, and on launders. Varying heat loads lead to thermal gradients and the resulting induced stresses.

Residual refractory and/or accretion thickness can be correlated to heat flux via analysis using either finite element analysis (FEA) or computational fluid dynamics (CFD). The shape of the wear profile does not have to be assumed; it would be at approximately at the isotherm for the liquidus of the slag (Fig. 6). Field measurement of the wear profile is very useful for estimating the variation of heat load on the block. It is technically possible to incorporate chemical reactions, electrical currents, and solidification to estimate heat fluxes and wear profiles, but it is too time-consuming

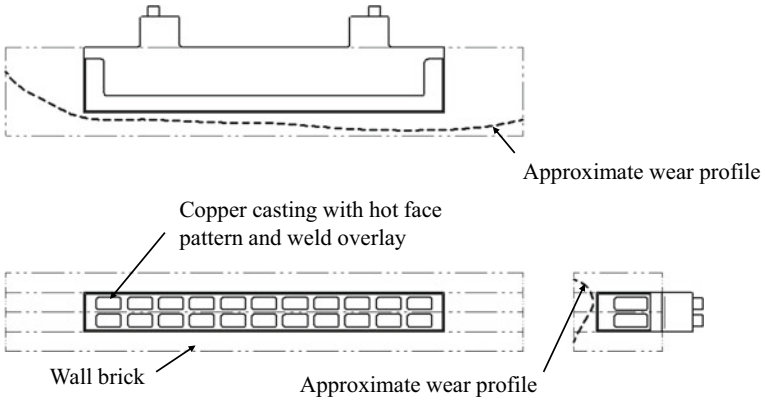

Fig. 6 Worn refractory around a wall cooling block

for general design practice. Accurate data for such modelling needs to be available for large temperature ranges.

Steady-state analysis is normally employed for the furnace crucible and the various cooling elements for furnaces with relatively stable heat loads.

Areas with highly variable heat loads, such as tapholes and launders, often experience an initial peak heat flux. This is evident by a sharp temperature rise of the cooling medium, which fall off to a more stable value after a short time. CFD modelling of the variable flow conditions is useful for estimating peak temperatures and can also be used to calculate corresponding stresses.

One-dimensional (1D) analysis can be used to estimate temperatures within a refractory lining (e.g., upper sidewall of a cylindrical furnace). Two-dimensional (2D) and 2D axisymmetric analyses are helpful for preliminary design, or for a furnace with a constant. Three dimensional (3D) is suitable for final design analysis to account for geometric features that often lead to uneven heating or cooling (e.g., pipe bends at corners of a block, blocks exposed on the hot face and end faces, and variable heat flux across the hot face).

An isotherm plot of a roof burner block is shown in Fig. 7, which was modelled using CFD. The block is exposed to splash from the melt below. A plot of water isotherms is included in Fig. 8, which indicates both that water temperatures are uneven on the hot face and that the maximum temperature is much larger than the discharge temperature. Using a constant convection coefficient and average bulk temperature would not provide the maximum temperature required for establishment of suitable alarm limits.

It is beneficial to locate thermowells within the thermal model to extract accurate values. The information is used for the preparation of performance curves for the cooling blocks.

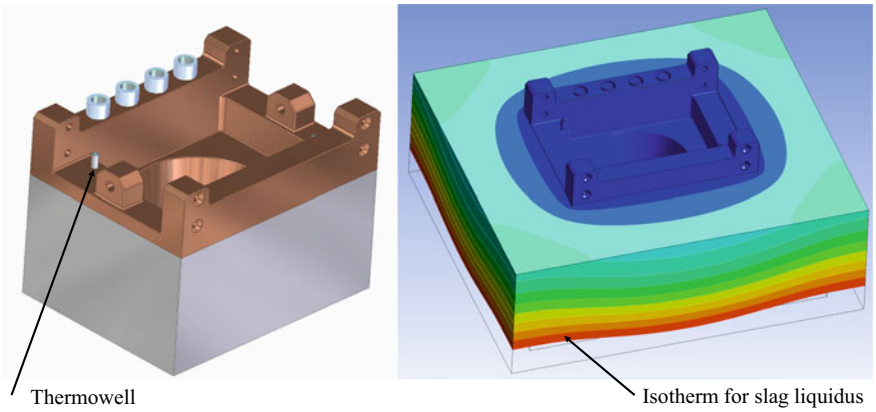

Fig. 7 Copper casting and isotherms for a roof burner block and surrounding refractory

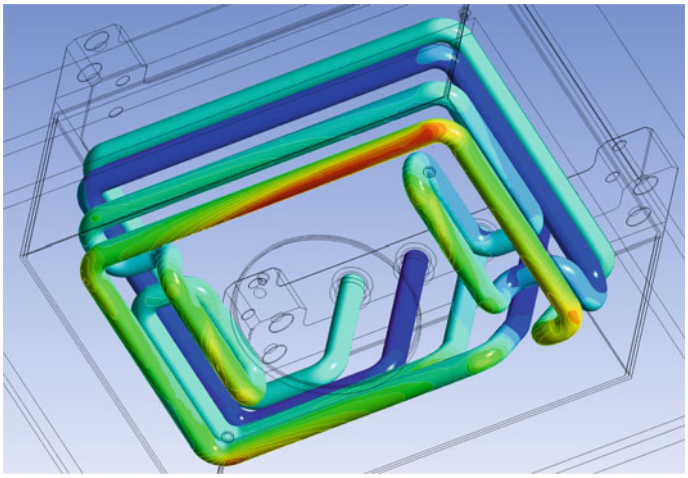

Fig. 8 Water isotherms for a roof burner block, 2 cooling circuits (view from below)

After the furnace has reached a stable operation, field data should be compared to calibrate the analytical models used for the design. Prior to designing any modifications, field data must be collected and analyzed. If the modelling does not correlate well to field observations, then revision will be necessary to create a validated model.

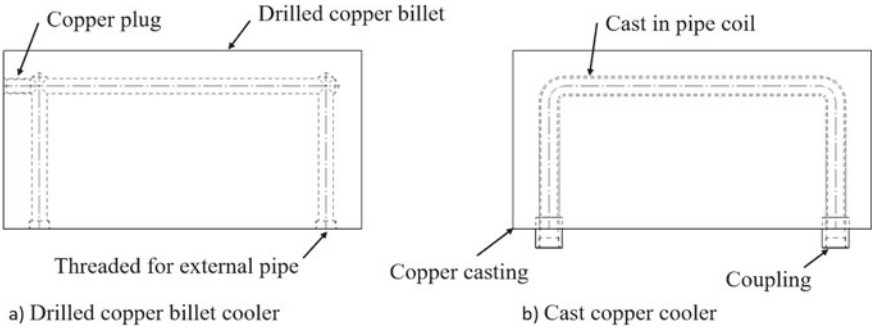

Fig. 9 Drilled billet and cast copper blocks

Cooling Block Design

Cooling blocks were introduced in refractory linings to slow or arrest local corrosion. For regions with relatively low heat flux, external shell cooling using forced air, falling water film, and/or water sprays has proven to be adequate.

For nonferrous smelting, drilled billets and copper castings (Fig. 9) are both employed, although there are advantages and disadvantages to each. Drilled billet coolers are normally manufactured from hot-worked, deoxidized, low residual phosphorous copper. Phosphorous acts as a deoxidant to permit the welding of plugs. Hot working is used to refine the grain size which increases resistance to crack propagation and reduces the possibility of through thickness defects. If the drilled water passage is outside the furnace, then electrolytic copper is still used due its lower cost but only if the risk of a coolant leak into the furnace is small.

Copper castings can be manufactured to more complex shapes than rectangular billets. Copper castings cannot be hot worked to increase notch toughness. If a pure copper pipe bonds to the cast material, then it is unlikely to arrest propagation of a crack. For comparison, the steel pipe used in an iron casting is deliberately coated with a material such as sodium silicate with the intention to prevent bonding. The result is decreased conduction across the interface, but it reduces the risk of a crack penetrating the pipe and causing a loss of water into the furnace.

Copper pipe has been used for the pipe coil for many decades. Unfortunately, the pipe coil needs to be cooled during the casting process. Steam generation can cause vibration of the pipe coils during casting and solidification. The cooled pipe will not expand then shrink as much as the cast around copper during the solidification process. Differential shrinkage leads to shear stresses at the interface more than the nominal yield stress of the copper. Nickel-copper (i.e., Monel) pipe coils have been used since 1960s. It does not need to be cooled during the casting process. Most modern copper foundries have developed the expertise to cast high-purity copper castings without cooling the pipe. To overcome issues with pipe bonding to the cast copper, copper-nickel pipe technology (U.S. patent [2]) exists to improve bonding and heat transfer and reduce interface shear stresses at the pipe to cast copper interface.

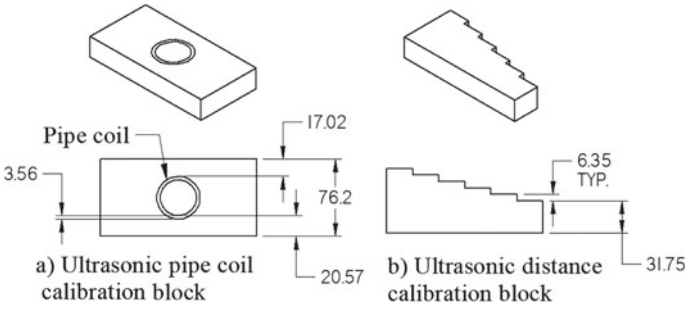

Fig. 10 Ultrasonic testing calibration block for checking bond to pipe and to locate pipe coil (**a**) and stepped block for calibration of ultrasonic inspection equipment (**b**)

It also does not need to be cooled during the casting process. Any cooling of the pipe coil during the casting process should be avoided, to minimize locking in residual stresses before even putting the block into service.

Regardless of which pipe material is used, it is important to be able to use ultrasonic testing to evaluate the movement of the pipe coils at several locations on the solidified casting. This is in addition to all other quality assurance testing. Permitted tolerances on pipe coil shifting are checked against calculated values, as the centre of the pipe cannot be found directly. The pipe wall thickness is often similar to the value of the tolerance for shifting of the pipe coil, so it is critical that the inspector must know whether the ultrasound echo is to the inside or outside of the pipe. A calibration block for testing bond is shown in Fig. 10a. It is helpful to have a calibration block to check where the expected echo is to occur to confirm if the pipe is expected to be bonded or just in contact. The ultrasonic inspection equipment should also be calibrated for a copper casting; an example is included in Fig. 10b.

Infrared testing is also commonly used to highlight areas of reduced contact or bond between the pipe coil and the cast copper.

In the 1980s, it was found that there was considerable room for improvement at copper foundries regarding the manufacture of pipe coils for castings, and for the welding of copper plugs into drilled billet coolers. Neither carbon nor stainless steel are suitable for the pipe coils due to excessive porosity, poor contact, and negligible bond to the cast copper. Many tests and requirements were introduced to ensure that the pipe coils meet standard requirements for ovality, minimum bend radius, being free of internal defects, with sound welds, and are also well cleaned externally. Copper castings can develop defects due to impurities on the surface of the pipe. Nickel alloys can pick up iron during bending and/or if stored on steel supports, which leads to local gas defects in the copper. Welding of nickel with copper bearing alloys requires clean welding techniques and is best performed in a shop under controlled conditions.

Most copper blocks used to just have smooth flat faces. These were susceptible to large fluctuations in heat load and large stresses due to sudden loss of accretions on the hot face and subsequent direct hot face contact with molten material. Several hot

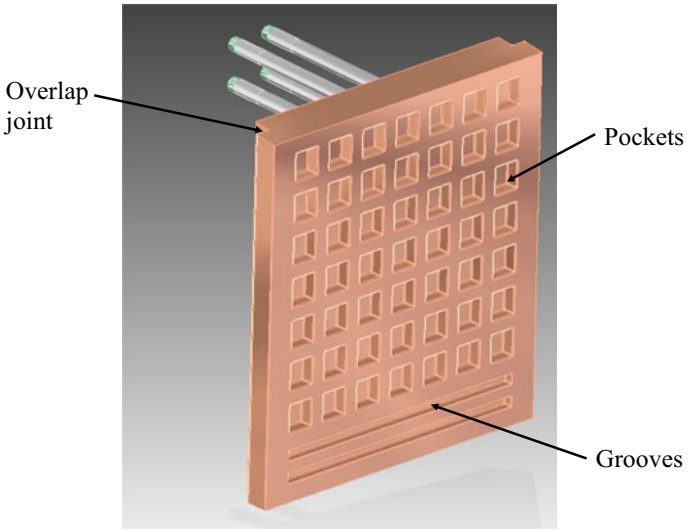

Fig. 11 Copper casting with pockets, grooves, and ends for overlap joints

face patterns have been introduced to improve mechanical retention of accretions including grooves, pockets (Fig. 11), and pins. Both pockets and grooves reduce the exposed area of copper after loss of surface accretion, which greatly decreases the instantaneous heat load to the block. If the pattern can retain either refractory or accretions against the copper, it can lower the magnitude of sudden changes in heat load to the cooler. In general, it is best eliminating sharp edges on a hot face of the copper to avoid premature cracking and loss of accretions. It is preferable to orientate a groove perpendicular to the flow of molten material. Tapered pins will retain accretions better than cylindrical pins; both are designed to melt back slowly if temporarily exposed to metal or an aggressive matte.

Nickel with chrome weld overlays on some copper blocks (such as launders) has proven to be very effective at reducing oxidation and abrasion but is best applied using gas tungsten arc or laser welding. Heating of the copper block needs to be controlled to maintain sufficient preheat but also avoid oxidation. Field repair of the weld overlay may be possible if it has not worn back to the copper. Once the copper has been exposed, it would be best to remove the block and have the weld overlay reapplied in a shop.

Blocks which are expected to be removed for replacement during operation should have design features to assist with ease of removal and manipulation (e.g., lugs for attachment of sling, shouldered eye bolts, lug to load to break seal).

Conclusions

1. Steel structure
    a. Limit design vessels to ductile distortions to avoid sudden failure.
    b. Include all loads which could be acting simultaneously.
    c. Do not assume that individual bricks are mechanically bonded to transfer tensile loads to other refractory or the steel structure.
    d. Allow for changes in load distribution due to vessel distortion and refractory wear.
2. Refractory
    a. Estimate the force load path both in plan and elevation, and layout the refractory to keep it within the brick.
    b. Use vertical steps between courses of about one half the brick thickness for load transfer and reduced cracking.
    c. Avoid increasing the wall thickness at tapholes unless it is certain that it is necessary to maintain wall stability (and in some cases protection for the cooling blocks), to the completion of the campaign.
3. Thermal analysis
    a. Calibrate thermal models with operating data to validate alarm limits and other controls for safe operation.
    b. Use 3D, not just 2D, for checking temperatures of cooling blocks. Peak calculated values should be used to establish alarm settings.
4. Copper cooling blocks
    a. Eliminate sharp edges and cracks on the hot faces to reduce stress concentrations, cracking, and loss of accretions.
    b. Use ultrasonic testing to evaluate bond versus contact and coil position at several points along the length of embedded pipe coils, in addition to thermal imaging.

References

1. MacRae A, Steinborn B (2018) Top submerged lance furnace lining cooling system upgrade. Paper presented at Extraction 2018, 26–29 Aug 2018, Ottawa, Canada
2. MacRae A (2020) Method for stabilizing thermal conduction of block coolers with cast-in coolant pipes. U.S. Patent 10,684,078 B1, 16 June 2020

The Importance of Understanding Mechanisms in Open-Bath (DC) Processes Related to Furnace Containment

Harmen J. Oterdoom, Markus A. Reuter, and Johan H. Zietsman

Abstract The paper starts with a discussion on "furnace containment systems". Recently, there have been several experiences with DC furnaces for continuous processing of particulate feed, some of which have experienced containment challenges. The Kazakh high-carbon ferrochrome DC operation is used to investigate what process mechanisms could take place in such a furnace. Several scenarios have been simulated with a dynamic multi-zone model to see how and especially how rapidly deviations in feed composition, quantity, or charging location can affect the operation. Of interest also are how fast these deviations could be detected and especially what data could be monitored to recognise them. This paper contributes to understanding fundamental mechanisms inside DC furnaces, which are becoming even more important due to an increased interest in open-bath furnaces for smelting DRI. A better understanding of process mechanisms can support in de-risking new equipment and processes, ensuring a safer operation, also for green steel production.

Keywords Furnace · Integrity · Process · Design · Thermochemistry · Simulation · DC · Ferrochrome · DRI

H. J. Oterdoom (✉)
University of Pretoria, Dusseldorf, Germany
e-mail: u18195530@tuks.co.za

M. A. Reuter
SMS Group, Dusseldorf, Germany
e-mail: markusandreas.reuter@sms-group.com

J. H. Zietsman
University of Pretoria, Pretoria, South Africa

Ex Mente Technologies, Pretoria, South Africa

J. H. Zietsman
e-mail: johan.zietsman@up.ac.za

© The Minerals, Metals & Materials Society 2024

G. Alvear et al. (eds.), *Advances in Pyrometallurgy*, The Minerals, Metals & Materials Series, https://doi.org/10.1007/978-3-031-50176-0_2

Introduction

This paper deals in general with electric smelting furnaces (ESFs), as used for products like FeNi, FeSi, FeCr, CaC_2, TiO_2-slag or possibly in the near-future (again) hot metal and even steel. Some comments are therefore specific to this type of furnace. The focus is on DC furnaces, though where applicable AC furnaces are mentioned. As it is the intention of this conference to exchange ideas, any lists, definitions, and statements are certainly open for discussion.

A specific further focus of this paper is the furnace containment system, which serves to safely and reliably contain the process materials and energy of a pyrometallurgical process. Loss of containment is a well-known concept in the chemical industry and dozens of causes for loss of containment of chemical reactors are listed in [1] for a quick overview or study the original book describing Chemical Process Quantitative Risk Analysis [2] for more detail.

While a containment system is intact, it receives little attention. It is only when the possibility of containment failure arises, or when it has already failed, that the containment system and related personnel get full attention. In the aftermath of a failure, reactions by people involved can range from multiple parties and levels cooperating to solve the issue and prevent its reoccurrence, to blame games, dismissal, and even litigation. The costs of these should be considered when deciding on (cutting) budgets for design of equipment and process and test work.

When the integrity of any component of a furnace containment system is in doubt, there are only a few options:

(1) changing the operation to (hopefully) be within a safe range,
(2) halting operation for quick repairs with limited downtime,
(3) halting operations for major repairs with long downtime, or
(4) continue without concessions.

If a sudden failure occurs, operation is practically always halted for a certain time to do repairs and possibly evaluate and improve process and equipment design.

This paper discusses the general concept of furnace containment, and how its' complexity requires a multidisciplinary approach to minimize risk. Because all aspects cannot be covered in a single paper, this paper focuses on the important role thermochemical calculations can play, using smelting of Kazakh chromite in a DC furnace as an example.

Components of a Furnace Containment System

Components of a furnace containment system are those components that all contribute to furnace containment and each upon failure could cause a containment system failure. A containment system can include back-ups or redundancies for components or sub-systems. Components essential for the functioning of the system include at least:

- Hearth and sidewall refractory.
- Cooling elements, typically used to protect refractory or equipment exposed to high temperatures.
- The steel holding refractory and copper together.
- The roof, constructed from steel or bricks, with or without copper cooling elements.
- Cooling media, like water, air, (in)directly protecting steel, copper, and refractory.
- Transport (and cooling) of cooling media.
- Insulation of electrical equipment by distance and insulating pieces preventing short circuits.
- Taphole closing equipment, be it manual or with machines.
- Back-up systems like uninterrupted power supply, water tanks, or diesel generators.
- Instrumentation to monitor all of the above.
- Equipment to clean and maintain the hardware and software components of the system.
- Consumables for the system, ranging from injection paste to anti-scaling chemicals.
- People with the right experience and skills to monitor, maintain, and operate all above.

Other items can be vital to ensuring furnace containment and campaign life, even if not considered to be a part of the containment system itself. However, poor design or failure of certain aspects can cause a containment issue, for example:

- The physical design of the charging system—location, method.
- The off-gas system—blockage, pressure control, connections, overpressure systems.
- Control logic—safety, trip, feeding, power input, electrode control.
- Process design—what is supposed to happen inside the furnace.

Many authors have reported on operating, maintaining, or monitoring mentioned components separately or combined. Containment issues have also been contributors to general project delay and even failure. On other occasions, projects became a success despite one or multiple containment failures.

Describing, Evaluating, and Comparing Loss of Containment: Data and Definitions Required!

A containment failure can cause furnace failure or even project failure, but not necessarily so. Smaller events are solved with minor downtime and operation continues. To possibly be able to quantify progress, the above definitions have been selected. Unfortunately, it is not an easy task acquiring accurate data for analysis that includes, for example:

- start date of a furnace campaign,
- containment issues including analyses of causes,
- containment failures including analyses of causes,
- downtime,
- changes made, and
- restart date.

Unfortunately, minor containment issues are hardly reported, meaning that acceptance of deviance as a cause can hardly be detected. When containment failures can be found in the public domain, even when explosions are involved, root cause analyses and details are not abundantly available [3, 4]. Furthermore, there seems to be little standardisation how things could be reported to be useful for stakeholders in the electric furnace industry. The following descriptions could be useful in more standardisation of incident reports:

- Wear is an anticipated and gradual degradation of any component of the containment system. Refractory is a typical one. Based on the whole containment system, also ageing of a workforce, lowered cleaning standards, or degradation of rubber hoses in cooling water systems should be considered.
- Containment system failure occurs when a component requires actual repair or replacement 33%[1] faster than anticipated, while requiring over 1%[2] of the expected total furnace operational time for it. A containment problem does not necessarily lead to loss of significant production or a furnace.
- Containment system issue is when a component failed and needed action, but downtime was less than 1% of planned annual production time. Examples are a small run out, eruptions without significant damage, small damage to cooling systems.
- Local failure is where a containment failure is strongly localised and concerns only a part of any of the components that form the entire component. Examples are hydration of or a crack in refractory, a water leak, a hole in the roof, or a short circuit.
- A global failure is where the containment failure affects the whole component of the containment system. Examples are a total dissolution of refractory, but also all operators going on strike, the entire computer system crashing, or a malfunctioning plugging machine.
- Instantaneous containment issues are events where suddenly the containment is lost. Typical examples are foaming, explosions or eruptions, a run out or a short circuit.
- Furnace or vessel failure is when the furnace consisting of refractory, cooling, and steel fails and needs considerable repairs. The same values as given under containment failure could be used to set a limit.

[1] 33% is arbitrary but could be a good starting point. For a relining this means after 2 instead of 3 years or 7 instead of 10.

[2] 1% is arbitrary too and with 8000 planned hours equals 80 hours of unplanned repair time for cleaning-up a small run-out or fixing burned cables and hoses.

- Furnace campaign is considered the time between big revamps of a furnace, like a relining. These can be accompanied by load increase when operational experiences have been good, or system upgrades when not.

It is important to document what the reasons were for (remedial) action, since "refractory repair" is a too unclear and imprecise statement. For example, sometimes only part of the refractory wears and needs replacement, while the rest can stay. The roof, sidewall, and hearth can have very different campaign times.

No Panacea

Solutions to prevent containment issues include test work, thermochemical and CFD calculations preferably combined, training, monitoring, and significant detailed discussions to decide on the best possible design, followed by a thorough process to ensure all is supplied, constructed, and commissioned properly. However, none of these will be a silver bullet, nor will all of them combined guarantee success. Furnace containment will always be a combination of technology, design, operation, thermochemistry, kinetics, humans, experience, and communication. All of these cannot be covered in a single paper.

Thermochemical Calculations: Foresight, Onsite, Hindsight All for Insight

Thermochemical calculations, when properly applied, are extremely useful in every stage of a project. Incomplete use of such methods is when only a single static calculation is done. Though such a calculation could say what to expect theoretically under very specific conditions, typically the nominal load operating conditions, reality may be different. Knowing what could happen around the operating point is extremely useful.

Ideally, thermochemical calculations are combined with CFD simulations. Although the computational expense can be prohibitive, progress has been made to significantly reduce the time-consuming equilibrium calculations [5]. The CFD simulation can prompt and stimulate ideas about potential temperature distributions, which affect thermochemical equilibria. Especially in large vessels with significant temperature gradients the equilibria may differ significantly in different zones of a furnace. That effect will even be enhanced if certain reaction products from one zone can move to a different zone. Not to be neglected are also the thermodynamics and growth/maintenance/control of bottom build-ups and slag solidification /freeze lining/ as described in [6].

It is important to also consider transient situations like start-up or shut down, restarts, or ramp-ups. The higher the design load of a furnace is, the more important

it can be to do operational simulations and CFD modelling at regular load intervals to see if potential problems can be identified.

Before a Contract Is Signed

A range of calculations with the targeted feed materials should be done to evaluate process inputs and expected process outputs. Calculations should include reasonable variation in the feed materials, cover possible process temperatures, and preferably include the refractory intended to be used.

Having these calculations available and ready for specific cases means that it is possible to identify deviations from expectations during commissioning and operation. Not having different scenarios prepared means more time is needed during commissioning to find out if what is happening is within reason or not.

During Commissioning and Operation

No matter how many calculations have been made before a furnace is started up, there will probably be surprises. Some of these will be or could be related to reactions and heat transfer taking place inside the furnace. Having people on site that can observe the operation and apply these observations directly to calculations is invaluable.

Analyses from feed materials and products can be used directly in calculations, and the calculations can give indications what samples should be taken where to understand the process better. A typical example is to ask for samples from abnormal locations or during abnormal conditions, so any model can be adjusted to a wider range of application.

When Something Has Gone Wrong

If something does go wrong, thermochemical calculations can support in determining what has happened. This can also be the time when it is discovered what should have been sampled or analysed for, because important data proved to be missing.

Detailed Understanding

No matter at what stage of a project, before commissioning, during normal operation, or in the aftermath of a furnace failure, doing calculations forces one to understand

the fundamental phenomena within a furnace. The next section focuses on the development of a multi-zone model to help assist among others containment design and maintenance as well as operational integrity.

Multi-zone Thermochemical Modelling and HSC

For the energy balance of a reaction, only the absolute difference between the begin and end situation matters as enthalpy is a thermodynamic state variable. If it is known, or at least there is a reasonable understanding of feed composition as well as products, then that is theoretically enough for producing an energy balance. When a reactor, such as an electric furnace, is designed, then expected heat losses are added to the energy needed for the reactions, and the total energy requirement can be estimated. Such a model is shown in Fig. 1.

If the intent is to calculate and not guestimate what is produced in a process, the use of thermochemical software is imperative. Such software makes it possible to not only perform equilibrium calculations but also represent non-linear molten solutions. As is well known, not many furnaces are in perfect equilibrium, and the calculated deviation from equilibrium is either accepted or manipulated by using correction factors. Such simplification is acceptable if a furnace is in steady state, with the expected and invariable raw materials, and operates continuously at the designed furnace load. However, there are limitations as shown in the next sections for using, for example, single-zone models compared to multi-zone modelling approaches.

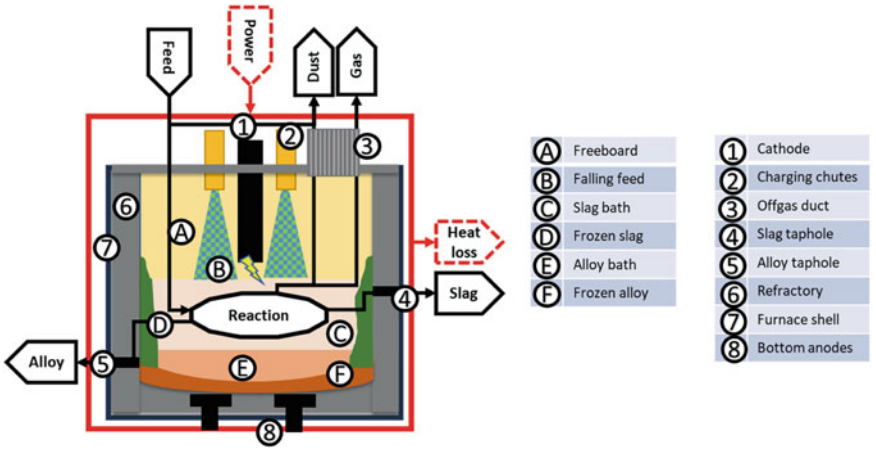

Fig. 1 The main components and zones in a DC furnace. The figure shows the unrealistic principle of a single reaction zone where all feed materials mix, react, segregate, and then leave the furnace instantly

Arguments Against Using a Single-Zone Model

Nor knowing or even underestimating what could happen inside a furnace increases risk for loss of process control and therefore loss of containment. Below are given some considerations that argue against using a single-zone approach:

- Assuming steady state
  In reality, furnaces are not always in steady state, sometimes hardly at all. The disturbance of the steady state can come, for example, from changes in feed materials, different electrical setpoints even at a constant load, a change in feeding pattern be it deliberate or by blockage of a chute, load reductions, short or long shutdowns, and restarts.
- Only Considering Feed and Furnace Products
  During the smelting operation certain compounds can form that are not directly measured in the products coming out of the stack or tapholes. Such half-products can play important roles in transfer of heat and mass. One example is the formation of SiO gas in silicon (alloy) production. The SiO represents a large quantity of energy and Si that could be lost to the fumes. Reductants in the charge can be optimised to recover as much as possible of the formed SiO gas. In another example, Barcza et al. [7] demonstrated the possible formation of significant quantities of Mg and SiO gas in case the slag bath got overheated in a DC FeCr smelting operation.
- Ignoring How Materials Move Inside the Furnace
  The furnace is not a perfectly stirred reactor, nor is it a single-zone reactor where all input materials mix, react, and separate as given in Fig. 1. Though such a calculation based on composition and temperatures of input and output streams plus the heat losses will give an idea about the overall process, it will not give insight to how the process works.

  Material streams can split, segregate, and move co- and counter-current to other streams, with which they can mix, interact, and react. Some feed material can short circuit to the slag taphole, while a stream of formed SiO gas could interact and react with a falling stream of particles. Only a model with a lot of flexibility could try to simulate that.
- Furnace Size and Physics
  The bigger furnaces get, the more important it becomes to consider the presence of different zones with different temperatures, as well as the transport of materials between those zones. Feed materials and gases travel longer distances, giving more time for new equilibria to develop. Estimations for shell volumes of DC furnaces are in the range of 1500–2000 m^3 for Koniambo and Kazchrome. The SNNC AC furnaces (FeNi) have shell volumes of 3800 m^3 for the round, 3 electrodes furnace [8] and just over 5000 m^3 for the rectangular, 6 electrodes furnace [9]. Possibly cubic meter of furnace per electrode in relation to furnace load could be used as an indicator for the effect of furnace size and load on physics, and this may be worth investigating, a bit in line with the work done by Hundermark and Nelson [10].

Multi-zone Modelling of a DC HCFeCr Furnace

Multi-zone dynamic modelling can at least partially address some of the issues mentioned. The concept has, for example, been generally described in 1995 [11], and examples include ilmenite smelting in a DC furnace [12], fuming of zinc from lead slags in a DC furnace [13], or lead smelting in a top submerged lance smelter [14].

In Fig. 2, a version of a multi-zone model is given for a DC HC FeCr furnace made in HSC SIM. Material streams, or parts thereof, can be directed from each numbered zone to any other numbered zone. Each numbered zone can be given its own temperature, heat flux, and calculation type (mixing or equilibrium).

With simulations it is important to realise what the limitations are. Two important considerations of HSC dynamic simulator are

- HSC SIM is not a CFD-type software but is used to do thermochemical and mass balances for reactors and flowsheets. The HSC model cannot estimate freeze linings, build-ups, or simulate how(much) energy transfer takes place via radiation, convection, or conduction. The tool is specifically of interest to understand energy flows, transported both physically and chemically by streams of materials. Other energy streams can be allocated to reaction zones in a similar way like material streams.
- HSC by itself does not calculate the activity coefficients for species, but the values can be fixed and/or adjusted in a transparent manner, especially as furnaces usually operate in a certain operating window. In this case, activity coefficients are approximated by an equation that considers C:Cr_2O_3 ratio and temperature,

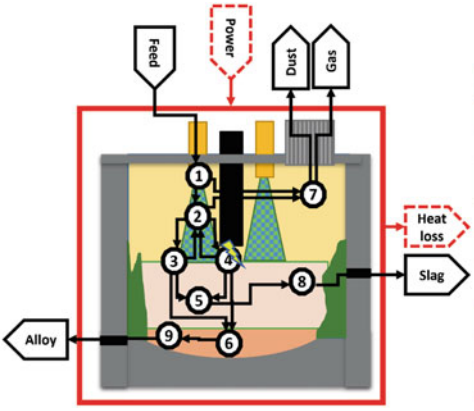

Zone	Description
1	Feed entering, 25°C
2	Freeboard reaction zone, 25 – 1600°C
3	Bulk slag bath reaction zone, 1800°C
4	AAZ reaction zone, 1800 – 2500°C
5	Bulk slag bath mixing zone, 1800°C
6	Bulk alloy bath mixing zone, 1800°C
7	Pre-stack mixing zone, 1200 – 1600°C
8	Pre-tapping slag zone, 1800°C
9	Pre-tapping alloy zone, 1700°C

Fig. 2 Multi-zone model where feed material enters the furnace in 1, dried to then fall through the freeboard reaction zone 2 and end up in the colder slag bath 3 or the hotter arc attachment zone 4. Formed slags and alloys from zones 3 and 4 mix in zones 5 and 6, respectively. Zones 8 and 9 allow for cooling of, respectively, slag and alloy to reach tapping temperature, or even interact with short-circuiting material streams. Process gases from zone 3 and 4 react in the freeboard reaction zone 2 with incoming feed

based on FactSage estimates of activity coefficients and experimental published data in the case that there are no appropriate solution models available in FactSage for specific components.

Showcase Using the Multi-zone Dynamic Simulation Model

In this section, a simplified version of the model shown in Fig. 2 will be used to show how such a model can be used to reduce risks of containment loss by getting better insight to the process.

From Balanced Feed-to-Power Ratio to Underfeeding

In open-bath processes, it is important to maintain the feed-to-power ratio (FtP). With the correct FtP the total feed input is exactly matched to the energy required for the process plus the energy to compensate for heat losses. If the FtP is set too high, then more material is charged than can be smelted, meaning the furnace burden/bath will freeze. If the FtP is set too low, then the surplus of energy can heat up the process, change equilibria, and create possibly undesired side reactions. As argued by Barcza et al. [7], the actual FtP should be within 0.5% accuracy of the FtP for a perfect balance between feed rate and energy input.

Part A

To simulate the possible effects of a reduction of 5% in feed-to-power ratio, a model was used as defined by Fig. 3.

- Smelting of chromite at 40 MW was balanced and calibrated, which includes the furnace heat losses and internal energy flows. All feed passed through drying zone 1 into smelting zone 3, and all 40 MW goes to zone 3.
- The energy lost from, gained in, or required for each zone to maintain the balance is calculated and set to a fixed value.
- Next, the furnace is filled with a slag bath 8 and an alloy bath 9 made of the slag and alloy of the calculated equilibrium compositions above.
- Slag formed in zone 3 mixes with the slag bath 8.
- Alloy formed in zone 3 mixes directly with the alloy bath 9.
- The formed process gas interacts in zone 7 with mechanical dust which then leaves via the stack.
- A simplification is that in the current simulation, the physical heat losses of the furnace are considered constant.

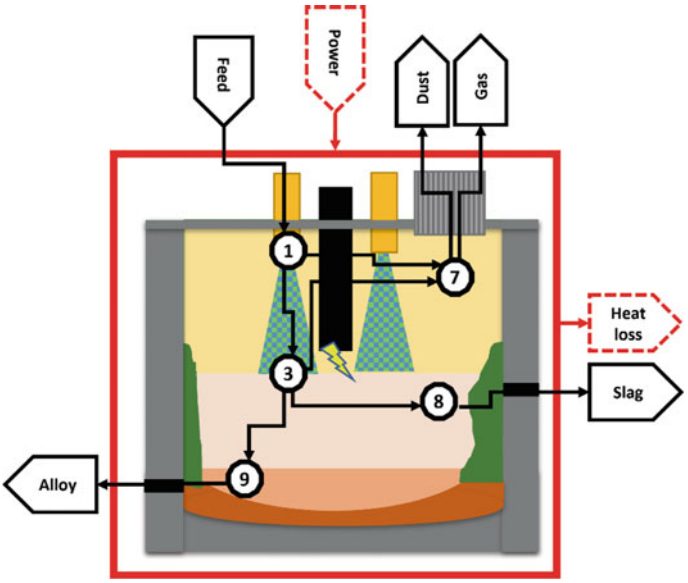

Fig. 3 Simple multi-zone model where feed material after drying in 1 reacts in the bath 3, from where slag goes to the slag bath 8 and alloy goes to the alloy bath 9 collect in separate volumes, and the process gases interact with the mechanical dust in 7

- After 20 min, the feed rate is cut by 5%, meaning that an underfeeding situation is created. This is shown in Fig. 4.
- Instantly the temperatures in the reaction zone increases and the reaction products from the reaction zone change, as is shown on the left in Fig. 5 but noticeable only for C, Si, and temperature.
- After 40 min the reductant charging rate is increased by 10%, giving a higher C content in the feed, as shown by the C:Cr_2O_3 ratio in Fig. 4. Note this increases the FtP too. Instantaneously, the reaction products from zone 3 change, shown on the left in Fig. 5.

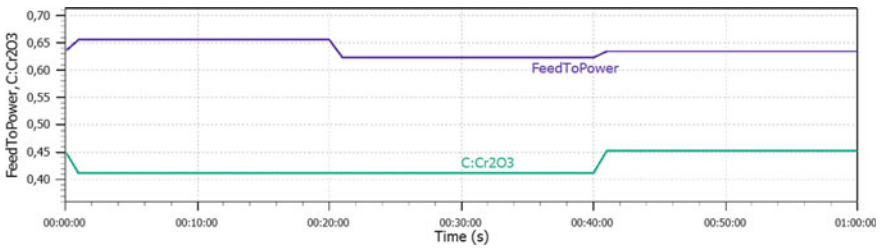

Fig. 4 Overview of the 1-h simulation where first the feed rate is cut to simulate a too low FtP, and next the reductant feed rate is increased to simulate a too high C content in the feed

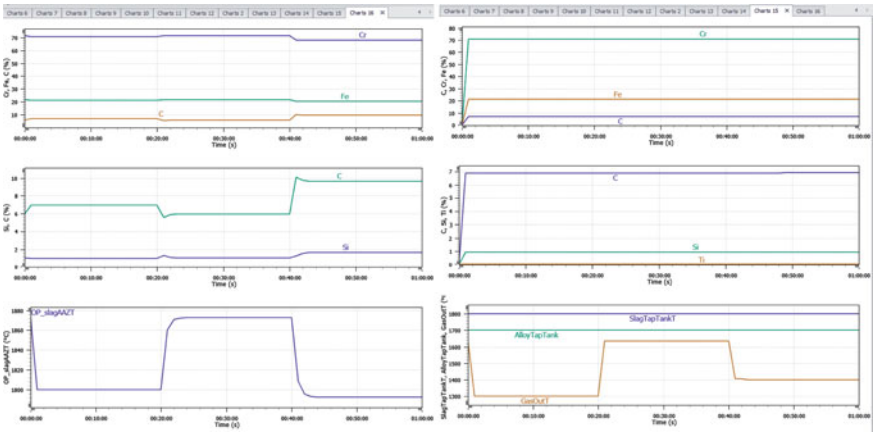

Fig. 5 Graphs of 1 h of simulations with on the left the data for zone 3 only where a response in composition is shown in the top two graphs. The bottom graph shows the temperature of all reaction products as these leave zone 3. On the right the effect on the total alloy bath. The upper 2 graphs show compositions and the bottom one the temperatures of gas leaving the furnace, the slag bath, and the alloy bath. Only an effect is visible on off-gas temperature because this responds more instantly

- The effect on the total slag bath in composition and temperature is after 1 h negligible, as can be seen on the right side of Fig. 5.

The changes made have effects both on the freshly produced materials, consisting of small quantities per time unit, and on the entire furnace bath. Some results are shown in Fig. 5 with on the left the changes to the total composition of the freshly produced alloy, and on the right the effect on the composition of the total alloy bath.

As can be seen, effects of a 5% FtP change followed by a 10% increase in reductant are visible on the freshly produced material in the left side of Fig. 5: the formed alloy is completely different. When looking at changes in the total bath in the right-hand side of Fig. 5, the effect on composition and temperature is near negligible over a short period of time. A high Si content in the alloy could damage alumina-chrome refractory, leading to containment problems.

Results for slag, not shown, show less detectable changes in the reaction zone and near undetectable in analyses of the slag bath and thus tapped slag.

Another result, not shown, is that a too low FtP ratio regarding the energy balance can be corrected for by only increasing the amount of reductant. The increased presence of C allows more endothermic reactions, thus fixing the energy balance by compensating for the lack of ore. However, the products are different. This can lead to a situation where the energy balance is in order, but slowly compositions of the baths are changed, possibly with negative effects for product quality, refractory, liquidus temperature, and tapping.

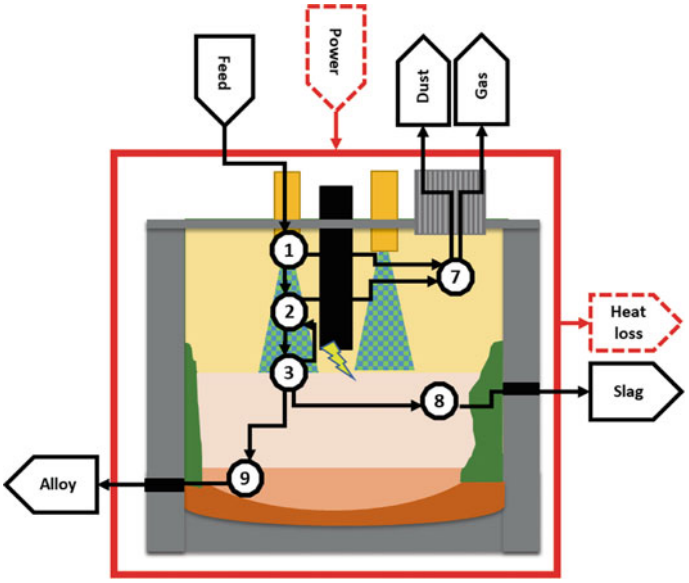

Fig. 6 Model where falling feed interacts in zone 2 with the process gas coming from the reaction zone 3

Part B

The results can be compared with the same input values for the case where the process gas does interact with the falling feed as depicted by Fig. 6.

In this model, only 70% of the electrical power input is needed for the reactions in zone 3 since significant work has been done in zone 2 by preheating and pre-reduction. The products from zones 1 and 2 are given in Table 1. Depending on the equilibrium temperature set for zone 3 for the Gibbs calculation, this variation explores the interaction of process gas and falling feed and illustrates the formation of significant quantities of Cr_3C_2. If the temperature in this zone reaches 1300 °C, and reaction time is sufficient, it would be clear then that most Fe will be pre-reduced, while most Cr will be present as Cr_3C_2.

For ease of comparison, the formed oxide phases were calculated back to the species shown. Instead of the feed mix arriving directly in zone 3, now an intermediate product arrives in the slag bath. Composition, quantity, and temperature are different.

Note that the freeboard reaction zone 2 is now a single-step equilibrium reaction with a single equilibrium temperature. Multiple steps may be required to simulate the counter-current behaviour of process gas and charged feed.

Having postulated the above, significant emphasis should be on process kinetics/mass transfer and therefore the time aspect. Questions such as (i) How fast do ore particles heat up, (ii) are entire particles, or only the surface, and (ii) is the time in the freeboard enough to allow for the heat exchange and reactions need to be addressed. Arguments in favour of fast heating and kinetics include the facts that the

Table 1 Comparison of the material mix that leaves drying zone 1 and reaction zone 2

		Feed mix after drying in zone 1	Feed mix after reactions in zone 2
Flowrate	tph	25.6	20.2
Temperature	°C	25	1300
Cr_2O_3	m-%	38.2	16.1
CrO	m-%	0	2.6
FeO	m-%	10.1	0.1
MgO	m-%	15.9	20.2
SiO_2	m-%	8.2	10.4
Al_2O_3	m-%	8.8	11.2
CaO	m-%	0.6	0.7
Ti_2O_3	m-%	0.1	0.1
C	m-%	15.7	6.3
LOI	m-%	2.3	0
Cr-C-alloys	m-%	0	22.3*
Fe-C-alloys	m-%	0	10**
Sum	m-%	99.9	100

* Mainly Cr_3C_2
** Mainly Fe

- ore is very fine,
- Mg(g) and SiO(g) gas are present, and
- atomic (Boudouard) C is present due to reactions between Mg(g) and SiO(g) gas with CO(g) gas, as well as probably from the Boudouard reaction between reductant in the feed and any CO_2 formed from reduction by CO(g) gas.

In this model set-up, alloy formed in zones 2 and 3 flows directly into the alloy bath. In reality, the formed alloy falls through the slag bath where it could react with the slag. Especially at temperatures above 1800 °C, FactSage shows that C and Cr in alloy will both act as a reductant for MgO and SiO_2 in the slag. Barcza et al. [7] showed something similar where at high temperatures MgO and SiO_2 were preferentially reduced by added reductant, but without investigating the interaction of the formed process gas with the counter-current falling feed mix.

Combining different areas of expertise remains necessary. Observations from the field can give a feeling for operational variability or valuable observations regarding behaviour of the operation, while CFD simulations can shed light on heat transfer and mass flows inside a furnace.

The above implies that the proposed model can still be modified in various ways to more fully explore the different operating regimes and modes. Results could then be applied to or compared with other open-bath smelting processes like titania slag, charge chrome, or DRI.

Relevance to Furnace Integrity of the Dynamic Simulation Results

DC furnaces are believed to be extremely sensitive to control of the FtP ratio. While it is not denied being very careful regarding the FtP, the sensitivity may be more complicated as it does appear to depend at least on

- possibility for fuming of slag compounds, acting as a brake on the heating-up of a bath,
- the intermediate products that can form, and
- the volume of slag and alloy bath present.

Therefore, all can be used to improve operational safety and campaign life by process design. The following points may be highlighted:

- Stronger formation of Mg(g) and SiO(g) gas than observed in analyses is possible. These gases can condensate or cause sticking of feed in the cooler zones of the furnaces, ducts, and feed pipes and block these.
- Mg(g) can form solid deposits, that upon breaking loose are dislodging, and then subsequently falling into the slag bath can cause significant eruptions.
- A strong interaction with falling feed of SiO and Mg gases can prevent those issues but may allow for formation of carbides with a very high melting point. Such carbides may not "transform" to Cr_7C_3 before reaching the tap hole, and the increased quantity of suspended Cr_3C_2 solids may cause tapping problems due to increased viscosity.
- Alloy from the alloy bath or falling through the slag bath can act as a reductant for MgO and SiO_2 in the slag.
- Larger baths have the advantage that changes to its chemistry are slower. Additionally, bath movement near the slag wall can be less than when the same load is applied in a smaller furnace.
- Deeper slag baths may prevent unwanted side reactions between the slag and alloy baths.
- Formation of Mg(g) and SiO(g) can cause a relative increase in
  - CaO in a part of the slag which may damage refractory.
  - Al_2O_3 in tapped slag which could lead to the incorrect conclusion alumina refractory is dissolving.
- Knowing what to look for can prevent being surprised by operational problems.

Summary

Furnace containment systems cover more than refractory, steel, and cooling systems only. Using experience on containment from the chemical industry and sharing operational experience from ESFs are two ways to increase understanding and ideally reduce containment issues. Focusing on process simulations, following items are to consider:

- Dynamic multi-zone modelling is nothing new and is a useful tool for understanding what could happen or has happened inside a furnace, because it allows to investigate process steps and intermediate products.
- Examples are given how the multi-zone modelling exposes possible internal process routes and how these could affect operation and thus furnace containment.
- Different intermediate products or reaction species can form under different process pathways, even when the products leaving the furnace show no significant difference.
- The larger the furnaces are, the harder it may become to detect process-related problems early due to dilution effects of large volumes for alloy, slag, and freeboard. Off-gas and dust show more plug-flow behaviour and could be valuable sources of information.
- FtP control loops should always be combined with mass balancing control to ensure both the energy balance and composition and quantity of final products are according to expectation.
- Multi-zone modelling allows for theoretical testing of many scenarios, which in turn could be linked with other information sources, ranging from pilot testing and industrial operation to CFD and furnace dig outs. By combining all sources, it may be possible to ensure controlled containment as long as possible.
- Recognizing deviations and responding swiftly and correctly is only possible if multiple scenarios had been investigated. Investigating an occurring problem during operation is hard, risky, and expensive.
- If DRI will be processed in open-bath furnaces, probably with some kind of FtP control, care must be taken to consider what could happen in the different reaction zones in relation to the furnace design. The feed, alloy, and slag will differ from open-bath production in ferrochrome, titania slag, and ferronickel, so careful process design is recommended.

References

1. Process Safety Integrity (2023) Loss of containment. https://processsafetyintegrity.com/incidents/loc/. Accessed 2 Sept 2023
2. Center for Chemical Process Safety (1999) Guidelines for chemical process quantitative risk analysis, 2nd edn. Wiley, New York

3. Oterdoom H (2014) Furnace explosions with a focus on water—part 1. Paper presented at the 53rd annual conference of Metallurgists, Vancouver, Canada, 28 September–1 October, 2014
4. Oterdoom H (2014) Furnace explosions with a focus on water—part 2. Paper presented at the 54th annual conference of metallurgists, Toronto, Canada, 23–26 Aug 2015
5. Roos W, Bogaers A, Zietsman J (2022) Geometrical acceleration of complex equilibrium calculations for integration in high-temperature models. https://www.researchgate.net/publication/359891998_Geometric_acceleration_of_complex_chemical_equilibrium_calculations_-_Algorithm_and_application_to_two-_and_three-component_systems.pdf. Accessed 13 Sept 2023
6. Zietsman J (2004) Interactions between freeze lining and slag bath ilmenite smelting. https://www.researchgate.net/publication/328968752_Interactions_Between_Freeze_Lining_and_Slag_Bath_in_Ilmenite_Smelting.pdf. Accessed 13 Sept 2023
7. Barcza N, Curr T, Jones R (1990) Metallurgy of open-bath plasma processes. Pure Appl Chem 62(9):1761–1772
8. Rodd L et al (2010) SNNC: a new ferronickel smelter in South Korea. Paper presented at the 12th international ferroalloys conference, Helsinki, Finland, 6–9 June 2010
9. Sagermann T (2013) Order for SMS Siemag from Korea. SMS Siemag. Accessed 4 Sept 2021. Order for SMS Siemag from Korea. SMS Siemag to deliver the world's largest submerged arc furnace to POSCO SNNC (rudmet.ru). Similar information available at: https://www.rudmet.ru/news/1646/?language=en
10. Hundermark RJ, Nelson LR (2017) Considerations for scale-up of ferronickel electric smelting furnaces. JOM 69(2):335–342
11. Robertson DGC (1995) The computation of the kinetics of reactions between multiple phases. Paper presented at the EPD congress during the 124th TMS annual meeting, Las Vegas, Nevada 12–16 Feb 1995
12. Zietsman J (2022) Modelling of slag freeze linings: supporting furnace design and operation. https://www.researchgate.net/publication/359109174_Modelling_of_Slag_Freeze_Linings_to_Support_Furnace_Design_and_Operation.pdf. Accessed 13 Sept 2023
13. Robertson DGC, Nelson LR, Swamy KN (1994) Kinetic simulation of the zinc fuming of lead blast furnace slags in center-fed, hollow graphite electrode, DC plasma-arc furnaces. Paper presented at the 123rd TMS annual meeting, San Diego, Califórnia, 28 February–2 March, 1994
14. Rezende J et al (2021) A dynamic thermochemistry-based process model for lead smelting in the TSL process. J Sustain Metall. https://doi.org/10.1007/s40831-021-00387-7

Freeport-McMoRan Miami—Waste Heat Boiler Availability Improvements

Avi Nanda, Kurt Westerlund, and Bradley Fox

Abstract Freeport-McMoRan Inc. (FCX) uses ISASMELT™ top-submerged lance (TSL) technology for the primary smelting of copper concentrates at the Miami smelter. The furnace was installed in 1992 with a capture system designed to cool and contain molten splash, dust, and gases generated from smelting reactions. The capture system is comprised of water radiant roof and wall panels, some of which generate steam. "Waste heat boiler" (WHB) is often used to refer to the primary furnace's off-gas handling system because of the useful steam it generates. The waste heat boiler system must be available to operate the primary smelting furnace. Issues related to a waste heat boiler often make up a significant portion of a smelter's downtime. Thus, effectively maintaining and operating the waste heat boiler is critical to a smelter's overall effectiveness. The Miami smelter's boiler maintenance and operational improvements to date will be reviewed in this paper.

Keywords Copper smelting · Waste heat boiler · Off-gas

Introduction

The Miami smelter, established in 1915, now consists of an ISAMELT™ TSL furnace, an electric settling furnace, four Hoboken converters, two anode refining vessels with one casting wheel, and one double contact sulfuric acid plant. The ISA furnace off-gas system was designed and supplied by Ahlstrom now Sumitomo SHI FW (SFW) in 1992. The top of the furnace is contained by a set of four boiler panels, known as "roof blocks" supplied by Oschatz. The uptake (hood) above the furnace is a high-pressure system that does not recover waste heat. The uptake and waste heat boiler (WHB) are separated by a vertical expansion joint to allow for dissimilar

A. Nanda (✉) · B. Fox
Freeport-McMoRan Inc., Phoenix, AZ, USA
e-mail: ananda@fmi.com

K. Westerlund
Kamwest Oy, Helsinki, Finland

© The Minerals, Metals & Materials Society 2024

G. Alvear et al. (eds.), *Advances in Pyrometallurgy*, The Minerals, Metals & Materials Series, https://doi.org/10.1007/978-3-031-50176-0_3

Table 1 Miami Smelter WHB operating parameters

Copper concentrate feed rate (mtph)	118.5
Gas flow rate (Nm^3/h)	76,000
Dust mass flow (kg/h)	1840
Heat transfer (MW)	28.3
Steam drum pressure (bar(g))	55.2
Boiler operating pressure after superheaters (bar(g))	38
Superheated steam temperature (°C)	350
Steam generation (kg/h)	29,500

thermal expansion. The boiler has three main purposes: cool furnace off-gas, produce steam for process use, and dust recovery (Table 1).

The boiler water system is comprised of a steam drum, feed water pumps, circulating water pumps, headers with nozzles, boiler tube panels, and mechanical rappers. The downcomer section of panels (radiation) operates as the first region of steam generation in the waste heat boiler. The horizontal section (convection) consists of boiler panels, five saturated steam bundles, and two superheaters. The superheated steam is utilized to regenerate molecular sieves at the Miami Air Products Oxygen Plant, anode refining, and a steam turbine for a blast air blower. The off-gas exits into an electrostatic precipitator (ESP) supplied by Babcock and Wilcox which removes dust from process gas prior to sulphur dioxide conversion at the double contact sulphuric acid plant (Fig. 1 and Table 2).

Project Background

Extensive boiler panel replacements were completed in the 2019 plant turnaround. This included several radiation panels, and all convection wall panels. Following the turnaround there were several external boiler leaks, and issues with accretions restricting furnace draught. A multi-disciplinary focus group was convened to determine the root cause of the leaks, and to implement corrective/preventative actions. The focus group included a technical consultant (Kamwest Oy) who specializes in WHB solutions, and support from the original equipment manufacturer (SFW).

Boiler leaks are commonly caused by out-of-specification deionized water, excess thermomechanical stresses, dew point corrosion (commonly caused by undesired ingress air), undesired impacts (commonly caused by the process or rappers), and poor-quality control (manufacturing or install). Water quality is managed by periodically sampling and addition of necessary chemicals. Water conductivity is continuously monitored with the process variable having alarm limits set in the human–machine interface. The potential for explosions caused by combustion of natural gas or volatiles can be prevented with effective operating procedures and process automation (Fig. 2).

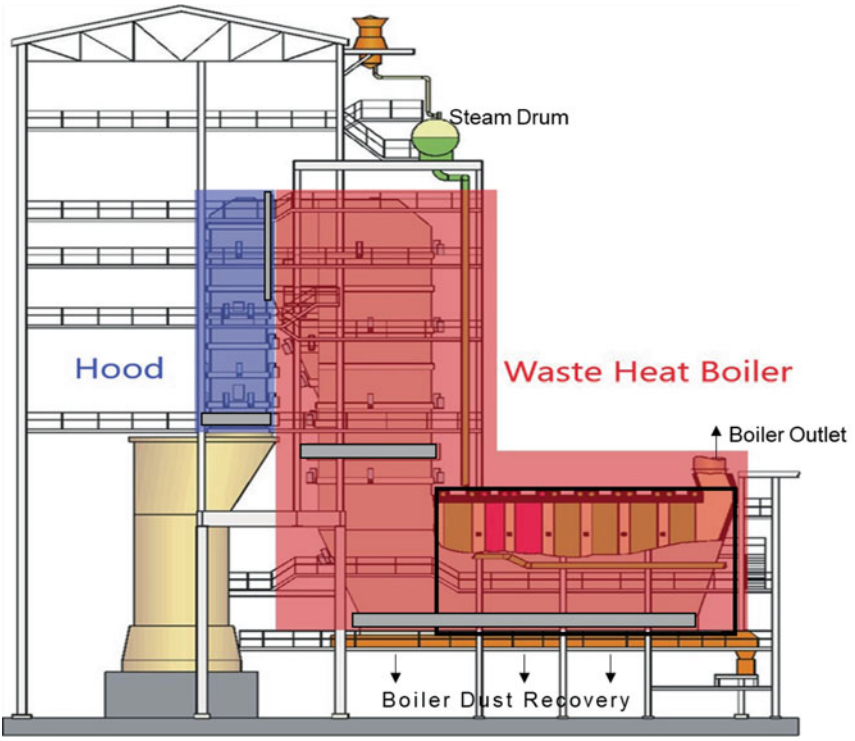

Fig. 1 Miami Smelter ISASmelt off-gas overview (expansion joints shown in grey)

Table 2 Off-gas temperature in various WHB regions

	Gas inlet	Uptake hood outlet	Convection section inlet	Boiler outlet
Temperature (°C)	1205	1038	788	405

The convection section is designed to expand nearly 50 mm horizontally when at maximum operating temperature. The convection section inlet temperature and oxygen in off-gas composition are critical parameters to monitor and control to mitigate accretions forming in the convection section (Fig. 3).

A main horizontal beam supports the convection bundles and wall panels. The bundles and wall panels thermally expand horizontally together towards the boiler outlet, and downwards (Fig. 4).

Fig. 2 Sulphur dioxide dewpoint corrosion of boiler tube due to ingress air

Off-Gas Control

Dust originates from the smelting bath and to a minor extent from the copper concentrate directly which can by-pass the bath to the uptake. The dust coming from the bath also contains entrained slag particles. The slag particles are mostly composed of fayalite slag. These molten tiny droplets fall out on uptake walls; they freeze and are knocked down by wall hammering and occasionally safe blasting (Table 3).

WHB Off-Gas Reactions

The WHB acts as a reactor of the dust and gas. Inside the furnace (temperature about 1200 °C) the stable form of metals are oxides. As the temperature decreases the stable form converts from oxides to sulfates. This occurs at varying temperatures for different metals. Figure 5 shows the sulfation driving force is high at lower temperatures. Metal oxides are prone to sticking to boiler tubes and prove difficult to remove. The oxygen content can be increased by injecting air to assist with sulfation occurring at a higher temperature. This will prevent accretions on the convection section walls, tube bundles, or electrostatic precipitator (Fig. 5).

Figure 6 shows how the increase in oxygen O_2 content at 40% SO_2 increases the formation of SO_3. The equilibrium curve moves upwards with more oxygen O_2 content in the gas. This explains the reaction $Cu_2O + 2SO_3 + 1/2O_2 = CuSO_4$ and how an increase in SO_3 and O_2 drives the reaction towards $CuSO_4$ (Fig. 7).

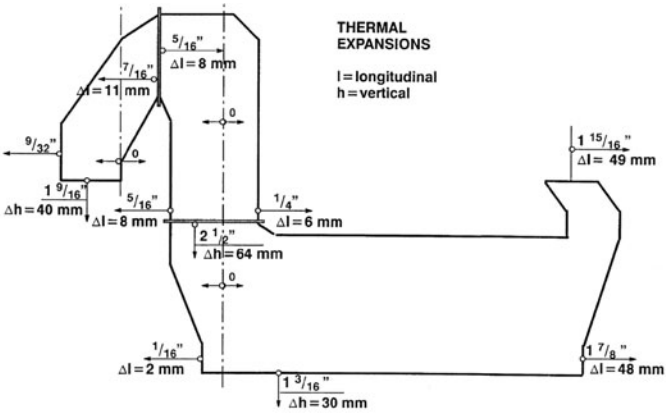

a Original Thermal expansion map with fixed points, horizontal and vertical specifications from IOM

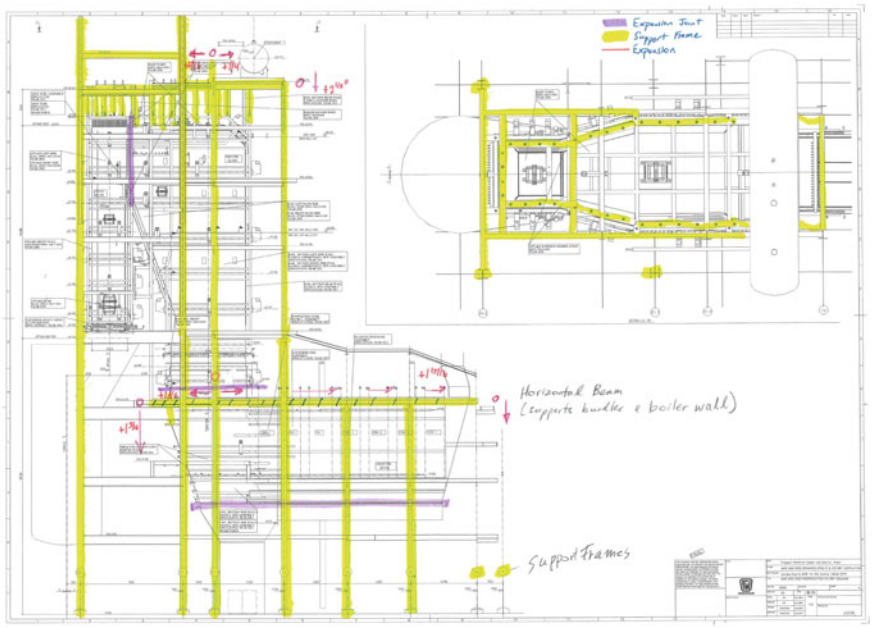

b Existing boiler structure with key thermal expansion specifications

Fig. 3 **a** Original thermal expansion map with fixed points, horizontal and vertical specifications from IOM. **b** Existing boiler structure with key thermal expansion specifications

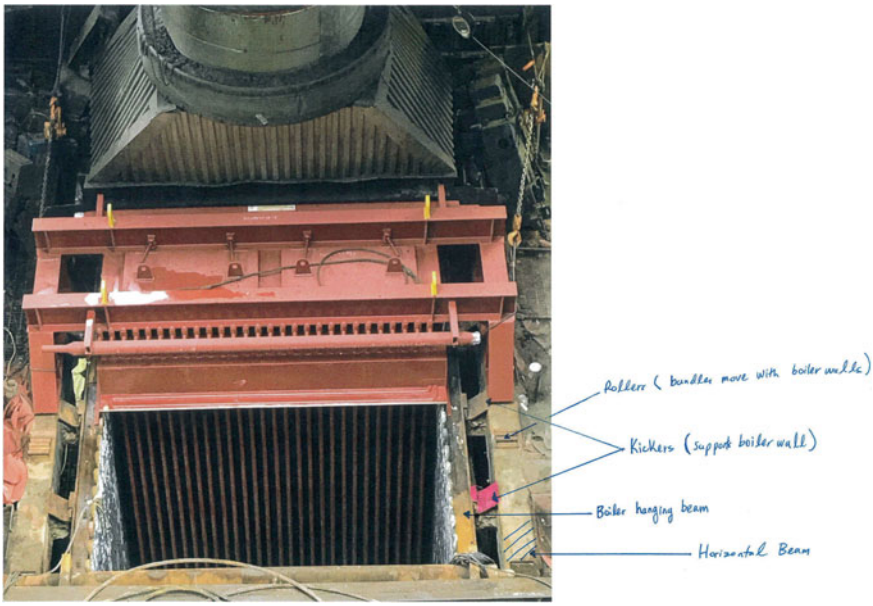

Fig. 4 Boiler convection section outlet side top-view with one bundle removed

Table 3 Typical ISASmelt off-gas composition at FMI Miami Smelter

INPUT SPECIES (4) Formula	Temper. °C	Amount kmol	Amount kg	Amount Nm³	Latent H kWh	Total H kWh
GAS INTO Smelter WHB	1111.000	2869.954	104537.723	64326.000	35040.59	-97158.62
O2(g)	1111.000	56.825	1818.335	1273.655	574.45	574.45
SO2(g)	1111.000	867.300	55558.203	19439.317	13648.27	-57858.93
CO2(g)	1111.000	52.233	2298.771	1170.733	796.14	-4911.31
H2O(g)	1111.000	818.511	14745.637	18345.775	9749.87	-45232.69
N2(g)	1111.000	1075.085	30116.778	24096.520	10269.87	10269.87
Dust	1111.000	10.022	1558.665	4.772	300.25	-1011.96
Cu2O	1111.000	1.784	255.270	0.943	41.86	-41.69
Fe3O4	1111.000	1.744	403.816	0.978	108.91	-431.51
S2(g)	1111.000	0.201	12.890	4.506	2.21	9.39
PbO	1111.000	0.762	170.105	0.918	18.29	-27.87
ZnO	1111.000	3.989	324.637	0.958	60.27	-325.66
Cd	1111.000	0.095	10.678	0.001	1.00	1.00
NiO	1111.000	0.004	0.275	0.000	0.06	-0.18
Se	1111.000	0.025	1.942	0.000	0.29	0.29
Bi2O3	1111.000	0.483	224.867	0.025	27.69	-49.26
As2O3	1111.000	0.711	140.705	0.038	35.01	-94.35
Au	1111.000	0.000	0.000	0.000	0.00	0.00
Ag	1111.000	0.000	0.000	0.000	0.00	0.00
SiO2	1111.000	0.224	13.483	0.005	4.66	-52.12
Sulphatisation Air	25.000	535.389	15446.158	12000.000	0.00	0.00
O2(g)	25.000	112.432	3597.681	2520.000	0.00	0.00
N2(g)	25.000	422.957	11848.477	9480.000	0.00	0.00

OUTPUT SPECIES (4) Formula	Temper. °C	Amount kmol	Amount kg	Amount Nm³	Latent H kWh	Total H kWh
GAS INTO Smelter WHB	350.000	2869.954	104537.723	64326.000	9367.89	-122831.31
O2(g)	350.000	56.825	1818.335	1273.655	157.69	157.69
SO2(g)	350.000	867.300	55558.203	19439.317	3561.36	-67945.84
CO2(g)	350.000	52.233	2298.771	1170.733	203.35	-5506.11
H2O(g)	350.000	818.511	14745.637	18345.775	2580.80	-52401.76
N2(g)	350.000	1075.085	30116.778	24096.520	2864.69	2864.69
Dust	350.000	2.240	1756.343	-209.347	110.35	-2230.74
CuSO4	350.000	3.568	569.454	0.158	39.08	-725.44
Fe3O4	350.000	1.744	403.816	0.078	29.11	-511.31
SO2(g)	350.000	-9.365	-599.903	-209.901	-38.45	733.66
PbSO4	350.000	0.762	231.119	0.037	7.91	-186.85
ZnSO4	350.000	3.989	644.003	0.169	45.63	-1340.42
Cd	350.000	0.095	10.678	0.001	0.40	0.40
NiO	350.000	0.004	0.275	0.000	0.02	-0.23
Se	350.000	0.025	1.942	0.000	0.11	0.11
Bi2(SO4)3	350.000	0.483	340.773	0.067	13.35	-327.72
As2O3	350.000	0.711	140.705	0.038	12.05	-117.31
Au	350.000	0.000	0.000	0.000	0.00	0.00
Ag	350.000	0.000	0.000	0.000	0.00	0.00
SiO2	350.000	0.224	13.483	0.005	1.15	-55.63
Sulphatisation Air	350.000	529.169	15247.118	11860.582	1421.77	1421.77
O2(g)	350.000	106.212	3398.641	2380.582	294.75	294.75
N2(g)	350.000	422.957	11848.477	9480.000	1127.02	1127.02
		kmol	kg	Nm³	kWh	kWh
BALANCE:		-14.002	-1.363	-353.536	-24440.84	-25469.71

CFD Modelling for Sulfation Air

The feed port in a TSL serves as a source of ingress air which will promote sulfation. The draught control (consistency and pressure) will affect the volume of ingress air and resulting off-gas temperature/oxygen content. Air can be injected in the off-gas system to increase the oxygen content and promote dust/gas mixing. Computational Fluid Dynamics (CFD) model was used to plan the best air injection inlet point angles and velocities. Figure 8 shows the flow model for the gas velocities in the Miami Smelter's WHB without and with sulfation air. Modeling concluded air injection

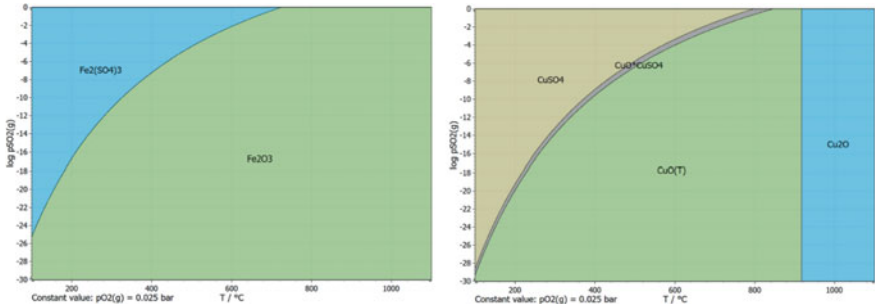

Fig. 5 The predominance areas of Fe-S-O and Cu-S-O at fixed oxygen partial pressure (0.025 bar) [1, p. 15]

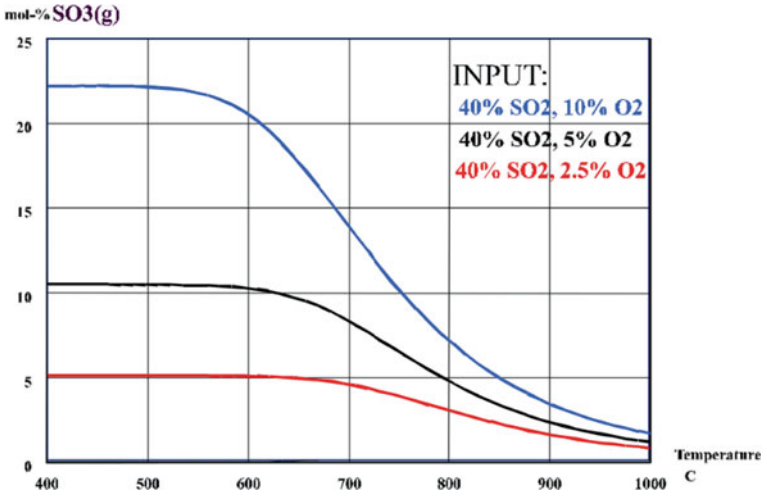

Fig. 6 Chart displayed SO_3 formation at varying off-gas temperature and oxygen compositions [2, p. 50]

through the hood and WHB roof (at certain angles) promoted off-gas mixing which would increase sulfation and lower the convection section inlet temperature.

Boiler/hood roof doors with nozzles were fabricated to complete a trial. The air injection pipes were composed of Hastelloy C to withstand the off-gas temperature and the potential of dew point corrosion from ambient air injection. Caps were installed at the end of the pipe to allow for punching of any blockages while the air supply was connected 45° to the injection pipe. The dust content in TSL off-gas is a function of some of the following operating parameters: blowing rate, lance depth, feed moisture content, feed size distribution, furnace draught, and feed alignment. The air addition was set to a fixed ratio to feed rate. Additionally, a minimum air flow rate was set to a velocity which would cool the pipes. The trial was conducted for 2 months while monitoring the convection section inlet temperature, convection

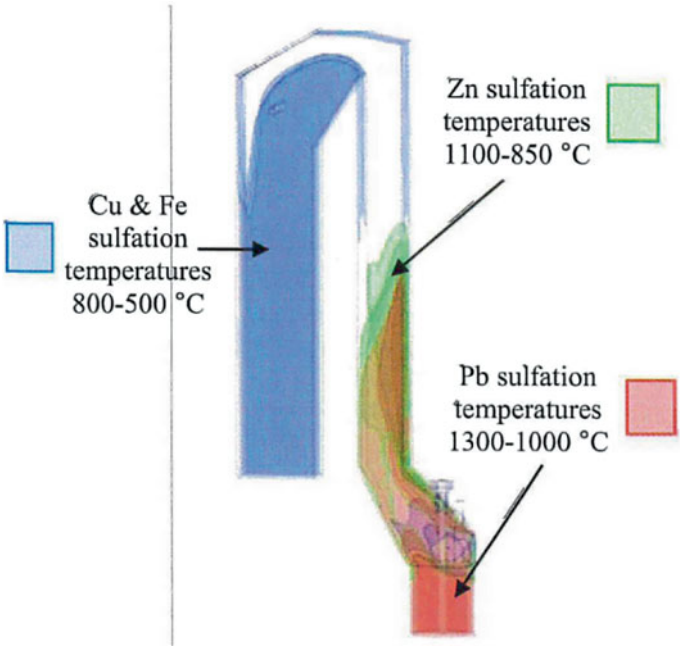

Fig. 7 Approximate dust sulfation locations in a top-submerged lance furnace (TSL) off-gas system (at −10 Pa) [3, p. 9]

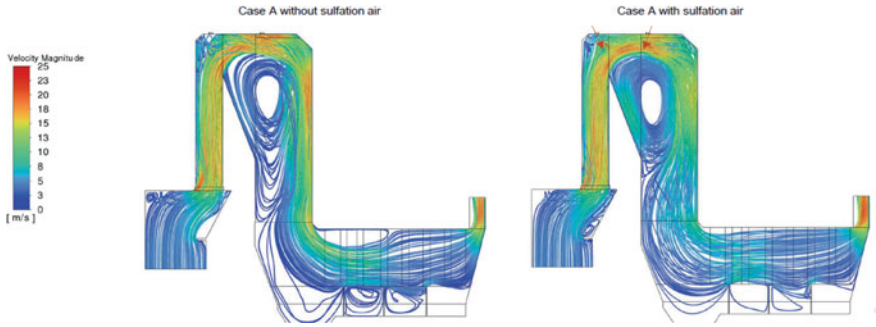

Fig. 8 CFD model completed by SFW for Miami' Smelter's off-gas system

section differential pressure, and convection dust. The trial was operated for 2 months and proved to be successful to mitigate accretions in the convection section (Figs. 9 and 10).

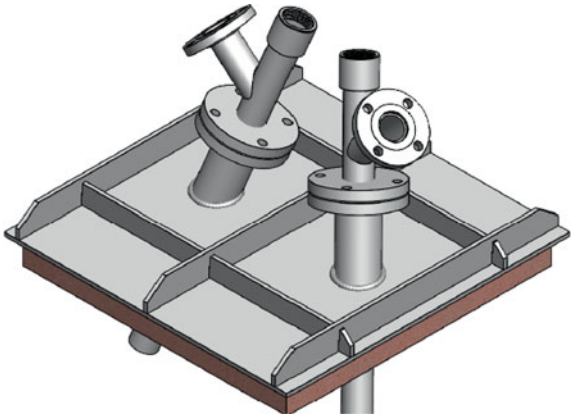

Fig. 9 Boiler door with air injection nozzles installed

Fig. 10 Sulfated dust reclaimed in convection section

Installation Improvements

Following OEM installation instructions is key to sustaining WHB reliability.

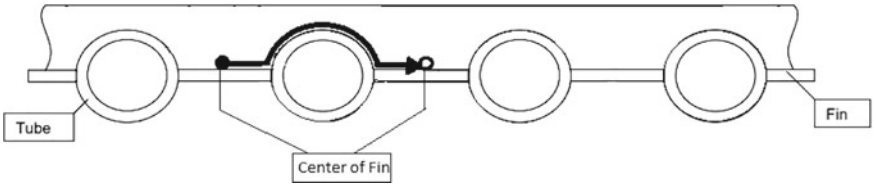

Fig. 11 Scallop bars welding procedure. Full weld that does not start/stop on tube

Buckstay Installation

The horizontal buckstays, I-Beams, are to keep the boiler walls from moving when the gas pressure inside the boiler varies. The buckstays are also used to transfer the hammer impact for boiler dust cleaning hammers through the boiler wall; this is the reason why they are welded to the boiler walls. Mechanical rappers should be set to as low as feasible frequency and impact settings to reduce stresses on backstays and boiler panels while removing build-up. In addition, the perpendicular alignment of the anvil attached to the backstay, and hammer impact square with the anvil is critical to ensure the force is evenly distributed across the backstay. When the boiler is heated up, the Buckstays must also be heated. If the inner part of the buckstay is hotter than the outer, the I-beam will bend and tear itself from the boiler wall, causing boiler leaks (Fig. 11).

Insulation

The sides of the I-beam must be kept free from insulation to allow for convective air heating in the open space under the insulation (Fig. 12).

Boiler Wall Panel Types

The boiler will corrode and start leaking at areas where the temperature of the boiler walls drops under the acid dew point; typical places are the concentrate feed port, lance port, doors, and where you have gaskets—leaking cold air into the boiler, e.g., in the dust hopper. Overlay welding protects against corrosion, erosion, and adds wall thickness to prolong lifetime. Alloy 33 overlay has been successfully utilized at the Miami Smelter to reduce corrosion damages and leaks. Alloy 33 has a high chrome concentration (28%) which offers the basis for excellent corrosion resistance in oxidizing media. A low addition of molybdenum improves phosphorus acid resistance and simplifies sulfuric acid passivation (Figs. 13 and 14).

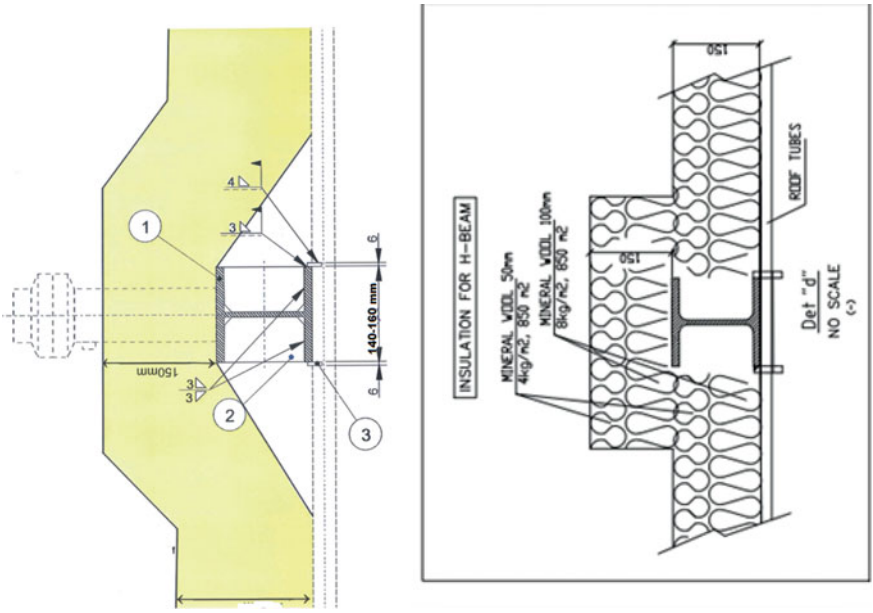

Fig. 12 Insulation example and specification for evenly heating buckstays

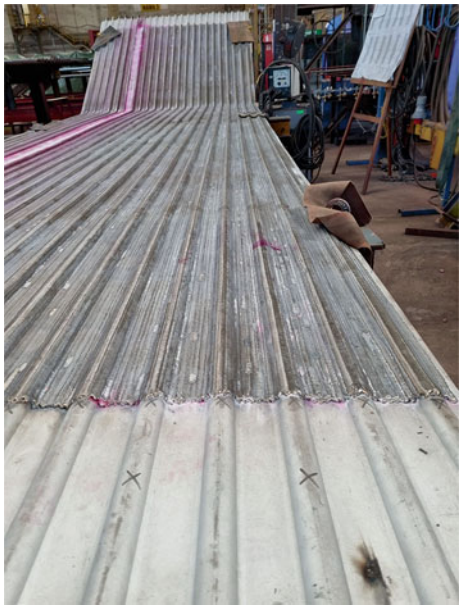

Fig. 13 Fin tube boiler wall with overlay welding

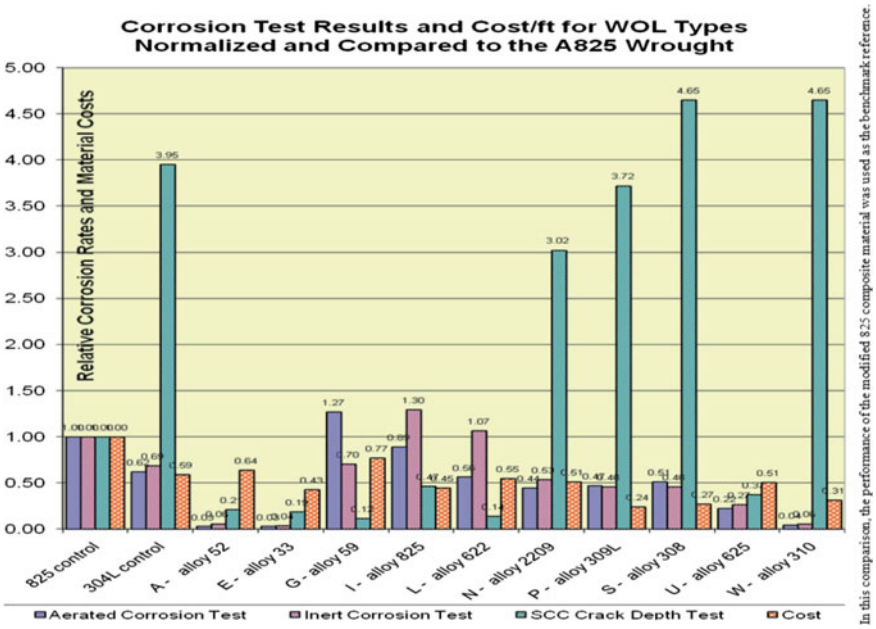

Fig. 14 Weld overlay materials corrosion testing [4, p. 3]

The Miami Smelter boiler uses membrane walls with overlay welding, omega panels, and double omega panels. Additionally, overlay welding on critical parts on the omega tubes. A wall with a smooth surface on the inside (normal omega tube) is preferred for a region like in the hood uptake which encounters slag from splashing. Double omega can be utilized in places that are difficult to reach, like in the apex. The double omega is stiffer than the single omega and is used in hoppers where we expect large accretions falling and bending the tubes (Figs. 15 and 16).

Fig. 15 Double omega tube on left; single omega on right

Fig. 16 Double omega panel with overlay cladding

Maintenance Improvements

Monitoring the boiler's thermal expansion and undesirable sources of ingress air are key to maintaining boiler health.

Managing Boiler Thermal Expansion

The boiler wall panels are attached to a set of guides which hold the panels in-line while allowing for thermal expansion (Fig. 17).

Excessive tensile stresses were determined to be the root cause of the external tube leaks in the convection wall panels. Upon inspections it was discovered that the pin in the boiler guides was lodged causing thermal expansion to be restricted. The boiler structure had moved over time causing misalignment of guides. After some discussion with SFW, it was decided to install new guides with a slightly wider

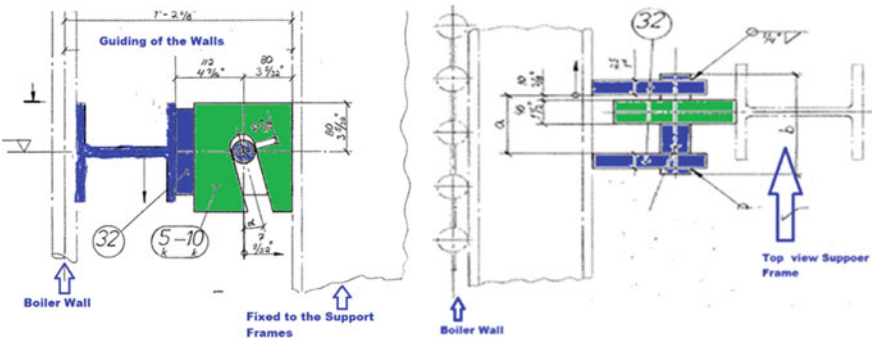

Fig. 17 Boiler guides attachment to guide beams and wall panels

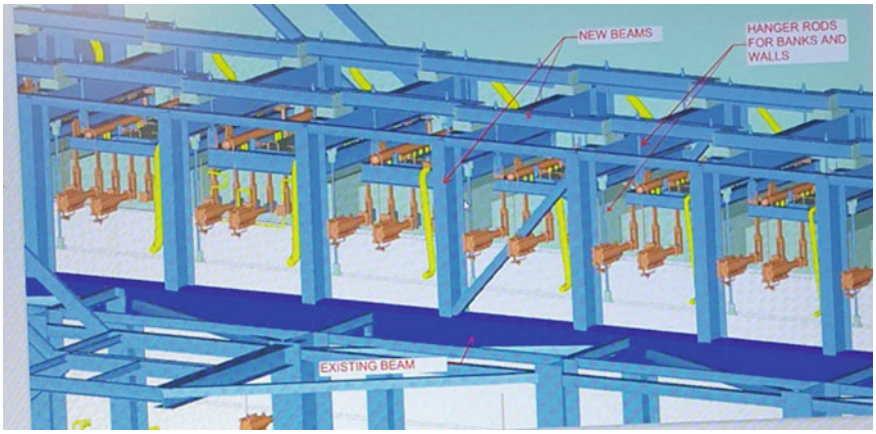

Fig. 18 Model of hanging structure for convection wall panels

slot opening to mitigate the guides restricting wall panel movements. The guides were replaced in a 4-day outage; no external leaks in the convection section occurred following the replacement of the guides. The cold and hot measurements are taken during every outage (see Fig. 3a) to monitor thermal expansion. The boiler expansion is now near the design specification because of the guides being replaced.

Convection Section Wall Panel Support Options

The convection section wall panels can be arranged by one of hanging support, rolling, or sliding. Hanging the convection section was considered as an option due to ease of maintenance (Fig. 18).

It was not pursued due to the heavy superstructure above the convection section where the convection bundles are lifted for replacement. It was instead decided to replace support from small rollers which have higher friction to smooth sliding pads during the next turnaround (Figs. 19 and 20).

Monitoring Ingress Air

Potential sources for ingress air must be identified (inspection doors, dust removal doors, expansion joints, roof blocks) and inspected on a frequent basis to mitigate undesired ingress air. A daily inspection route is completed using a machine which generates smoke. Smoke will be drawn in with the boiler draught if any voids are present. In addition, an off-gas oxygen analyzer downstream of the ESP is continuously monitored.

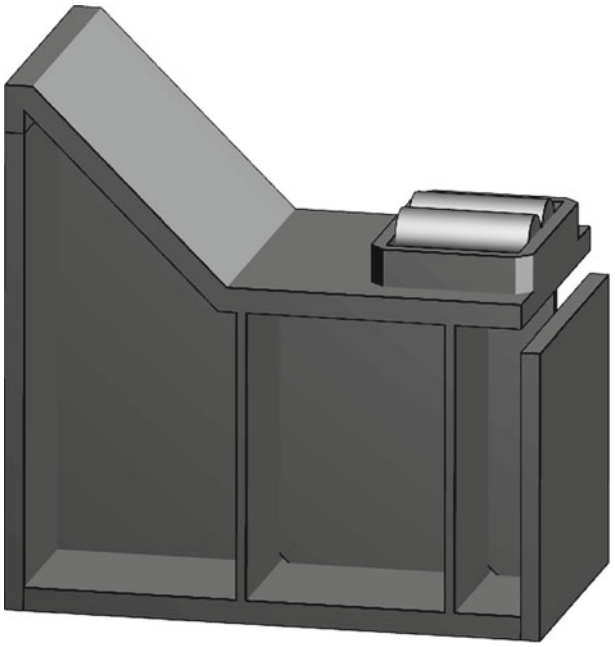

Fig. 19 Original convection section supports with small rollers

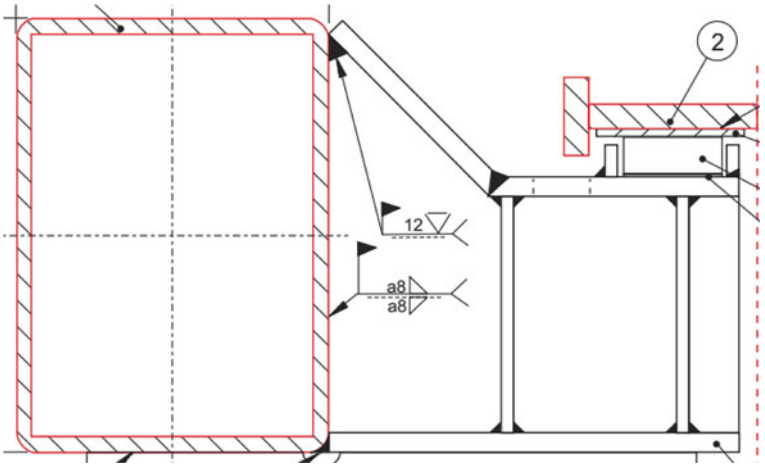

Fig. 20 Convection sections support cantilever console installation with sliding pads under boiler hanging beam (labelled 2)

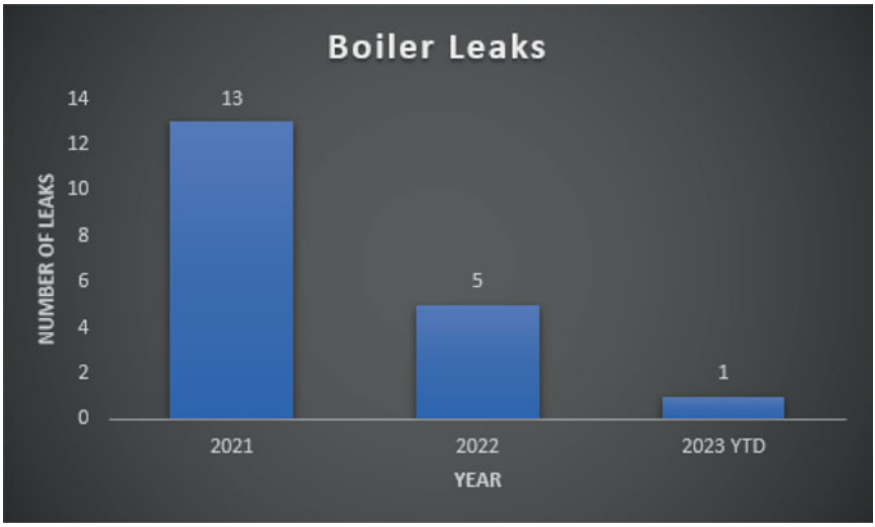

Fig. 21 Chart showing reduction in boiler leaks

Results

A significant reduction in boiler leaks was experienced in 2022, and year-to-day June 2023 because of the improvements implemented by the WHB focus group (Fig. 21).

The reduction in lost production due to improve operating, maintenance, and inspection practices contributed to a record annual throughput for the Miami Smelter (Fig. 22).

Drawings, procedures, and specifications generated during the focus group's efforts were documented. Additionally, work orders were generated in the enterprise resource management system (SAP) to ensure that inspections and maintenance activities were captured and completed.

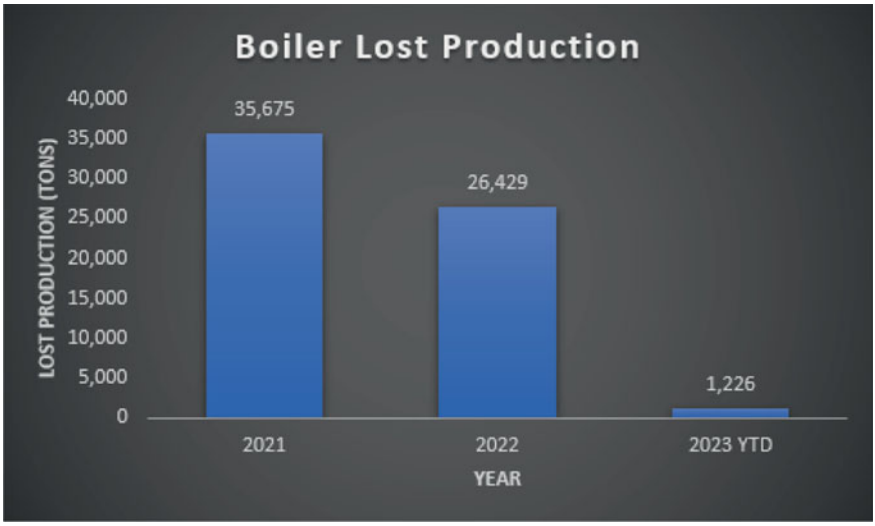

Fig. 22 Chart showing reduction in lost production from boiler leaks

Acknowledgements The authors would like to thank Freeport-McMoRan Miami management (Mark Albertsen, Michael Cross, and Miguel Palacios) for sponsoring the focus group. Sumitomo SHI FW's support was instrumental in developing these improvements (Jukka Nikarmaa, Tomi Raisanen, Rauno Peippo, Olli Jäntti, Jukka Pekkinen, and Heikki Lankinen). Also, SFW for permission to use some figures from their design. Risto Saarinen and Bengt Lindqvist of Kamwest Oy for their technical support. The Miami Smelter Converter Maintenance group (Sonny Tarron and Adam Mills) for their support in replacing the boiler guides. Lastly, the Miami WHB focus group team members (Larry Giannotti, Alexandro Guerrero, Chuck Durbin, Daniel Derhammer, Keith Taylor, Jeff Peltz, and Lonny Brewer) for their cooperation and efforts to complete the improvements.

References

1. Taskinen P, Jokilaakso A (2021) Espoo reaction sequences in flash smelting and converting furnaces: an in-depth view. Metall Mater Trans B 52B:3524–3542
2. Ranki-Kilpinen T (2004) Sulphation of cuprous and cupric oxide dusts and heterogeneous copper matte particles in simulated flash smelting heat recovery boiler conditions. In: Helsinki University of Technology Doctoral Thesis in Materials and Earth Sciences, Helsinki
3. Gwynn-Jones S, Conradie P, Nikolic S (2017) Using CFD analysis to optimise top submerged lance geometries. In: 12th international conference on CFD in oil and gas, metallurgical and process industries, Trondheim, pp 555–564
4. Kulig JA (2011) Weld overlay materials comparison for recovery boiler service. In: TAPPI pulping, engineering, environmental, recycling and sustainability conference, Portland

Composite Copper-Graphite Cooler for PGM Furnace Sidewall

Hugo Joubert, Gerrit de Villiers, Pfariso Mbedzi, and John Davis

Abstract The corrosion of copper cooling elements in the sidewall of platinum group metal (PGM) furnaces is unique in its severity and nature. 'Chloride-accelerated sulphidation' has been identified as the most likely corrosion mechanism and is prominent in the zone directly adjacent to the slag-concentrate interface. Tenova Pyromet developed a new composite copper-graphite cooler for implementation in one of Sibanye-Stillwater's circular PGM furnaces at their Marikana smelter complex. The cooler design is unique as, in addition to the hot face, the sides, bottom, and top of the cooler are completely covered with graphite, preventing contact between the copper cooler and the sulphur- and chlorine-bearing species thought responsible for the corrosion. The design of the cooler and test work performed to evaluate its effectiveness are discussed. The coolers have been in operation since August 2022. The implementation and performance of the coolers to date are discussed.

Keywords Platinum · Furnace containment · Copper cooling · Graphite · Heat transfer

Introduction

Sibanye-Stillwater's Marikana smelter complex currently consists of five circular electric smelting furnaces and three Peirce Smith-type converters. Furnace 1 and Furnace 2 are operated as the default furnaces and Furnaces 3–5 are used as standby furnaces. The feed material to the furnaces consists of PGM-based floatation concentrate and the furnace electrodes are operated in an immersed mode in the liquid slag bath.

Several crucible design improvements have been implemented on Furnace 1 since its commissioning in March 2002. In November 2020, Tenova Pyromet was awarded a study contract to perform the basic engineering and a cost-based estimate for a

H. Joubert (✉) · G. de Villiers · P. Mbedzi · J. Davis
Tenova Pyromet, Johannesburg, South Africa
e-mail: Hugo.Joubert@tenova.com

© The Minerals, Metals & Materials Society 2024

G. Alvear et al. (eds.), *Advances in Pyrometallurgy*, The Minerals, Metals & Materials Series, https://doi.org/10.1007/978-3-031-50176-0_4

further crucible upgrade on Furnace 1. One of the main objectives of the crucible upgrade was to increase sidewall campaign life from 30 months to a minimum of 48 months at a nominal power input of 15 MW. Following completion of the study Tenova Pyromet was contracted to implement the Furnace 1 crucible upgrade. The project commenced in May 2021 and the first matte was tapped from the upgraded furnace during September 2022.

The crucible upgrade included a complete redesign of the furnace hearth, sidewall and tapholes, an increase in crucible diameter, and the lifting of the matte taphole centre line above the hearth skew area. The sidewall redesign included the development of composite copper-graphite coolers installed adjacent to the slag bath and the slag-charge interface. The coolers are designed to form and maintain a competent slag freeze lining adjacent to the slag bath whilst reducing the risk of sulphidation corrosion of the cooled copper elements imbedded in each composite cooler.

Water-cooled copper cooling elements installed in PGM smelting furnace sidewalls adjacent to the slag-charge interface suffer from severe corrosion. Examples of worn sidewall copper plate coolers removed from one of the Sibanye-Stillwater smelting furnaces are shown in Fig. 1. Labile sulphur and small quantities of chlorides contained in the dried, un-calcined concentrates that are fed to the furnace have been identified as the culprits. The corrosion mechanism is best described as 'chloride-accelerated sulphidation' whereby the labile sulphur reacts with the copper to form copper sulphide as the main corrosion product, and where the corrosion process is likely accelerated by the presence of chloride-bearing species. The corrosion of water-cooled copper cooling elements in PGM smelting furnaces, as well as the sulphidation corrosion mechanism most likely responsible, has been well documented by others [1–5]. Tenova Pyromet independently commissioned test work to better understand the corrosion mechanism and kinetics, and to test a surface protection layer to potentially inhibit the corrosion process [6].

Fig. 1 Examples of corroded copper plate coolers removed from Sibanye-Stillwater Furnace 2

This paper provides an overview of the methods to protect sidewall copper cooling elements against sulphidation corrosion and a detailed description of the composite copper-graphite cooler designed for the Sibanye-Stillwater Furnace 1 crucible upgrade. Test work conducted to confirm the cooling efficiency and capacity of the cooler is described. The implementation of the coolers in the upgraded furnace sidewall is discussed. Finally, the performance of the coolers since the startup of the upgraded furnace is discussed.

Protection Against Sulphidation of Copper Coolers

Corrosion rates above 23 mm per annum for a copper test element tested at a temperature of 125 °C were reported during the test work commissioned by Tenova Pyromet [6]. The test work confirmed 'chloride-accelerated sulphidation' as the corrosion mechanism responsible for the copper cooling element wear. Tests were conducted at 90, 125, and 200 °C. The temperatures represent the typical range experienced by sidewall copper cooling elements during furnace operation. The wear rate recorded at 125 °C was an order of magnitude higher compared to that recorded at 90 °C. Shaw et al. [5] reported a similar ratio increase in wear rate with temperature. The wear rate recorded at 200 °C was similar to that at 125 °C. However, this could have been influenced by a relatively low exposure time at the test temperature due to limitations of the test rig [6].

Three potential remedies were identified to prevent or limit the sulphidation of the copper cooling elements. These include the application of a protective diffused coating (calorizing), a protective weld layer using materials such as Hastelloy, and the use of graphite to cover the exposed copper surfaces.

Calorizing, also known as aluminizing, is a diffusion metallizing process whereby aluminium is diffused into the surface of a base metal through high-temperature vapours. The diffused layer is typically 1 mm thick and does not change the high-temperature mechanical properties of the base metal, in this case copper. Calorizing has been successfully implemented in iron blast furnaces to protect copper tuyeres against damage from molten iron resulting in so-called hot metal "bullet-hole" burns [7, 8]. Tenova Pyromet has been investigating the use of calorizing since 2015 as a method to protect copper cooling elements against damage from superheated matte [9], as well as against sulphidation [6], and a patent was registered for the same [10]. Calorizing showed promise as a protective layer against sulphidation of copper during the commissioned test work [6]. Figure 2b shows the effects of sulphidation on an un-calorized and cooled copper test piece compared to an identical but calorized test piece in Fig. 2a. The black corrosion product visible in Fig. 2b consists mainly of copper sulphide. The corrosion rates were calculated for the cleaned test pieces (see Fig. 2c) by measurement of the mass loss during the test period. A zero corrosion rate was reported for the calorized test piece over the test period compared to 23.5 mm per annum for the un-calorized test piece.

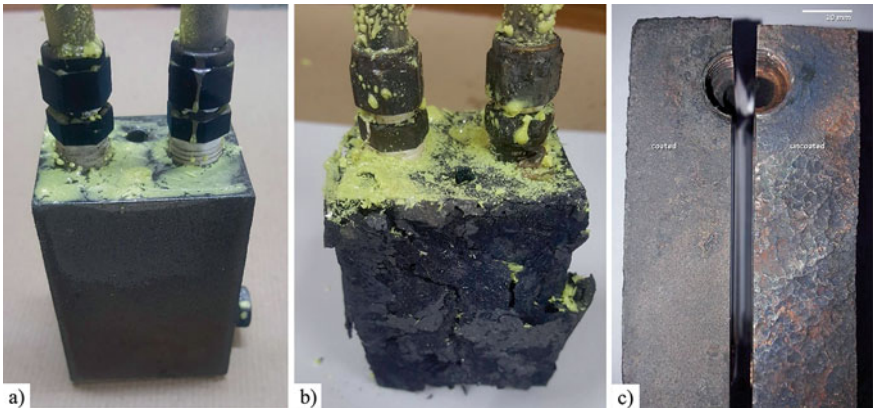

Fig. 2 Sulphidation test work at 125 °C for 5 days: **a** Calorized copper test block; **b** Un-calorized copper test block; **c** Cleaned calorized and un-calorized test blocks side by side [6]

Based on the promising test work results it was decided to calorize the hot face of one of the Sibanye-Stillwater Furnace 2 slag taphole blocks. The wear on the taphole block over the furnace campaign did not improve as expected. One hypothesis is that the thin carolized layer may have worn away through erosion or similar mechanisms and left the base copper metal exposed for sulphidation to take place.

The use of a welded Hastelloy layer on the surface of copper cooling elements to protect against sulphidation in PGM smelting furnaces has been investigated and implemented previously, including Sibanye-Stillwater [4]. A Hastelloy weld layer was applied to the front part of copper plate coolers during the Furnace 2 sidewall replacement in July 2020. The Hastelloy weld layer is machined flat with the rest of the plate cooler to ensure a tight interface and efficient heat transfer with the surrounding refractory bricks, see Fig. 3a. These coolers were removed and inspected in February 2023. As shown in Fig. 3b, the Hastelloy weld layer remained mostly intact whilst the base copper behind the weld layer suffered from sulphidation corrosion. The use of the Hastelloy weld layer on the copper plate coolers helps to extend the furnace sidewall campaign life. However, the cost of applying and machining the layer becomes prohibitive when applied to larger coolers and cooler surface areas.

Tenova Pyromet commissioned pot tests to evaluate the use of graphite in PGM smelting furnace sidewall linings [11]. Graphite was found to better resist corrosion by matte and slag produced in PGM smelting furnaces compared to traditionally used fused grain magnesium-chromite refractory bricks. When used in combination with copper cooling elements, the graphite temperatures can be maintained sufficiently low to prevent accelerated and prolonged oxidation of the graphite whilst forming a protective barrier against sulphidation of the copper cooling element surfaces [5]. Tenova Pyromet has separately recognised the potential of graphite to work in combination with copper cooling elements in PGM smelting furnaces to overcome the problem posed by sulphidation and foreseen its use in a patent [12].

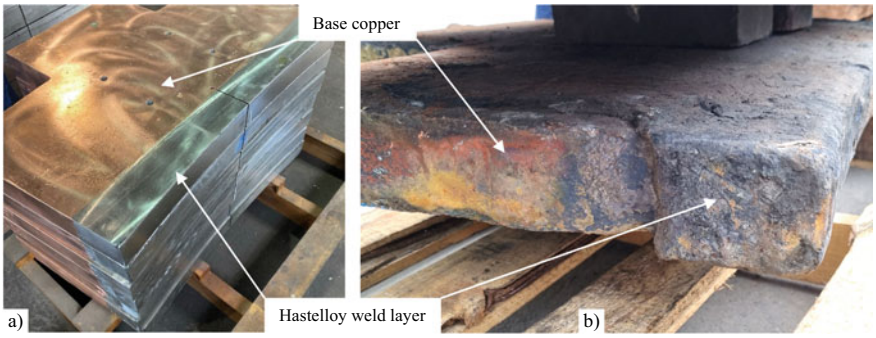

Fig. 3 **a** Machined Hastelloy weld layer on new copper plate coolers; **b** Used plate cooler showing corroded base copper behind Hastelloy weld layer

Tenova Pyromet first used graphite on the hot face of sidewall copper cooling elements in a PGM furnace in 2017. Graphite blocks were attached through a dovetail arrangement and a carbon-based cement on the hot face of Tenova's MAXICOOL® copper cooling elements as shown in Fig. 4a. After 3 years of operation, one of the coolers were removed and inspected. The hot face graphite was still in excellent condition. Corrosion of the copper surfaces on the sides of the cooler not covered by the graphite was noted and identified as sulphidation (Fig. 4b). Approximately 5 mm of base copper was worn away on the affected surfaces. The wear of the copper relative to the new graphite blocks installed during refurbishment of the cooler is visible in Fig. 4c.

Based on the experiences described above, both a Hastelloy weld layer and graphite cladding are effective in protecting copper cooling elements from sulphidation in PGM smelting furnaces. Graphite has the added advantage of a high thermal conductivity ensuring the cooling efficiency of the lining-cooling system by careful

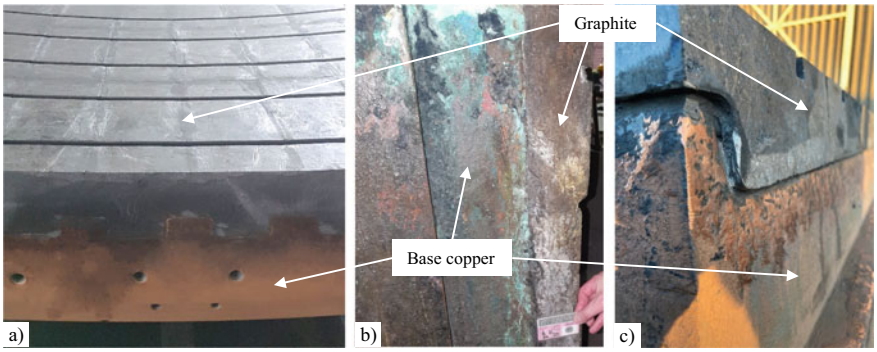

Fig. 4 **a** Graphite block installation on the hot face of MAXICOOL® copper coolers; **b** Sulphidation corrosion of the base copper surfaces not covered by graphite; **c** Copper wear relative to graphite blocks

design. Furthermore, the use of graphite is more cost-effective when implemented on larger coolers and cooler surface areas compared to a machined Hastelloy weld layer. For both the Hastelloy and graphite options, the sulphidation corrosion of any base copper surfaces left exposed behind the line of direct protection takes place and remains a determining factor in cooler and furnace sidewall campaign life. The coverage of the base copper needs to be extended to all surfaces that may be exposed to furnace gas.

Improved Composite Copper-Graphite Cooler Design

For the Furnace 1 crucible upgrade it was decided to design new composite copper-graphite sidewall coolers where all the base copper surfaces internal to the furnace crucible outer perimeter are covered with graphite. This applies to each individual cooler as shown in Fig. 5. The coolers are designed to be installed from the outside of the furnace shell and to push up against the adjacent coolers in the same row. Two rows of coolers are installed with a combined height that is sufficient to cover the maximum extent of the furnace slag bath. Tenova Pyromet's patented containment system is used to cover the vertical and horizontal interfaces between adjacent coolers, as well as the horizontal interfaces between the coolers and the adjacent refractory brick work [13]. The containment system includes a radial binding system to allow normal radial expansion whilst preventing growth over time. A vertical hold down system contains vertical sidewall growth over the extent of the furnace campaign life. The vertical hold down system is similar in design and operation as that described by Joubert et al. in 2005 [14].

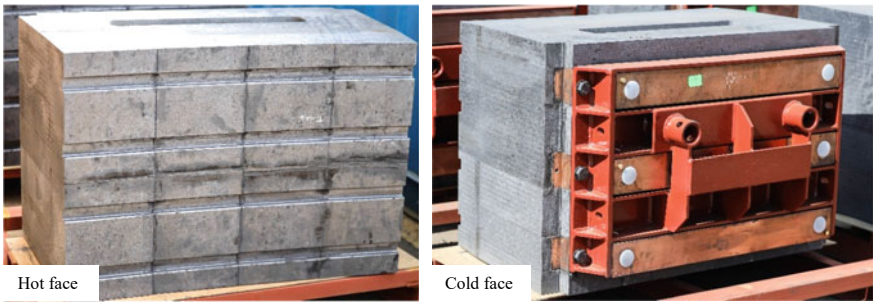

Fig. 5 Furnace 1 composite copper-graphite cooler design

Test Work

Tenova Pyromet performed a series of workshop tests on the newly designed composite copper-graphite cooler prior to implementation in the upgraded crucible of Sibanye-Stillwater's Furnace 1 [15]. The test work had three main objectives. The first objective was to confirm the constructability of the composite cooler design. Secondly, the cooling efficiency of the composite cooler and its ability to remove the expected slag sidewall heat load even under extreme operating conditions were to be tested. And finally, the test work was to confirm that the composite cooler assembly maintains its integrity following extreme heating and cooling cycles.

During the construction of the test composite copper-graphite cooler, various lessons were learned to improve the constructability. These lessons were important to ensure the timely and durable construction of the coolers. These learnings are not discussed further in this paper as the focus is on the thermal efficiency of the composite cooler design.

The test setup shown in Fig. 6 was used to evaluate the thermal efficiency of the composite copper-graphite cooler design. The test setup included the test composite cooler, a gas fuel burner and insulated enclosure (hot box) to heat the hot face of the test cooler, a cooling water supply system, and various instruments to measure the cooling water pressure drop and flow rate, and the cooling water, copper, graphite, and hot box temperatures. A data logger was used to record the measured temperatures. Photos of the composite cooler test setup are shown in Fig. 7.

To test the thermal efficiency of the composite cooler, the hot box was heated to approximately 1200 °C over a 4-h period followed by a stable temperature period to soak the test cooler and reach thermal equilibrium. The hot box and test cooler were then allowed to cool down overnight. To test the integrity of the composite cooler under thermal cycling the test was repeated three times, two of which were on consecutive days. The flow rate of the cooling water that cools the integrated copper elements was kept constant at the design value during the test. The cooling water flow rate and the recorded cooling water inlet and outlet differential temperatures were used to calculate the composite cooler hot face heat flux. The key maximum temperatures measured and corresponding calculated heat flux for consecutive test runs 2 and 3 are listed in Table 1.

The maximum heat flux achieved during the test runs is approximately 80 kW/m^2 at a maximum hot box temperature of 1196 °C. This is higher than the Furnace 1 crucible upgrade design base maximum value of 66 kW/m^2 whilst the maximum slag operating temperature specified is 1650 °C. The reason for the higher heat flux at lower hot box temperatures compared to what is expected in the operating furnace is the absence of the protective slag freeze lining that will form during actual furnace operation on the hot face of the composite cooler. For the same reason, the maximum graphite hot face temperatures recorded during the test runs are higher than what is expected during furnace operation. At the recorded maximum temperatures of approximately 800 °C, accelerated oxidation of the graphite is expected to commence. The position of the thermocouple measuring the graphite hot face

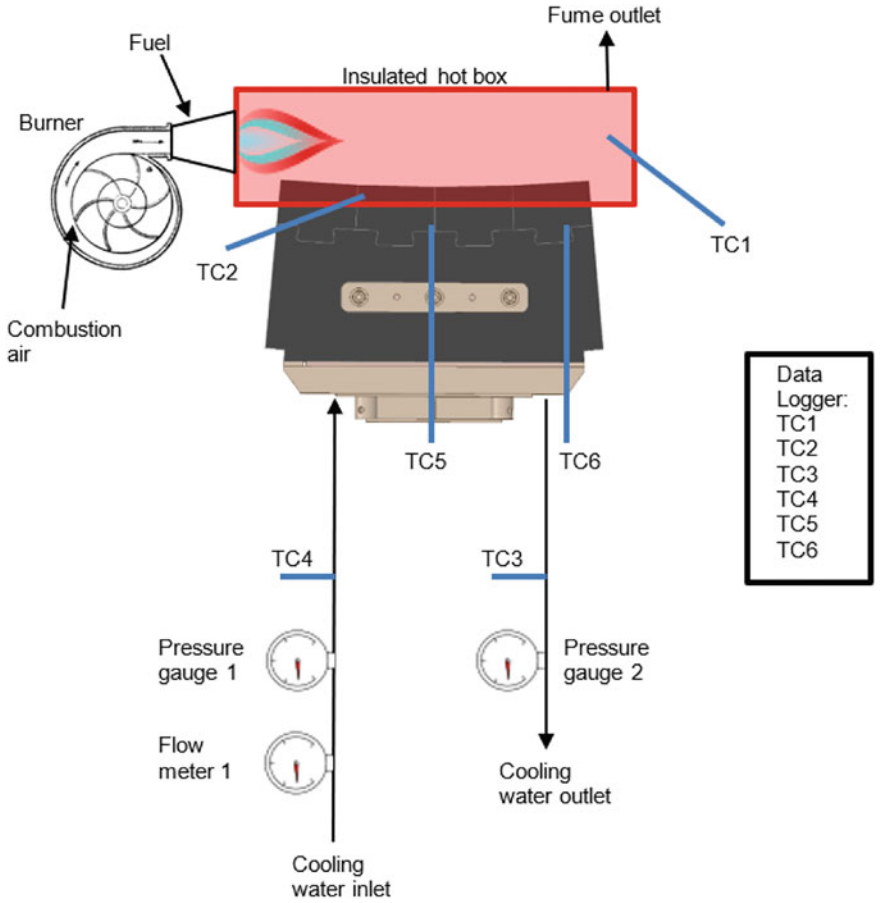

Fig. 6 Composite copper-graphite cooler test setup

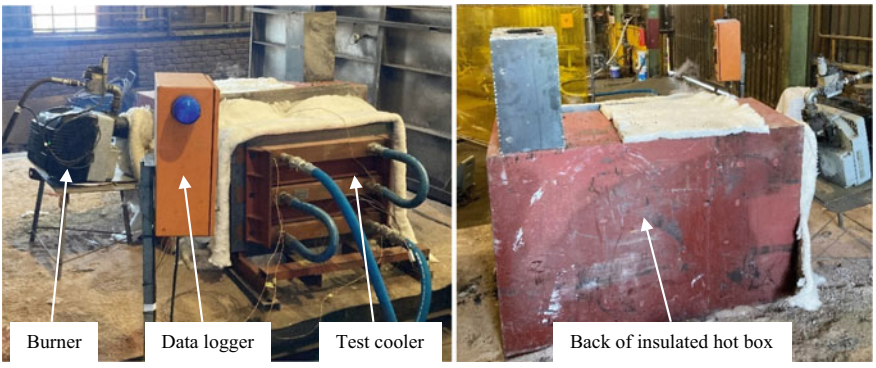

Fig. 7 Photos of composite copper-graphite cooler test setup

Table 1 Test run 2 and 3 results compared with FEA results

Description	Unit	Test run 2	Test run 3	Steady-state FEA
Maximum graphite hot face temperature	°C	764.6	823.1	788
Maximum middle copper element temperature at TC5	°C	236.4	255.8	312
Maximum bottom copper element temperature at TC6	°C	266.0	280.1	315
Maximum hot face heat flux based on water dT	kW/m^2	79.3	82.7	110

temperature is indicated in Fig. 8b. The maximum expected graphite temperature during furnace operation has been calculated to remain below 500 °C. The higher maximum heat flux and graphite temperature achieved during the test runs provide for a thorough evaluation of the cooling efficiency and integrity of the composite cooler.

The maximum copper temperatures recorded during the test runs are listed in Table 1. The temperatures are well below the maximum design limit of 450 °C. The design limit is set to prevent the onset of corrosion by oxidation of the copper and to ensure the copper elements retain their structural integrity [16]. The copper temperatures at TC5 and TC6 are measured approximately 40 mm from the copper element hot face. The higher bottom copper element temperatures compared to the middle copper element temperatures are due to the burner orientation. As shown in Fig. 7, the burner flame is directed from the top left-hand corner of the hot box, when

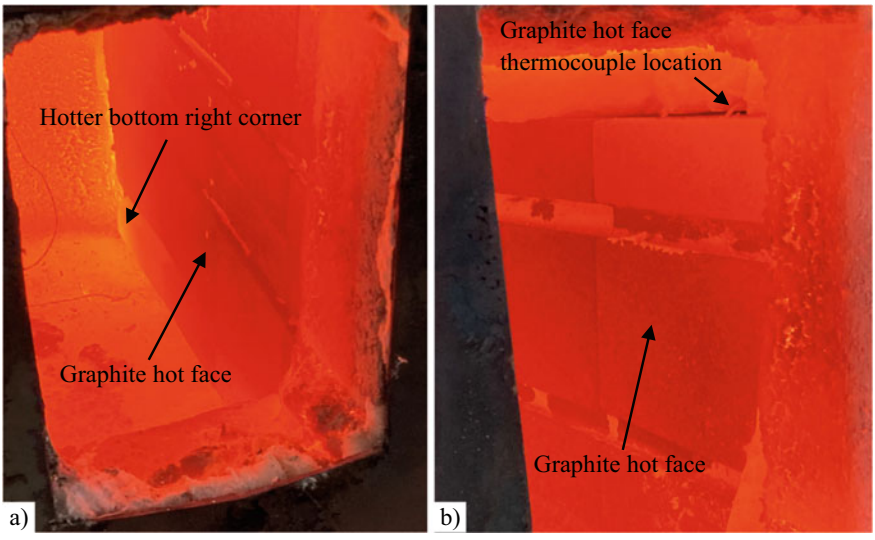

Fig. 8 Photos of hot box inside and graphite hot face on completion of test run 3

viewed from side where the cooler is installed, towards the bottom right-hand corner. This resulted in a higher heat load on the bottom right-hand corner graphite hot face of the composite cooler as indicated in Fig. 8a.

Three-dimensional thermal finite element analysis (FEA) modelling was conducted to obtain theoretical estimates for the composite cooler temperatures and the hot face heat flux for comparison with the values measured during the test runs [15]. The boundary conditions used in the FEA model were selected to correspond with the boundary conditions achieved during the test runs, including the hot box maximum temperature, the cooling water inlet temperature, and the ambient conditions. The temperature and heat flux results from the FEA modelling are shown in Table 1 for comparison to the test run results. The copper temperatures at locations corresponding to the copper thermocouple locations in the test composite cooler were extracted from the FEA model for comparison.

The maximum graphite temperature calculated during the FEA modelling corresponds well with the graphite hot face temperatures measured during the test. The maximum copper temperatures and the heat flux predicted in the FEA model are higher compared to that measured during the test. On closer inspection of the data collected during the test, it was noted that whilst the graphite hot face temperature started to decline once the burner has been switched off at the end of the test, the copper temperatures and the cooling water outlet temperature that were used to calculate the heat flux continued to rise for at least 7 min. It was concluded that the test setup had not yet reached steady-state conditions at the maximum hot box temperature level, and as a result the copper and outlet cooling water temperatures were lower compared to that calculated in the steady-state FEA model. The thermal soaking period allowed for at the maximum hot box temperature was not long enough. Other factors such as contact resistances between the graphite and copper not accounted for in the FEA model may have contributed to this discrepancy, although to a lesser extent.

The test work results confirmed that the composite copper-graphite cooler cooling efficiency is adequate to remove the maximum anticipated furnace sidewall heat load. Higher hot face heat fluxes were achieved during the test campaign than the anticipated maximum heat flux expected during furnace operation. The maximum copper temperatures measured at these elevated heat flux levels were within the maximum design limit. Valuable information gathered during the test work was used to confirm the cooling water requirements and to improve the cooling water channel design in the copper elements. The integrity of the cooler during thermal cycling was confirmed, and the information gathered during the test assisted in further improving the constructability of the cooler, including the integration of the graphite with the copper cooling elements to ensure all front, top, bottom, and side copper surfaces were protected against potential sulphidation corrosion.

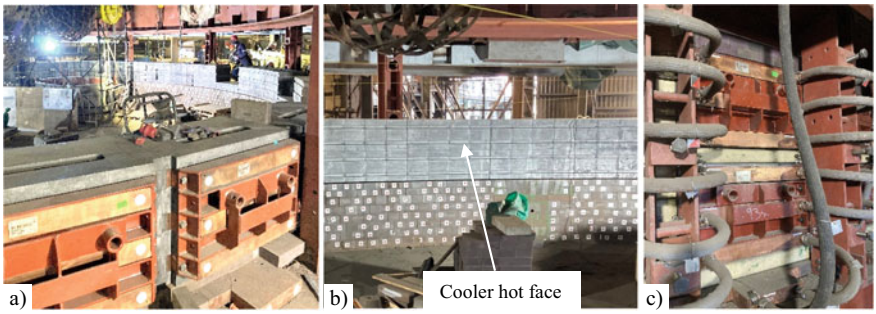

Fig. 9 Photos showing the composite copper-graphite coolers during installation as part of the upgraded Furnace 1 crucible

Implementation

Furnace 1 was shut down for the crucible upgrade from April to August 2022. Following the demolition of the old furnace crucible, the newly designed and supplied furnace base plate, hearth refractory lining, shell, sidewall refractory lining and cooling system, as well as matte and slag tapholes were installed. The overall changes and improvements to the furnace crucible as well as the project implementation are the subject of a separate paper [17]. The newly developed composite copper-graphite sidewall coolers, that are the main subject of this paper, are shown during installation in Fig. 9. Figure 9a, b shows the back and front of the first row of coolers during installation. Figure 9c shows the back of the two rows of coolers during the installation of the cooling water piping and instrumentation. The installation method and the lessons learned during the installation of the coolers will be discussed in the separate paper [17].

Performance

Following the startup of the upgraded Furnace 1 in September 2022, the furnace power input was ramped up to the nominal 15 MW design capacity by November 2022. The average slag sidewall heat flux as calculated using the cooler cooling water temperature differential as well as the temperature of the bottom copper element forming part of the bottom row of composite coolers is plotted relative to the furnace power input as shown in Fig. 10. The bottom copper element temperature corresponds to the test cooler temperature measurement TC6 as recorded in Table 1. The data for December 2022 is plotted in Fig. 10a and the same for June 2023 in Fig. 10b.

During December 2022, the slag sidewall heat flux averaged approximately 25 kW/m^2 for the periods of relatively stable power input at the 15 MW nominal level. During June 2023, the average heat flux was slightly higher at between 27

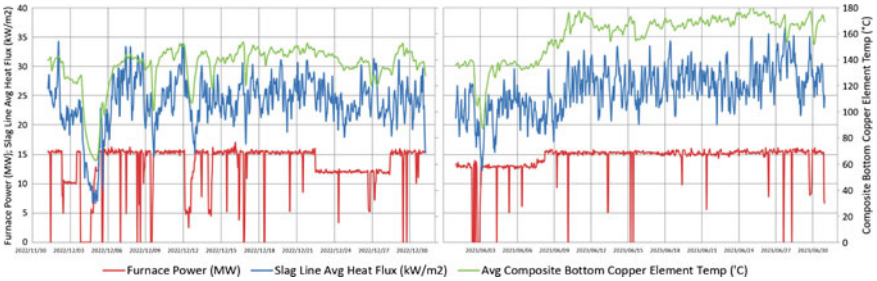

Fig. 10 Furnace power, average slag sidewall heat flux, and average bottom copper element temperature for **a** December 2022 and **b** June 2023

and 28 kW/m^2. The average bottom cooling element temperature was also higher during June 2023 at approximately 170 °C for periods of relatively stable 15 MW operation versus approximately 150 °C during the December 2022. During a deep matte taphole repair in early July 2023, it was noted that the lower sidewall refractory lining adjacent to the slag-matte tidal zone and directly underneath the hot face of the composite coolers has worn back, in line with expectations. This likely increases the heat load on the bottom of the composite coolers and partially explains the increased slag sidewall heat flux and in particular the increase in the bottom cooling element temperature over the period from December 2022 to June 2023. In addition, the slag and matte tapping temperatures were, respectively, in the range of 15–35 °C higher in June 2023 compared to December 2022.

In Fig. 11, the slag sidewall heat flux distribution around the circumference of the furnace is plotted for December 2022 as well as June 2023. The 50th and 99th percentile heat flux values are plotted for both periods. The heat flux values as well as the distribution pattern around the furnace circumference are similar for the two periods. This is a good indication of a stable furnace operation. The 50th percentile heat flux is between 20 and 40 kW/m^2, and the 99th percentile heat flux is between 35 and 60 kW/m^2. This is below the maximum design base heat flux of 66 kW/m^2 and well below the maximum heat flux of 80 kW/m^2 achieved during the composite cooler test campaign. The higher heat flux values closer to slag taphole 3 (STH3) are attributed to this taphole being tapped more often compared to the other slag tapholes. Although not plotted, the 99th percentile bottom copper element temperature for December 2022 is 172 °C and for June 2023 it is 206 °C. These values are well below the maximum bottom copper element temperature (TC6) of 266 and 280 °C recorded during the test campaign (see Table 1).

To date no signs of sulphidation corrosion have been detected on the visible surfaces of the composite cooler copper cooling elements. No wear of the graphite hot faces has been reported during visual inspections through the freeboard inspection ports. Most of the graphite hot face areas are covered with a slag freeze lining as intended. Where the graphite hot faces are exposed, the original horizontally machined dovetails for slag retention are still visible and appear to be undamaged. All interfaces between adjacent coolers and between coolers and the refractory

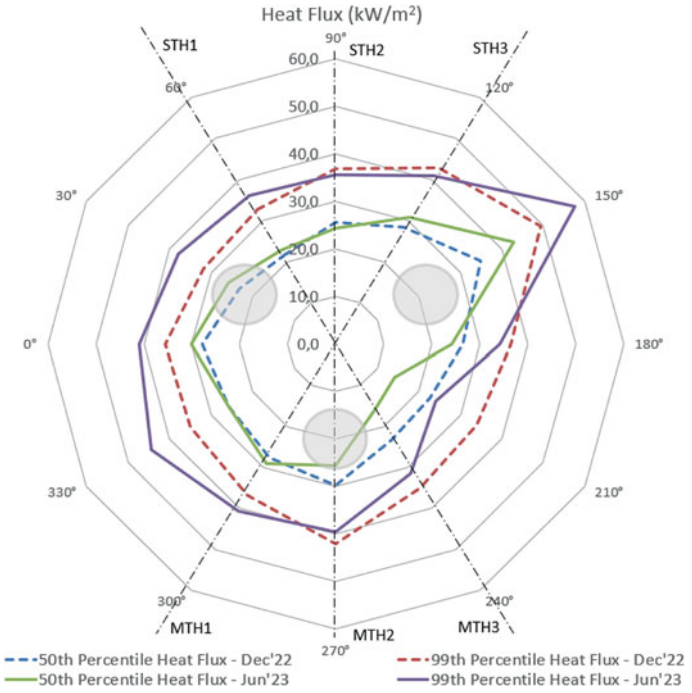

Fig. 11 50th and 99th percentile slag sidewall heat flux, respectively, for December 2022 and June 2023

lining below and above remain tight. No differential movement between adjacent coolers has been reported to date and the containment system has retained its original integrity.

Conclusions

Graphite cladding and a Hastelloy weld layer have proved to be effective in inhibiting sulphidation corrosion of cooled copper element surfaces in PGM smelting furnace sidewalls. Any copper element surfaces within the crucible perimeter not adequately covered, and adjacent to the slag-charge tidal zone, are susceptible to sulphidation corrosion. Tenova Pyromet developed a composite copper-graphite cooler where all surfaces within the crucible perimeter are protected by a graphite layer.

The thermal efficiency and durability of the composite cooler were confirmed by means of test work. The cooler was tested at heat loads significantly higher compared to loads anticipated during operation. The cooler performed well under extreme thermal cycling conditions and maintained its integrity. The constructability of the composite copper-graphite cooler was confirmed during the test work.

The composite cooler has performed as intended since the startup of Sibanye-Stillwater's upgraded Furnace 1 in September 2022. The recorded heat fluxes are in line with expectations and the 99th percentile heat flux is below the maximum design base value. Copper temperatures are in line with expectations and well below the design limitation. No signs of sulphidation corrosion have been detected to date. Based on the initial performance of the composite copper-graphite cooler, the furnace sidewall is expected to achieve the targeted 48-month campaign life.

Acknowledgements The authors wish to thank Thos Begbie & Company (Pty) Ltd. for accommodating the test work in their workshop facility and Elite Refractory Services (Pty) Ltd. for building the hot box and for making available the burner and data logger for the test work. The authors furthermore wish to thank Tenova Pyromet and Sibanye-Stillwater for granting permission to publish the work.

References

1. Nelson LR, Geldenhuis JMA, Emery B, de Vries M, Joiner K, Ma T, Sarvinis J, Stober FA, Sullivan R, Voermann N, Walker C, Wasmund B (2006) Hatch developments in furnace design in conjunction with smelting plants in Africa. Presented at Southern African Pyrometallurgy 2006. SAIMM, Johannesburg, 5–8 Mar 2006
2. Thethwayo BM, Garbers-Craig AM (2012) Corrosion of copper coolers in PGM smelters. Paper presented at the 4th international platinum conference, platinum in transition "boom or bust". SAIMM 2010
3. Thethwayo BM (2010) Sulphidation of copper coolers in PGM smelters. Masters of Science Dissertation, University of Pretoria
4. Eksteen JJ, Van Beek B, Bezuidenhout, GA (2011) Cracking a hard nut: an overview of Lonmin's operations directed at smelting of UG2-rich concentrate blends. Paper presented at Southern African Pyrometallurgy 2011 international conference, Cradle of Humankind, South Africa, pp 231–251
5. Shaw A, De Villiers LPVS, Hundermark RJ, Ndlovu J, Nelson LR, Pieterse B, Sullivan R, Voermann N, Walker C, Stober F, McKenzie AD (2013) Challenges and solutions in PGM furnace operation: high matte temperature and copper cooler corrosion. J South Afr Inst Min Metall 113(3):00–00
6. Nkosi S, Goso X (2018) Preliminary mechanisms and kinetics of corrosion of uncoated and coated Cu blocks. Mintek External Report no. 7727, Confidential
7. Copeland C, Street S (2013) A practical engineering approach to improving the reliability of blast furnace tuyeres. Iron Steel Technol 10(9):47–62
8. Shellhammer T, Walsh R (2011) High-conductivity copper in the blast furnace. Iron Steel Technol 8(3):58
9. Gwynn-Jones S et al (2016) Base metals initiative: calorizing test campaign. Tenova Pyromet internal report, Confidential
10. Francis BJ et al (2018) Element for use in non-ferrous smelting apparatus. WO 2018/002832 A1. World intellectual property organisation under the Patent Cooperation Treaty (PCT). https://rb.gy/fbz5d
11. McDougall I, Eksteen JJ (2012) Sidewall design to improve lining life in a platinum smelting furnace. Paper presented at the TMS 2012 international smelting technology symposium, Orlando Florida, 11–15 Mar 2012
12. Joubert H (2008) A furnace. 2007/05868. South African Patent Office. https://rb.gy/k6sza

13. De Villiers G et al (2020) Lining and cooling arrangement for a metallurgical furnace. WO 2020/109941 A1. World intellectual property organisation under the Patent Cooperation Treaty (PCT). https://rb.gy/tjlsv
14. Joubert H, Nourse RB, Masters B, Hundermark R (2005) Copper cooling design, installation and operational results for the slag cleaning furnace at Waterval Smelter, Rustenburg Platinum, South Africa. Paper presented at COM2005 44th conference of metallurgists, international symposium on nickel and cobalt production, Calgary, Alberta, Canada, 21–25 Aug 2005
15. Joubert H (2021) Testing of Tenova composite graphite-copper sidewall cooler design. Tenova Pyromet internal report, Confidential
16. Joubert H, Mc Dougall I (2019) Designing furnace lining/cooling systems to operate with a competent freeze lining. TMS 2019 148th annual meeting & exhibition supplemental proceedings, pp 1181–1195. Springer, Cham
17. Joubert H, De Villiers G, Nel J, Senekal D, Mbedzi P, Davis J (2024). PGM furnace crucible upgrade and performance. Submitted for the SAIMM Southern African pyrometallurgy 2024 international conference, 13–14 Mar 2024

Part II
Panel Discussion: Oh No! What Went Wrong. Furnace Design Lesson Learnt

Electric Furnace Integrity Practices and Design Improvements Over 45 Years of Operation

Laura Shultz

Abstract The smelter operates a single six-in-line electric AC furnace. This furnace treats nickel sulphide concentrates produced by Glencore and third-party feeds and as such its performance is key to the company's nickel supply chain. The furnace was constructed in 1978 and upgraded in 1994 to double the power density. The sprung arch roof was rebuilt in 2004, and the walls were rebuilt in 2004 and 2015. The hearth, however, remains the original installation. Work is underway to replace the entire furnace including the hearth in 2026. Since 1994, the smelter has successfully operated with a single furnace. Importance has been placed on the development of furnace integrity practices and equipment improvements. Another key focus has been robust practices on matte and slag tapping operations and maintenance. This paper will review the design considerations of the upcoming rebuild and approach taken to ensure its safe and reliable operation.

Keywords Nickel/Copper/Cobalt · Pyrometallurgy · Furnace integrity

Introduction

The smelter at Sudbury Integrated Nickel Operations, located in Sudbury, Ontario, processes approximately 550,000 tonnes of nickel, copper, and cobalt bearing feeds annually. This results in an annual production of up to 80,000 tonnes of nickel and 3000 tonnes of cobalt. Two company-owned mines, Nickel Rim South Mine and Fraser Mine located in Sudbury, feed the Strathcona Mill to produce nickel concentrate. The Raglan Mine in Northern Quebec feeds the Raglan Mill. Raglan concentrate is shipped and railed to the smelter. Custom feed materials are purchased from third-party mining companies and recyclers and are received in bulk by rail or truck, either in filter cakes or containers such as bags or barrels. These materials are treated to maximize the smelter capacity.

L. Shultz (✉)
Sudbury Integrated Nickel Operations, A Glencore Company, Falconbridge, ON, Canada
e-mail: laura.shultz@glencore.ca

© The Minerals, Metals & Materials Society 2024

G. Alvear et al. (eds.), *Advances in Pyrometallurgy*, The Minerals, Metals & Materials Series, https://doi.org/10.1007/978-3-031-50176-0_5

There is a single electric furnace that treats all nickel sulphide concentrates produced by Glencore as well as third-party feeds and as such its performance is key to the company's nickel supply chain.

Electric Furnace Operation

The electric furnace is a six-in-line electric furnace measuring 30 m × 10 m. The furnace operates with up to 55 MW of power and calcine is directed along the length of the furnace through feed pipes toward the electrodes. A calcine layer is maintained, and regular dips are taken to confirm bath levels.

In addition to the calcine fed into the furnace, reverts, secondary materials, and coke are added by mixing in with the calcine in the drag conveyors. The coke is added to maintain reductive conditions and create a metallised furnace matte for improved pay-metal recoveries.

The matte fall in the furnace accounts for approximately 37% of the total calcine fed to the furnace. On average, 18 matte taps are taken out each 12-h shift. The nature of this process requires that furnace matte be tapped ladle by ladle and transported via cranes to the converter aisle. Ventilation hoods pull fume and gas to a dedicated baghouse.

Primarily, the taphole wear at the matte end of this furnace is caused by the frequent opening and closing of the tapping holes to meet production requirements. Water-based clay is used when plugging the holes and boiling of this clay is a significant contributor to wear. The matte temperature is also controlled to manage taphole wear.

There are three matte tapping channels on the furnace, and the tapping frequency on each taphole is managed to give time for cooling in order to lengthen the time between repairs. Typically, two tapholes are utilized on rotation of each shift, changing between tapholes after a series of taps.

There is one slag taphole that is in operation approximately 18–20 h per day, directing slag via copper launders into a water granulation system and to a storage area on site. The slag granulation system also includes a wet H_2S scrubber.

Regular maintenance is performed on the matte tapholes, with substantial repairs to the blocks in the tapping channel taking place during shutdowns taken every 8 months. The furnace walls are repaired every 10–11 years.

Previous Rebuilds of the Electric Furnace

The six-in-line electric furnaces were constructed in 1978 as part of the flowsheet upgrade to two fluid bed roasters (with off-gas to acid plant), two electric furnaces and converter aisle operation. The No. 2 furnace was upgraded in 1994 to double the power density and the No. 1 furnace was taken out of service when the flowsheet moved to a single furnace operation.

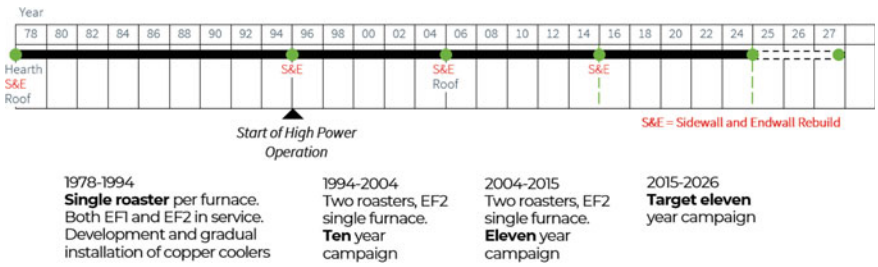

Fig. 1 No. 2 electric furnace campaign history

Over the remaining years, the walls and sprung arch roof were rebuilt in 2004, and upgrades made from finger-style copper coolers to shallow plate coolers. The walls were subsequently rebuilt in 2015, including further copper cooler upgrades. The hearth, however, remains the original installation circa 1978 (Fig. 1).

2004 Rebuild—Roof and Wall Replacement, Change to Shallow Drilled Plate Coolers

The scope in 2004 involved the removal and reinstallation of the sprung arch roof panels, sidewalls, and endwalls. There was also an upgrade in design from drilled finger coolers in the upper walls to tongue and groove plate coolers.

The walls had been in service for 10 years at the time of the repair. Frozen slag build-up was observed to be present on the walls which provided protection on the brick over the campaign. The greatest amount of wear was observed on the matte end wall [1]. The sprung arch roof had been in use since 1978, for a 26-year campaign. Some damage to the roof was observed during tear out as shown in Fig. 2a.

During the removals of the walls down to the hearth skew brick elevation, it was found that there was significant penetration of metal into the working lining of the hearth, and the skews had undergone some rotation from their original position. In order to level the area to rebuild the walls, ram was used to tie into the wall for the next campaign (Fig. 3).

2015 Rebuild—Wall Replacement and Additional Row of Sidewall Cooling

In the 2015 rebuild, the scope included replacement of the furnace sidewalls and endwalls. Both endwalls were trimmed back during this outage to allow the buckstays to be reset on both sides of the furnace to ensure the ability for furnace growth over the next campaign.

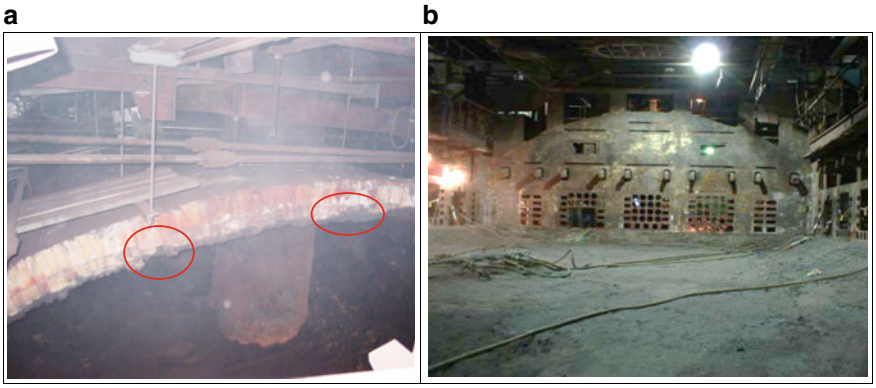

Fig. 2 **a** 2004 rebuild—damaged observed in some sections of the roof, **b** 2004 rebuild—demolition completed

Fig. 3 **a** 2004 rebuild—upgrade to drilled Cu plate coolers. View along north wall. **b** 2004 rebuild—roof and matte endwall completed

The wall cooling was improved by adding an additional row "0" of sidewall cooling and upgrades were made to install wrap around coolers to replace dog-leg-style coolers in rows 4 and 5. Cooler improvements were also made to the matte end wall to install a brick lintel system. This allowed for 'top-down' tapping channel repairs. Further improvements included replacing upper spring sets and installation of new spring sets with safety systems, upgrades to the roof compression springs, installation of corner springs to allow for installation of controlled furnace atmosphere injection ports, and hold down safety system installation.

Observation during the tear out was that the plate coolers remained in excellent condition after 10 years of operation and therefore the majority of these coolers were put back into service following cleaning and testing.

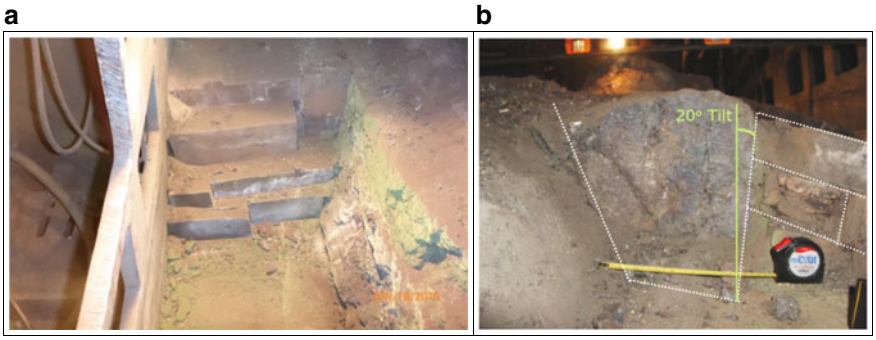

Fig. 4 **a, b** 2015 rebuild—brick observations at skew level

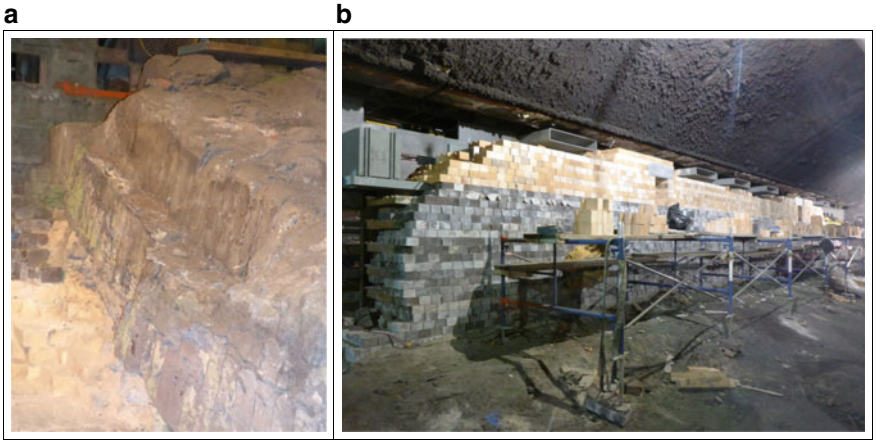

Fig. 5 **a** 2015 rebuild—trimming of matte endwall and hearth refractory. **b** Installation of sidewall refractory with plate coolers and CFA inlet ducting

The skew brick had continued to rotate in the 11 years of operation since 2004 and measured at rotation of 9–20° [2]. The ram repair used from 2004 was still visible, and further ram repairs made in 2015 to complete the tie-in to the wall (Fig. 4).

The furnace endwall trimming to allow for buckstay reset and refractory tie-ins required extensive lancing and chipping to remove the metallic build-up present in the furnace. This did cause delays extending the removal by 4 days (Fig. 5).

Upcoming 2026 Furnace Rebuild

For the 2026 furnace rebuild project, the process flowsheet will be largely unaffected. The replacement is primarily an in-kind replacement of an end-of-life asset.

The hearth is original and has been assessed to be at its end of life due to physical distortion, which is a result of cumulative bath infiltration and thermal cycling over its life. This makes it unable to build straight walls when completing the reline, and the critical hearth/sidewall joint cannot be reliably renewed. The binding system has worn with time and furnace distortion. No comparable furnace hearth has achieved this life.

While this is an in-kind replacement with regard to furnace technology and process operation, there are some improvements planned with primary focus on increased longevity, operation, and monitoring of the furnace. There are upgrades planned both for the furnace crucible design and wraparound equipment (Figs. 6 and 7).

The scope of work for 2026 is to demolish the refractory walls, roof, and hearth. To remove the hearth will require removal of the thick FeNi heel. It is expected that lancing will be required to cut and enable removal of sections of build-up. The furnace steel, including binding system, shell plate, and tie rods, will be removed. The furnace foundations will remain in place.

Wrap around improvements include adding pressurized leak detection on the furnace cooling water circuits, installation of new tapping machines at both the matte and slag ends, and modifications to the matte end uptake duct to accommodate the installation of an emergency stack on the furnace off-gas system.

Improvements to the crucible design are primarily being incorporated to modernize the furnace, improve binding loads, and address previous concerns. One key change for this rebuild is to optimize the hearth radius to improve the loading from hold downs into the skew bricks by bringing them farther back under the wall. It is also planned to lower the skews below the slag-matte wash zone, which will require a slightly larger hearth radius [3]. This is to help mitigate the issues with skew rotation observed during the 2004 and 2015 rebuilds as discussed above.

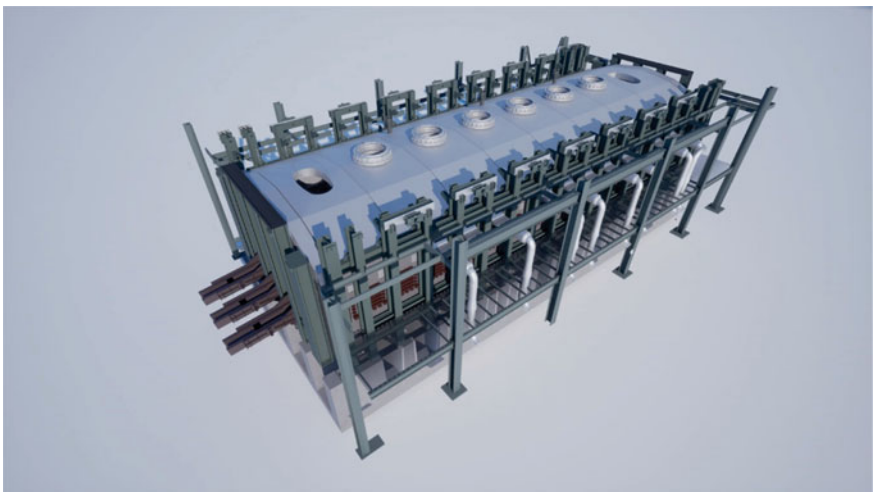

Fig. 6 2026 rebuild—model depiction of furnace No 2 rebuild

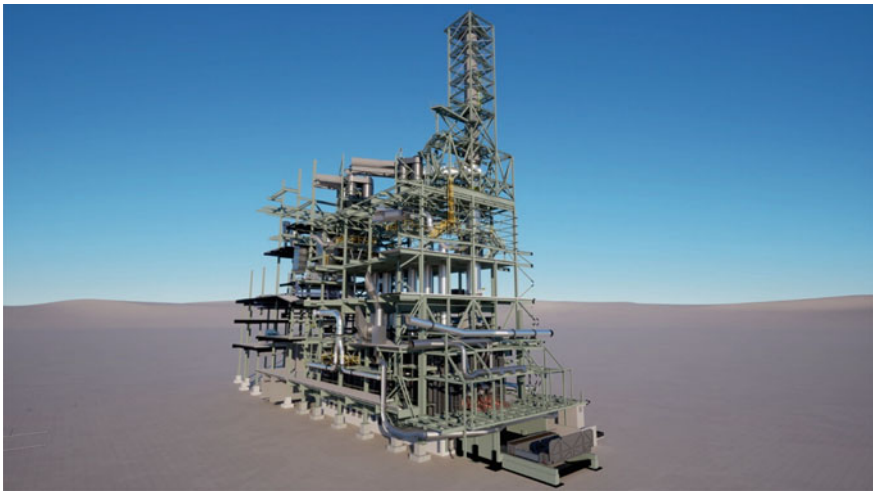

Fig. 7 2026 rebuild—model depiction showing new matte end emergency stack

There is consideration for increasing the sidewall height by approximately 10% in order to provide more space for gas within the freeboard. Raising the sidewalls will allow for a raise in elevation on the controlled furnace atmosphere inlet ports that provide tail-gas to the furnace and minimize the occurrence of calcine dust being entrained into the off-gas system prior to smelting, especially when the calcine bank nears the inlet duct elevation. The roof crown elevation will remain the same, so a shallower arch will be implemented for the taller sidewalls.

As part of the rebuild, the furnace steel will be replaced essentially in kind with new buckstays and hold down assemblies, new shell plate and tie rods. Some improvements are planned for spring measurements with the installation of an online binding measurement system, as well as minor changes to the bindings to improve ergonomics.

Overall, most of the furnace refractory copper cooling is planned to be reused. All copper coolers will be assessed during removal, and where suitable will be reinstalled. A portion of spares will be ordered to replace those that are no longer usable. For the top cooling rows, near the buckstays, an upgrade will be made from the existing dog-leg cooler design to a cast wraparound cooler (similar to the success from the lower dog-leg cooler replacement in 2015) to improve heat flux capacity and future tolerance for feed variations.

Safe Operation Over 45 Years

Since 1994, the smelter has successfully operated with a single electric furnace. The ability to meet our goal of zero harm is ensuring that safe practices are in place. Importance has been placed on the development of furnace integrity practices and improvements to equipment such as binding systems and copper cooling. Another key focus at this facility has been robust practices on matte and slag tapping operations and maintenance.

As a single furnace operation, ensuring reliability and safe operation is a key focus for the site.

Strong furnace integrity programs, tapping best practices, weekly short block change repairs, and larger tapping channel repairs every 8 months are a key focus. Further information on tapping practices and procedures has been covered in a previous paper [4].

Operating temperatures, bath levels, calcine levels, and power inputs are managed on a 24/7 basis by a Control Room Supervisor. A mature alarm management program exists to provide feedback on critical furnace measurements.

Furnace operators adhere to best practices when tapping, conduct preoperational checks on key furnace systems, measure furnace springs daily, and make adjustments when required. Furnace bath level readings are taken every 2 h to verify operating parameters, and furnace matte and slag samples are collected and analysed for composition every 4 h.

The furnace integrity program is managed by a dedicated vessel integrity engineer and a technologist. Several tasks for observations, measurements, and audits are conducted on a weekly, monthly, and annual basis, and reported through to management as a key performance metric. Third-party integrity audits are also conducted on the furnace integrity every 18–24 months.

The integrity program continues to monitor compliance to standards and identify needed repairs as the furnace grows. Recently, repairs have been made to extend tie rods and free bound steel components.

The process technical group manages feed blend and feed ratios to optimize furnace chemistry, metallurgical targets, monitoring of matte, slag and cooling water temperatures, water flows, electrode performance, tapping conditions, and wear.

Summary

The six-in-line electric furnace was constructed in 1978. Since 1994, with the upgrades to No. 2 furnace, the flowsheet moved to a single furnace operation.

The walls and sprung arch roof were rebuilt in 2004, and upgrades made from finger-style copper coolers to shallow plate copper coolers. The walls were subsequently rebuilt in 2015. The hearth, however, remains the original installation circa

1978. A complete in-kind replacement of the roof, walls, and hearth is planned for summer 2026.

Over the next 3 years, as the furnace continues to operate, the robust furnace integrity programs, scheduled repairs, and best practices remain key for ensuring strong and safe operation up until the complete replacement in 2026.

References

1. Thomson L, Ojala A, Ducharme D (2004) Furnace June 2004 rebuild internal report. Falconbridge, Ontario
2. Granger C (2015) Furnace 2015 rebuild internal presentation. Falconbridge, Ontario
3. Furnace Replacement Project Pre-feasibility Final Report (2023) Hatch Engineering and Sudbury INO Smelter
4. Thomson L (2014) Monitoring, repair and safety practices for electric furnace matte tapping. SAIMM furnace tapping conference 2014, Muldersdrift, South Africa

Part III
Refractories

Characterization of a Nickel Flash Smelter Refractory Material—The Effect of Thermal Gradient

J. Lehmusto, S. Söyrinki, J. Lagerbom, T. Jokiaho, Z. Que, J. Määttä, L. Hupa, E. Huttunen-Saarivirta, and M. Lindgren

Abstract Magnesia-chromite ($MgCr_2O_4$) spinel-based refractories are applied in nickel and copper flash smelting furnaces, where the refractories experience high temperatures but also thermal gradients due to the cooling of the walls. In the gas space, the refractories are subjected to an aggressive environment with high SO_2 concentrations. Furthermore, the increased use of recycled material streams has introduced new reactive impurities, such as halides, to the process. Therefore, the interactions between the refractories and gaseous species as well as the related reaction mechanisms need to be understood. This study presents a comparison between as-received and spent refractories from a nickel flash smelting furnace to identify the reactive species and shed light on their reaction mechanisms. The thermal gradient

J. Lehmusto (✉) · L. Hupa
Faculty of Science and Engineering, Abo Akademi University, Turku, Finland
e-mail: juho.lehmusto@abo.fi

L. Hupa
e-mail: leena.hupa@abo.fi

S. Söyrinki · J. Lagerbom · T. Jokiaho · Z. Que · E. Huttunen-Saarivirta
VTT Technical Research Centre of Finland Ltd., Espoo, Finland
e-mail: saara.soyrinki@vtt.fi

J. Lagerbom
e-mail: juha.lagerbom@vtt.fi

T. Jokiaho
e-mail: tuomas.jokiaho@vtt.fi

Z. Que
e-mail: zaiqing.que@vtt.fi

E. Huttunen-Saarivirta
e-mail: elina.huttunen-saarivirta@vtt.fi

J. Määttä
Institute of Biomedicine, University of Turku, Turku, Finland
e-mail: jmaatta@utu.fi

M. Lindgren
Metso, Pori, Finland
e-mail: mari.lindgren@mogroup.com

© The Minerals, Metals & Materials Society 2024

G. Alvear et al. (eds.), *Advances in Pyrometallurgy*, The Minerals, Metals & Materials Series, https://doi.org/10.1007/978-3-031-50176-0_6

over the refractory is expected to affect the microstructure and contribute to the diffusion of elements within the structure. Therefore, special attention was paid to the role of the thermal gradient in the abovementioned interactions.

Keywords Flash smelting · Gas-phase reactions · Thermal gradient · Refractory wear

Introduction

The flash smelting process is one of the most widely used methods to extract nickel from sulfide ores due to its cost-effectiveness and environmentally sustainable nature; once initiated, the process is continuous and nearly autothermal [1, 2]. In particular, the use of sulfide ore concentrates as feedstock results in high SO_2 concentrations in the gas phase of the smelter, up to 70 vol.% [3, 4]. The availability of high-grade sulfidic nickel ores has decreased, and therefore lower grade ores with higher amounts of impurities are processed. Nickel-bearing side streams from other processes may be processed to recover valuable metals and they may contain new types of impurities. To protect the structural materials of the smelter interior, it is covered with ceramic refractories, usually based on a magnesia-chromite ($MgCr_2O_4$) spinel. This material is known to possess excellent durability against heat, thermal shocks, and melt erosion forces [5, 6]. In addition to the interactions with the reactive gaseous compounds, the refractories experience a thermal gradient of around 1000 °C over the material. Such harsh conditions may result in the gradual degradation of the refractories over time.

The reactions between the phases included in the magnesia-chromite refractories and the flash smelting environment have been addressed previously in a few fundamental studies [7–10]. However, the aging of refractories in nickel flash smelting furnaces is rarely addressed in the literature. Because of this, very little is known about the degradation of gas-space refractories. Another feature, the effect of which on refractory behavior is unknown, is the significant thermal gradient over the refractory material in the furnace. To better understand the interactions between the gas phase and the refractory material, and how the thermal gradient affects the migration of species into the material, unused refractories and spent refractories sampled from a nickel flash smelting furnace were analyzed and compared. Furthermore, a comparison was also done with samples in contact with nickel flash smelting slag to elucidate the specific effect of the SO_2-containing gas phase on the refractory lining.

Materials and Methods

The studied material was a magnesia-chromite product of type MCr50, ISO 10081-2, with a given composition of (in wt.%): 59.5 MgO, 19.0 Cr_2O_3, 13.5 Fe_2O_3, 6.0 Al_2O_3, 1.3 CaO, and 0.5 SiO_2, with an apparent porosity of 17.0 vol.%. The microstructure of as-received material was analyzed and compared to that of spent refractories from the roof lining of a nickel flash smelting furnace. The characterization was carried out with scanning electron microscopy (SEM), energy-dispersive spectroscopy (EDS), electron back-scattered diffraction (EBSD), micro-computed tomography (μ-CT), and X-ray diffraction (XRD).

Refractory fingers were inserted into a crucible filled with slag in an induction furnace. The hold time at 1450 °C was 6 h and during that time an inert gaseous atmosphere was created with argon. After cooling, cross-sectional samples were prepared for microscopy investigation. The main constituents of the slag were 7% MgO, 4% NiO, 31% SiO_2, and 52% of iron oxides.

Results and Discussion

Two phases were identified in the as-received material with XRD: a MgO (magnesia; periclase) phase and a $(Fe,Mg)(Al,Cr)_2O_4$ (magnesia-chromite spinel; picotite) phase. Cross-sectional SEM–EDS examinations supported this observation. In addition, Ca-rich areas were identified in the vicinity of MgO areas with EDS (Fig. 1). The porosity and density distribution of the as-received material was specified with μ-CT, revealing the porosity of 10% and three types of regions with different densities. Based on phase identification and elemental analyses, it was possible to define that low-density areas consisted mainly of MgO, medium-density areas of $MgCr_2O_4$ precipitates and $(Fe,Mg)(Al,Cr)_2O_4$ embedded in MgO, and high-density areas of larger $MgCr_2O_4$ and/or $(Fe,Mg)(Al,Cr)_2O_4$ regions. The difference in the porosities given by the manufacturer (17%) and measured with μ-CT (10%) likely originates from the set threshold values for the μ-CT measurement. However, the combinatory characterization of the microstructure and composition of the refractory material by several methods provided novel information regarding the three-dimensional phase and elemental distributions. Furthermore, the results function as a reference point to the characterization of the spent refractories.

Regarding the spent refractories, the exposure to high temperatures and a reactive process environment resulted in changes in the microstructure in comparison to the as-received material. Close to the process environment, the morphology of the spent refractory was essentially denser, showing clear signs of sintering (Fig. 2), whereas the microstructure of the material in the colder end of the refractory was similar to that of the as-received material. Based on μ-XRF images, the slag had not penetrated the material. Process material had created a separate reaction layer on top of the refractory but no penetration of components into the pores of materials was

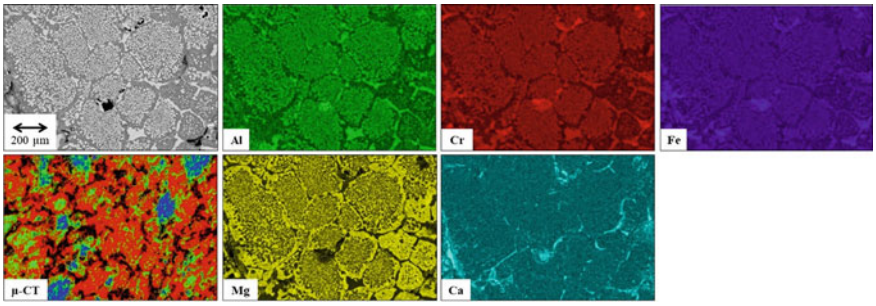

Fig. 1 A cross-sectional SEM image of the as-received material with the corresponding elemental EDS maps. The left image on the lower row is a three-dimensional µ-CT density map of the ac-received material

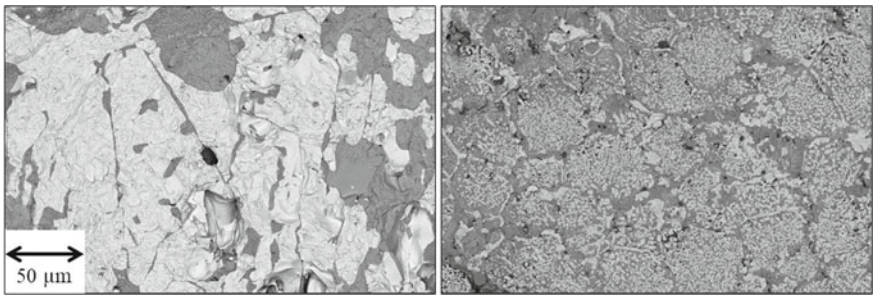

Fig. 2 Two example cross-sectional SEM images of the microstructure of a spent refractory; close to the process environment (left) and towards the colder end of the refractory (right)

observed. The only visually observable differences of the colder end were the lower porosity compared to the as-received material and the presence of microcracks (not shown in Fig. 2).

In the elemental maps of the spent refractory, areas rich in Ca, O, and S were identified between the $(Fe,Mg)(Al,Cr)_2O_4$ (Fig. 3). This indicates the presence of calcium sulfate ($CaSO_4$), which may have formed in the reaction with SO_2 [11]:

$$CaO(s) + SO_2(g) + {}^1/_2\, O_2(g) \rightarrow CaSO_4(s) \quad (1)$$

or with SO_3:

$$CaO(s) + SO_3(g) \rightarrow CaSO_4(s) \quad (2)$$

Typical process dust of a nickel flash smelting furnace is known to catalyze the SO_2-to-SO_3 conversion [12], so either or both of the sulfur oxides may have reacted with the refractory. The loss of porosity shown in Fig. 2 can at least partly be explained by the formation of $CaSO_4$: since the molar volume of $CaSO_4$ is roughly three

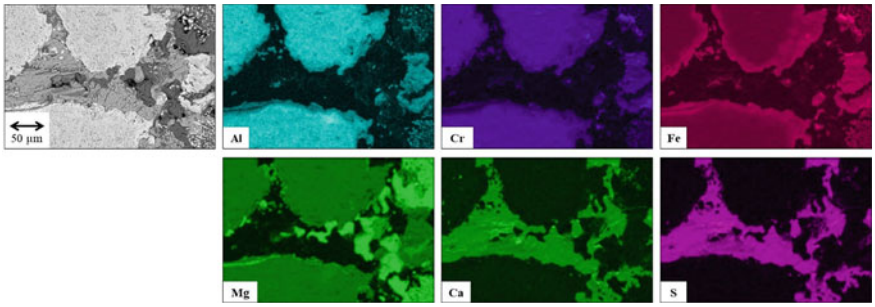

Fig. 3 A cross-sectional SEM image of the spent refractory material with the corresponding elemental EDS maps

times that of CaO, the pores were filled through the increase in the internal volume. However, no extensive microcracking was seen close to the $CaSO_4$-rich areas. Thus, the formation of $CaSO_4$ alone does not explain the degradation of the refractory material through cracking.

When analyzing cross-sectional samples of the spent refractories with µ-XRF, other elements in addition to S were identified (Fig. 4). The depth of diffusion and the concentration profile depended on the element. Due to the chemical complexity of the flash smelter gas phase, it is still to be clarified, how exactly does the temperature gradient affect the diffusion of different elements and whether the penetration and possible reactivity of these species play a role in the refractory wear. Nonetheless, the identified species indicate that the porosity in the refractory brick is high enough for gaseous species to diffuse into the refractory, possibly affecting the lifetime of the material.

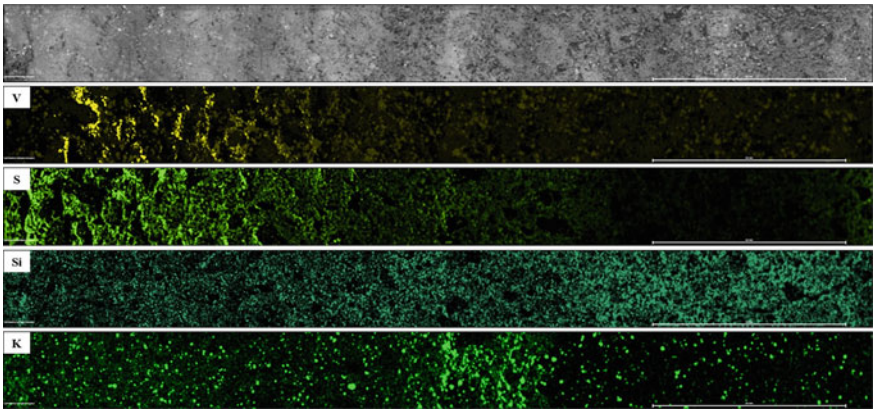

Fig. 4 µ-XRF maps showing examples of the effect of the temperature gradient on diffusion in a spent refractory brick from the roof lining of a nickel flash smelting furnace. The cooler end of the sample is to the left

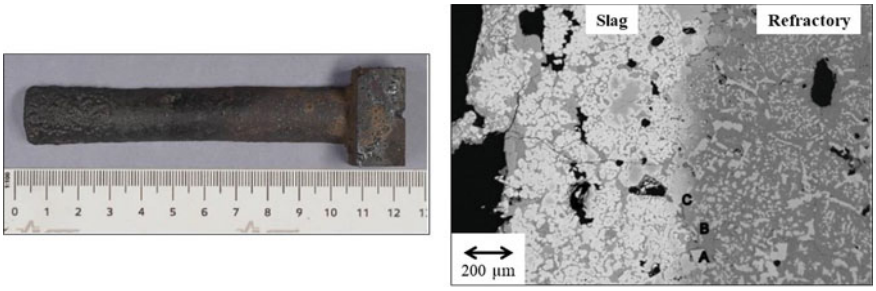

Fig. 5 A refractory sample and an SEM cross-sectional image of the slag/refractory interface after the immersion test

In the immersion tests, the slag had evidently reacted with the refractory, for some slag had deposited onto the refractory surface, forming a dense interface between the two materials (Fig. 5). When the chemical composition of the slag was analyzed after the immersion test, it contained higher amounts of Cr and Al compared to the initial composition. Furthermore, Ca had leached into the slag. The dissolution of Cr, Al, and Ca from the refractory provided further evidence of the interaction between the slag and the refractory. This may eventually influence the stability of the phases and contribute to the selection of elements, which are available to react with the gas phase. For example, if no Ca is available, SO_2/SO_3 in the gas phase might react with MgO instead, forming $MgSO_4$ analogously to Reactions (1) and (2).

Conclusions

The microstructure of as-received magnesia-chromite ($MgCr_2O_4$) spinel-based refractories was compared with similar refractories collected from the gas-phase lining of a nickel flash smelting furnace. The main focus of the comparison lay on the interactions between gaseous species and the refractory material. Special emphasis was put on the role of the prevailing temperature gradient in the diffusion of species into the refractory material. In another set of comparative tests, refractory samples were immersed in nickel flash smelting slag to further clarify, which structural or chemical changes in the refractory originate from the interactions with the gas phase. Based on the results, further conclusions can be drawn:

- The porosity of the refractory allows gaseous species to diffuse deep into the material.
- Temperature gradient affects both the microstructure of the material and the penetration depth of gaseous species.
- Elements such as As, K, Pb, and S were identified inside the refractory. Sulfur had reacted with Ca, forming $CaSO_4$, which led to voluminal changes, and possibly, the formation of internal stresses.

- The possible reactions including other penetrated species need to be studied further. However, their role in refractory wear cannot yet be excluded.
- Similar to the reactions with the gas phase, interactions with the slag resulted in a densified microstructure.
- Although the reactions between the slag and the refractory material are not considered to be as significant as the gas-phase-related reactions, the leaching of Ca from the refractory to the slag may contribute to the formation of $MgSO_4$ instead of $CaSO_4$ within the refractory.

As for future studies, to better understand the effect of thermal gradient on the diffusion of impurities, controlled laboratory-scale experiments with individual gaseous species should be carried out in the presence of a thermal gradient. Furthermore, modeling on the gas-phase stability and solidification of species would support the interpretation of μ-XRF results, for example. Experiments on how the changes in the microstructure and chemical interactions with the impurities affect the mechanical properties of refractories would most likely provide valuable information about the role of cracking, for example, in the wear process.

Acknowledgements The research has been funded by Business Finland, Åbo Akademi, VTT Technical Research Centre of Finland Ltd., and Metso via the TOCANEM project (Register numbers 41752/31/2020 for Åbo Akademi, 36409/31/2020 for VTT Technical Research Centre of Finland Ltd., and 40513/31/2020 for Metso). The financial support is acknowledged. This work has been carried out partly within the Academy of Finland project "Initiation and propagation of high-temperature corrosion reactions in complex oxygen-containing environments" (Decision no. 348963).

References

1. Mäkinen T, Taskinen P (2008) Trans Inst Min Metall Sect C 117:86
2. Schelsinger ME, King MJ, Sole KC, Davenport WG (2011) Extractive metallurgy of copper, 5th edn. Elsevier, Amsterdam, pp 89–110
3. Ranki-Kilpinen T, Peuraniemi EJ, Mäkinen M (2002) Sulfide smelting 2002. TMS, Warrendale, pp 261–272
4. Crundwell FK, Moats MS, Ramachandran V, Robinson TG, Davenport WG (2011) Extractive metallurgy of nickel, cobalt and platinum group metals. Elsevier, Amsterdam, p 610
5. Malfliet A, Loftian S, Scheunis L, Petkov V, Pandelaers L, Jones PT, Blanpain B (2014) Degradation mechanisms and use of refractory linings in copper production processes: a critical review. J Eur Ceram Soc 34:849–876
6. Lee WE, Zhang S (1999) Melt corrosion of oxide and oxide-carbon refractories. Int Mater Rev 44:77–104
7. Gerle A, Piotrowski J, Podwórny J (2017) The Influence of order in the cation sublattice of $MgAl_2O_4$, $MgCr_2O_4$ and $MgFe_2O_4$ spinels on the kinetics of topochemical reactions with sulphur oxides. J Ceram Sci Technol 8(2):183–192
8. Liow J-L, Tsirikis P, Gray NB (1998) Study of refractory wear in the Tuyere region of a Peirce-Smith nickel conventor. Can Metall Q 37:99–117
9. Fotoyi NZ, Eric RH (2011) Interaction of MgO-MgR_2O_4(R: Al, Cr, Fe) refractories with SO_2-containing gases. In: Jones RT, den Hoed P (eds) Southern African Pyrometallurgy. Southern African Institute of Mining and Metallurgy, Johannesburg, 6–9 Mar 2011

10. Gregurek D, Schmidl J, Spanring A (2021) Refractory challenges in nickel and cobalt processing furnaces in Ni-Co 2021. In: The 5th international symposium on nickel and cobalt. The minerals, metals & materials series. Springer, Berlin
11. Wieczorek-Ciurowa K (1992) Catalytic sulphation of limestone/lime with platinum. J Therm Anal 38:2101–2107
12. Lehmusto J, Laurén T, Lindgren M (2019) The catalytic role of process dust in the SO_2-to-SO_3 conversion in flash smelting heat recovery boilers. JOM 71(9):3305–3313

Anchorage Force and High-Temperature Stability of Refractory Fiber Modules

Dong Yue, Jiulin Tang, Bo Liu, and Liangying Wen

Abstract Refractory fiber modules are widely used in new or upgraded high-temperature forging furnaces because of their lightweight, heat-insulating, and heat-retaining properties. The service life and operational efficiency of the furnace is strongly related to the stability of the internal fiber module anchorage structure. We have analyzed the force characteristics of the anchoring structure of refractory fiber modules and established the force equilibrium of the stable and non-dislodging interaction of refractory fiber modules with different anchorage structures and its correlation with the preset force F_0 provided by the anchoring weld. The shrinkage characteristics of the refractory fiber modules in the anchorage structure, the stability and oxidation resistance of the anchorage structure, and the pre-positioned weld material to high temperatures are investigated through high-temperature simulation experiments. Combined with the actual application, we propose the installation layout mode to effectively reduce the high-temperature shrinkage gap between the refractory fiber modules, and optimize the position distribution of the anchored metal structural parts in the refractory fiber anchorage structure and the anchorage welding adjustment scheme. The optimized scheme was applied to the repair and renovation project of a heating furnace in a factory, which achieved significant economic and social benefits.

Keywords Heating furnace · Refractory fiber module · Anchorage structure · Mechanical characteristics · High-temperature stability

D. Yue · B. Liu · L. Wen (✉)
School of Materials Science and Engineering, Chongqing University, Chongqing 400044, China
e-mail: cquwen@cqu.edu.cn

J. Tang
Equipment Department, Dongfang Electric Group, Dongfang Boiler Co. Ltd., Sichuan 643001, China
e-mail: huangaijian5236@163.com

© The Minerals, Metals & Materials Society 2024

G. Alvear et al. (eds.), *Advances in Pyrometallurgy*, The Minerals, Metals & Materials Series, https://doi.org/10.1007/978-3-031-50176-0_7

Introduction

As an important part of heating furnace lining, it plays a role in the operation of heating furnace insulation and heat conservation, saving fuel [1–3]. Heating furnace lining materials are mainly shaped refractory materials, unshaped refractory materials, and refractory fiber. Compared with other refractory materials, refractory fiber has the advantages of high-temperature resistance, low dead weight, low density and thermal conductivity, stable chemical properties, etc. [4–6]. Refractory fiber as a kind of furnace lining material, its material selection and installation in the heating furnace directly affect the operation of the heating furnace [7, 8].

Loosening or detachment of lining materials on the roof of a heating furnace is the main cause of lining material damage. Many researchers have conducted further studies to solve the problem of its loosening or detachment. In Shi's work [9], the damaged parts of a company's hydrogen conversion furnace lining removal and rust removal, and then welded anchor nails to install the refractory fiber module, and finally in the combination of the new lining and the old lining with high-alumina ceramic fiber spray for articulation processing, so that the old lining and the new lining between the articulation of the lining close to the problem of rapid repair of lining damage. In addition, in the process of welding anchor nails, he pointed out that it should strictly control the distance error between two adjacent anchor nails; to ensure that the refractory fiber module is installed close. Yao [10] analyzed the causes of damage to the loose ceramic fiber lining of a company's heating furnace, and the results showed that the anchor nails of the refractory fiber module were corroded or broken, which was the main cause of damage to the lining. For this reason, the loose ceramic fiber lining replacement for dense ceramic fiber spray lining and modified lightweight low-conductivity castables composite lining structure, to achieve not only to prevent the anchor nails of corrosion off, but also improve the effect of heat insulation. However, the use of composite lining structure, first of all, is not convenient for on-site construction, and secondly, the density of modified lightweight low-conductivity castables is higher than that of refractory fibers, which aggravates the burden on the structure of the heating furnace body. And once the lining is damaged, it cannot be repaired quickly, which is not conducive to normal production operation. To inhibit the shrinkage of refractory ceramic fiberboard above 1300 °C, Naoya et al. [11] coated the surface of the fiberboard with silica sol containing multiple alumina particles. When an alumina-silica sol slurry with a mass fraction of 50% was coated on the surface, the line shrinkage of the fiberboard decreased from 4.3 to 1.5% after the refractory ceramic fiberboard was heated at 1400 °C for 8 h. This phenomenon indicates that coating a layer of refractory material on the surface of the furnace lining material can also achieve the effect of significantly reducing fiber shrinkage.

Heating furnace roof refractory fiber modules are mainly installed and fixed in the form of anchors. At present, there are more anchoring methods, such as Wang et al. [12] proposed an adjustable anchor for fixing the insulation layer and refractory lining, which reduces the construction difficulty of the insulation lining and increases

the interchangeability between anchors in each part. Luo et al. [13] proposed an anchor for installing ceramic fiber module furnace lining, which can avoid the damage of the anchor in contact with high-temperature furnace gas, so that the ceramic fiber module is not easy to fall off. Lu et al. [14] proposed a ceramic fiber large module structure with a wide range of applications, which uses a full-fiber furnace lining to accelerate the construction speed and improve the surface flatness of the lining. Wang et al. [15] proposed a chromium-containing fiber blanket and felt composite ceramic fiber module, which is a composite combination of different types of refractory fibers, with better thermal insulation properties. There have been more forms of anchorage structure or composite structure, but in the actual application of the discovery there are anchors easy to damage there use of short life and refractory fiber module installation, and construction difficulties and other problems.

A factory's trolley-type high-temperature heating furnace lining with full refractory fiber modules, in the production process, has the frequent occurrence of the roof of the refractory fiber module loosening and falling phenomenon, resulting in the furnace temperature curve deviation from the requirements of the process. Therefore, the quality of the processed workpiece is reduced, and has to stop the furnace maintenance frequently. The occurrence of these problems seriously affects the normal production and operation of enterprises, which not only cause the production cost to increase but also cause the need to solve energy waste and waste emissions and other problems. In this paper, for the refractory fiber furnace lining material of a factory heating furnace problems in the operation process, from the refractory fiber module does not fall off the force balance relationship, analysis of different anchoring structure under the refractory fiber module of the force characteristics and factors affecting the stability of its safety condition, the optimization of the refractory fiber module anchoring structure to improve the application of the application of verification.

Anchor Structure and Force Characterization

There are two types of refractory fiber module anchors for the roof of a heating furnace in a factory, as shown in Figs. 1a and 2a. The anchoring method shown in Fig. 1a is furnace roof steel plate—bolted anchor nails—refractory fiber module. The anchoring method shown in Fig. 2a is furnace roof steel plate—U-hook and crossbar blocking combination anchors—refractory fiber module. In Figs. 1a, 2, 3, 4, and 5 are the furnace roof steel plate, cross bar, nut, bolt anchoring nail, and refractory fiber module, respectively. In Figs. 1, 2a, 3, and 4 are the furnace roof steel plate, the U-shaped hook (consisting of two anchoring rods), the cross bar, and the refractory fiber module, respectively. Anchoring in the refractory fiber module support process, through the interfacial bonding or friction to form an anchor bearing role and the use of interfacial stress transfer to inhibit the refractory fiber module loosening in a relatively static and stable state. Figures 1b, c and 2b, c are the anchorage structure unit and refractory fiber module force situation, where F_0 for the anchorage welding to provide the preset tension. τ_1 for the anchorage structure unit and refractory

fiber module between the average shear stress. τ_2 for the adjacent two refractory fiber module between the average shear stress. F_1, F_2 is the tensile force from the anchorage to the fiber module or from the fiber module to the anchorage (both equal in magnitude and opposite in direction) and G is the gravitational force of the fiber module. The refractory fiber module is a square with side length l, density ρ, and gravitational force G is ρl^3. The anchoring structure unit is made of round steel with a diameter of D or anchoring screws welded and fixed to the steel plate of the furnace roof to form a metal structure body, which supports all the loads of the anchored metal structure body and the refractory fiber module by the pretension of the anchoring welded ends. Assuming that the pretension of a single anchor rod is F_0, the different anchoring methods are mainly manifested in the differences in the metal structure body. For example, Fig. 1b shows that there is only one anchorage weld end for each unit of the anchorage structure I, i.e., the prestressing is $1 \times F_0$. Figure 2b shows that there are two anchorage weld ends for each U-hook in the anchorage structure II, and the preset stress assigned to each unit of the anchorage structure is $(2 \times 2 \times F_0)/2$, which is equal to $2F_0$.

For the anchoring structure unit shown in Fig. 1b, the length of the bolt anchor nail is 1/5 of the side length l of the refractory fiber module, the length of the cross bar within the refractory fiber module is 1/3 of the side length l of the refractory

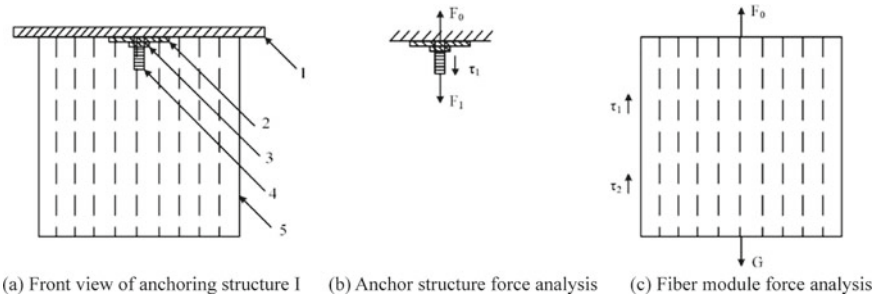

Fig. 1 Anchorage structure of refractory fiber module I and force analysis

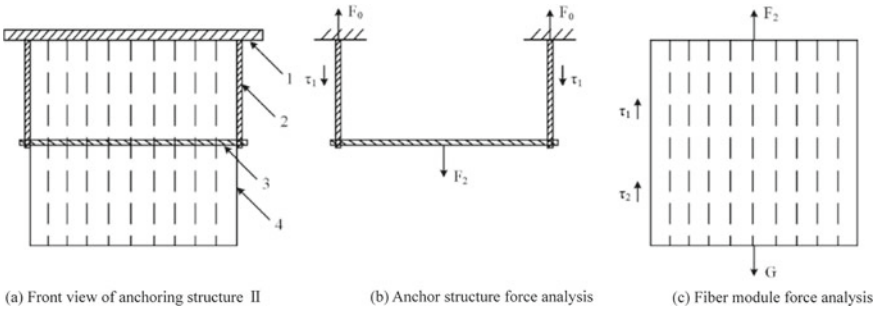

Fig. 2 Anchorage structure of refractory fiber module II and force analysis

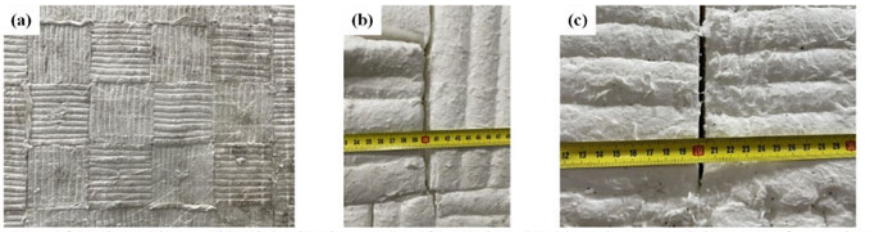

Fig. 3 Formation of high-temperature shrinkage joints in the anchoring unit of the refractory fiber module on the simulation top

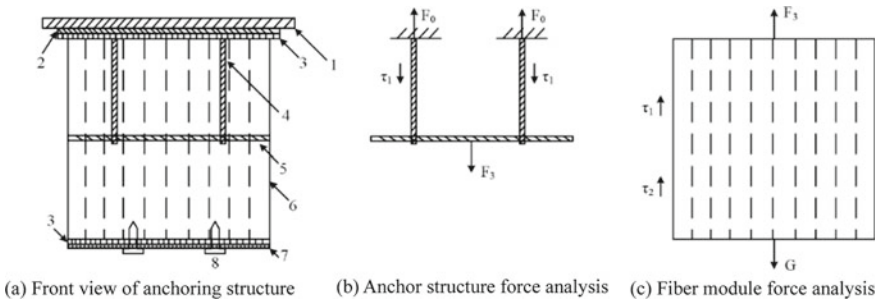

Fig. 4 Anchorage structure and stress analysis of new refractory fiber module

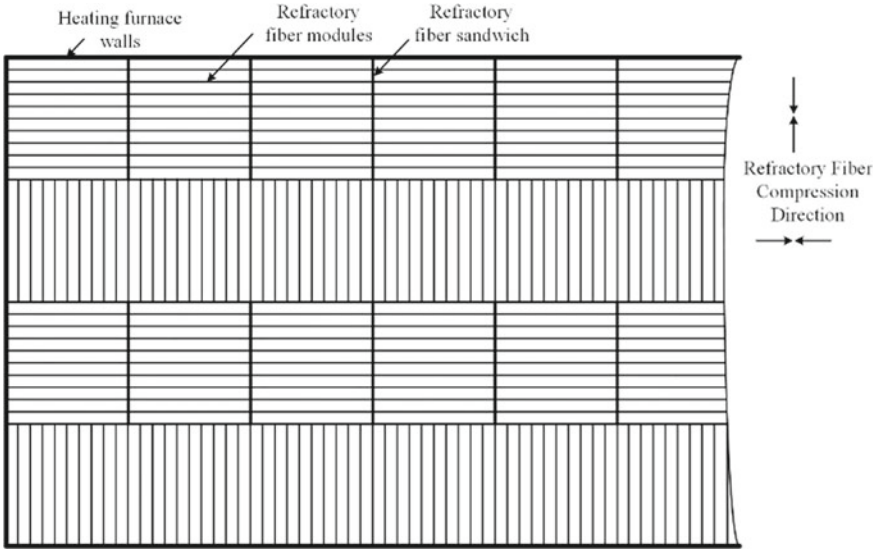

Fig. 5 Arrangement of refractory fiber modules

fiber module, and the average shear stress between the anchoring structure unit and the refractory fiber module is denoted by τ_1, the shear tensile force applied to the refractory fiber module by the anchoring structure I shown in Fig. 1 can be expressed as follows:

$$P_I = \tau_1 \left(\pi D \times \frac{l}{5} + \frac{l}{3} \times \pi D \right) = \frac{8}{15} \tau_1 \pi D l \tag{1}$$

For the anchoring structural unit in Fig. 2b, the unilateral length of the U-shaped hook is 1/2 of the side length l of the refractory fiber module, and the length of the crossbar is noted as l. The shear stress between the anchoring structural unit and the refractory fiber module is still expressed by τ_1, and the shear tensile force provided by the anchoring structural unit to the refractory fiber module can be expressed as follows:

$$P_{\mathrm{II}} = \tau_1 \left(2 \times 2 \times \pi D \times \frac{l}{2} \times \frac{1}{2} + l \times \pi D \right) = 2\tau_1 \pi D l \tag{2}$$

When the refractory fiber module is in a static and stable state, the forces on the refractory fiber module shown in Figs. 1c and 2c are in equilibrium, i.e., $\Sigma F = 0$.

The refractory fiber module in Fig. 1c has the following equations:

$$\sum F = F_1 + P_I + \tau_2 l^2 \times 4 - G = F_1 + \frac{8}{15} \tau_1 \pi D l + \tau_2 l^2 \times 4 - \rho l^3 = 0 \tag{3}$$

From Eq. (3) and combined with the force relation of the anchoring structure unit in Fig. 1b, the basic condition for the non-displacement of the refractory fiber module in the anchoring structure I can be obtained as follows:

$$F_1 = \rho l^3 - 4\tau_2 l^2 - \frac{8}{15} \tau_1 \pi D l < F_0 \tag{4}$$

Similarly, the basic condition for the non-displacement of the refractory fiber module shown in Fig. 2c in the anchoring structure II can be obtained as follows:

$$F_2 = \rho l^3 - 4\tau_2 l^2 - 2\tau_1 \pi D l < 2F_0 \tag{5}$$

As can be seen from the above, if the diameter D of the round steel or screw; the edge length l of the refractory fiber module; and the density ρ, τ_1, τ_2 are the same, when the anchoring structure II is compared with the anchoring structure I, the anchoring structure unit of the former provides the preset tensile force to the refractory fiber module twice as much as the latter, and the shear tensile force is also larger. It can be seen from Eqs. (4) and (5) that the stability of the refractory fiber modules on the roof of the heating furnace is related to the shear tensile force of the refractory fiber modules in close contact with each other, the shear tensile force provided by the anchoring structure unit, and the pre-positioned tensile force F_0 at

its welded end. In the process of the anchoring structure, the preset tension F_0 is the basic guarantee of the stability of the anchoring structure, so the analysis of the factors affecting the stability of the anchoring structure is essential to determine the cause of the loosening and shedding of the refractory fiber module on the furnace roof.

Anchor Structure Material and Stability Analysis

During furnace operation, the refractory fiber modules in the roof anchorage unit may shrink to varying degrees, creating gaps and reducing the interaction between their contact surfaces. In the case of gas-fired furnaces, high-temperature gases generated by combustion penetrate through the shrinkage gaps, causing oxidative burns on the anchored metal structural elements and affecting their structural stability, which in turn affects the stability of the refractory fiber modules in the furnace roof.

Materials of Refractory Fiber Modules

The use of heating furnace temperature due to workpiece thermal processing requirements is different, the general use of the temperature range of 900–1250 °C. For the use of high-temperature heating furnace, the ability to choose the right refractory material directly affects the service life of the furnace [16, 17]. A factory heating furnace lining mainly used refractory fiber module materials which are high-alumina aluminum silicate and zirconium-containing aluminum silicate. The refractory fiber with temperature and performance differences between the two materials is mainly related to the content of Al_2O_3, SiO_2 and the content of impurity Fe_2O_3 [18]. According to GB/T 5988–2022 (refractory material heating permanent line change test method), we experimentally tested the line shrinkage of the above two refractory fibers provided by two different manufacturers, as shown in Table 1.

As can be seen from Table 1, several refractory fiber line shrinkages to meet the relevant standard requirements. However, several refractory fibers in the heating

Table 1 Linear shrinkage of different types of refractory fibers (test temperature 1050 °C)

Types of refractory fiber	Zirconium-containing 1–1#	High aluminum 1–2#	Zirconium-containing 2–1#	High aluminum 2–2#
Wire shrinkage (%) *	≦ − 4(− 1.32)	≦ − 4 (− 1.88)	≦ − 3 (− 1.44)	≦ − 3 (− 1.83)

* *Note* The results of line shrinkage in the table, the former is the national standard of refractory fiber line shrinkage, and the measured refractory fiber line shrinkage is in parentheses

furnace temperature conditions are different degrees of contraction, and due to contraction will inevitably lead to contraction gaps between the refractory fiber module, thus creating a channel for high-temperature gas into the roof steel plate and refractory fiber module top contact surface. Figure 3a shows the state of the refractory fiber modules (300 mm × 300 mm × 300 mm) of the furnace roof in seamless close contact before the simulation experiment. The states of the simulated furnace roofs with refractory fiber modules of different materials with shrinkage gaps after holding at 1050 °C for 100 h are shown in Fig. 3b, c, respectively. The maximum shrinkage gap width of the high-alumina aluminosilicate fiber module is 6 mm, and the maximum shrinkage gap width of the zirconia aluminosilicate fiber module is 4 mm. For the gas-fired high-temperature furnace, the formation of such shrinkage gaps is extremely unfavorable to the stability of the roof of the refractory fiber module. Because the gas combustion of high-temperature gas is composed of the main components of H_2O, CO_2 and a small amount of O_2, these components have an oxidizing effect. In the heating furnace operation process, high-temperature oxidizing gases from the refractory fiber shrinkage gap will run into the penetration of the roof refractory fiber module, resulting in fixed refractory fiber module anchors or anchors' welding points will be affected by the oxidation of burns, so that the anchors to provide the preset tensile force F_0 will be smaller or even lost, ultimately resulting in the roof refractory fiber module of the stability affected or even fall off.

Anchoring of Metal Structural Parts and Preset Solder Material

A force analysis of the anchor structure of the refractory fiber module shows that the preset tension applied to the refractory fiber module by the anchors welded to the heating furnace shell is very important for the stability of the refractory fiber module against falling off. Welding is the process of joining similar or dissimilar metals by melting a wire at a high temperature. When welding dissimilar metals, the metal to be welded and the brazing material have a significant effect on the quality of the weld. Choosing the right material can effectively inhibit the diffusion of carbon in the fusion zone and reduce the thermal stress at the weld when welding dissimilar steels, thus reducing the likelihood of stress damage [19]. A factory heating furnace roof refractory fiber module anchor structure used in the anchor is Ni–Cr-based 1Cr18Ni9Ti-type stainless steel, welding rod-type CHS102-type stainless steel. Its chemical composition is shown in Table 2.

As can be seen in Table 2, 1Cr18Ni9Ti-type stainless steel anchor chemical composition and CHS102-type stainless steel welding rod of the molten metal chemical composition are similar, and stainless steel Ti elements can be generated with the C element TiC, which reduces the formation of chromium carbide, which in turn reduces the chromium carbide in the austenite grain boundary precipitation resulting in chromium-depleted zone and the susceptibility to intergranular corrosion, so it has

Table 2 Chemical composition of 1Cr18Ni9Ti and 0Cr25Ni20 austenitic stainless steel and CHS102 and CHS402 electrode

Element	Mass fraction /%		Element	Mass fraction/%	
	1Cr18Ni9Ti	CHS102 electrode		0Cr25Ni20	CHS402 electrode
C	≤ 0.12	≤ 0.08	C	≤ 0.25	0.08–0.20
Si	≤ 1.00	≤ 0.90	Si	≤ 1.50	≤ 0.75
Mn	≤ 2.00	0.50–2.50	Mn	≤ 2.00	1.00–2.50
S	≤ 0.030	≤ 0.030	S	≤ 0.030	≤ 0.030
P	≤ 0.035	≤ 0.040	P	≤ 0.035	≤ 0.030
Cr	17.00–19.00	18.00–21.00	Cr	24.00–26.00	25.00–28.00
Ni	8.00–11.00	9.00–11.00	Ni	19.00–22.00	20.00–22.50
Ti	5*(C-0.02)	–	Mo	–	≤ 0.75
Mo	–	≤ 0.75	–	–	–

a certain degree of resistance to intergranular corrosion ability [20, 21]. However, 1Cr18Ni9Ti-type stainless steel anchor and CHS102-type stainless steel electrode combination in a factory heating furnace use conditions, there are the following problems: ① welded joints σ-phase embrittlement. If there is a long time in the 650–850 °C temperature conditions, the ferrite part of the weld will be transformed into a brittle σ phase, with the extension of time, the σ phase gradually increased, leading to the welded joints on the plasticity and toughness decrease, and ultimately make the welded on the roof of the furnace steel anchorage metal structural parts of the stability of the deterioration of ② welded joints thermal cracking. The type of stainless steel in the Ni element is easy to S, P and other impurity elements to form a low melting point eutectic, in the welding structure cooling crystallization process to form a liquid film. Austenitic stainless steel has a small thermal conductivity, large coefficient of linear expansion, which in the welding thermal cycling process is prone to the formation of large thermal stresses, so it will make the austenitic stainless steel joints have a greater tendency to thermal cracking in the welded joints in the use of the process which is easy to damage; and ③ welded joints stress corrosion. Austenitic stainless steel welded joints have a large resistivity, small thermal conductivity, limitations, in a corrosive environment by tensile stress, and easy to produce cracking phenomenon [22–26].

Anchor and welding rod molten metal resistance to high-temperature oxidative burnout ability is also an important factor affecting the anchorage pre-positioning tension. In order to analyze and compare, in the process of simulation experiments using laboratory high-temperature furnace with 0Cr25Ni20-type high chromium-nickel heat-resistant stainless steel and CHS402 stainless steel electrode as a comparison of the experimental samples, its chemical composition is shown in Table 2. 0Cr25Ni20-type high-chromium-nickel heat-resistant stainless steel anchorages from Table 2 can be seen from the chemical composition, and the chemical

Table 3 Burnout rate of different types of stainless steel and welding rods

Steel type or electrode type	Testing temperature (°C)	Holding time (h)	Burnout rate (%)
1Cr18Ni9Ti	1050	100	45.54
0Cr25Ni20	1050	100	0.06
CHS102	1050	100	41.15
CHS402	1050	100	1.69

composition of CHS402 stainless steel electrodes is also similar to the chemical composition of the melt-deposited metal.

Table 3 shows the oxidative burn rate of two stainless steel anchorage specimens and two stainless steel welding rod specimens placed in an electric furnace in an air environment and heated to 1050 °C with a cumulative holding time of 100 h.

From the results in Table 3, 1Cr18Ni9Ti austenitic stainless steel specimens at high temperatures, the oxidative burn rate is as high as 45.54%, in addition, CHS102 stainless steel electrode specimen's oxidative burn rate also reached a high 41.15%. Under the same conditions, 0Cr25Ni20-type heat-resistant stainless steel oxidative burn rate of 0.06% and CHS402-type stainless steel electrode specimen's oxidative burn rate of 1.69% have shown better resistance to high-temperature oxidative erosion performance. Compared with 1Cr18Ni9Ti-type heat-resistant stainless steel and CHS102-type stainless steel electrodes, 0Cr25Ni20-type heat-resistant stainless steel and CHS402-type stainless steel electrodes have better resistance to high-temperature oxidative erosion, mainly because the latter two contain higher chromium, which can combine with oxygen to form a more stable Cr_2O_3 oxide film covering the surface of the metal to prevent it from further oxidation [27, 28].

It can be seen that in the heating furnace conditions, in order to ensure the stability of refractory fiber module hanging in the furnace roof, we must give full consideration to the anchorage of metal structural components and welding rod material matching, as well as resistance to high-temperature erosion, because of the organization of the material, the chemical composition of large differences in reasons, leading to the material of internal stress or damage to the stability of the anchorage structure, which ultimately affects the anchorage provided by the size of the preset tensile force.

Optimization and Application of Refractory Fiber Module Anchoring Structure

In order to reduce the size of the shrinkage gap of the refractory fiber module in the heating furnace and reduce the degree of damage to the refractory fiber module, we propose an improved anchoring method and structure of the refractory fiber module as shown in Fig. 4 [29]. The optimized refractory fiber module anchoring structure is shown in Fig. 4a, including furnace roof steel plate mesh 1, adhesive 2, refractory fiber screed 3, hook 4, crossbar 5, refractory fiber module 6, refractory coating 7,

and high-temperature ceramic nails 8. Figure 4b, c shows the force of the anchored structural unit and the refractory fiber module, respectively, where F_3 is the stress of the anchor to the refractory fiber module or the refractory fiber module to the anchor (both equal in magnitude and opposite in direction), and the symbols of F_0, τ_1, τ_2, and G have the same meanings as the previous ones.

For the anchored structural unit in Fig. 4b, if the hook length is 1/2 of the side length l of the refractory fiber module, the crossbar length is l, and the average shear stress between the anchored structural unit and the refractory fiber module is still τ_1, the shear tensile force provided to the refractory fiber module by the anchored structural unit in Fig. 4b can be expressed as follows:

$$P_{\mathrm{III}} = \tau_1 \left(2 \times \pi D \times \frac{l}{2} + l \times \pi D \right) = 2\tau_1 \pi Dl \tag{6}$$

When the refractory fiber module is in a static and stable state, the forces on the refractory fiber module shown in Fig. 3c are in equilibrium, i.e.:

$$\sum F = F_3 + P_{\mathrm{III}} + \tau_2 l^2 \times 4 - G = F_3 + 2\tau_1 \pi Dl + \tau_2 l^2 \times 4 - \rho l^3 = 0 \tag{7}$$

From Eq. (7) combined with the force relationship of the anchoring structure unit in Fig. 3b, the basic condition for the non-displacement of the anchoring structure of the refractory fiber module can be obtained as follows:

$$F_3 = \rho l^3 - 4\tau_2 l^2 - 2\tau_1 \pi Dl < 2F_0 \tag{8}$$

Comparing Eqs. (6) and (8) with Eqs. (2) and (5), respectively, it can be seen that the basic conditions for the shear pull of the metal parts on the refractory fiber modules and non-displacement of the optimized anchorage structure shown in Fig. 4 are the same as those for the anchorage structure II shown in Fig. 2.

Comparison of Figs. 4 and 2 can be seen, in which Fig. 4 shows the optimized refractory fiber module anchoring structure in the furnace to avoid high-temperature oxidizing atmosphere and metal anchors and anchors' welded end contact and other advantages are:

① The anchoring structure of the metal hook from the two refractory fiber modules adjacent to the position of movement to a single fiber module can avoid the refractory fiber module shrinkage gaps when the metal hook and the furnace from the escape into the high-temperature oxidizing gas contact burn damage.

② The heating furnace roof steel plate into a perforated steel mesh, anchorage welding point is located outside the refractory fiber module on the roof of the steel mesh, and in the refractory fiber module and the roof of the steel mesh laid between a layer of fire-resistant fiber blankets, insulation, and heat preservation at the same time completely blocked with the furnace high-temperature oxidizing gas contact to prevent the anchorage weld head of the burn damage and easy

to repair. At the same time, the refractory fiber blanket can also prevent high-temperature furnace gas through cracks in the overflow, play a role in protecting the furnace steel skeleton, and reduce heat loss.

③ In the refractory fiber module to the fire surface laying a layer of refractory fibers, spraying refractory coatings, and so on are to prevent the high-temperature furnace gas on the refractory fiber module of the erosion of scouring to prevent the high-temperature furnace gas fled into the refractory fiber module burnt anchorage structure, which is conducive to prolonging the entire lining of the furnace. service life.

At the same time, when optimizing the fiber module anchoring structure on the furnace roof, we also consider changing the fiber module installation arrangement to effectively reduce the high-temperature shrinkage gap between the fiber modules, as shown in Fig. 5.

The detailed operation steps are as follows. In the process of installing the refractory fiber modules on the roof of the furnace, two adjacent rows of fiber modules are placed in the direction of 90 degrees, as shown in the first and second rows of fiber modules at the top of Fig. 5. This cross layout can ensure that the parallel fiber compression direction placed in one row of fiber modules in the vertical compression direction of the contraction gap can be provided by the adjacent row of fiber modules to compensate for the compression margin, as shown in Fig. 5, in the second row of fiber modules and the first three rows of fiber modules between the contraction gap can be provided by the first three rows of fiber modules of the compression margin to compensate for the filling. But for the same line of vertical fiber compression direction in the fiber module (such as Fig. 5, the second line of fiber modules), the contraction gap between the two fiber modules does not get compression margin compensation; therefore, in the installation of the line of fiber modules in the two fiber modules placed between the prefabricated same material of refractory fiber blanket will be folded and compressed to the original thickness of the 2/3 and squeezed by the neighboring fiber modules which can achieve the purpose of compensating for the contraction gap. Our improved refractory fiber anchoring structure and installation method are applied to the repair and renovation of heating furnaces in a factory for verification, including 7.5 m × 41 m large annealing furnace, 5 m × 5 m quenching furnace, and 4.8 m × 5.5 m and 3.8 m × 10.5 m forging furnace. Compared with the pre-improvement, the installation process of the refractory fiber module on the roof is safer, more convenient, and faster, which greatly reduces the labor intensity of the construction personnel and eliminates the problem of frequent shedding of the refractory fiber module on the roof of the furnace. It prolongs the service life of the whole furnace, saves 11,700,000 m^3/year of natural gas, and the direct economic benefit reaches 319,700,000 m^3/year, which is very good for the life cycle of the furnace, reduces the energy consumption, and reduces the emission of CO_2 and waste. It has a good promoting effect on the use cycle of heating furnace, reduce energy consumption, reduce CO_2 and waste emission, and has significant economic and social benefits.

Conclusion

The following main conclusions are drawn from the force analysis and high-temperature simulation experiments on the anchoring structure of refractory fiber modules:

(1) The preset tension F_0 of the welded metal anchors, which is established by matching the heating furnace shell, the anchoring metal components, and the welding rod material, is the basic guarantee for the stability of the anchoring structure of the refractory fiber module on the furnace roof, and the preset tension of the double anchoring structure is $2F_0$.
(2) High-temperature oxidizing gas from the refractory fiber shrinkage joints into the refractory fiber–shell interface ablation of the anchoring metal parts and anchoring weld joints is the main reason for the reduction or even loss of the preset tensile force F_0, causing the fiber module to loosen and fall.
(3) As it was proposed to reduce the shrinkage gap of refractory fiber module layout optimization mode and improve the anchoring metal parts in the roof of the welding position, shape and anchoring metal parts welding material matching program is feasible, the application effect is good.

Acknowledgements The work is supported by the National Natural Science Foundation Project of China (51974046). The authors of this paper would also like to express their special thanks to Dongfang Electric Group Dongfang Boiler Co., Ltd. for providing the solid model for the project modelling calculations.

References

1. Liu YP, Wen Z, Liu XL et al (2012) Application status and analysis of gas trolley heating furnace. Ind Heat 41(1):1–6 (in Chinese)
2. Zhu XG (2011) Improvement practice of lining construction quality of walking beam type reheating furnace of steel rolling. Ind Furnace 33(4):52–55 (in Chinese)
3. Gao Y (2021) Discussion on the application of refractory in the transformation of heating furnace. Sci Technol Inform 19(17):33–35 (in Chinese)
4. Li SG, Wang XH (2014) Design, construction and application of all fiber heating furnace lining. Appl Energy Technol 4:30–31 (in Chinese)
5. Zhao ZK, Ha ZQ (2014) Discussion on refractory lining of kiln. Brick-Tile 3:13–18 (in Chinese)
6. Varrik NM, Zimichek AM, Sumin AV et al (2020) Preparation of continuous aluminum oxide fibers with silicon oxide and zirconium oxide additives. Fibre Chem 51(6):430–436
7. Liu JK, Wu SC, He GB (2021) Transformation analysis of new high temperature refractory fiber module in stainless steel rolling heating furnace. Metall Equip S2:29–31+11 (in Chinese)
8. Chen C (2010) Energy saving application of refractory fiber in natural gas heat treatment furnace. Inner Mongolia Sci Technol Econ 5:89–90 (in Chinese)
9. Shi LY (2018) Discussion on repair and improvement of lining structure of heating furnace. China Petrol Chem Stan Q 38(7):79–80 (in Chinese)
10. Yao Q (2011) Application of high density type ceramic fibers liner in heating furnace. Energy Conserv Petrol Petrochem Ind 1(1):21–24+53 (in Chinese)

11. Naoya T, Shinobu H, Yusuke D et al (2018) High-temperature shrinkage suppression in refractory ceramic fiber board using novel surface coating agent. Ceram Int 44(14):16725–16731
12. Wang SH, He XH (2006) Adjustable anchor. China patent, ZL200520049788.1. 23 Aug 2006 (in Chinese)
13. Luo JM, Zhang XM, Tang S (2012) Ceramic fiber module furnace lining and its anchor. China patent, ZL201120167366.X. 21 March 2012 (in Chinese)
14. Lu L, Yan YK, Lu JY et al (2010) Ceramic fiber module. China patent, ZL200920281899.3. 24 Nov 2010 (in Chinese)
15. Wang DH, Wang J (2013) A ceramic fiber module composed of chromium containing fiber blanket and felt. China patent, ZL201220315054.3. 30 Jan 2013 (in Chinese)
16. Wang K, Chen A, Yao FY et al (2010) Discussion on lining material and structural form of super large trolley heating furnace. Ind Furnace 32(2):41–43 (in Chinese)
17. Feng QC (2018) Property classification and application of refractories. Sci Technol Inf 16(3):108–109 (in Chinese)
18. Liu JX, Yang JP, Chen MR et al (2018) Effect of SiO_2, Al_2O_3 on heat resistance of basalt fiber. Thermochim Acta 660:56–60
19. Xiao LR, Lei YC, Zhu Q et al (2018) Effect of welding on microstructures and mechanical properties of T91/316L dissimilar welding joints. Mater Rep 3601–3605 + 3633 (in Chinese)
20. Gu YF, Xu YW, Shi Y et al (2022) Corrosion resistance of 316 stainless steel in a simulated pressurized water reactor improved by laser cladding with chromium. Surf Coat Tech 441:128534
21. Young AM, Kral MV, Bishop CM (2022) Carbide formation accompanying internal nitridation of austenitic stainless steel. Mater Charact 184:111662
22. Zhao TL, Wang DL, Shi QH et al (2021) Automatic welding technology of skid mounted pipeline of stabilized austenitic stainless steel TP321. Weld Technol 50(8):44–48 (in Chinese)
23. Xu XQ, Lin G, Niu J et al (2018) Effect of stabilization treatment on hydrogen embrittlement in high temperature heat-affected zone of TP321 stainless steel. Trans Mater Heat Treat 39(7):99–105 (in Chinese)
24. Sun G, Li XL, Du J et al (2020) Study of reasons for pitting corrosion occurred on flange made of 1Cr18Ni9Ti stainless steel. J Phys Conf Ser 1575(1):012007
25. Zhang SH, Zhao YT, Zhou JW (2014) The effect of welding materials on 1Cr18Ni9Ti and 2Cr13 steel welding joints fracture microstructure pattern. Adv Mater Res 2951(881–883):1464–1468
26. Bystrianský V, Bystrianský J, Dumská K et al (2021) Effect of impurities in dissimilar metal welds on their corrosion behavior. Mater Corros 72(8):1370–1376
27. Zatkalíková V, Markovičová L, Uhríčik M et al (2020) Susceptibility to the intergranular attack in austenitic stainless steels. IOP Conf Ser Mater Sci Eng 726(1):012017
28. Zhang SC, Li HB, Jiang ZH et al (2019) Effects of Cr and Mo on precipitation behavior and associated intergranular corrosion susceptibility of superaustenitic stainless steel S32654. Mater Charact 152:141–150
29. Wen LY, Tang JL, Xiao XD et al (2022) A hanging structure of refractory fiber module for heating furnace. China patent, ZL202123263619.6, 22 Apr 2022 (in Chinese)

Study on Slag Phase Erosion Behavior and Mechanism of Carbon Composite Brick in Hydrogen-Rich Blast Furnace Hearth

Mingbo Song, Kexin Jiao, Cui Wang, Jianliang Zhang, and Chuan Wang

Abstract In this study, through thermodynamic calculation, the possible reactions of carbon composite bricks in a high-temperature water vapor environment were analyzed. The morphology of carbon composite bricks after water vapor erosion was investigated through a water vapor oxidation experiment. In addition, a damage investigation was carried out on a blast furnace using hydrogen-rich gas smelting. During the period, a green-white phase with a thickness of 150 mm–200 mm was found inside the carbon composite brick in the taphole area. The carbon bricks in this area were sampled, and XRD, chemical analysis, and SEM–EDS detection were carried out. The test results show that there is blast furnace slag erosion and harmful element Zn erosion in carbon composite bricks. The erosion of harmful elements caused the expansion and ring cracking of carbon composite bricks, resulting in further slag erosion, which eventually led to the macroscopic slag phase erosion in the taphole area. The service life of carbon composite bricks can be effectively improved by optimizing the structure of carbon composite bricks, reducing the number of pores, optimizing the pore structure, and promoting the formation of a slag-rich protective layer on the hot surface of carbon composite bricks by improving the structure of blast furnace slag system.

Keywords Hydrogen-rich blast furnace · Carbon composite bricks · Slag phase erosion · Ring crack expansion

M. Song · K. Jiao (✉) · C. Wang · J. Zhang · C. Wang
School of Metallurgical and Ecological Engineering, University of Science and Technology Beijing, Beijing 100083, China
e-mail: jiaokexin_ustb@126.com

J. Zhang · C. Wang
School of Chemical Engineering, The University of Queensland, St Lucia, QLD 4072, Australia

© The Minerals, Metals & Materials Society 2024

G. Alvear et al. (eds.), *Advances in Pyrometallurgy*, The Minerals, Metals & Materials Series, https://doi.org/10.1007/978-3-031-50176-0_8

Introduction

Under the condition of global carbon neutrality, reducing carbon emissions has become a new trend in the development of the steel industry [1–3]. The blast furnace is the largest vertical reactor, which currently bears the vast majority of the current hot metal production work [4]. In the normal production process, the blast furnace hearth is full of high-temperature slag iron, so the blast furnace hearth becomes the limiting link of the blast furnace life. In recent years, with the continuous improvement of blast furnace smelting strength, accidents of blast furnace hearth burning have occurred from time to time, which also makes blast furnace workers pay more attention to the research of blast furnace hearth refractory [5–9].

Zuo et al. studied the dissolution of Al_2O_3 and SiO_2 in carbon composite bricks through blast furnace slag erosion experiments, which is the main reason for the erosion of carbon composite bricks during use [10]. Therefore, slag corrosion resistance has become an important performance of refractory materials in the hearth [11]. Through static and dynamic erosion experiments, the researchers studied the high-temperature slag-iron erosion, chemical erosion behavior, and thermal stress erosion of hearth carbon bricks under different atmospheres [12–15]. However, there are few studies on the erosion behavior of hearth refractory in a water vapor environment. In the context of hydrogen-rich smelting, the research on the erosion phenomenon and erosion mechanism of carbon composite bricks in the hearth area is not sufficient [16, 17].

With the help of blast furnace damage investigation, the erosion of the hearth refractory after service can be studied intuitively. In this study, the erosion behavior of carbon composite bricks after service was studied through damage investigation and sampling of refractory materials in the hearth area of a hydrogen-rich blast furnace. The water vapor erosion experiment in the laboratory stage studied the erosion phenomenon of carbon composite bricks under the action of water vapor, and the erosion mechanism of carbon composite bricks under the condition of hydrogen-rich smelting was clarified.

Experimental

Experimental Apparatus and Samples

Through cutting, grinding, and polishing, the sample is made into a sheet sample with a specification of Øφ12 × 5 mm, as shown in Fig. 1.

The experiment uses a single variable method. When a certain component is changed, other factors remain unchanged. The schematic diagram of the experimental device is shown in Fig. 2.

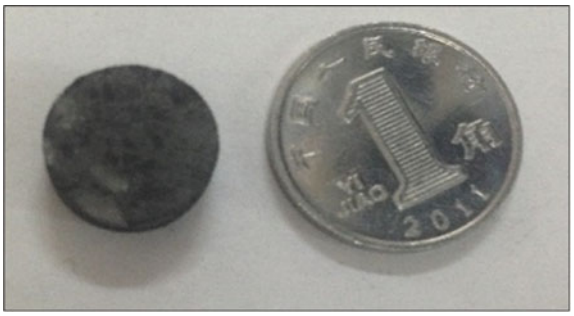

Fig. 1 Morphology of carbon composite brick sample

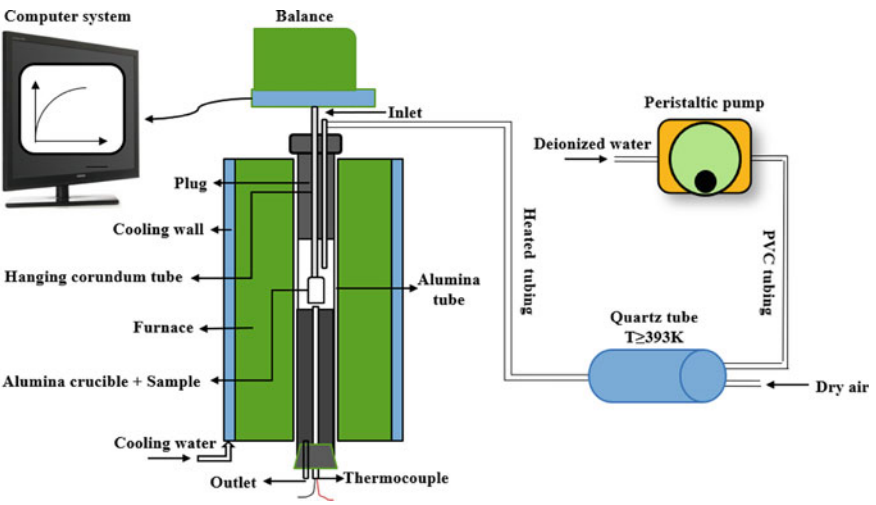

Fig. 2 Schematic diagram of high-temperature water vapor thermogravimetric device

(1) Heating and sample preparation: Run the high-temperature tube furnace, open the FP-93 temperature control instrument, set the heating program (group number, segment number, etc.), and heat the high-temperature furnace to the specified temperature; at the same time, prepare samples and weigh them.
(2) Set the reaction atmosphere: Open the XMTD temperature control instrument, adjust the temperature of the mixing tank to 300 °C; open the XMTG digital display regulator, and adjust the temperature of the heating line to 100 °C. Open the gas cylinder and adjust the gas flow; when the above two temperatures reach the specified value, the injection pump is opened and the continuous mode operation is adopted to adjust the water vapor flow and run, and the ventilation is about 30 min in advance.
(3) Software operation: Open the balance, open the preheating 30 min in advance and the computer switch, open the computer reading window, click on ‘open the

serial port', set the data preservation path, and detect whether the connection is successful.

(4) Lofting and counting: Put the sample into the reaction furnace, insert the quartz tube to ventilate, and click on 'clear the buffer' to start the measurement.

(5) End of the operation: Click 'close the serial port' and 'save the data', take out the sample, turn off the water vapor generating device (pay attention to the jet pump, turn off XMTD and XMTG after 10 min, turn off the gas flowmeter when the indication is reduced to room temperature, turn off the gas), and turn off the balance.

Experimental Scheme

The experimental schemes at different temperatures are shown in Table 1. The water vapor content is 20%, and the volume flow rate is calculated as follows:

The volume flow rate of carrier gas (air or argon, taking air as an example) is 200 ml/min.

$$w_{\mathrm{H_2O}(g)} = 20\% = \frac{V_{\mathrm{H_2O}(g)}}{V_{\mathrm{H_2O}(g)} + V_{\mathrm{air}}} \times 100\%, \quad V_{\mathrm{H_2O(g)}} = 50 \text{ ml/min}$$

Because the liquid water density at 4 °C is $\rho_{\mathrm{H_2O(l)}} = 1.0 \times 10^3$ kg/m^3.
The density of water vapor at 100 °C = 0.6 kg/m^3.
According to the gas isothermal equation:

$$\mathrm{V_{H_2O(l)}} = \frac{\rho_{\mathrm{H_2O}(g)} \mathrm{V_{H_2O}}(g)}{\rho_{\mathrm{H_2O(l)}}} = \frac{0.6 \times 50}{1.0 \times 10^3} = 0.03 \text{ ml/ min}.$$

The volume flow rate was 1.8 ml/h.

Table 1 Experimental scheme of oxidation resistance of refractory at different temperatures

Peer group	Brick type	Temperature/°C	Atmosphere
1	Carbon composite bricks	800	Air (200 ml) + 20% H_2O (1.8 ml/h)
2	Carbon composite bricks	1000	Air (200 ml) + 20% H_2O (1.8 ml/h)
3	Carbon composite bricks	1200	Air (200 ml) + 20% H_2O (1.8 ml/h)

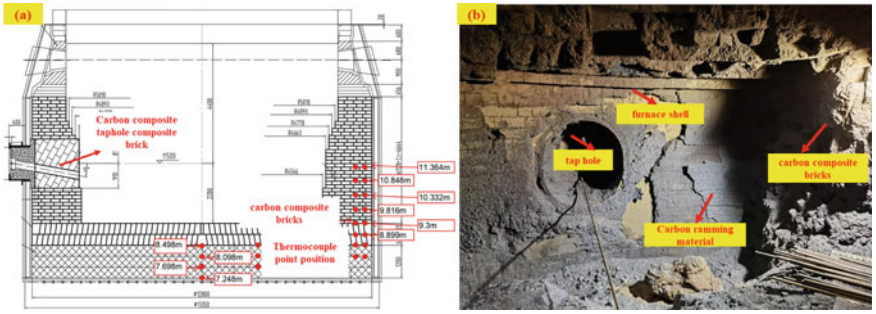

Fig. 3 Blast furnace hearth refractory configuration and sampling position with **a** blast furnace hearth refractory configuration and **b** macroscopic morphology of sampling position in taphole area

Sample Preparation After Service

The sample was taken from an 1860 m^3 hydrogen-rich blast furnace with 26 tuyeres and 2 tap holes. The refractory configuration of the hearth area and the size of the hearth area are shown in Fig. 3. It can be seen that the side wall of the hearth adopts the refractory configuration of small carbon composite bricks, and the hot surface of the bottom of the furnace is laid with two layers of large carbon composite bricks. The taphole adopts the combination of cold surface integral pouring technology and hot surface carbon composite taphole composite brick.

Analysis and Detection Methods

XRD was used to analyze the phase of the original brick sample of carbon composite brick. The Gibbs free energy of the possible reaction between the water vapor and carbon brick phase was calculated by FactSage. SEM–EDS was used to observe the microstructure of the sample and analyze the elemental composition.

Results and Discussion

Thermomechanical Analysis

Figure 4 shows the X-ray diffraction (XRD) patterns of carbon composite bricks. The main components of carbon composite bricks are C, SiO_2, Al_2O_3, and SiC, and the mass fractions of C, Si, and Al are 10.70%, 7.17%, and 36.62%, respectively.

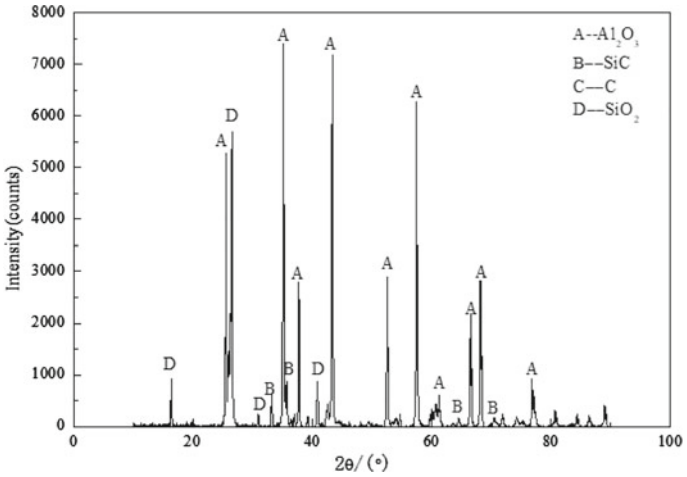

Fig. 4 XRD patterns of carbon composite bricks

The oxidation process of carbon composite bricks under wet air, dry air, and wet argon conditions is mainly that graphite C or SiC reacts with oxygen in water vapor or air to form CO or CO_2 and H_2. The equation of the specific reaction and the Gibbs free energy can be seen as shown in Fig. 5:

$$2C_{(s)} + O_{2(g)} = 2CO_{(g)},\ \Delta G_1^{\theta} = -0.1746\,T - 224.47,\ \text{kJ/mol} \tag{1}$$

$$C_{(s)} + O_{2(g)} = CO_{2(g)},\ \Delta G_2^{\theta} = -0.0012T - 394.58,\ \text{kJ/mol} \tag{2}$$

$$C_{(s)} + H_2O_{(g)} = CO(g) + H_{2(g)},\ \Delta G_3^{\theta} = -0.1426T + 134.83,\ \text{kJ/mol} \tag{3}$$

$$\frac{1}{2}C_{(s)} + H_2O_{(g)} = \frac{1}{2}CO_{2(s)} + H_{2(g)},\ \Delta G_4^{\theta} = -0.0559T + 49.779,\ \text{kJ/mol} \tag{4}$$

$$\frac{2}{3}SiC_{(s)} + O_{2(g)} = \frac{2}{3}SiO_{2(s)} + \frac{2}{3}CO_{(g)},\ \Delta G_5^{\theta} = 0.0518T - 666.67,\ \text{kJ/mol} \tag{5}$$

$$\begin{aligned}\frac{1}{3}SiC_{(s)} + H_2O_{(g)} &= \frac{1}{3}SiO_{2(s)} + \frac{1}{3}CO_{(g)} + H_{2(g)},\ \Delta G_6^{\theta} \\ &= -0.0297T - 67.78,\ \text{kJ/mol}\end{aligned} \tag{6}$$

$$\frac{1}{2}SiC(s) + H_2O(g) = \frac{1}{2}SiO_{2(s)} + \frac{1}{2}CH_{4(g)},\ \Delta G_7^{\theta} = 0.0812T - 212.97,\ \text{kJ/mol} \tag{7}$$

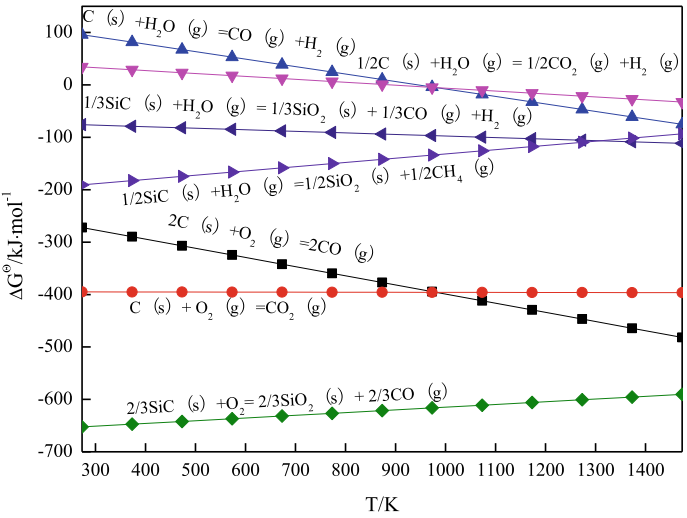

Fig. 5 Gibbs curve of refractory in different atmospheres

(1) The reaction of refractories in the air and water vapor atmosphere is negative at high temperatures (above 1000 K: this is the lowest temperature of refractory working environment in hydrogen-rich smelting blast furnace hearth), indicating that the reaction can be carried out from the thermodynamic point of view under the experimental temperature conditions.
(2) The reaction of graphite C, SiC, and O_2 can be carried out at 800 °C, and the reaction of SiC and water vapor can be carried out at 800 °C.
(3) The reaction of graphite C with O_2 and water vapor decreases with the increase in temperature, indicating that the oxidation reaction of graphite C is endothermic, and the higher the temperature, the easier the reaction.
(4) The reaction between SiC and O_2 increases with the increase in temperature, indicating that the oxidation reaction of SiC is exothermic. The higher the temperature, the more unfavorable the reaction between SiC and O_2.
(5) The reaction of SiC with water vapor to generate CH_4 increases with the increase in temperature, indicating that the reaction is exothermic, and the higher the temperature, the more difficult it is to carry out. The reaction of SiC with water vapor to generate CO decreases with the increase in temperature, indicating that the reaction is endothermic, and the higher the temperature, the easier the reaction is to carry out.

In summary, under the experimental conditions, graphite C and SiC in carbon composite bricks can be oxidized under air and water vapor conditions.

Analysis of Experimental Results of Water Vapor Erosion

Figure 6 shows the weight loss curve of carbon composite brick under different temperatures and wet air conditions. It can be seen from the diagram that in the temperature range of 800–1200 °C, the weight loss rate at 800 °C is the slowest, while the weight loss rate at 1000 °C and 1200 °C is similar. It can be seen from the kinetic curve that the reaction rate at 1200 °C was faster than 1000 °C at the beginning of the reaction, and the two almost coincided in the later period. The time for the three to reach the maximum weight loss rate was 2.5 h, 2 h, and 2 h, respectively.

Figure 7 shows the scanning electron microscope (SEM) images of the reaction cross section of carbon composite bricks after reaction at 800, 1000, and 1200 °C under humid air conditions. The surface of carbon composite bricks is the most rough at 1000 °C, indicating a high degree of oxidation. The effect of temperature on the oxidation performance of carbon composite bricks is more complicated. The oxidation process of carbon composite bricks consists of SiC oxidation weight gain and graphite C oxidation weight loss. In the temperature range of 800–1100 K, the main reaction is the oxidation of C. The oxidation reaction of SiC and the oxidation reaction of graphite C mainly occur at the temperature of 1100–1500 K.

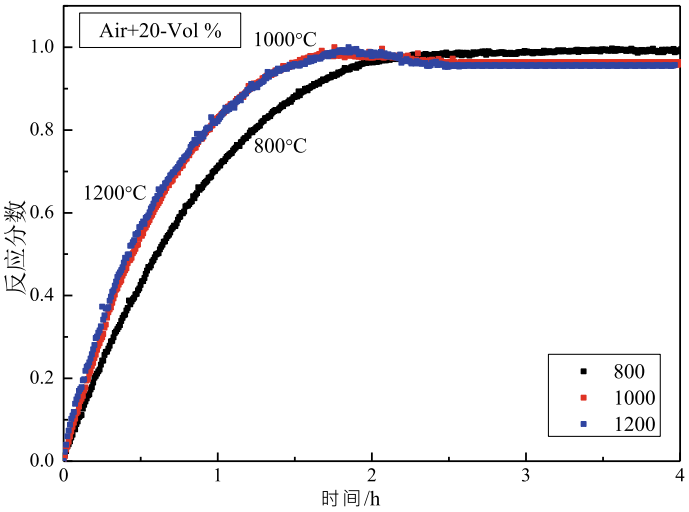

Fig. 6 Oxidation behavior of carbon bricks at different temperatures

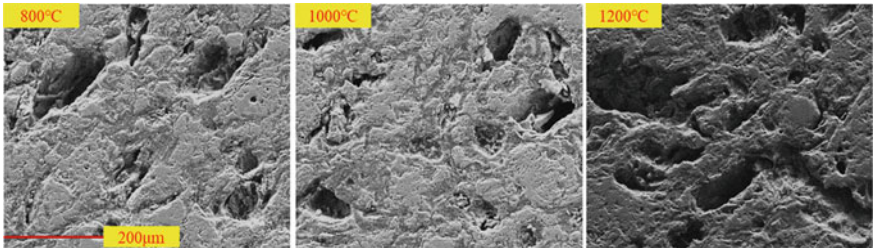

Fig. 7 SEM diagram of carbon composite brick after reaction under wet air condition

Analysis of Erosion Mechanism of Carbon Composite Brick After Service

In the process of damage investigation, it was found that there was obvious slag phase erosion in the taphole area. The location of slag phase erosion is shown in Fig. 8. It is located inside the carbon composite brick on the hot surface of the castable, which is different from the erosion phenomenon of the carbon brick on the hot surface.

According to the difference in macroscopic morphology, the eroded samples can be divided into cyan slag phase erosion area, white-brown slag phase erosion area,

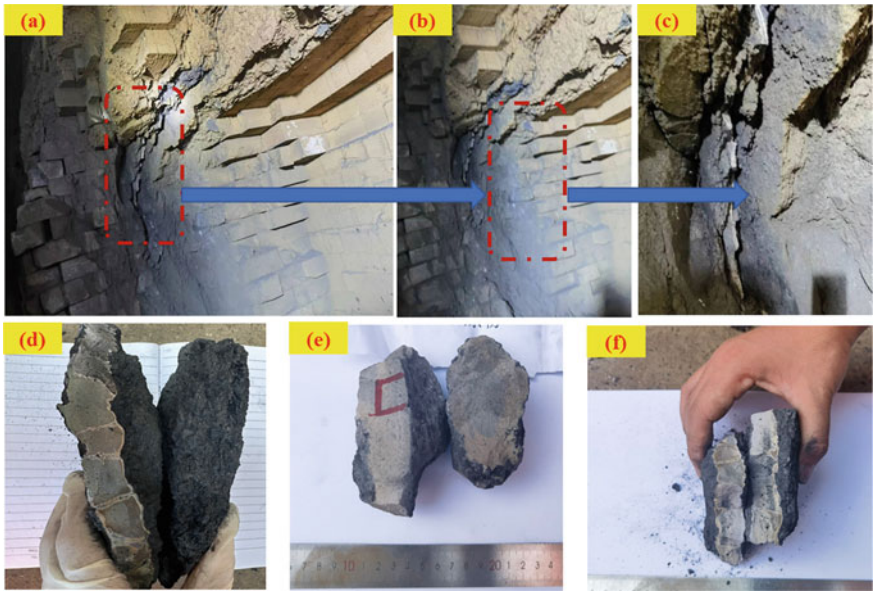

Fig. 8 Macroscopic morphology of slag phase erosion area and sample morphology with (**a**, **b**, **c**) Macroscopic morphology of slag phase erosion area with erosion samples with different morphologies (**d** Blue-white sample, **c** Grey-brown sample, Dark-brown sample)

and gray-brown slag phase erosion area. The samples in the non-region were tested by SEM–EDS.

As shown in Fig. 9, the eroded samples of the blue-white slag phase can be divided into three levels according to the degree of erosion, and the elemental composition of different regions is analyzed, respectively. The results are as follows (Table 2).

The area where P1 is located is the area where the carbon composite brick is located after service, and the bright white area in the sample is the Pb erosion enrichment area; the area where P3 is located is a slag phase erosion enrichment area, and the existing phase is similar to the final slag of the blast furnace. P2 is the transition zone between the slag phase and the carbon composite brick, in which there is also ZnO.

As shown in Fig. 10, the erosion area in the gray-brown sample can also be divided into three levels according to the erosion interface. The P1 area is the slag phase enrichment area, and the element content is similar to the P3 area in the blue-white erosion sample. The P2 region of the gray-brown sample is also a ZnO-rich region. Unlike the P3 region in the bluish-white sample, there is no obvious Pb enrichment in the P3 region of the gray-brown sample, and more ZnO appears in it (Table 3).

The dark-brown sample also exhibits the same phase distribution as the above two samples, and the detection results are shown in Fig. 11. The P1-P3 areas are eroded carbon composite bricks, and there is also the enrichment of the ZnO phase. The main phase in the P4 region is similar to that of the blast furnace slag, and there is also a phenomenon of NaO_2 enrichment. A small amount of NaO_2 appears in the P5 region (Table 4).

Table 2 Blue-white sample EDS results in Fig. 9 (atomic%)

Elements	C	Si	O	Al	Mg	Ca	F	Pb	Zn	Mn	Possible phase
P1	46.30	11.79	15.34	4.19				22.39			C, SiO_2, Al_2O_3, PbO
P2		19.00	48.41	8.15	6.48	13.06	1.93		1.73	1.23	SiO_2, Al_2O_3, MgO, CaO, F, ZnO, MnO
P3		19.16	50.76	8.15	4.28	14.13	2.42			1.11	SiO_2, Al_2O_3, MgO, CaO, F, ZnO, MnO

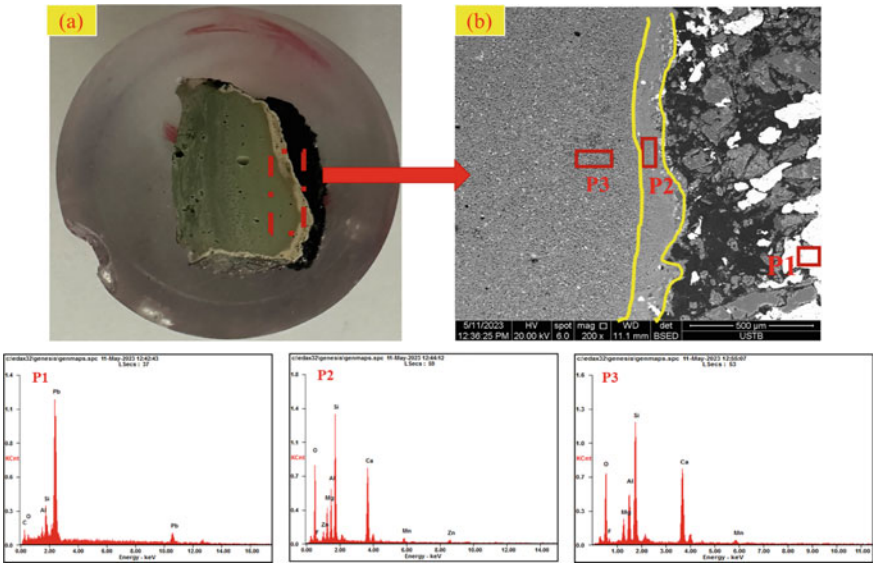

Fig. 9 The macroscopic and microscopic morphology of the blue-white sample with **a** Macroscopic morphology of the blue-white sample and **b** Microstructure of the sample

Table 3 EDS results in Fig. 10 (atomic%)

Elements	C	Si	O	Al	Mg	Ca	F	Pb	Zn	Mn	Possible phase
P1		19.21	51.08	8.33	4.42		2.25			1.20	SiO_2, Al_2O_3, MgO, CaO, F, MnO
P2	12.74	14.11	44.96	5.98	4.66	13.00	1.3		1.76	1.48	C, SiO_2, Al_2O_3, MgO, CaO, F, ZnO, MnO
P3	38.56	2.15	35.35	18.31		1.02			3.99	0.63	C, SiO_2, Al_2O_3, MgO, CaO, ZnO, MnO

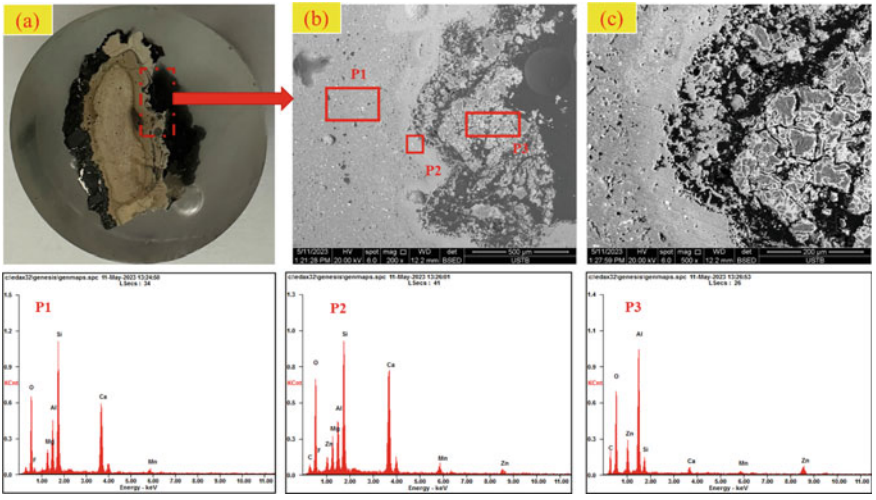

Fig. 10 The macroscopic and microscopic morphology of the gray-brown sample with **a** Macroscopic morphology of the gray-brown sample and **b** Microstructure of the sample

Table 4 EDS results in Fig. 4 (atomic%)

Elements	C	Si	O	Al	Mg	Ca	F	Pb	Zn	Mn	Na	Possible phase
P1	18.40	6.42	43.73	22.62	0.39	2.35			5.12			C, SiO_2, Al_2O_3, MgO, CaO, ZnO
P2	57.04		10.99					25.63	6.35			C, ZnO, PbO,
P3	11.73	17.00	47.79	7.89	4.27	10.72						C, SiO_2, Al_2O_3, MgO, CaO, ZnO
P4		16.50	49.44	6.32	4.92		3.78	0.18		1.05	3.07	SiO_2, Al_2O_3, MgO, CaO, PbO, NaO_2
P5	13.42	15.85	45.76	7.23	3.61	11.04	1.45			0.68	0.095	SiO_2, Al_2O_3, MgO, CaO, NaO_2

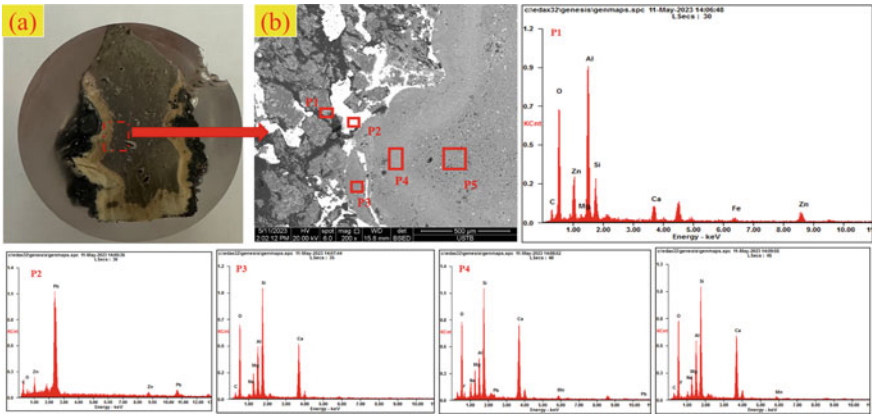

Fig. 11 The macroscopic and microscopic morphology of the dark-brown sample with **a** Macroscopic morphology of the dark-brown sample and **b** Microstructure of the sample

Damage Mechanism Analysis of Hearth Carbon Composite Brick

According to the above detection and experimental results, the phenomenon of slag phase erosion in the blast furnace is analyzed. It is considered that the occurrence of erosion has gone through the following stages.

Water Vapor Oxidation and Carbon Brick Microcrack Generation

In the process of smelting, a hydrogen-rich blast furnace inevitably produces a large amount of water vapor in the tuyere area of the hearth. On the one hand, it reacts with water gas in the dead material column of the hearth, and on the other hand, it diffuses along the refractory of the hearthside wall. According to the results of electron microscope observation, the oxidation reaction of carbon composite bricks occurs under the action of water vapor and oxygen, which leads to the weight loss of carbon bricks and the appearance of cracks.

Erosion of Slag Phase and Harmful Elements

Under the working conditions of steam and hearth temperature changes, the microcracks generated by carbon bricks become the path of slag phase and harmful element erosion. The content of Al_2O_3 and SiO_2 in the carbon composite brick is high, and the slag phase in the blast furnace is more likely to react when in contact with the carbon composite brick. The K and Na in the blast furnace also penetrate the carbon composite brick in the form of steam, and the products are nepheline and garnet.

Formation of Slag Phase Erosion Layer

After the slag phase is eroded into the carbon brick, it continuously reacts with the carbon brick and solidifies in the area where the cold surface temperature is low. Due to the different crystallization temperatures, the samples after the slag phase erosion have slight differences in the macroscopic morphology, and a small amount of Pb erosion occurs in the carbon brick after service. The erosion of water vapor and the fluctuation of hearth temperature lead to the generation of micro-cracks in carbon bricks, and the further erosion of the slag phase and harmful elements leads to the erosion of the slag phase in the hearth area.

Corrosion Resistance Analysis of Carbon Composite Brick Under Actual Production Conditions

Based on the results of the water vapor oxidation experiment and damage investigation, it can be seen that the carbon composite brick will cause a certain degree of structural damage due to the erosion of water vapor at high temperatures. The area of slag phase erosion of carbon composite bricks after service is concentrated in the taphole area, and the structure of carbon composite bricks on the hot and cold surfaces of the eroded area is relatively intact, which is related to the actual production of the blast furnace. Due to the frequent iron tapping in the taphole area, the slag-iron erosion of the refractory in this area is more serious. In this case, once a string of gas appears at the taphole, it will cause further erosion of high-temperature water vapor and alkali metal vapor. Therefore, in actual production, for the taphole area, more attention should be paid to the leakage of cooling equipment to ensure good cooling intensity, which can reduce the erosion of carbon composite bricks to a certain extent.

Conclusions

1. During the damage investigation of a blast furnace injected with hydrogen-rich gas, a slag phase erosion layer with a thickness of 5–15 cm was found in the taphole area.
2. The microscopic morphology observation and composition phase analysis of the samples in the slag phase erosion area were carried out. It was found that there was an obvious interface between the carbon brick and the slag phase after erosion. There was an enrichment of harmful elements such as Zn and Na in the interface transition area. The enrichment of Pb appeared on the carbon brick matrix.
3. Through the experimental study on the resistance of carbon composite bricks to water vapor oxidation, the thermodynamic conditions for the oxidation of carbon composite bricks in a water vapor environment were clarified. The microscopic

morphology observation results after the test showed that the oxidation of water vapor led to micro-cracks and a large number of pores in carbon bricks.

4. The pores and cracks on the surface of the carbon composite brick become the path of slag and harmful element steam. The slag and harmful elements that erode into the carbon composite brick react with the carbon composite brick, and the product forms a macroscopic slag phase erosion phenomenon.
5. The slag phase erosion area is concentrated in the taphole area, and the carbon composite bricks on the cold and hot surfaces of the erosion area are retained in the completed state. The frequent erosion of slag and iron in the Iron Mouth area is the main cause of abnormal erosion in this area. Because of this abnormal erosion phenomenon in hydrogen-rich blast furnaces, the composition of the slag phase can be regulated to promote the formation of a slag-rich protective layer on the hot surface of carbon composite brick. The existence of a slag-rich protective layer can prevent the diffusion of water vapor and alkali metal vapor, and prevent the erosion of carbon composite bricks.

Acknowledgements This work was financially supported by the National Natural Science Foundation of China (No. 52204334).

References

1. Wang XY, Li B, Lu C et al (2022) China's iron and steel industry carbon emissions peak pathways. Res Environ Sci 35(2):339
2. Shao YJ, Xu L, Liu XP, Chen HZ (2022) Discussion on the solution of "carbon neutrality" in China's steel production. China Metall 32(4):1
3. Xin Y, Cui YK, Tian JL et al (2022) Application status and prospect of low carbon technology in iron and steel industry. Chin J Eng 44(4):801
4. Liu ZJ, Zhang JL, Zuo HB, Yang TJ (2012) Recent progress on long service life design of Chinese blast furnace hearth. ISIJ Int 52:1713–1723
5. Akihiko S, Hitoshi N, Nariyuki Y et al (2003) Investigation of blast-furnace hearthside wall erosion by core sample analysis and consideration of campaign operation. ISIJ Int 43:321–330
6. Zhang FM (2013) Design and operation control for a long campaign life of blast furnaces. J Iron Steel Res Int 20:53–60
7. Zhang S, Lee WE (2002) Carbon containing castables: current status and prospects. Br Ceram Trans 101:1–8
8. Prompt N, Ouedraogo E (2008) High-temperature mechanical characterization of an alumina refractory concrete for blast furnace main trough: Part I. General context. J Eur Ceram Soc 28:2859–2865
9. Luz AP, Miglioli MM, Souza TM et al (2012) Effect of Al_4SiC_4 on the Al_2O_3–SiC–SiO_2–C refractory castables performance. Ceram Int 38:3791–3800
10. Zuo HB, Wang C, Zhang JL, Zhao YA, Jiao KX (2015) Oxidation behavior and kinetics of Al_2O_3-SiC-SiO_2-C composite in air. Ceram Int 41:9093–9100
11. Zuo HB, Wang C, Liu YL (2017) Dissolution behavior of a novel Al_2O_3-SiC-SiO_2-C composite refractory in blast furnace slag. Ceram Int 43:7080–7087
12. Zhou Y (1998) Analysis and countermeasures of "garlic like" erosion on blast furnace hearth. Iron and Steel 33(2):4–6

13. Cheng K, Jorg M (2006) Factors affecting the service life of carbon bricks at the bottom and hearth of blast furnace. Ironmaking 25(1):11–15
14. Xiao Y (2002) Damage of refractory materials for blast furnace. Refractor Lime 2:7–10
15. Luo M, Li Y, Jin S et al (2013) Microstructure and mechanical properties of multi-walled carbon nanotubes containing Al_2O_3-C refractories with addition of polycarbosilane. Ceram Int 39(5):4831–4838
16. Wang Q, Li Y, Luo M et al (2014) Strengthening mechanism of grapheme oxide nanosheets for Al_2O_3-C refractories. Ceram Int 40(1):163–172
17. Liu Y, Zhang J, Hou X et al (2015) Oxidation behavior of carbon bricks for blast furnace hearth under high temperature and water content. Min Metall 24(S1):75–81

A Modified Rotating-Finger Test Aiming to Quantify Refractory Wear Based on Fundamental Equations Governing Refractory Dissolution and Erosion

Burhanuddin Burhanuddin and Harald Harmuth

Abstract Design of wear-resistant refractories necessitates an in-depth understanding and accurate quantification of the continuous wear. However, the experimental methods reported in the literature are mostly phenomenological and unable to reveal the physicochemical background of continuous wear. Main goals of this work are scientific investigation of continuous refractory wear and acquisition of data for quantitative simulation of continuous wear to design wear-resistant refractories. A modified rotating-finger test (RFT) device was equipped with high-resolution laser to scan the sample surface for dimension measurement. Generally, refractory dissolution in molten slag is controlled by diffusion through a boundary layer and diffusivity is the most important parameter to quantify dissolution. The data obtained from modified RFT studies were applied to accurately determine effective binary diffusivity using simulation method or mass transfer equation. Also, results of erosion studies were applied for inverse calculation of erosion parameters. Continuous wear of alumina in silicate slag will be exemplified here.

Keywords Refractory · Dissolution · Diffusivity · Erosion · Rotating-finger test

Introduction

Refractories used in the vessels of pyrometallurgy are exposed to corrosive melts at high temperatures and experience wear due to dissolution and subsequent erosion [1, 2]. Improved refractory materials with enhanced lifetimes are desired for cost and resource efficiency, and their design demands a comprehensive understanding and accurate quantification of the continuous wear [3]. Wear parameters could be quantified experimentally but most of the methods reported in the literature are phenomenological and unable to reveal the physicochemical background of continuous wear. Rotating-finger test (RFT) is the most obliging technique for dissolution

B. Burhanuddin (✉) · H. Harmuth
Chair of Ceramics, Montanuniversitaet Leoben, Peter-Tunner Strasse 5, 8700 Leoben, Austria
e-mail: burhanuddin.burhanuddin@unileoben.ac.at

© The Minerals, Metals & Materials Society 2024

G. Alvear et al. (eds.), *Advances in Pyrometallurgy*, The Minerals, Metals & Materials Series, https://doi.org/10.1007/978-3-031-50176-0_9

studies, where the effective diffusive boundary layer thickness could be controlled via experimental parameters, such as the geometry of the sample and crucible assembly, Reynolds number, and Schmidt number [4]. A number of RFT studies on dissolution of refractories are available in the literature [5–26]. Some of them evaluated by post-mortem analysis and determined the wear using microstructural assessment, however they were unable for quantitative wear measurement [10, 11, 21–24]. On the other hand, some of them used the dissolution parameters, e.g., sample weight, change in sample dimension to quantify dissolution. But in most of the cases, diffusivity results are missing though the dissolution of refractory is a diffusion controlled process and diffusivity is the most important parameter to quantify it [3, 4, 16, 27–30].

One of the aims of this research work is to compare and assess different diffusivity determination methods. In this research work, dynamic corrosion of alumina was investigated in a silicate slag with CaO/SiO_2 wt ratio 0.93 at 1450, 1500, and 1550 °C with 200 rpm. A modified RFT device equipped with high-resolution laser was employed in this study for in situ wear profile measurement. The modified RFT device has been referenced here as continuous wear testing device (CWTD). Furthermore, dissolution parameters were obtained from highly accurate measured specimen dimensions and utilized for the diffusivity determination. An important step for evaluating CWTD measurements is the quantification of mass transfer, viz. the determination of the associated Sherwood number. The most versatile method to determine mass transfer coefficients associated with RFT studies is computational fluid dynamics (CFD) simulation where flow field around the actual sample geometry could be considered. Our research group reported a simulation method to determine diffusivity of dense ceramics even for the remarkably high Schmidt number [31]. This technique has incorporated two usually neglected phenomena in the literature, the advection in the orthogonal direction to the solid–liquid interface and the influence of Stefan's flow on the boundary layer thickness, and thus enhanced the accuracy and reliability of the method. The only disadvantage of this method is the requirement of higher effort for its implementation. On the other hand, mass transfer equations could be applied to determine diffusivity with less effort. Levich [32] reported the renowned mass transfer equation rooted in Cochran's equation [33] for the mass transfer from a disc. The mass flux density can accurately be estimated using this equation for a finite shape when the boundary layer thickness is greatly lesser than the disc radius. For the mantle of a cylindrical sample, Eisenberg et al. [34] reported an equation to quantify mass flux. Kosaka and Minowa [35] reported the Sherwood relations to quantify dissolution of metal cylinder into molten metal. Sherwood relations for the heat transfer through an annular gap were reported by Tachibana and Fukui [36]. After appropriate modification, these equations could be applied to quantify solid dissolution in a liquid. But unfortunately, there is no Sherwood correlation reported in the literature that could be applicable to the sample mantle in finger test experiments with bottom clearance for the system with large Schmidt numbers. Our research group reported a Sherwood relation derived from the results of RFT studies using above-mentioned simulation method [37]. This is the only Sherwood correlation reported in the literature which indirectly considered the effect of actual sample geometry and is applicable for finger test experiments

with bottom clearance for the system with large Schmidt numbers. Diffusivities of alumina for all individual corrosion steps at three experimental temperatures were determined using the above-mentioned mass transfer equations and compared. Additionally, diffusivity for a single step at each temperature obtained from the simulation method was compared with the results determined using mass transfer equations.

On the other hand, dissolution of refractory matrix promotes the subsequent erosion by the applied shear force on the refractory/melt interface due to the fluid flow. The CWTD could also be used for erosion studies of refractories. In the slag-refractory system, erosion profiles measured by high-resolution laser device could be applied for the inverse calculation of the erosion parameters. Our research group published a model based on CFD simulation together with optimization tool for inverse calculation [38]. In this paper, erosion of coarse-grain alumina refractory in a silicate slag with CaO/SiO_2 wt ratio 0.65 at 1450 °C with 200 rpm would be exemplified from our previous publication [38] to show the applicability of CWTD.

Materials and Methods

Materials

For the dissolution studies, fine-grain alumina dense ceramics (Ants Ceramics Private Limited, India) with 99.7 wt% purity and 3870.6 kg/m^3 bulk density were investigated. They were 20 mm in diameter and 110 mm in length. On the other hand, cylinder of 30 mm in diameter was core drilled from standard refractory alumina brick for the erosion study. The bulk density and length of coarse-grain refractory cylinder were 3230 kg/m^3 and 90 mm, respectively. Each cylinder featured one axial and one side drill to attach it with the rotor shaft of CWTD.

Synthetic silicate slags made out of alumina, quartz, magnesia, and decarburized calcium carbonate powders (S3 Handel und Dienstleistungen UG, Bad Oeynhausen, Germany) were used to investigate continuous wear of alumina refractories. A silicate slag (S1) with CaO/SiO_2 weight ratio 0.93 in the $CaO–Al_2O_3–SiO_2$ system was used for the dissolution studies of alumina fine ceramics and a silicate slag (S2) with CaO/SiO_2 weight ratio 0.65 in the $CaO–Al_2O_3–SiO_2–MgO$ system was used for the erosion study of alumina coarse-grain refractory. Slag compositions, dynamic viscosities (η), and liquidus temperatures (T_L) are listed in Table 1. The slag densities (ρ) and the mass fractions of alumina (w_s) in saturated slags at three experimental temperatures are listed in Table 2. The dynamic viscosities and the thermo-chemical properties of the slags were determined using FactSage® 7.3. A method reported in Ref. [39] was employed to determine slag density.

Table 1 Chemical compositions, viscosities, and liquidus temperatures of slags

Slag no.	C/S	CaO (wt%)	Al_2O_3 (wt%)	SiO_2 (wt%)	MgO (wt%)	$\eta_{1450\,°C}$ (Pas)	$\eta_{1500\,°C}$ (Pas)	$\eta_{1550\,°C}$ (Pas)	T_L (°C)
S1	0.93	38.07	21.00	40.93	–	1.28	0.88	0.62	1301
S2	0.65	32.42	11.16	49.56	6.86	1.02	0.73	0.53	1265

Table 2 Slag densities and mass fractions of alumina in saturated slags

Slag no.	$\rho_{1450\,^\circ C}$ (kg/m^3)	$\rho_{1500\,^\circ C}$ (kg/m^3)	$\rho_{1550\,^\circ C}$ (kg/m^3)	$w_{s,1450\,^\circ C}$ ()	$w_{s,1500\,^\circ C}$ ()	$w_{s,1550\,^\circ C}$ ()
S1	2611	2600	2589	0.4154	0.4505	0.4879
S2	2595	2587	2579	0.3765	0.4096	0.4464

Experiments

In this study, dynamic corrosion studies of dense alumina ceramics were performed at 1450, 1500, and 1550 °C with 200 rotations per minute (rpm). CWTD was employed to perform these studies. The complete description of the device and the experimental method could be followed in Ref. [40]. Cylindrical sample was attached to the rotor shaft using alumina bolt. A slag-filled platinum-10wt% rhodium (Pt-Rh10) crucible with 65 mm inner diameter and 100 mm inner height was placed on a high-alumina safety crucible inside the CWTD furnace. At room temperature, the gap between Pt-Rh10 crucible and sample bottom was adjusted to around 20 mm and the position of the Pt-Rh10 crucible was fine-tuned to make the cylindrical sample position at the center of the crucible. Afterwards, experimental parameters were set in control computer. The CWTD furnace was heated and cooled at the rate of 5 °C per minute. It was heated till 5 °C below the target temperature and kept for 60 min for temperature uniformity and to ensure the completion of slag melting. Afterwards, it was heated to target temperature and maintained that temperature for all corrosion steps. Sample was submerged into the molten slag 3 °C below the target temperature and rotated for the defined time. The corrosion times per one single step were defined as 150, 90, and 60 min at 1450, 1500, and 1550 °C, respectively. After each corrosion step, sample was extracted from the slag and rested above the crucible for 30 min to allow the slag to drop down from the sample surface before laser measurement. Afterwards, laser scanner measured the sample, rotating with 2 rpm and produced 3000 profiles for the whole sample mantle. After the laser measurement, sample was immersed again into the slag for the next corrosion step.

The erosion experiment was conducted at 1450 °C with 200 rpm for a single erosion step with the step size of 30 min. The experimental procedure was exactly similar like dissolution experiments mentioned above. Inverse calculation of the erosion parameters was conducted using the experimental erosion profile. This was attained by combining CFD simulations with an optimization solver to resolve a nonlinear least-squares problem [38]. The governing erosion law has been represented by Eq. (1).

$$\dot{\varepsilon} = k_\mathrm{d} \cdot (\tau - \tau_\mathrm{c})^a \tag{1}$$

Here, $\dot{\varepsilon}$ is the erosion rate, k_d the detachment rate, τ is the wall shear stress, τ_c is the critical shear stress, and a is an exponent.

Diffusivity Determination

As it is already mentioned that the CFD simulation is the most promising method to determine mass transfer coefficients for dissolution experiments because of the incorporation of realistic boundary conditions and flow field around the actual sample geometry. But the large Schmidt numbers of slags complicate the simulation by demanding an unfeasible fine spatial resolution. Our research group reported a method combining CFD with an asymptotic boundary layer approach [31] to overcome the aforementioned complication and this method was also employed here to determine diffusivity.

In case of mass transfer equation-based diffusivity determination approaches for RFT studies, Eq. (2) was used to represent the total mass flux density (j_{tot}) including diffusion, convection, and the influence of Stefan flow on boundary layer thickness for the whole dissolving surface.

$$j_{\mathrm{tot}} = \chi_{\mathrm{D}} \cdot \frac{D}{A_{\mathrm{tot}}} \cdot \left\{ A_{\mathrm{m}} \cdot \frac{\mathrm{Sh}_{0,\mathrm{m}}}{(R_2 - R_1)} + A_{\mathrm{t}} \cdot \frac{\mathrm{Sh}_{0,\mathrm{t}}}{R_t} \right\} \cdot \rho_{\mathrm{s}} \cdot B \tag{2}$$

Here, χ_{D} is a correction factor as the Sherwood numbers in this equation do not consider the effect of interface advection on the boundary layer thickness and it is defined in Eq. (3). D is the effective binary diffusivity, A_{tot} is the total surface area combining mantle and bottom tip, A_{m} is the mantle surface area, A_{t} is the surface area of bottom tip, R_1 is the sample radius, R_2 is the crucible radius, R_{t} is bottom tip radius, and ρ_{s} is the slag density. $\mathrm{Sh}_{0,\mathrm{m}}$ and $\mathrm{Sh}_{0,t}$ are the Sherwood numbers without considering the influence of the interface advection on the boundary layer thickness for the sample mantle and bottom tip, respectively. As Eq. (2) indicates, $\mathrm{Sh}_{0,\mathrm{m}}$ and $\mathrm{Sh}_{0,t}$ are defined with $R_2 - R_1$ and R_{t} as significant lengths, respectively. B is the dimensionless concentration difference and defined in Eq. (4).

$$\chi_{\mathrm{D}} = \frac{\mathrm{Sh}}{\mathrm{Sh}_0} \approx \frac{1}{1 + 0.566 \cdot B} \tag{3}$$

Here, Sh and Sh_0 are the Sherwood numbers with and without considering the influence of the interface advection on the boundary layer thickness.

$$B = \frac{w_{\mathrm{s}} - w_0}{1 - w_{\mathrm{s}}} \tag{4}$$

Here, w_0 and w_{s} are the mass fractions of the dissolving species in the slag bulk and saturated slag, respectively.

While in [3] a single Sherwood equation was employed for mass transfer determination, in the present study, four different Sherwood correlations reported by Kosaka and Minowa [35], Eisenberg et al. [34], Tachibana and Fukui [36], and Guarco et al. [37] were used for the sample mantle to assess their applicability for RFT studies. Exponent of the Schmidt number in the Sherwood correlation reported by Tachibana

and Fukui [36] was modified from 1/4 to 1/3 and the acceptance of this modification was already tested in [3, 31]. In all cases, Sherwood relation reported by Levich [32] was applied for the bottom tip of the sample.

$$\mathrm{Sh}_{0,\mathrm{Kosaka}} = 0.0547 \cdot \mathrm{Re}^{0.75} \cdot \mathrm{Sc}^{\frac{1}{3}} \cdot \frac{R_2 - R_1}{R_1} \tag{5}$$

$$\mathrm{Sh}_{0,\mathrm{Eisenberg}} = 0.0642 \cdot \mathrm{Re}^{0.7} \cdot \mathrm{Sc}^{0.356} \cdot \left(\frac{R_2 - R_1}{R_1}\right)^{0.3} \tag{6}$$

$$\mathrm{Sh}_{0,\mathrm{Mod\_Tachibana}} = 0.21 \cdot \mathrm{Re}^{0.5} \cdot \mathrm{Sc}^{\frac{1}{3}} \cdot \left(\frac{R_2 - R_1}{R_1}\right)^{0.25} \tag{7}$$

$$\mathrm{Sh}_{0,\mathrm{Guarco}} = 0.10 \cdot \mathrm{Re}^{0.65} \cdot \mathrm{Sc}^{\frac{1}{3}} \cdot \left(\frac{R_2 - R_1}{R_1}\right)^{1.49} \cdot \left(\frac{BC}{l}\right)^{0.32} \tag{8}$$

Here, Re is the Reynolds number, Sc is the Schmidt number, BC is the bottom clearance (gap between sample tip and crucible bottom), and l is the immersion length. In Eqs. (5)–(8), characteristic lengths for the Sherwood numbers and for the Reynolds number were $(R_2 - R_1)$ and R_1, respectively.

Results and Discussion

Mean Corroded Profile (MCP)

A laser measurement consisted of 3000 profiles for the whole sample mantle and a representative mean corrosion profile (MCP) was produced by averaging all 3000 profiles in circumferential direction. So, the dissolution experiments generated MCP for each corrosion step in addition to a reference MCP measured before the sample immersion into the slag. Detailed evaluation technique could be found in Ref. [40]. Figure 1 represents the MCPs of individual corrosion steps along with the reference MCP of virgin sample for the alumina dissolution at 1450, 1500, and 1550 °C with 200 rpm. The un-corroded parts of all the MCPs coincide with each other and with the reference MCP. The corroded portions of all the MCPs could be clearly differentiated and do not overlap. With dissolution time, corroded sample radius and length decreased. As expected, for a similar dissolution time, changes in radius and length were larger at higher temperature. Figure 2 displays the virgin and worn alumina samples after the dissolution experiments in S1 with 200 rpm at 1450, 1500, and 1550 °C. The MCPs for the end dissolution steps precisely represent the worn sample shape.

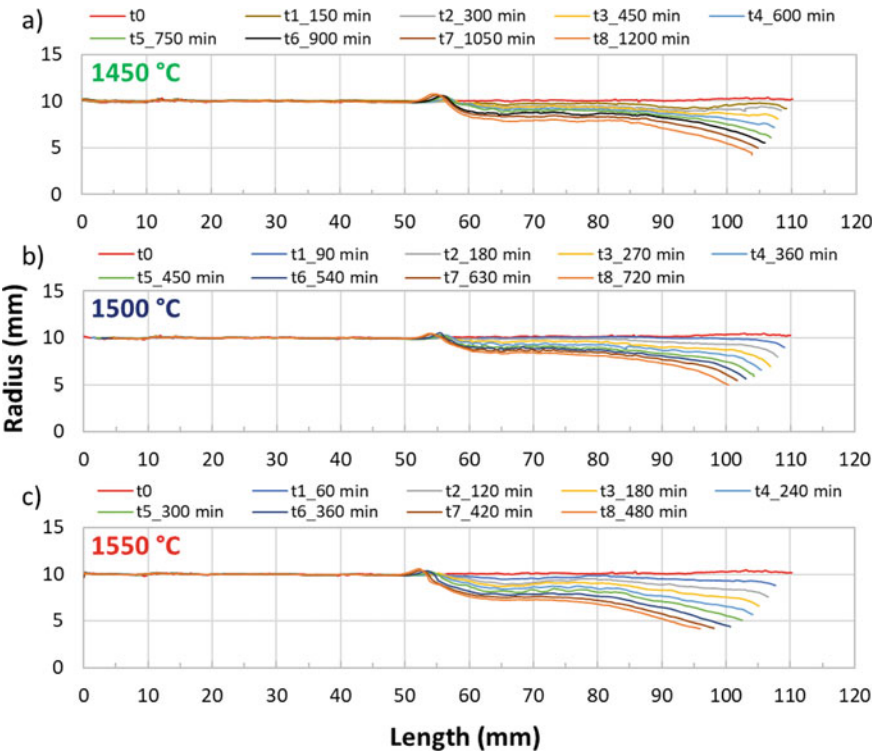

Fig. 1 **a–c** MCPs for alumina dissolution in S1 with 200 rpm, respectively, at 1450, 1500, and 1550 °C

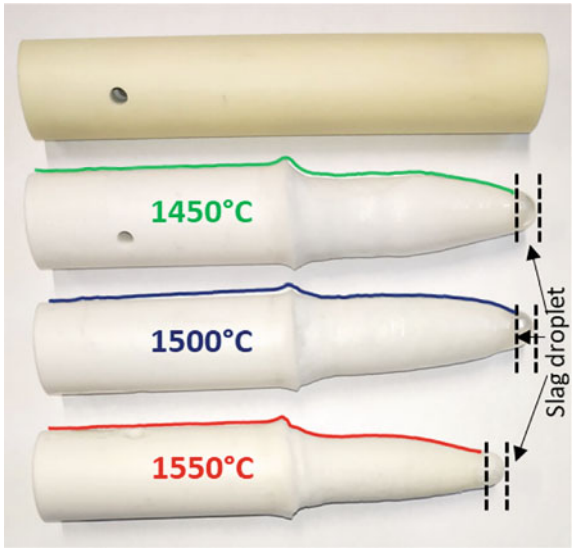

Fig. 2 Virgin and worn samples with the superimposed MCPs of the end corrosion steps of alumina dissolution in S1 with 200 rpm at 1450, 1500, and 1550 °C

Dissolution Parameters

The dissolution parameters of alumina dissolution, e.g., sample length, mean corroded radius, corroded volume, mass loss, surface area, tip radius, and immersion length were obtained from the MCPs and these parameters are foreseen to be more precise than the hand measurements of the post-mortem analysis because of high-resolution laser measurement. Figure 3 represents the first four of the dissolution parameters from the above-mentioned list. At the higher temperature, the slag viscosity is lower and the saturation limit is higher and these are reasons behind the increase of the absolute values of all these parameters with rising temperature. The mean rate of change in the sample length rises 2.6 times and 2.3 times with an increase in temperature from 1450 to 1500 °C and 1500 to 1550 °C, respectively. Whereas, when experimental temperature was increased from 1450 °C to 1500 °C and 1500 °C to 1550 °C, the mean rates of change in corroded radius, volume, and mass amplified 1.5−1.7 times and 2.0–2.3 times, respectively. Nearly linear tendency of dissolution parameters over time is the sign of a quasi-steady dissolution.

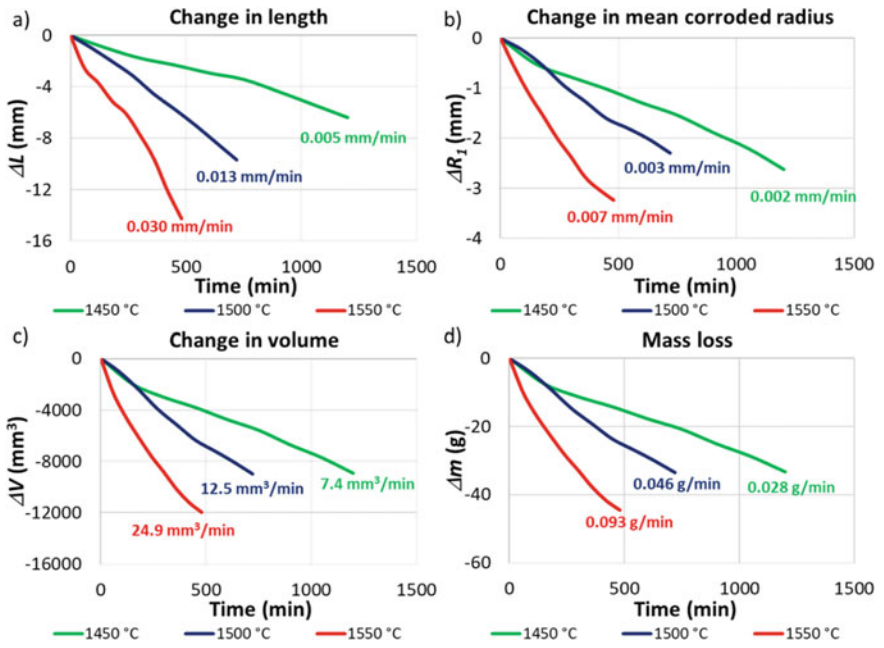

Fig. 3 **a**–**d** Change in radius, mean corroded radius, volume, and mass, respectively, for alumina dissolution over time at 1450, 1500, and 1550 °C with 200 rpm. The inserted values within the graphs represent the mean rate over the total corrosion time

Diffusivity

Effective binary diffusivities for each corrosion step were calculated using aforementioned Sherwood relations and compared in Fig. 4a–c. Results obtained from Guarco [37] and modified Tachibana [36] equations are showing good match with each other, whereas results from Eisenberg [34] are close with them at the beginning, but deviating at the later steps. Kosaka [35] equation is always over estimating the diffusivity. Diffusivity of one step at each temperature has been compared with the simulation [31] results, and again results obtained from Guarco [37] and modified Tachibana [36] equations are showing good agreement with simulation results. Guarco equation [37] indirectly includes the effect of deviation of sample geometry from perfect cylinder as it was derived from the above-mentioned simulation results. Figure 4d shows the Arrhenius plot which was produced with the diffusivities of the corresponding corrosion steps where a similar mass loss, relative to the initial mass was observed at different temperatures. Diffusivities from Guarco [37] equation have been used here and they were converted to those for the virgin slag composition using the Stokes–Einstein relation to eliminate the influence of changing slag composition during the experiment. The linear trend of Arrhenius plot confirms the plausibility of diffusivity and gives the opportunity to estimate diffusivity at any temperature between 1450 and 1550 °C without performing experiments.

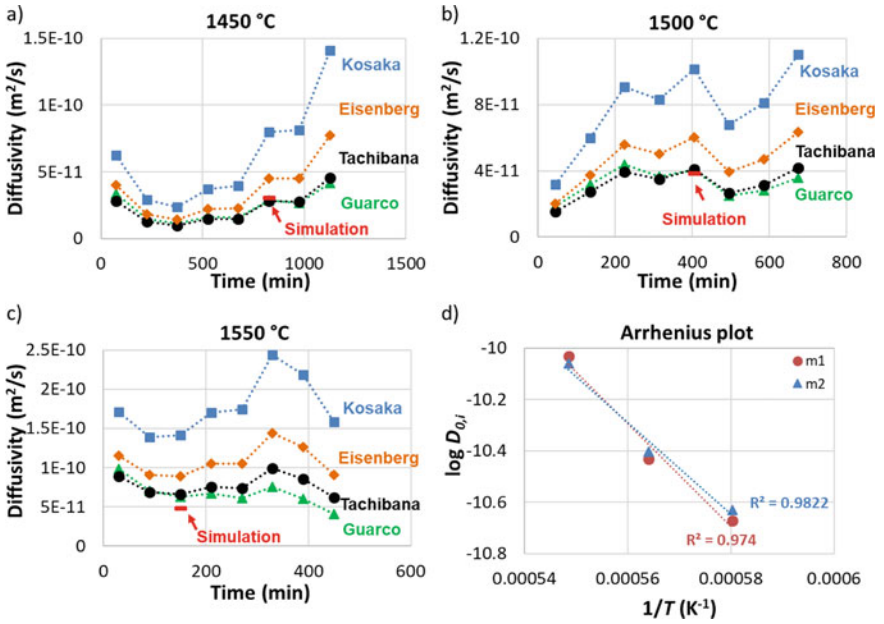

Fig. 4 **a–c** Diffusivities of alumina using different Sherwood relations, respectively, at 1450, 1500, and 1550 °C with 200 rpm. **d** Arrhenius plot of diffusivities obtained using Eq. (8)

Erosion Study

MCP obtained from the erosion experiment was used for the inverse calculation of erosion parameters. Figure 5 represents the experimental eroded sample profile along with simulated profile which showed best fit for the erosion of alumina refractory in S2 slag at 1450 °C with 200 rpm. It shows quite good fitting quality. At the slag line, both profiles are deviating a bit may be due to insufficient dissolution of refractory matrix at that region. In this study, the exponent a was fixed at a value of 1. The erosion rate, detachment rate, and critical shear stress were 1.771×10^{-7} m/s, 7.220×10^{-9} m/(s Pa), and 29.58 Pa, respectively [38]. This study proved the applicability of CWTD for determination of erosion parameters by inverse calculation.

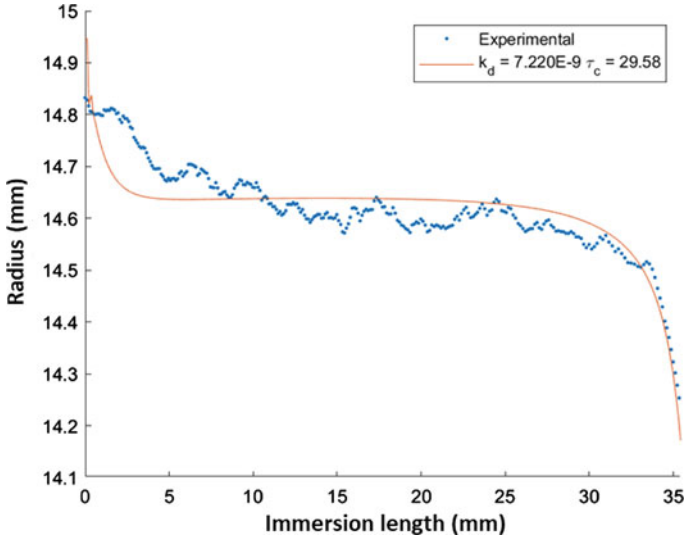

Fig. 5 Experimental and simulated profile for the erosion study of alumina refractory in S2 at 1450 °C with 200 rpm. Reprinted from [38] (CC BY 4.0 http://creativecommons.org/licenses/by/4.0/)

Summary

The CWTD, a modified RFT device is very much capable to conduct dissolution and erosion studies of refractories. High-resolution laser measurements enhance the accuracy of the dissolution parameters obtained from the experiments compared to the hand measurement in post-mortem analysis. Furthermore, the binary effective diffusivity, the fundamental parameter to quantify dissolution, was successfully

determined. The diffusivity from the simulation [31] is more reliable as it considers the flow field around the actual sample geometry of that particular corrosion step. Nevertheless, the diffusivity can also be reliably determined using the mass transfer equations with less effort. In this study, the applicability of different Sherwood relations to determine diffusivity has been verified. Diffusivities obtained from Guarco [37] and Tachibana equations ([36], after modification) showed good agreement with the simulation results, whereas diffusivities from Eisenberg [34] equation were close with them at the beginning, but deviating at the later steps. Kosaka [35] equation always overestimated the diffusivity. In case of erosion study, inverse calculation of erosion parameters was successfully achieved and it helped to understand the fundamentals of refractory erosion. Furthermore, erosion of refractory was accurately quantified with these parameters.

Acknowledgements The authors gratefully acknowledge the financial support under the scope of the COMET program within the K2 Center "Integrated Computational Material, Process and Product Engineering (IC-MPPE)" (Project No. 859480). This program is supported by the Austrian Federal Ministries for Transport, Innovation, and Technology (BMVIT) and the Digital and Economic Affairs (BMDW), represented by the Austrian Research Funding Association (FFG), and the federal states of Styria, Upper Austria, and Tyrol.

References

1. Reynaert C, Sniezek E, Jacek S (2020) Corrosion tests for refractory materials intended for the steel industry—a review. Ceram Silikaty 64:278–288. https://doi.org/10.13168/cs.2020.0017
2. Harmuth H, Vollmann S (2014) Refractory corrosion by dissolution in slags—challenges and trends of present fundamental research. Iron Steel Rev 58:157–170
3. Burhanuddin GJ, Harmuth H, Vollmann S (2022) Application of an improved testing device for the study of alumina dissolution in silicate slag. J Eur Ceram Soc 42:3652–3659. https://doi.org/10.1016/j.jeurceramsoc.2022.02.056
4. Burhanuddin HH, Vollmann S (2022) Quantification of magnesia dissolution in silicate melts and diffusivity determination using rotating finger test. Appl Sci 12:12791. https://doi.org/10.3390/app122412791
5. Amini SH, Brungs MP, Jahanshani S, Ostrovski O (2006) Effects of additives and temperature on dissolution rate and diffusivity of lime in $Al_2O_3-CaO-SiO_2$ based slags. Metall Mater Trans B 37:773–780. https://doi.org/10.1007/s11663-006-0059-y
6. Deng T, Glaser B, Sichen D (2012) Experimental design for the mechanism study of lime dissolution in liquid slag. Steel Res Int 83:259–268. https://doi.org/10.1002/srin.201100258
7. Cooper AR, Kingery WD (1964) Dissolution in ceramic systems: I, Molecular diffusion, natural convection, and forced convection studies of sapphire dissolution in calcium aluminum silicate. J Am Ceram Soc 47:37–43. https://doi.org/10.1111/j.1151-2916.1964.tb14638.x
8. Goriupp J, Rief A, Schenk J (2012) Quantifying of a dynamic refractory wear test setup for MgO-C products. BHM Berg- Huettenmaenn Monatsh 157:340–344. https://doi.org/10.1007/s00501-012-0028-5
9. Liang Y, Huang A, Zhu X et al (2015) Dynamic slag/refractory interaction of lightweight Al_2O_3–MgO castable for refining ladle. Ceram Int 41:8149–8154. https://doi.org/10.1016/j.ceramint.2015.03.026

10. Guo M, Jones PT, Parada S et al (2006) Degradation mechanisms of magnesia-chromite refractories by high-alumina stainless steel slags under vacuum conditions. J Eur Ceram Soc 26:3831–3843. https://doi.org/10.1016/j.jeurceramsoc.2005.12.025
11. Um H, Lee K, Kim K-Y et al (2014) Effect of carbon content of ferromanganese alloy on corrosion behaviour of MgO–C refractory. Ironmak Steelmak 41:31–37. https://doi.org/10.1179/1743281212Y.0000000098
12. Bui AH, Park SC, Chung IS, Lee HG (2006) Dissolution behavior of zirconia-refractories during continuous casting of steel. Met Mater Int 12:435–440. https://doi.org/10.1007/BF03027711
13. Um H, Lee K, Choi J, Chung Y (2012) Corrosion behavior of MgO–C refractory in ferromanganese slags. ISIJ Int 52:62–67. https://doi.org/10.2355/isijinternational.52.62
14. Jansson S, Brabie V, Jonsson P (2005) Corrosion mechanism and kinetic behaviour of MgO-C refractory material in contact with $CaO-Al_2O_3-SiO_2-MgO$ slag. Scand J Metall 34:283–292. https://doi.org/10.1111/j.1600-0692.2005.00748.x
15. Jeon J, Kang Y, Park JH, Chung Y (2017) Corrosion-erosion behavior of $MgAl_2O_4$ spinel refractory in contact with high MnO slag. Ceram Int 43:15074–15079. https://doi.org/10.1016/j.ceramint.2017.08.034
16. Zuo H, Wang C, Liu Y (2017) Dissolution behavior of a novel Al_2O_3-SiC-SiO_2-C composite refractory in blast furnace slag. Ceram Int 43:7080–7087. https://doi.org/10.1016/j.ceramint.2017.02.138
17. Jiao K, Fan X, Zhang J et al (2018) Corrosion behavior of alumina-carbon composite brick in typical blast furnace slag and iron. Ceram Int 44:19981–19988. https://doi.org/10.1016/j.ceramint.2018.07.265
18. Hirata T, Morimoto T, Ohta S, Uchida N (2003) Improvement of the corrosion resistance of alumina-chromia ceramic materials in molten slag. J Eur Ceram Soc 23:2089–2096. https://doi.org/10.1016/S0955-2219(03)00023-2
19. Yu X, Pomfret RJ, Coley KS (1997) Dissolution of alumina in mold fluxes. Metall Mater Trans B 28:275–279. https://doi.org/10.1007/s11663-997-0094-3
20. Nightingale SA, Monaghan BJ, Brooks GA (2005) Degradation of MgO refractory in $CaO-SiO_2-MgO-FeO_x$ and $CaO-SiO_2-Al_2O_3-MgO-FeO_x$ slags under forced convection. Metall Mater Trans B 36:453–461. https://doi.org/10.1007/s11663-005-0036-x
21. Aneziris C, Pfaff E, Maier H (2000) Corrosion mechanisms of low porosity ZrO_2 based materials during near net shape steel casting. J Eur Ceram Soc 20:159–168. https://doi.org/10.1016/S0955-2219(99)00149-1
22. Chen L, Guo M, Shi H et al (2016) Effect of ZnO level in secondary copper smelting slags on slag/magnesia-chromite refractory interactions. J Eur Ceram Soc 36:1821–1828. https://doi.org/10.1016/j.jeurceramsoc.2016.02.004
23. Guo M, Parada S, Jones PT et al (2009) Interaction of Al_2O_3-rich slag with MgO-C refractories during VOD refining-MgO and spinel layer formation at the slag/refractory interface. J Eur Ceram Soc 29:1053–1060. https://doi.org/10.1016/j.jeurceramsoc.2008.07.063
24. Banda WK, Steenkamp JD, Matinde E (2020) An investigation into the wear mechanisms of carbon- and silicon carbide-based refractory materials by silicomanganese alloy. J South African Inst Min Metall 120:333–344. https://doi.org/10.17159/2411-9717/959/2020
25. Jansson S, Brabie V, Jönsson P (2008) Corrosion mechanism of commercial doloma refractories in contact with $CaO–Al_2O_3–SiO_2–MgO$ slag. Ironmak Steelmak 35:99–107. https://doi.org/10.1179/030192307X231595
26. Bui AH, Ha HM, Chung IS, Lee HG (2005) Dissolution kinetics of alumina into mold fluxes for continuous steel casting. ISIJ Int 45:1856–1863. https://doi.org/10.2355/isijinternational.45.1856
27. Harmuth H, Burhanuddin (2022) Evaluation of CLSM measurements for dissolution studies—a case study investigating alumina dissolution in a silicate slag. Ceram Int 48:28174–28180. https://doi.org/10.1016/j.ceramint.2022.06.120
28. Calvo WA, Pena P, Tomba Martinez AG (2019) Post-mortem analysis of alumina-magnesia-carbon refractory bricks used in steelmaking ladles. Ceram Int 45:185–196. https://doi.org/10.1016/j.ceramint.2018.09.150

29. Liu J, Guo M, Jones PT et al (2007) In situ observation of the direct and indirect dissolution of MgO particles in $CaO-Al_2O_3-SiO_2$-based slags. J Eur Ceram Soc 27:1961–1972. https://doi.org/10.1016/j.jeurceramsoc.2006.05.107
30. Verhaeghe F, Liu J, Guo M et al (2007) Dissolution and diffusion behavior of Al_2O_3 in a $CaO–Al_2O_3–SiO_2$ liquid: An experimental-numerical approach. Appl Phys Lett 91:124104. https://doi.org/10.1063/1.2786854
31. Guarco J, Burhanuddin VS, Harmuth H (2022) Method for determination of effective binary diffusivities in dissolution of dense ceramic materials. Ceram Int 48:7456–7463. https://doi.org/10.1016/j.ceramint.2021.11.264
32. Levich VG (1962) Physicochemical hydrodynamics. Prentice-Hal, Englewood Cliffs, N. J.,l
33. Cochran WG (1934) The flow due to a rotating disc. Math Proc Cambridge Philos Soc 30:365–375. https://doi.org/10.1017/S0305004100012561
34. Eisenberg M, Tobias CW, Wilke CR (1954) Ionic mass transfer and concentration polarization at rotating electrodes. J Electrochem Soc 101:306. https://doi.org/10.1149/1.2781252
35. Kosaka M, Minowa S (1966) Mass-transfer from solid metal cylinder into liquid metal. Tetsu-to-Hagane 52:1748–1762. https://doi.org/10.2355/tetsutohagane1955.52.12_1748
36. Tachibana F, Fukui S (1964) Convective heat transfer of the rotational and axial flow between two concentric cylinders. Bull JSME 7:385–391. https://doi.org/10.1299/jsme1958.7.385
37. Guarco J, Burhanuddin VS, Harmuth H (2022) Sherwood correlation for finger-test experiments. Results Eng 15:100610. https://doi.org/10.1016/j.rineng.2022.100610
38. Guarco J, Vollmann S, Harmuth H, Burhanuddin (2022) Method for inverse calculation of erosion parameters in slag-refractory systems. Mater Today Commun 33:1–10.https://doi.org/10.1016/j.mtcomm.2022.104736
39. Xin J, Gan L, Jiao L, Lai C (2017) Accurate density calculation for molten slags in $SiO_2-Al_2O_3-CaO-MgO$ systems. ISIJ Int 57:1340–1349. https://doi.org/10.2355/isijinternational.ISIJINT-2017-070
40. Kircher V, Burhanuddin HH (2021) Design, operation and evaluation of an improved refractory wear testing technique. Measurement 178:109429. https://doi.org/10.1016/j.measurement.2021.109429

Flexosphere Technology—Improved Flexibility and Corrosion Resistance of Fired Magnesia-Chromite Bricks

Francesca Capó Tous, Jürgen Schmidl, Bernd Neubauer, and Dean Gregurek

Abstract Flexospheres are a recent product development successfully implemented in fired magnesia-chromite bricks at RHI Magnesita. This technology focuses on inhibiting the corrosion mechanism and increasing flexibility of the refractory product. During development, the experimental investigations included chemical and physical analyses as well as standardised corrosion testing at RHI Magnesita's Technology Center Leoben (Austria). The results showed that the Flexosphere technology not only improves corrosion resistance, but also contributes to the formation of a more flexible structure, which results in better thermal shock resistance. Furthermore, a RH degasser field trial validated the laboratory results, revealing a clear performance increase compared to the standard product. Thus, the outstanding properties achieved with the patented Flexospheres make this development suitable for applications under aggressive conditions, such as the tuyere area in copper furnaces or the RH degasser in the steel industry, by guaranteeing a significant quality improvement of the magnesia-chromite product.

Keywords Ceramics · Pyrometallurgy · High-temperature materials · Refractories

Fundamentals of Magnesia-Chromite Bricks

Magnesia-chromite bricks ($MgO\text{-}Cr_2O_3$) are employed when resistance to hot erosion and thermal shock is necessary. Moreover, chromite acts as an excellent corrosion barrier against slags of different basicity and has a maximum hot modulus of rupture between 1000 and 1400 °C. Chromite has the generic formula (Mg, Fe)(Cr, Al, Fe)$_2O_4$ and belongs to the spinel group.

F. C. Tous (✉) · B. Neubauer · D. Gregurek
RHI Magnesita GmbH, Leoben, Austria
e-mail: Francesca.capotous@rhimagnesita.com

J. Schmidl
RHI Magnesita GmbH, Vienna, Austria

© The Minerals, Metals & Materials Society 2024

G. Alvear et al. (eds.), *Advances in Pyrometallurgy*, The Minerals, Metals & Materials Series, https://doi.org/10.1007/978-3-031-50176-0_10

Chromite-containing basic bricks find their application in the iron and steel industry (mostly in RH degassers, AOD converters, and safety lining applications), as well as in the nonferrous metallurgy industry, cement rotary kilns, lime shaft kilns, furnaces for refractory production, and glass furnace regeneration chambers [1].

Thermomechanical degradation and corrosion are the main phenomena involved in refractory wear and directly influence the lining lifetime. Therefore, improving refractory corrosion resistance is of vital importance for the ferrous, nonferrous, cement, and glass industries. The main wear mechanism of magnesia-chromite bricks is crack formation due to thermal shock, followed by infiltration into the refractory structure, which subsequently leads to dissolution and corrosion of the refractory product as well as further crack formation [2].

Optimisation of Magnesia-Chromite Bricks

The Flexosphere technology is based on the Spinosphere technology, which was first introduced by RHI Magnesita in magnesia-spinel grades to maintain the flexibility of cement rotary kiln bricks without compromising the hot properties [3]. The principle of this innovation was later transferred to magnesia-chromite bricks and primarily targets enhancement of flexibility and corrosion resistance.

It is well known that MgO has a high thermal expansion and therefore is characterised as a rather brittle material when compared to other refractory oxides. As MgO is one of the two main oxides in magnesia-chromite products, the Flexosphere technology was developed to improve absorption of thermal shock in aggressive environments. There are several methods to evaluate the thermal shock resistance of refractory materials, such as measurement of the dynamic Young's modulus, the wedge splitting test, and the V-modulus. Figure 1 illustrates Young's modulus (E) for two different materials. Material A demonstrates higher stress than B under the same deformation conditions, which indicates material A has a higher Young's modulus than B.

The dynamic Young's modulus is proportional to the compressive stress (σ) divided by a given axial strain or deformation (ε). Moreover, it can be measured with the ultrasonic method and further calculated as the density multiplied by the ultrasonic speed, according to the equation given below [4]:

$$E = \frac{\text{Stress}}{\text{Deformation}} = \frac{\sigma}{\varepsilon} = \rho \cdot v^2 (\text{GPa}) \tag{1}$$

Lower Young's moduli are characteristic of materials with a better thermal shock behaviour and give an indication of a material's flexibility.

The second competitive advantage of Flexospheres is the deceleration of slag penetration and subsequent corrosion of refractory magnesia-chromite bricks. There are several methods to assess the corrosion mechanisms of refractory samples, such as the crucible test, the rotary finger test, and the rotary slag test [2]. In the present

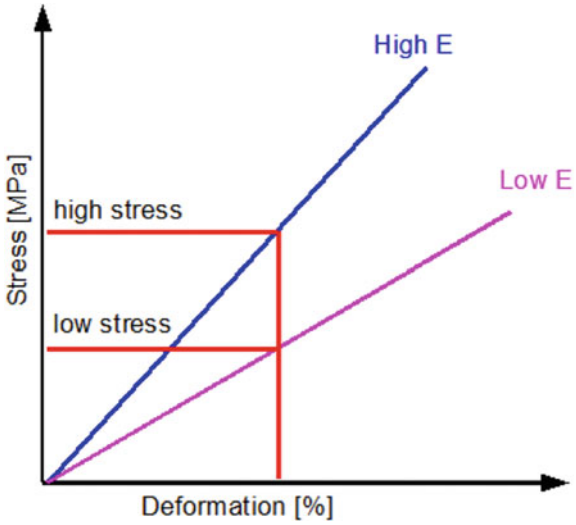

Fig. 1 Representation of Young's modulus (E) for different materials [4]

study, dynamic corrosion wear experiments were conducted in a high-frequency induction furnace (HF-IF) using the rotary finger test.

Experimental Procedure

The initial investigations performed at RHI Magnesita's Technology Centre Leoben (Austria) included preparing and mixing the raw materials, followed by shaping and pressing bricks (Fig. 2). The bricks were subsequently fired in one of RHI Magnesita's tunnel kilns to ensure strong ceramic bonding of the raw materials before various chemical and physical properties, including the flexibility and corrosion resistance, were evaluated.

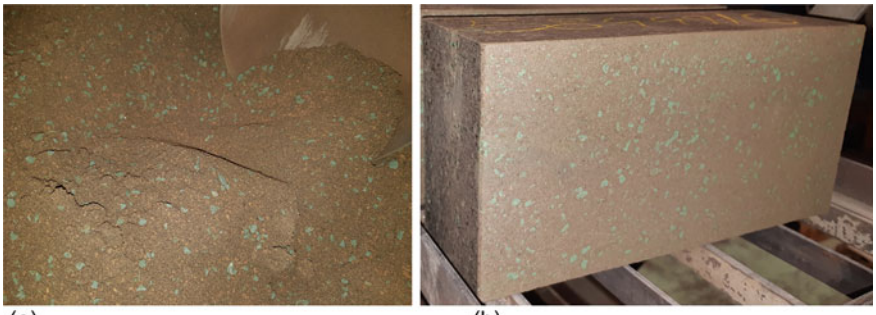

Fig. 2 Magnesia-chromite raw materials **a** after mixing and **b** brick pressing

Higher Flexibility and Corrosion Resistance of Magnesia-Chromite Bricks

Based on different investigations, the final refractory product was designed to increase flexibility to a maximum, while at the same time guaranteeing optimum mechanical properties. Figure 3 illustrates the dynamic Young's modulus of three specimens containing different amounts of Flexosphere (V_1, V_2, and V_3) compared to the standard magnesia-chromite product, during a heat up and cool down cycle. The results show that the samples with the Flexosphere technology have a lower dynamic Young's modulus than the standard product and, consequently, a higher flexibility to counteract thermal shock.

Another parameter to evaluate the flexibility of a product is the V-modulus, where a higher V-modulus indicates a more brittle material that is less stable against thermal shock. The Flexosphere-containing product showed lower V-modulus values indicating a higher capacity to absorb thermal fluctuations in comparison with the standard grade (Table 1).

To compare the corrosion resistance of specimens with the Flexosphere technology to standard magnesia-chromite material, rotary finger tests were conducted

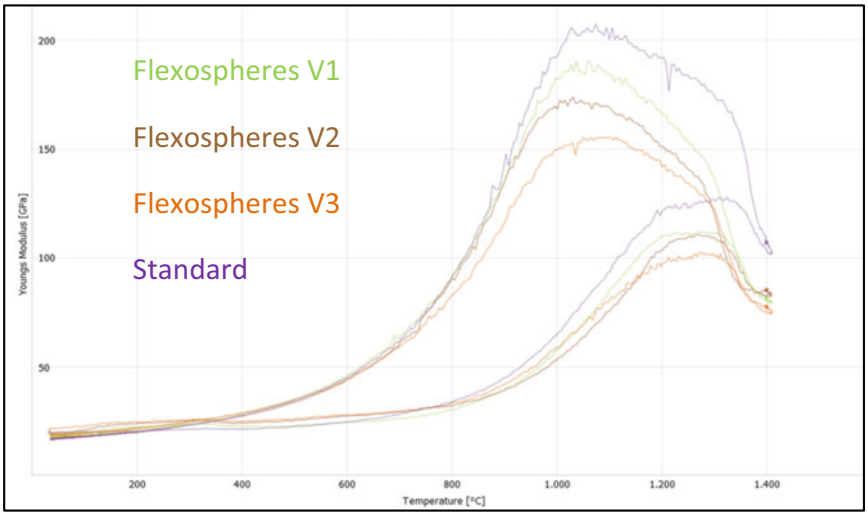

Fig. 3 Dynamic Young's modulus of three specimens containing different amounts of Flexosphere compared to the standard magnesia-chromite product, during a heat up and cool down cycle

Table 1 V-modulus of Flexosphere and standard magnesia-chromite products

	Unit	V-modulus
Standard product	N/mm^2	8190
Flexosphere product	N/mm^2	3437

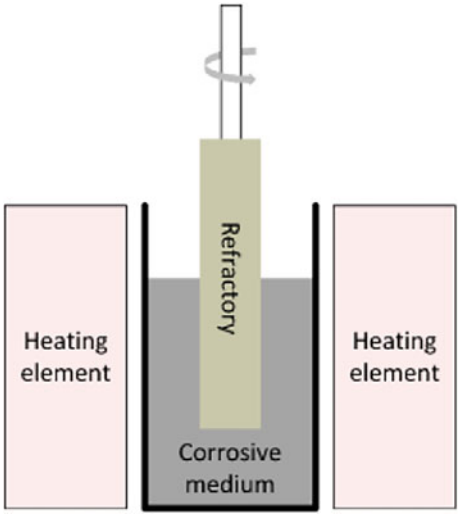

Fig. 4 Schematic view of a rotary finger test to evaluate the refractory corrosion mechanism

in a high-frequency induction furnace (HF-IF). Figure 4 illustrates the experimental setup, where typically 1–4 refractory fingers are submerged and rotated in the corrosive medium (i.e., metal or slag), which is contained in a crucible surrounded by heating elements [5].

Figure 5 shows macroscopic images of the fingers after a corrosion test to compare the Flexosphere technology with the standard product. Based on the maximum flux line depth, these results confirmed that the Flexosphere-containing refractory had a better performance than the standard sample due to minor slag infiltration into the refractory matrix and therefore a thicker unaltered refractory profile. The maximum flux line depth is calculated as follows:

$$d_i = \frac{t_i - t_c}{2} \tag{2}$$

where t_i is the original finger thickness and t_c is the finger thickness after the corrosion test.

Light microscopy was performed on the corrosion test samples and Fig. 6 shows a discontinuous slag precipitation zone on the Flexosphere-containing sample surface (A), the penetration zone (B), and the matrix (C).

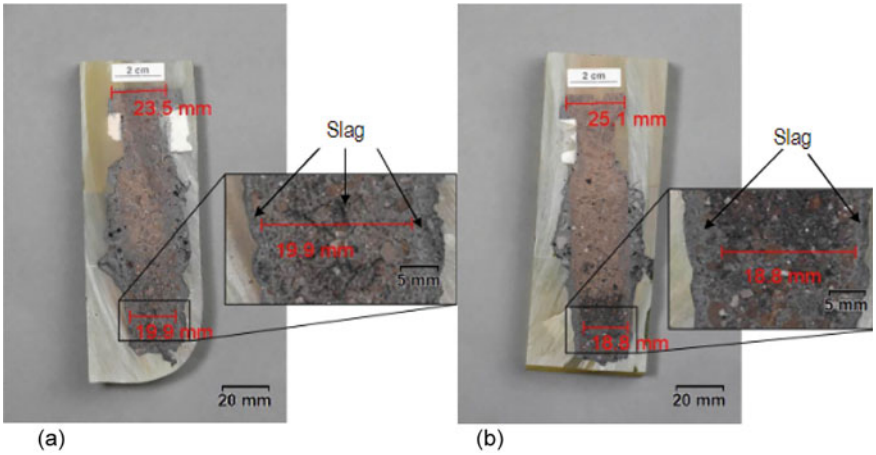

Fig. 5 **a** Flexosphere-containing and **b** standard magnesia-chromite fingers after the corrosion resistance test, highlighting the maximum flux line depth (d_i)

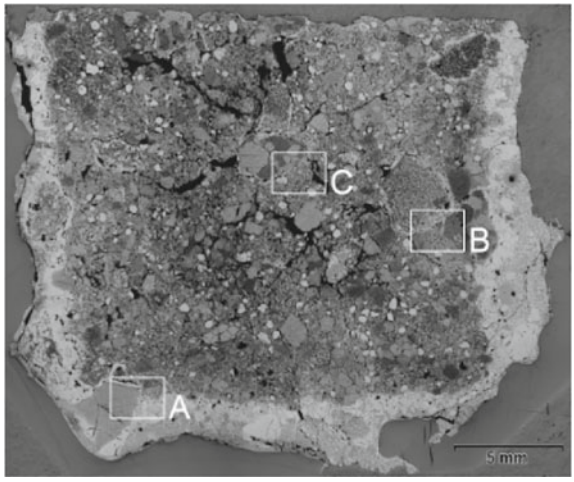

Fig. 6 Light micrograph of the Flexosphere-containing material after the corrosion resistance test showing a discontinuous slag precipitation zone on the sample surface (A), the penetration zone (B), and the matrix (C)

Field Trial—Successful Flexosphere Application in the Steel Industry

A field trial in the lower vessel of a RH degasser confirmed and extended the results observed in the laboratory-scale investigations. Magnesia-chromite bricks with the Flexosphere technology were installed as a panel in the lower vessel wear lining directly above one of the legs and the standard magnesia-chromite bricks were used to line an equivalent area above the other leg. Figure 7 shows a schematic section of the RH degasser, where the refractory with the Flexospheres technology is represented

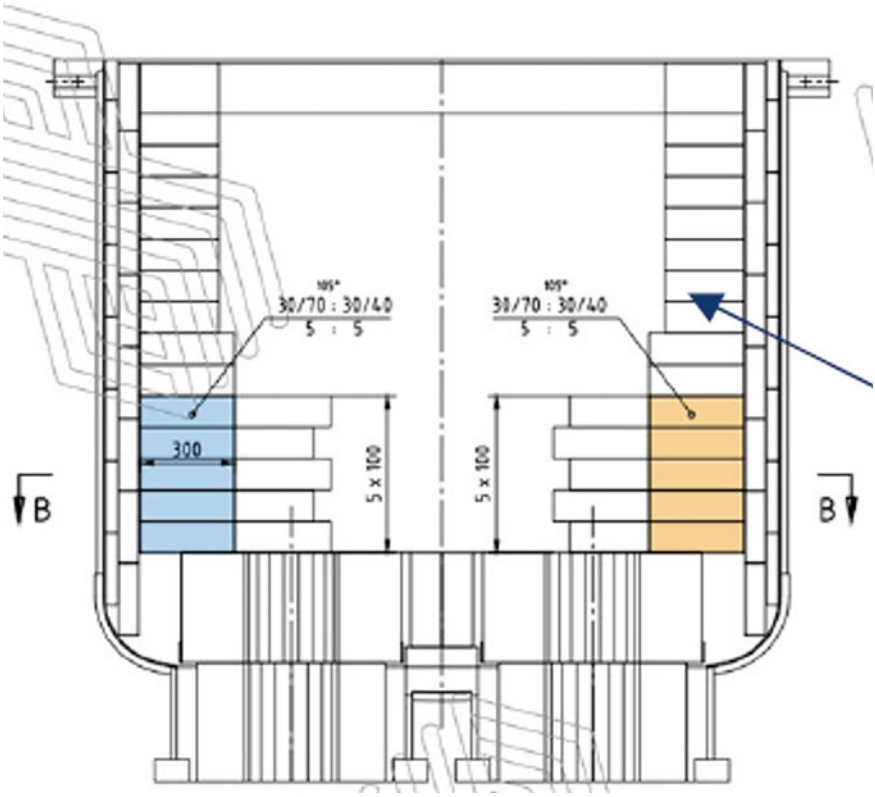

Fig. 7 Section of the RH degasser lower vessel lining showing the magnesia-chromite Flexosphere product on the left (blue) and the standard magnesia-chromite bricks on the right (yellow)

in blue and the standard product is marked in yellow. As the lining above the up leg usually experiences higher stresses than that above the down leg, the steel direction was switched after each leg/snorkel campaign to guarantee a uniform distribution of the wear rate.

During the trial, relative measurements of the lower vessel lining were performed after the first leg/snorkel campaign and indicated a + 11% performance increase of the Flexosphere-containing bricks compared to the standard magnesia-chromite material. At the end of the lower vessel campaign, absolute brick measurements could be made as the lining was dismantled and revealed a + 14% performance improvement with the new development. Overall, when variables such as measurement tolerances and swapping the up and down legs were taken into consideration, it was concluded that the Flexosphere material had an improved performance of 5–15% compared to the standard magnesia-chromite bricks (Fig. 8).

Fig. 8 Standard magnesia-chromite bricks installed above the left leg and magnesia-chromite with the Flexosphere technology installed above the right leg in the RH vessel

Conclusion

The holistic approach that combined laboratory investigations as well as a field trial at one of RHI Magnesita's customers enabled the development of an innovative magnesia-chromite product. The Flexospheres technology improves the corrosion resistance and flexibility against thermal shock of magnesia-chromite bricks, resulting in a product suitable for applications under aggressive conditions such as the tuyere area in copper furnaces and the RH degasser used in the steel industry.

References

1. Routschka G, Wuthnow H (2017) Praxishandbuch feuerfeste werkstoffe. Vulkan-Verlag, pp 117–124
2. Poirier J, Rigaud M (2017) Corrosion of refractories: the fundamentals. FIRE compendium series; Göller Verlag, pp 1–18, pp 33–37
3. Geith M, Jörg S, Krischanitz R (2021) Spinospheres technology—an advanced technology to improve cement rotary kiln brick properties. Presented at 17th unified international technical conference of refractories (UNITECR), Chicago, USA, 14–17 Sept 2021
4. Geith M, Jörg S, Krischanitz R (2017) Influence of flexibilizers on basic cement rotary kiln brick properties. Presented at the 15th unified international technical conference of refractories (UNITECR), Santiago, Chile, 27–30 Sept 2017
5. Reynaert C, Sniezek E, Szczerba J (2020) Corrosion tests for refractory materials intended for the steel industry—a review. Ceram Silikaty 64:1–9

Part IV
Industrial Applications of Improved Process Control: A Joint Session with Advances in Pyrometallurgy

A Digital Twin for Management of Molten Material Containment in Furnaces

Melvin Pong, Bien Ferrer, Frans Hannemann, Afshin Sadri, and Yale Zhang

Abstract The key challenge for pyrometallurgical furnace operators is to maximize production whilst balancing the risks of failure, i.e., ensure the molten materials remain contained in these furnaces until the next rebuild. To understand this risk, a deep understanding of the various failure modes is necessary, as well as the barriers that should be in place to prevent and mitigate them. The information needed to inform this risk, such as process and equipment conditions, changes over time and is often distributed across several people and systems within an organization. These circumstances make it difficult to get a "comprehensive picture" of the asset condition to evaluate whether the risk of molten material containment is becoming unacceptably high at any point in time. Hatch has applied the digital twin concept to online monitoring of risk barrier status using the risk-bowtie methodology and real-time asset and operational information to visualize the live risk profile of a particular unwanted event; in this case, a runout.

Keywords Barrier management · Bowtie analysis · Digital twin · Molten material · Risk management · Runout · Safety barriers

M. Pong (✉)
Pyrotech Performance Engineering, Technologies, Asset Performance Management Group, Hatch, Mississauga, ON, Canada
e-mail: melvin.pong@hatch.com

B. Ferrer
Pyrotech Performance Lead, Technologies, Asset Performance Management Group, Hatch, Mississauga, ON, Canada
e-mail: bien.ferrer@hatch.com

F. Hannemann · A. Sadri
Global Technologies, Asset Performance Management Group, Hatch, Mississauga, ON, Canada
e-mail: frans.hannemann@hatch.com

A. Sadri
e-mail: afshin.sadri@hatch.com

Y. Zhang
Digital Solutions – Decision Support, Hatch, Mississauga, ON, Canada
e-mail: yale.zhang@hatch.com

© The Minerals, Metals & Materials Society 2024

G. Alvear et al. (eds.), *Advances in Pyrometallurgy*, The Minerals, Metals & Materials Series, https://doi.org/10.1007/978-3-031-50176-0_11

Introduction

Smelting furnaces are designed using refractory lining to contain molten material while maintaining the structural integrity and cooling of the vessel to avoid failure. Assessing the risk of loss of containment is key to estimating remaining campaign life and future rebuild planning. Furnace refractory lining thickness is often the focal point in assessing loss of containment risk, but from the review of past records of furnace incidents, several other factors must also be considered to understand the failure mechanisms.

As furnace operations become more complex and the systems within the operations become increasingly integrated with one another, loss of containment incidents not only become more likely, but they become inevitable [1]. Barrier management is essential to reduce the risk of failures because the degradation of barriers is a key cause of loss of containment [2]. A major benefit of digitization is the automated collection of monitoring data instead of manual data collection [3], which is more time-consuming, more prone to errors, and less consistent. Within the process industries, digital systems made improvements in online sensing, increased connectivity with other systems, risk-based inspections, control of maintenance processes, operational procedures, and alarming systems [4]; digitization of the barrier management system for molten material containment will provide major benefits for risk reduction.

Incident Benchmarking

A review was conducted on records of 86 furnace incidents from Hatch engagements between 1983 and 2023, occurring in the Americas, Europe, Africa, Asia, and Australasia. Though not a comprehensive record of industry incidents, these records are expected to be representative of smelting furnace incident types generally.

In this review, a loss of containment incident is defined as one that resulted in downtime outside of or exceeding the planned duration of a scheduled maintenance outage, and includes one of the following characteristics:

1. Loss of molten material containment.
2. Furnace shut down ahead of a scheduled reline due to presence of excessive wear that could lead to loss of molten material containment, such as significant refractory wear or hearth flotation.

Explosions due to interactions between water and molten material are considered as a separate incident type and are excluded from this review.

A total of 57 out of the 86 furnace incidents recorded met the above definition and were considered for further review. The furnace types included 27 rectangular electric furnaces, 22 circular electric furnaces, and 8 rectangular flash furnaces. The suspected primary causes of these incidents are broken down in Fig. 1. The top three primary causes account for two-thirds of the containment incidents, and they are

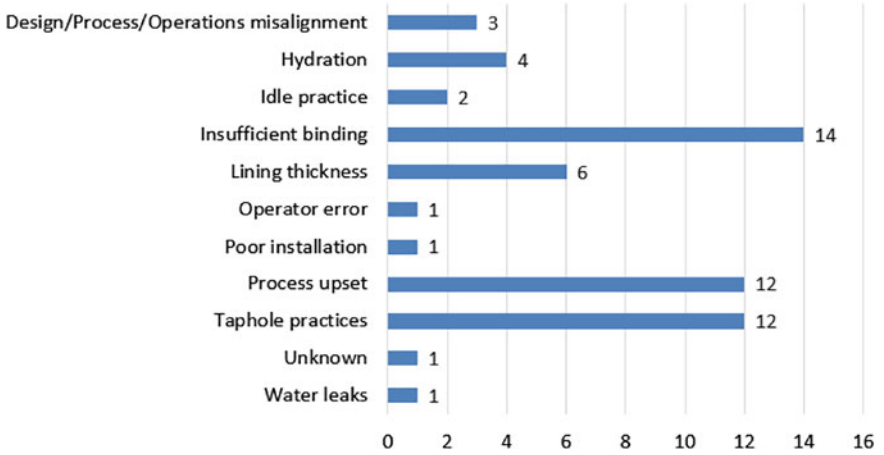

Fig. 1 Primary causes of loss of containment incidents

insufficient binding, poor taphole practices, and process upset. A binding system is applicable to rectangular furnaces, and its function is to maintain joint tightness between bricks and cooling elements by providing horizontal, transverse, and vertical refractory compression, as well as maintain the stability of an inverted arch.

In summary, there is a variety of causes that result in loss of containment incidents. There is no single cause to implement barriers against, resulting in the need for a more comprehensive barrier management system to handle the large number of causes and barriers.

Bowtie Analysis for Loss of Containment

Bowtie analysis is a risk assessment methodology which graphically describes the flow of causes to consequences of a Material Unwanted Event (MUE) and the preventive and mitigating barriers designed to control the hazard [5]. The resulting bowtie diagram allows the viewer to quickly and easily understand the causal relationships associated with the MUE and how the system of barriers work to prevent or mitigate the MUE. An example of a simple bowtie diagram is shown in Fig. 2.

Failure Mechanisms

Loss of molten material containment requires the molten material to physically escape the furnace crucible. Failure can occur through gaps in the furnace refractory or loss of refractory (i.e. refractory wear). The analysis of failure mechanisms

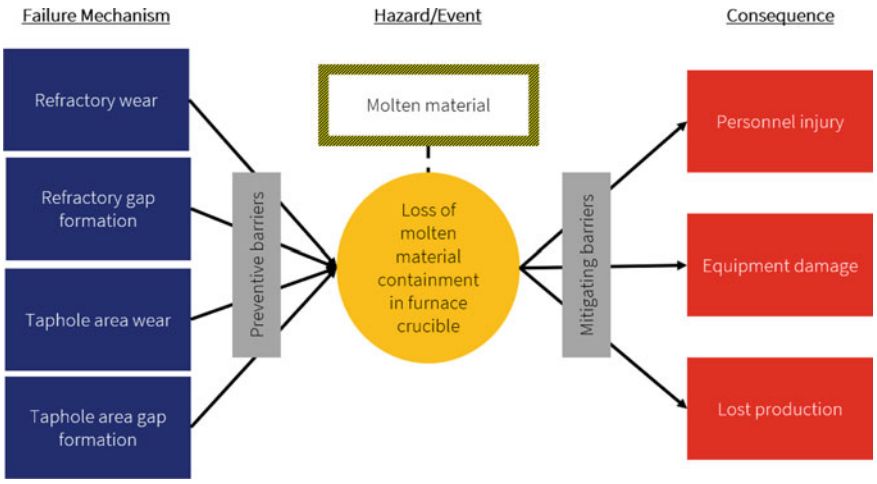

Fig. 2 Simplified bowtie diagram

focuses on insufficient binding, poor taphole practices, and process upset. Gaining a deeper understanding of the failure mechanisms is important to determine which barriers will be effective.

Insufficient binding was the result of failing to adjust binding loads of the binding system or failing to maintain the binding system which resulted in erroneous spring length measurements. In addition, there is more uneven thermal expansion during furnace start-ups and restarts, so gaps can form at the joints. While the furnace binding can also fail if the binding steel overheats and deforms, Hatch did not identify binding steel deformation as a cause for insufficient binding in the incidents from past engagements.

Poor taphole practices were from operational practices, which include drilling, lancing, and plugging, or from maintenance practices, such as poor installation or using poor quality material. Misaligned lancing causes damage to the taphole refractory and increase the taphole diameter and tapping rate [6]. Combined with low liquid viscosity due to high temperatures can even result in sufficient shear stresses that cause erosion of refractory if the refractory had been weakened by penetration into the refractory pores and corrosion [7]. Gases within taphole clay causing turbulence adjacent to the hot face taphole area, which leads to erosion in the area [8]. Deficient or incorrect taphole repairs can also lead to poor integration of new refractory with the existing refractory or poor integration of tapblocks with refractory, resulting in differential movement that leads to formation of gaps [9].

Process upset conditions involved high bath levels, temperatures, and chemistry. In matte smelting furnaces, poor control over bath levels would expose a greater height of refractory in the wash zone to slag corrosion as bath levels change, which accelerates wearing of the refractory [10]. The wash zone, which is an area of the furnace that is exposed to both matte and slag as bath levels change, and the matte tapholes,

which may experience "slagging" or tapping slag through the matte tapholes, are thus particularly vulnerable. In addition, highly superheated matte can contact and melt away the slag freeze lining [10], and therefore the area becomes susceptible to matte infiltration. Combined with erosion of the refractory lining due to intensive stirring of the furnace bath or erosion of the tapholes during tapping or plugging leads to refractory wear in these areas. Similar to superheated matte, superheated slag will also melt away the slag freeze lining and increase the potential for slag infiltration. Poor temperature control and poor slag chemistry control, i.e. fluxing, can lead to increasing slag superheats.

Preventive and Mitigating Barriers

A barrier is a physical or non-physical intervention that prevents a failure mechanism from manifesting, prevents a failure mechanism from developing into an MUE, or mitigates the consequences of an MUE if the MUE materializes [5]. Understanding the causes of loss of containment incidents and the failure mechanisms will direct focus to relevant preventive barriers. Some examples of preventive barriers and their respective failure mechanisms are shown in Table 1.

The consequences of loss of containment focus on personnel injuries and fatalities, equipment damage, and production losses, which have barriers that are managed by technical staff. Barriers may include evacuation system, furnace runout pit, and critical spares management. Other consequences may include reputational damage or legal repercussions, but these are outside the scope of a technical discussion and are sometimes excluded.

Table 1 Preventive barrier by failure mechanism

Failure mechanism	Preventive barrier
Gap formation due to insufficient binding	• Adjustment and maintenance of binding system • Controlled furnace start-up and restart
Gap formation due to poor taphole practices	• Maintenance of tapblock hold-backs, which prevent the tapblock from being pulled from the furnace • Quality assurance of taphole repairs
Refractory wear due to process issues	• Bath level control • Bath temperature control • Furnace cooling system
Refractory wear due to poor taphole practices	• Lance guides • Drilling practices • Plugging practices

Barrier Monitoring Techniques

Typical monitoring techniques already exist at most smelters. Most monitoring techniques can be incorporated into a barrier monitoring system. Some examples include thermocouples on refractory and copper coolers, water flow meters and resistive temperature detectors (RTD), non-destructive testing (NDT) results, furnace expansion measurements, and binding system spring length.

Advanced monitoring techniques developed by Hatch have been installed at multiple smelters with increasing adoption [11–14]. Other benefits include increased furnace availability and improved safety for personnel. Table 2 provides a summary of some of the advanced monitoring techniques.

Table 2 Barrier monitoring techniques

Parameter	Typical method	Advancements		
		Method	Benefits over typical method	Installations
Lining temperature	Thermocouples	Fibre optics [11]	Spatial resolution—multiple measurement points per strand	Multiple smelters—embedded in copper cooling elements and directly into furnace walls
Gaps and cracks formation	Acoustic emission (AE)	Furnace integrity monitoring system [12]	Continuous measurements and identification of location and position of gap openings and crack formation	Multiple smelters, rapid installation on the shell, new technology
Bath level	Soundings	Stinger	Temporal resolution—increase frequency without requiring physical access to roof or turning off furnace	Under development
		Furnace bath levels predictor	Continuous measurements without requiring physical access to roof or turning off furnace, but requires good thermal and sounding data	Multiple trials undertaken; available for initial deployment
Electrode tip length	Electrode dip test	ElectroDAR [13]	Continuous measurements, improved accuracy	Multiple trials underway

(continued)

Table 2 (continued)

Parameter	Typical method	Advancements		
		Method	Benefits over typical method	Installations
Furnace movement	Manual distance measurements	Lasers, draw wires	Continuous measurements	Multiple smelters
	Surveys	3D scans	Spatial resolution	Multiple smelters; increasing adoption with improving cost competitiveness
Binding loads	Manual spring length measurements	Load cells	Continuous measurements	Multiple smelters
Lining thickness	Acousto Ultrasonic-Echo (AU-E)	Furnace integrity monitoring system [12]	Continuous measurements	One test case with increasing interest
		Taphole acoustic monitoring [11]	Continuous measurements	One smelter
		Eddie current	Continuous measurements	Research stage

Digital Twin

At the most mature smelters, the risk management systems have strong frameworks to support internal initiatives that reduce MUE risk by maintaining the integrity of the relevant barriers. The initiatives may include desktop activities such as baseline risk assessments, bowtie analyses, and fault tree analyses, to field activities such as job hazard analyses (risk assessment) and furnace audits. These initiatives provide information on which barriers need to be implemented or which barriers need to be reviewed. However, the process of managing barriers remain challenging. A traditional alarming system across distributed control systems has the following issues:

- Only process parameters monitored by instrumentation can be alarmed, therefore manual measurements require an additional system, e.g. periodic data review is required to identify problems.
- High-level MUE risk is not reported and the impact of resolving alarms is not known.
- Prioritization of activities with greater impact of MUE risk is absent.
- An escalation system if alarms remain unresolved is absent.

In this context, a digital twin is a dynamic, virtual representation of a physical asset or process that serves as a robust foundation to integrate risk-bowtie models with real-time data for effective risk barrier monitoring and solves the above issues by providing the following advantages in managing the system of barriers:

- Collects and reports all the available information on the furnace from discrete manual measurements to continuous sensor measurements and stores it in a central location, making access to information easier.
- Provides real-time reporting on overview of MUE risk and individual barrier health using available furnace information.
- Prioritizes and recommends corrective actions with the greatest impact on MUE risk reduction when barrier health deteriorates.
- Triggers alerts up the chain of command about barriers that remain unresolved within a time limit.

A comprehensive bowtie analysis is key to developing a strong foundation for the digital twin to represent the system of barriers. Firstly, the incident benchmarking results identified the major causes of loss of molten material containment. Secondly, the theoretical understanding of the failure mechanisms, along with Hatch's practical experience in designing furnaces, was used to identify the barriers that can prevent the different failure mechanisms from materializing into the MUEs or reduce the impact of the MUEs. The screenshots of the resulting digital twin for risk barrier monitoring are shown in Figs. 3 and 4.

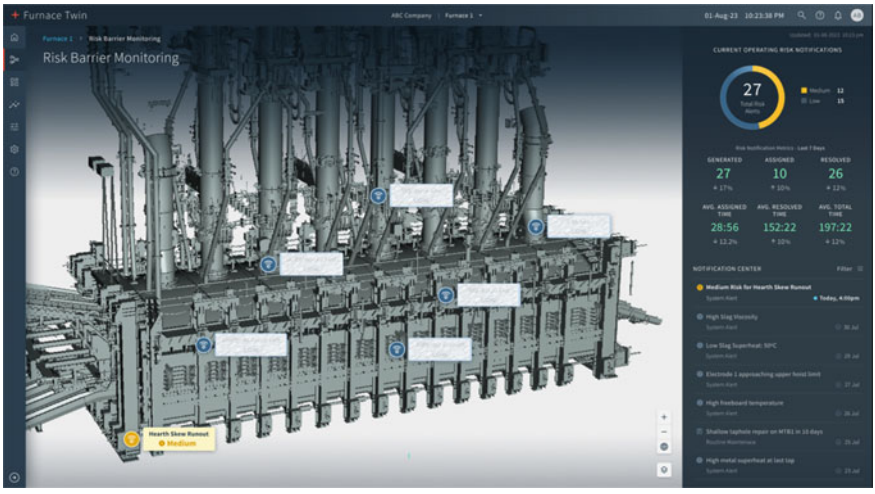

Fig. 3 Digital twin for risk barrier monitoring—landing page

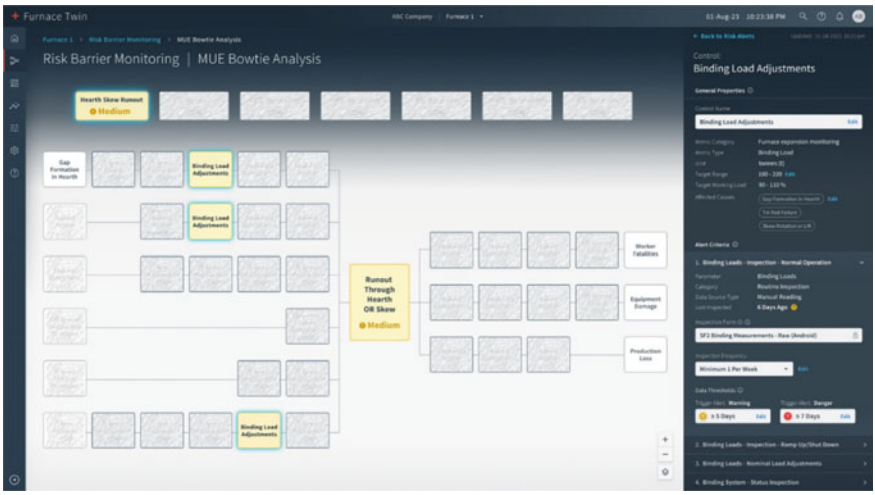

Fig. 4 Digital twin for risk barrier monitoring—bowtie diagram

Implementation Approach

Implementing a barrier monitoring system follows the same general steps for other MUEs.

1. Review baseline risk assessment, issue-based risk assessment, and risk management framework.
2. Review historical incidents or near hits.
3. Inventory the hazards, identify MUEs which exceed a pre-determined threshold, and identify MUEs of special concern.
4. Develop bowtie diagrams for each MUE using existing knowledge of failure modes that occur and barriers that are significant, including knowledge within the smelter and of similar operations.
5. Define performance requirements for each barrier to develop the "traffic light" system for barrier health.
6. Build Extract, Transform, and Load (ETL) pipeline to manage all data required to determine barrier health.
7. Customize digital twin of the furnace with the MUEs, KPIs, bowtie diagrams, barriers and their health, and notifications for prioritized corrective actions.
8. Incorporate the digital twin for risk barrier monitoring into existing risk management systems and workflows by implementing change management and embracing digital transformation.

Conclusion

Loss of molten material containment involves multiple causes beyond refractory lining wear. The failure mechanisms of the underlying causes must be understood to identify and implement the appropriate barriers that prevent and mitigate loss of containment incidents. Although advancements in monitoring techniques provide greater confidence to furnace operators on barrier health, operations and maintenance staff already handle many daily tasks, and with the burden of additional corrective actions that are needed to reduce the loss of containment risk, the staff will be overwhelmed by how to respond. A digital barrier monitoring system processes the available data, determines which corrective actions have the greatest impact on loss of containment risk, and guides the operations and maintenance staff on which actions to prioritize first. With the additional data on how loss of containment risk and barrier health change over time, furnace operators can improve on the design, operations, and maintenance of the furnace and its barriers, therefore pushing the furnace to increase production while maintaining within the risk tolerance.

References

1. Perrow C (2011) Normal accidents: living with high-risk technologies-updated edition. Princeton University Press, Princeton
2. Lauridsen O, Lootz E, Husebo T, Ersdal G (2016), Barrier management and the interaction between technical, operational, and organizational barrier elements. Paper presented at the 13th SPE international conference and exhibition on health, safety, security, environment, and social responsibility, Stavanger, 11–13 Apr 2016
3. Khan F, Amyotte P, Adedigba S (2021) Process safety concerns in process system digitalization. Educ Chem Eng 34:33–46
4. Lee J, Cameron I, Hassall M (2019) Improving process safety: what roles for digitalization and industry 4.0? PSEP 132:325–339
5. Center for Chemical Process Safety (2018) Bow ties in risk management: a concept book for process safety. Wiley, New York and London
6. Guthrie R (1992) Engineering in process metallurgy. Oxford University Press, Oxford
7. Campbell AP, Pericleous KA, Cross M (2002) Modeling of freeze layers and refractory wear in direct smelting processes. I&SM 29(9):41–45
8. Shaw A, de Villiers LPVS, Hundermark RJ, Ndlovu J, Nelson LR, Pieterse B, Sullivan R, Voermann N, Walker C, Stober F, McKenzie AD (2013) Challenges and solutions in PGM furnace operation: high matte temperature and copper cooler corrosion. J South Afr Inst Min Metall 113(3):251–261
9. Faux S, Walker C, Stober F, MacRosty R, Darini M, Kargutkar B (2018) Optimizing tap-hole performance using a risk-based asset management strategy. Paper presented at the 2nd furnace tapping conference, Kruger National Park, 14–17 Oct 2018
10. Nelson LR, Hundermark RJ (2016) The tap-hole—key to furnace performance. J South Afr Inst Min Metall 116(5):465–490
11. Braun W, Gebski P, MacRosty R, Pula R, Sadri A, Ying W (2016) Tap-hole monitoring technologies. J South Afr Inst Min Metall 116(1):1–9
12. Gebski T, Sadri A, Ying W (2011) Development of the system for furnace integrity monitoring based on real-time continuous acoustic emission data acquisition and analysis. Paper presented at the 50th conference of metallurgists, Montreal, 2–5 Oct 2011

13. Chataway D, Sadri A, Cramer M, Gerritsen T (2018) Development of electrode tip position measurement technology for electric furnaces. Paper presented at the 15th international ferro-alloys conference, Cape Town, 25–28 Feb 2018
14. Dhora A, MacRosty R, Rodd L, Walker C, Alhashme M, Ferrer B (2018) Optimizing smelter uptime through digital asset management. Paper presented at the 1st extraction meeting and exhibition, Ottawa, 26–29 Aug 2018

Part V
Poster Session

Corrosion Behavior of MgO-C Refractory in the Electric Arc Furnace that Entirely Uses Direct Reduced Iron as Raw Materials

Zhuogang Pang and Haibin Zuo

Abstract The corrosion behavior of MgO-C refractory in electric arc furnace (EAF) slags was investigated by adopting a rotating immersion method (25 r/min) at 1823 K. The EAF entirely uses direct reduced iron as raw materials, and the change of refractory radius, MgO content in slag, and contact angle were studied at various slag basicity conditions. The results showed that the reduction of radius diminished as the slag basicity increased from 1.6 to 2.47. The slag with higher basicity has a larger contact angle compared to lower basicity slags. In addition, the MgO solubility increased with a decrease in basicity and an extension of exposure time and subsequently stabilized after 60 min. The reduction of FeO_x and the formation of a magnesiowüstite (MW) intermediate layer occurred within the refractory. The MW layer is thicker in cases of low-basicity slag, but the slag penetration is deeper, leading to severe erosion.

Keywords Magnesia refractory · Corrosion behavior · Electric arc furnace slag · Direct reduced iron

Introduction

With the implementation of carbon reduction policies in the steel industry, the shaft furnace direct reduction-electric arc furnace route, as a tremendous potential alternative to the blast furnace-basic oxygen furnace route, has attracted the attention of many researchers [1, 2]. The use of direct reduction iron (DRI) in the electric arc furnace (EAF) will increase rapidly in the foreseeable future, which is beneficial to improve the quality of liquid steel and reduce CO_2 emissions [3, 4]. However, challenges also arise. As the gangue content in DRI is higher than that of traditional charge (melted iron and scrap), the volume of EAF slag will increase, and the

Z. Pang · H. Zuo (✉)
State Key Laboratory of Advanced Metallurgy, University of Science and Technology Beijing, Beijing 100083, China
e-mail: zuohaibin@ustb.edu.cn

© The Minerals, Metals & Materials Society 2024

G. Alvear et al. (eds.), *Advances in Pyrometallurgy*, The Minerals, Metals & Materials Series, https://doi.org/10.1007/978-3-031-50176-0_12

composition will also change. Simultaneously, the significant addition of DRI will lead to a decrease in basicity, impacting the removal of impurities and the foaming effect of slag. Therefore, lime is typically added during the smelting process to adjust slag basicity. These variations have a direct bearing on steel quality and exacerbate refractory degradation [5, 6]. MgO-C refractory is extensively employed in EAF due to its commendable thermal shock resistance and corrosion resistance. In addressing the issue of severe refractory erosion during high-proportion DRI smelting in EAFs, studying the extent of erosion in such cases and analyzing the erosion mechanisms is essential to minimize refractory degradation and prolong its service life and reducing production costs.

Numerous studies have investigated various slag-refractory interfacial reactions. Hyungsic Um et al. [7] explored the corrosion behavior of MgO–C refractory in ferromanganese slags, and found that the strong corrosion of MgO-C refractory occurred when MnO was included in the slag composition. Mohammed et al. [8] studied the MgO solubility in steelmaking slags to find that the Fe^{3+}/Fe^{2+} ratio was insignificant in changing MgO solubility, but the effect of P_2O_5 on the MgO solubility much more pronounced. Jung et al. [9] elucidate the effect of Fe_tO content on MgO solubilities in lime-based slags, and found that the Fe_tO activities in metallurgical slags containing iron oxide play the decisive role in determining the MgO solubilities into the slags. In summary, current research on the corrosion of MgO-C refractory mostly focuses on the effect of slag composition on the MgO solubility. However, the corrosion degree and mechanism of EAF slag using DRI as raw material on MgO-C refractory are not common, and there is a lack of systematic research.

This study adopted the rotating immersion method to test the corrosion degree of MgO-C refractory in EAF slags that entirely use DRI as raw materials. Based on this slag, corrosion experiments on refractories under different basicity conditions (1.6–2.47) were also conducted. The contact angle between slag and refractory was measured using a comprehensive melting-point and melting-rate system. A field emission scanning electron microscopy with energy-dispersive X-ray spectroscopy was used to analyze refractory microstructure and element distribution. Based on the research results and analysis, we inferred the corrosion process of MgO-C refractory in the EAF slag using DRI. We hope that the research results can assist in prolonging the lifespan of refractory materials when smelting high-proportion DRI in electric furnaces.

Experimental Procedure

Preparation of Pre-melted Slag

The reagent-grade powders of CaO, SiO_2, MgO, Al_2O_3, FeO, and Fe_2O_3 were adopted to prepare experimental EAF slags. The composition of experimental slag was listed in Table 1, and the composition of actual EAF slag that entirely uses H_2

shaft furnace DRI as raw materials was No. 5 in Table 1. The low-content elements, such as S and P in the actual slag, were not considered in the experimental design to avoid the influence of impurity elements on the experimental results. The oxide reagents were precisely weighed and thoroughly mixed in an agate mortar. Put 300 g synthetic slag into a platinum crucible and pre-melt in a resistance furnace under a high-pure argon atmosphere (99.999%, 0.5 L/min) at 1823 K for 2 h, and then the liquid slags were quickly quenched on a water-cooled copper plate. Thereafter, the re-solidified species were collected and ground into 200 meshes. The composition of quenched slags was carried out by X-ray fluorescence (XRF, S4 Explorer, Bruker AXS, Germany), and the total iron and ferrous content was tested with dichromate titration method. The results were also listed in Table 1, and it should be mentioned that few Mo (<0.03 mass%) infiltrated the slag, which has an ignorable effect on the corrosion between molten slags and refractory.

Corrosion Experiments

A Chinese refractory manufacturer provided the MgO-C refractory (DM97). The chemical compositions and physical properties of the magnesium-based refractory are presented in Table 2. The refractory was machined into cuboid samples (25 × 25 × 30 mm), and a through-bore (φ5 mm) opened at the top of the square cylinder. The Mo wire (φ3 mm) was passed through the through-hole of the refractory sample and fixed to a Mo bar that could push the refractory sample into the molten slag steadily, and a rotational motor was linked at the other end of the Mo bar. The schematic diagrams of the corrosion apparatus are shown in Fig. 1. A Mo crucible with 100 g quenched slag was placed in the uniform temperature zone of the furnace and heated to 1823 K. After holding for 1 h, the refractory sample was immersed in the liquid slag and rotated at a speed of 25 r/min under the drive of the motor. Take 5 g of slag sample with a molybdenum spoon and quench at 0, 30, 60, and 90 min. After 90 min of exposure time, turn off the motor and lift the sample away from the liquid level to remove the residual slag adhering to the surface of the refractory. Then, the refractory sample was rapidly quenched in a purified Ar atmosphere.

Wetting Experiments

The contact angles between slag and refractory were determined by a melting-point and melting-rate comprehensive measurement system (MTLQ-RD-1600, Chongqing University of Science and Technology, Chongqing, China). Figure 2 showed the

Table 1 Initial composition of slag used in the present study

No	Before pre-melted (mass pct)						After pre-melted (mass pct)						Basicity (CaO/SiO_2)
	CaO	SiO_2	MgO	Al_2O_3	FeO	Fe_2O_3	CaO	SiO_2	MgO	Al_2O_3	FeO	Fe_2O_3	
1	41.61	26.00	7.86	8.50	9.93	6.10	41.84	26.09	7.46	8.61	8.93	7.07	1.60
2	43.46	24.15	7.86	8.50	9.93	6.10	43.56	24.06	7.71	8.63	8.78	7.26	2.00
3	45.07	22.54	7.86	8.50	9.93	6.10	44.95	22.49	8.01	8.46	9.05	7.04	2.20
4	46.48	21.13	7.86	8.50	9.93	6.10	46.4	21.1	7.91	8.51	8.97	7.11	1.80
5	48.18	19.52	7.86	8.50	9.93	6.10	48.07	19.51	7.88	8.56	9.01	6.97	2.47

Table 2 The chemical composition and physical properties of magnesium-based refractories

Item	MgO	CaO	SiO_2	Al_2O_3	Fe_2O_3	Others	Bulk density	Apparent porosity	Cold crushing strength
DM-97	97.0%	1.60%	0.60%	0.20%	0.50%	0.10%	3.03 g/cm^3	4.5 vol%	40 N/mm^2

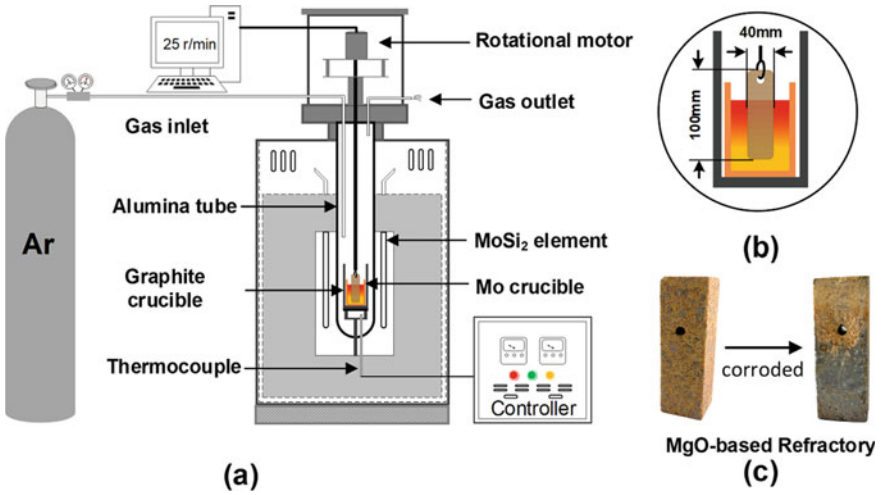

Fig. 1 The schematic diagrams of the corrosion apparatus

schematic diagrams of wetting test equipment. The system mainly includes a high-temperature furnace, a CCD camera, and an analysis computer. The height of cylindrical slag sample ($\varphi 8 \times 8$ mm) would reduce during the heating process (the heating rate was 10 K/min). During the experimental procedure, the contact angles were quantified by computing the mean of the angles observed on both the left and right sides of the droplet interface.

Analysis

The microstructure and element distribution of the initial sample were tested with a field emission scanning electron microscopy with energy-dispersive X-ray spectroscopy (FESEM-EDS; MIRA 3, Tescan, Czech Republic). The interface between the slag and refractories was cut off and inlaid in resin, which was also analyzed with FESEM-EDS. The chemical composition of quenched slag was analyzed with XRF.

Figure 3 showed the microstructure and element distribution of the refractory before corrosion tests. It could be seen from secondary electron image that the surface

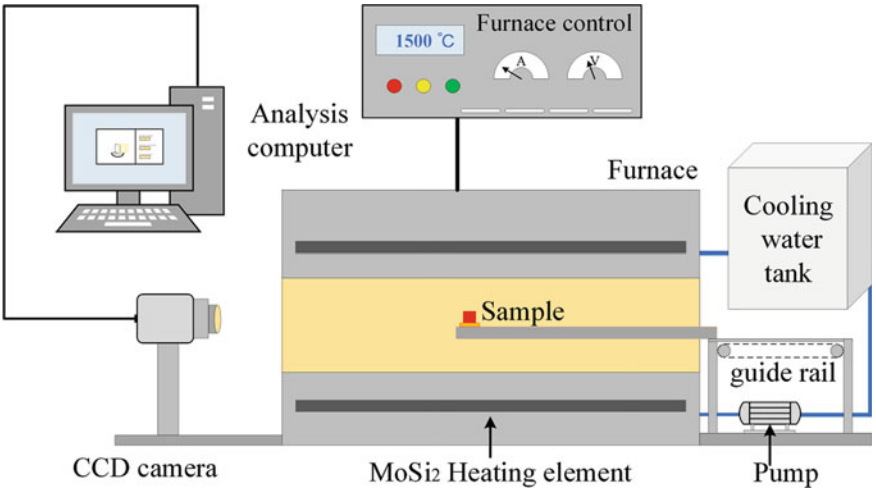

Fig. 2 The schematic diagrams of the wetting test equipment

of the sample was rough, with scattered holes of varying sizes. Using the equivalent circular diameter calculation method, the diameters of eight holes were randomly measured. The size of the pores was in the range of 36.6–94.6 μm, and the average size of pores was 62.75 μm. The backscatter electron image showed that the carbon is irregularly distributed in MgO, and distribution is more concentrated around the pores.

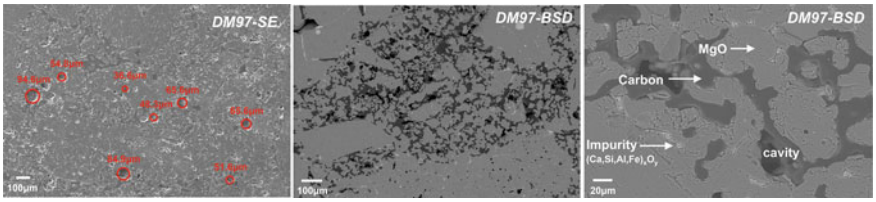

Fig. 3 SEM micrograph and element distribution of the refractory before corrosion tests

Results and Discussion

Corrosion Depth of Refractory and Wetting Performance of Slag

In this study, the dynamic rotation method was employed to assess the slag resistance of refractory materials, simulating the process of refractory erosion caused by the scour of slag in actual EAF smelting. Figure 4 illustrated the reduction in diameter of the refractory after 90 min of erosion by different basicity slags. It was evident that the slag basicity significantly impacted the reduction in refractory diameter, with the reduction diminishing as the slag basicity increased within the range of 1.6–2.47. Furthermore, as the basicity rose from 1.6 to 2.0, a noticeable decrease in diameter reduction was observed. However, as the slag basicity continued to increase, the magnitude of the diameter reduction became less pronounced.

The penetration of slag into the refractory material is a prerequisite for its occurrence of erosion. According to Washburn's equation that is used to describe the theoretical penetration depth of slag into the refractory, as shown in Eq. (1).

$$\frac{\mathrm{d}l}{\mathrm{d}t} = \frac{r\sigma\cos\theta}{4\eta l} \tag{1}$$

where l is the theoretical penetration depth of slag, mm; t is exposure time, s; r is the size of pores in the refractory, mm; σ is the surface tension of slag, N/m; θ is the contact angle between slag and refractory, °; and η is the viscosity of slag, Pa s.

It could be observed from Eq. (1) that slag properties such as viscosity, surface tension, and contact angle significantly influenced the penetration depth of slag. Therefore, we employed the FactSage 8.0 thermodynamic software to calculate the

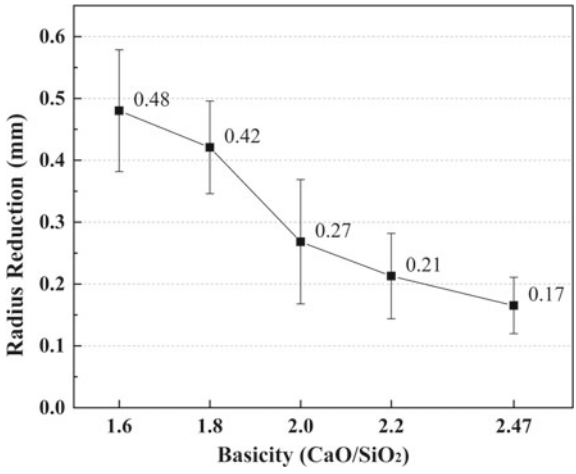

Fig. 4 The relationship between basicity and the reduction of sample radius

viscosities of different basicity slags at 1823 K. The slag viscosities, as a function of increasing basicity, were determined as follows: 0.063, 0.066, 0.067, 0.070, and 0.074 Pa s. Given the minor variation in slag viscosity, we conclude that the slag viscosity is not the primary factor contributing to the reduction of refractory radius at the experimental temperature. Additionally, the increase in slag basicity results in a larger molar volume, which in turn decreases the surface tension of the slag [10].

As another critical factor influencing the penetration depth of slag, we conducted a wetting performance experiment. Figure 5 illustrates the morphological changes in the wetting behavior of slags with basicity levels of 1.6, 2.0, and 2.47 as the temperature increased from 1673 to 1773 K. The slags were placed on a DM97 refractory plane. With the temperature rise, the slags gradually melted, and a higher basicity level made melting slag briquetting increasingly challenging. Additionally, the slag briquetting experienced some degree of expansion at high temperatures. This phenomenon could be attributed to the fact that the slag briquetting was pressed under high pressure at room temperature, and the elevated temperature caused the internal particles to expand in volume, resulting in a looser structure.

The contact angles were measured using ImageJ software, and the results were depicted in Fig. 6. The contact angle significantly decreased with increasing temperature at the basicity in 1.6 and 2.0. However, the slag with a basicity of 2.47 demonstrated the opposite trend. Real-time photos taken during the experimental process also reveal similar phenomena in low-basicity slags, as shown in the images in Fig. 6. It was speculated that the N_2 could not sweep the slag in contact with the plane during the heating process, and thus the temperature of the contact area would be higher than the upper surface, and it is more prone to melting and volume contraction.

In addition, comparing the contact angles at 1773 K, it was found that the slag with higher basicity has a larger contact angle compared to lower basicity slags. This phenomenon is particularly evident in the lag with a basicity of 2.47. This is attributed to the lower melting point of low-basicity slag, which forms a liquid phase at high temperatures and undergoes elemental migration with the refractory. In this

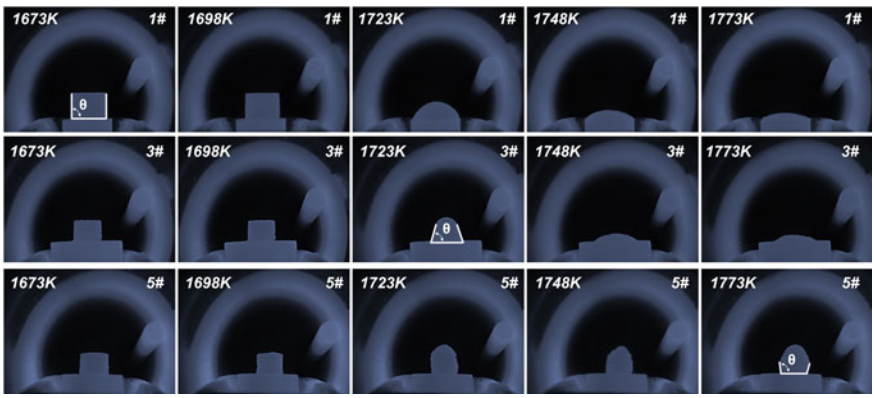

Fig. 5 Photos of slag during the wetting process

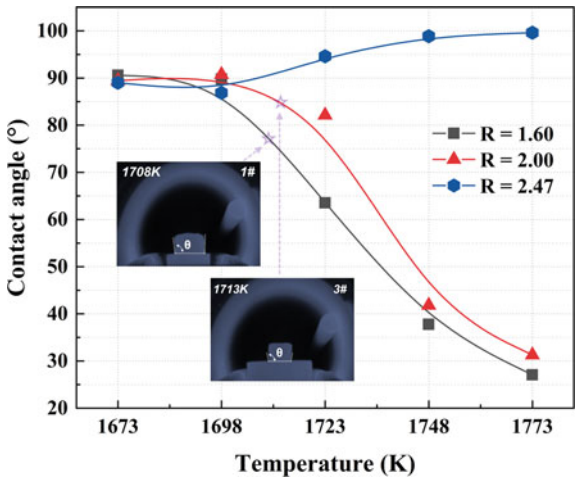

Fig. 6 Effect of basicity on the contact angle

process, MgO from the refractory enters the slag and acts as a network destroyer, reducing slag viscosity. Therefore, the contact angle between low alkalinity slag and the refractory substrate is smaller.

With higher basicity slags exhibiting larger contact angles, the wetting performance of slag was enhanced. To sum up, in Eq. (1), the "σ" and "θ" in the numerator decreased, while the "η" in the denominator increased. Thus, the theoretical penetration depth of the slag would be reduced.

MgO Dissolution and Degradation Mechanism

According to the research conducted by Park et al. [3], the erosion process of refractory could be categorized into two mechanisms: physical erosion and chemical dissolution. Physical erosion refers to the refractory-slag interface layer being stripped due to slag scouring, while chemical dissolution is a result of the interaction between refractory materials and the slag, leading to a reduction in the effective component content through elemental diffusion. Given that the refractory used in this study was MgO-C brick, with MgO constituting the effective component of DM97 at a remarkable content of 97%, we examined the extent of MgO dissolution into the slag. Figure 7 illustrates the MgO content in the slag and its variation rate at different exposure times. It was evident that the MgO content in the slag exhibited a progressive increase with extended exposure time, and it trended to decrease as increasing basicity at same exposure time. Due to the errors introduced from the pre-melted process and XRF testing, the MgO content in the initial slag fluctuated within the range of 7.5–8.0%. However, a more pronounced regularity in the increase of MgO content became apparent with prolonged exposure time. For instance, the final MgO content in the slag increased by 2.85% at the basicity of 1.6, whereas it only increased

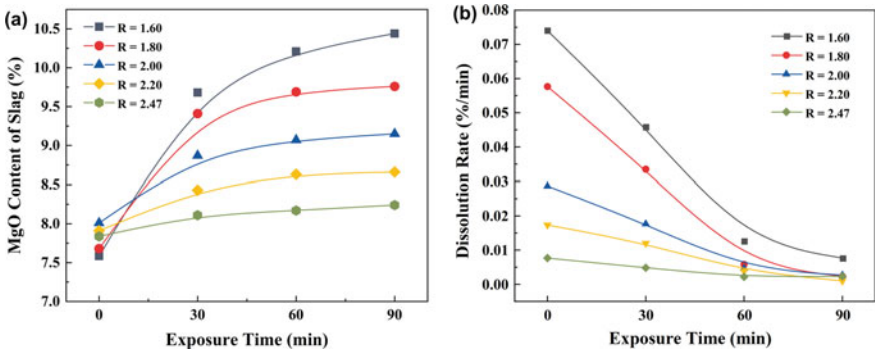

Fig. 7 Effect of exposure time on the content of MgO in the slag

by 0.4% at the basicity of 2.47. The results are consistent with previous research [7, 11–13] and correlate well with the observed trends in refractory diameter reduction. Furthermore, Fig. 7b indicated that as exposure time increased from 0 to 60 min, the dissolution rate of MgO in the slag rapidly decreased, subsequently stabilizing. Particularly, during the initial 60-min erosion process of slag with a basicity below 1.8, the MgO dissolution rate was significantly higher than that of a high-basicity slag. Based on these experimental results, it could be inferred that the MgO content in the slag reached saturation after an exposure time of 60 min.

In order to clearly illustrate the impact of slag basicity on the chemical dissolution in the refractory, the SEM–EDS analysis of the microstructure and elemental distribution of the refractory after dynamic erosion was conducted. Figure 8 presents the refractory's microscopic morphology and energy spectrum after being corrade. It could be observed that there was a significant infiltration of slag within the internal structure of the eroded refractory, and these slag infiltrations occurred through pores or cracks on the surface of the refractory. A noticeable pattern emerged by comparing samples subjected to erosion by various basicity slags: the depth of slag infiltration into the refractory material gradually decreased with higher slag basicity, which aligns with the variation trend of the theoretical penetration depth of slag as mentioned above. At the basicity range of 1.6 to 1.8, bright white particles precipitated within the refractory. According to the results of EDS, these particles were metallic iron. Moreover, as the slag basicity increased, the quantity of iron particles significantly decreased. When the basicity exceeded 2.0, these iron particles completely disappeared. It was presumed that during the infiltration of liquid slag into the refractory material through pores, a reduction reaction occurs between the slag and the carbon in the vicinity of the pores, leading to the reduction of FeO or Fe_2O_3 in the slag into metallic iron. However, as the basicity increased, the higher slag viscosity reduced the penetrating amount of slag, thus resulting in a reduction of generated metallic iron. Simultaneously, an interesting observation was made. When the slag basicity reached 2.0, the CaO content in the infiltrating slag rapidly increased. However, as the basicity continued rising, high-purity CaO particles precipitated as

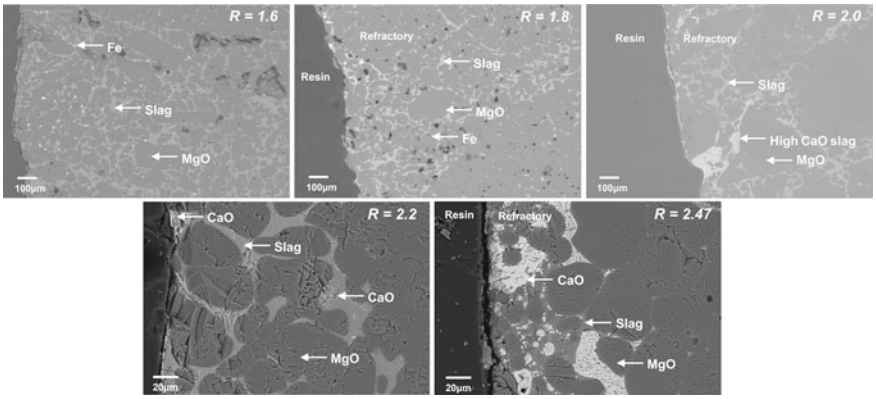

Fig. 8 SEM micrograph and elements distribution of the refractory after corrosion tests

elongated strips. To some extent, the precipitation of these particles limited direct contact between the slag and the refractory material, thereby reducing the dissolution of MgO into the slag.

Figure 9a displays the surface scanning image of the refractory corroded by slag with a basicity of 1.6. It could be observed that apart from the Mg element, elements such as Ca, Si, and Fe were also widely distributed within the refractory material. The distribution regions of these elements closely align with the light gray slag phase seen in the SEM images. Particularly, the distribution of Fe was mostly concentrated at the interface between the slag phase and the MgO phase.

To clearly illustrate the distribution characteristics of Fe at the interface, we conducted line scanning analysis at the interface between the slag and the internal MgO phase of the refractory. The results, as shown in Fig. 9b, indicated that at the slag-MgO phase interface, the intensities of Ca, Si, and Al elements exhibited minor fluctuations, while the intensities of Fe and Mg elements significantly increased. This demonstrated the formation of a magnesiowüstite (MW) intermediate layer at the interface between the slag and the MgO phase, which serves to protect the refractory material. The MW intermediate layer was produced as a result of the reaction

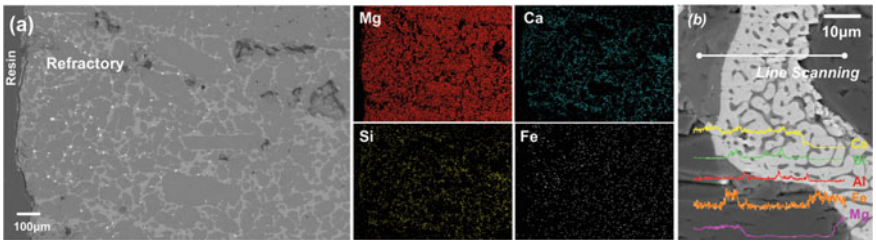

Fig. 9 Element distribution of refractory, **a** EDS mapping of refractory, **b** Line scanning of refractory

between FeO-containing slag and magnesia refractories, and it has been commonly observed in previous studies [3, 14, 15]. Additionally, it should be noted that the MW intermediate layer was found in all five sets of experimental samples. The thickness of the MW layer formed by low-basicity slag interacting with the refractory material was larger than that in the high-basicity experimental group. However, due to the deep penetration of slag into the refractory with low basicity, the MW layer did not play a dominant role in suppressing erosion. Therefore, the refractory material in the low-basicity experimental group experienced more severe erosion.

Based on the research results presented above, it could be inferred that the erosion of the DM97 refractory during EAF smelting entirely based on DRI raw materials can be divided into three stages:

(1) The slag infiltrates the interior of the refractory through pores or cracks on its surface. The slag viscosity and the wettability between the slag and the refractory primarily determine this stage. The slag with lower basicity has a lower viscosity and better wettability, so the refractory will suffer more severe erosion.
(2) A reaction occurs between the slag and the refractory components around the pores, with MgO dissolving into the slag. Meanwhile, ions such as Ca^{2+}, Si^{4+}, and Fe^{2+}diffuse into the interior of the refractory. Those reactions include the reduction of iron oxides in the slag to metallic iron by carbon and the formation of the MW intermediate layer by combining FeO and MgO.
(3) Large blocks of the MgO phase within the refractory are fragmented, ultimately detaching under physical erosion.

The chemical dissolution of MgO within the refractory promotes the fragmentation of large MgO phases. Therefore, reducing the activity of MgO in the slag by increasing slag basicity or MgO content is beneficial for inhibiting the erosion of the refractory. Considering that excessively high slag basicity can adversely affect its viscosity, foaming properties, and dephosphorization performance, based on the results of this study, the basicity of the slag during the oxidation period in an EAF with DM97 refractory can be considered in the range of 2.0 to 2.2.

Conclusions

The corrosion resistance of a MgO-C refractory in EAF slag that entirely use DRI as raw materials was investigated in this study via rotating immersion method (25 r/min) under dynamic conditions at 1823 K. Based on the experimental results, the corrosion mechanism was proposed. The conclusions are summarized as follows:

(1) The reduction in refractory diameter diminished as the slag basicity increased within the range of 1.6–2.47. The magnitude of the diameter reduction became less pronounced when the slag basicity exceeded 2.0. The slag with higher basicity has a larger contact angle compared to lower basicity slags.

(2) The MgO content in the slag exhibited a progressive increase with extended exposure time, and it trended to decrease as increasing basicity at same exposure time. The dissolution rate of MgO in the slag rapidly decreased during the initial 60-min erosion and subsequently stabilized.
(3) Substantial slag infiltrated into the refractory through surface pores or cracks. The Fe particles precipitated at the basicity between 1.6 and 1.8, and high-purity CaO particles precipitated as basicity continuous to increase. While the MW layer is thicker in cases of low-basicity slag, it's noteworthy that the slag penetration is actually deeper. Consequently, the MW layer did not exert a significant influence in mitigating erosion.
(4) The DM97 refractory erosion in DRI-based EAF smelting involves three stages: slag infiltration via surface pores or cracks, reaction and dissolution occur around pores, and the fragmentation and detachment of refractory.
(5) The basicity of the slag during the oxidation period in an EAF with DM97 refractory can be considered in the range of 2.0–2.2.

Acknowledgements The present work was financially supported by National Natural Science Foundation of China (Grant No. U1960205) and China Minmetals Science and Technology Special Plan Foundation (Grant No. 2020ZXA01). The authors gratefully acknowledge their support.

Conflict of Interest The authors declare that they have no known competing financial interests or personal relationships that could have appeared to influence the work reported in this paper.

References

1. Wang RR, Zhao YQ, Babich A, Senk D, Fan XY (2021) Hydrogen direct reduction (H-DR) in steel industry-An overview of challenges and opportunities. J Clean Prod 329:129797
2. Pimm AJ, Cockerill TT, Gale WF (2021) Energy system requirements of fossil-free steelmaking using hydrogen direct reduction. J Clean Prod 312:127665
3. Oh MK, Park JH (2021) Effect of fluorspar on the interfacial reaction between electric arc furnace slag and magnesia refractory: Competitive corrosion-protection mechanism of magnesiowüstite layer. Ceram Int 47:20387–20398
4. Yilmaz C, Turek T (2017) Modeling and simulation of the use of direct reduced iron in a blast furnace to reduce carbon dioxide emissions. J Clean Prod 64:1519–1530
5. Heo J, Park JH (2022) Interfacial reactions between magnesia refractory and electric arc furnace (EAF) slag with use of direct reduced iron (DRI) as raw material. Ceram Int 48:4526–4538
6. Oh MK, Park JH (2021) Effect of Industrial Waste fluxes (red mud and white mud) on dephosphorization and refractory corrosion: applications to electric arc furnace process using direct reduced iron. Metall Mater Trans B 52:3583–3595
7. Um H, Lee K, Choi J, Chung Y (2012) Corrosion behavior of MgO–C refractory in ferromanganese slags. ISIJ Int 52:62–67
8. Tayeb MA, Assis AN, Sridhar S, Fruehan RJ (2015) MgO Solubility in steelmaking slags. Metall Mater Trans B 46:1112–1114
9. Jung SM, Min DJ (2010) The effect of Fe_tO content on mgo solubilities in lime-based slags. ISIJ Int 50:1632–1636
10. Yan Z, Deng Z, Zhu M (2023) Penetration behavior of $CaO–SiO_2–FeO_x–MgO–(CaCl_2)$ slags in MgO refractory. Metall Mater Trans B 54:1582–1592

11. Han JS, Heo JH, Park JH (2019) Interfacial reaction between magnesia refractory and "FeO"-rich slag: formation of magnesiowüstite layer. Ceram Int 45:10481–10491
12. Song S, Zhao J, Pistorius PC (2020) MgO refractory attack by transient non-saturated EAF slag. Metall Mater Trans B 51:891–897
13. Sarkar R, Nash BP, Sohn HY (2020) Interaction of magnesia-carbon refractory with metallic iron under flash ironmaking conditions. J Eur Ceram Soc 40:529–541
14. Lee WE, Zhang S (1999) Melt corrosion of oxide and oxide-carbon refractories. Int Mater Rev 44:77–104
15. Zhang P, Seetharaman S (1994) Dissolution of MgO in CaO–"FeO"–CaF_2–SiO_2 slags under static conditions. J Am Ceram Soc 77:970–976

Corrosion of Alkali Metals on SiC-Si_3N_4 Refractory of Pusher Kiln

Jiang Diao, Hu Ruixin, Lei Jin, Liu Deman, Tan Wenfeng, Li Hongyi, and Xie Bing

Abstract When using pusher kiln to produce vanadium nitrogen alloy, alkali metals in raw materials will volatilize and deposit in the kiln, which will corrode refractories and hinder the smooth production. Therefore, it is of great significance to study the corrosion of refractory by sediment. In this paper, SiC-Si_3N_4 composite brick was used as the research object, and sodium carbonate and potassium carbonate were used as corrosion reagents to carry out corrosion experiments in a vacuum tube furnace. The results indicate that the surface of the composite brick occurs microporous and spalling phenomenon after being corroded by sodium carbonate or potassium carbonate for 3 h. The thicknesses of spalling layer and corrosion layer caused by sodium carbonate are 3.0 mm and 2.67 mm, respectively. The thicknesses of spalling layer and corrosion layer caused by potassium carbonate are 0.5 mm and 0.77 mm, respectively. It was found that the corrosion ability of sodium carbonate to SiC-Si_3N_4 composite brick is stronger than that of potassium carbonate. Combined with theoretical calculation and experimental characterization, it is found that the corrosion process is divided into three stages: corrosion reaction, slagging, and reduction of alkali metal oxides.

Keywords Alkali metals · Corrosion · Refractories

Introduction

Vanadium is widely used in railway, bridge, military industry, aerospace, machinery manufacturing, automobile, chemistry, new energy, steel materials, and other fields. In the iron and steel industry, vanadium is mainly added into the steel in the form of ferrovanadium or vanadium nitrogen alloy as an alloy additive to refine the grain and

J. Diao (✉) · H. Ruixin · L. Jin · L. Deman · T. Wenfeng · L. Hongyi · X. Bing
College of Materials Science and Engineering, Chongqing University, Chongqing 400044, China
e-mail: diaojiang@163.com

Chongqing Key Laboratory of Vanadium-Titanium Metallurgy and Advanced Materials, Chongqing University, Chongqing 400044, China

© The Minerals, Metals & Materials Society 2024

G. Alvear et al. (eds.), *Advances in Pyrometallurgy*, The Minerals, Metals & Materials Series, https://doi.org/10.1007/978-3-031-50176-0_13

enhance the vanadium precipitation strengthening [1–4]. At present, various manufacturers use vanadium oxide as raw material and use the push plate kiln method to produce vanadium nitrogen alloys. First, the vanadium oxide is crushed, mixed with the carbon powder, and then sent to the reduction nitriding equipment for reaction at high temperature, and finally cooled to obtain vanadium nitrogen alloy product [5]. The vanadium oxide raw materials used in the production of vanadium nitrogen alloys contain a certain amount of sodium and potassium salts. These alkali metal compounds will react with other compounds to generate alkali metal vapor at high temperature. Alkali metal vapor can react with CO_2 and other substances. When the steam is cooled and condensed, it will gradually deposit on the top wall of the pusher kiln, presenting as black and white hard and dense compounds. This kind of deposit is mainly distributed near the exhaust outlet. It will corrode refractory materials, cause furnace blockage and interrupt normal production, and result in huge economic losses. Ma et al [6] found that the main components of soot scale are carbon and carbonate (Na_2CO_3, K_2CO_3). Soot scale is prone to decomposition at high temperatures and cannot exist stably above 1400 °C. In the actual industrial production, the refractory lining material of pusher kiln is not unified. SiC-Si_3N_4 composite brick has attracted more and more attention in recent years because of its excellent properties in chemical stability, high temperature strength, thermal conductivity, thermal shock resistance, high softening temperature, oxidation resistance, and so on [7–10]. However, at present, there is no effective way to completely eliminate the problem of alkali metal volatilization and deposition in the synthesis process of vanadium nitrogen alloy, and the influence and mechanism of alkali metal and its compounds on SiC-Si_3N_4 brick lining are not clear. Therefore, this study takes SiC-Si_3N_4 composite brick as the object, carries out alkali metal corrosion experiment, and discusses the alkali corrosion resistance and corrosion mechanism of SiC-Si_3N_4 composite brick.

Materials and Methods

The refractory used in the experiment is industrial SiC-Si_3N_4 composite brick. The main phases are SiC (70% ~ 75%) and Si_3N_4 (18–25%). The chemical composition and main performance indexes of composite brick are shown in Table 1. Anhydrous sodium carbonate (purity ≥ 99.8%) and anhydrous potassium carbonate (purity ≥ 99.0%) were used as corrosion reagents to simulate the corrosion of alkali metals on the refractory materials of pusher kiln.

The corrosion experiment was carried out in a high-temperature vertical vacuum tube furnace. The target experimental temperature was set at 1350 °C. The corrosion time was 1 h, 2 h, and 3 h, respectively. A graphite crucible with diameter of 30 mm was used to hold the samples. In each experiment, the position of the crucible remained unchanged, and the crucible was placed and taken out from the upper end of the furnace tube. The corrosion reagent was located at the bottom of the graphite crucible, and the refractory was placed on the upper surface of the corrosion

Table 1 The chemical compositions and properties of SiC-Si_3N_4 composite brick

Composition content (wt.%)		Properties	
SiC	72	Apparent porosity (%)	16
Si_3N_4	21	Bulk density (g/cm^3)	2.62
Fe_2O_3	1.5	Compressive strength (MPa)	150
Others	5.5	High-temperature bending strength (1400 °C) (MPa)	43.0

reagent. Before carrying out the experiment, nitrogen was continuously injected into the furnace for 3 min, and the gas flow rate was set to 1 L/min to exhaust the air in the furnace as much as possible. After the furnace temperature was stable at the target temperature, put the sample in. The original sample was a block shaped refractory brick, and the corroded brick was cut along the erosion direction to obtain a layered sample. After spraying gold, it was scanned using a tungsten filament scanning electron microscope (TESCAN VEGA3). Use an angle grinder to cut off the eroded part of the refractory brick, crush and sieve it to below 200 mesh, and take out some samples for XRD (X-ray diffraction) analysis. The scanning angle is 10–90, and the scanning time is 10 min.

Results

Figure 1 shows the spalling layer and corrosion zone the corrosion zone of SiC-Si_3N_4 composite brick during Na_2CO_3 corrosion. As shown in Fig. 1, with the increase of corrosion time, the boundary of corrosion zone gradually expands, and some micropores appear on the surface of the sample, accompanied by obvious spalling phenomenon. After 3 h of Na_2CO_3 corrosion, the thickness of corrosion zone is more than 2.67 mm, and the thickness of spalling layer is 3 mm. Figure 1e shows the thickness variation of spalling layer and corrosion zone of the sample. With the increase of corrosion time, both the thickness of corrosion zone and spalling zone increase.

Figure 2 shows the vertical interface section of the corrosion zone of SiC-Si_3N_4 composite brick corroded by K_2CO_3. After being corroded by K_2CO_3 for 3 h, SiC-Si_3N_4 composite brick also appears in obvious spalling phenomenon, but there is no obvious deformation on the whole. As shown in Fig. 2e, after 3 h of corrosion, the thickness of corrosion zone is 0.77 mm, and the thickness of spalling zone is 0.5 mm. The thickness of corrosion zone and spalling zone with K_2CO_3 as corrosion reagent is obviously smaller than that with Na_2CO_3 as corrosion reagent. It indicates that the corrosion resistance of SiC-Si_3N_4 composite brick to K_2CO_3 is stronger than that to Na_2CO_3. In other words, Na_2CO_3 is easier to react with SiC-Si_3N_4 composite brick.

Figure 3 shows the XRD patterns of spalling zone, obvious corrosion zone, and slight corrosion zone of SiC-Si_3N_4 composite brick with Na_2CO_3 as the corrosive

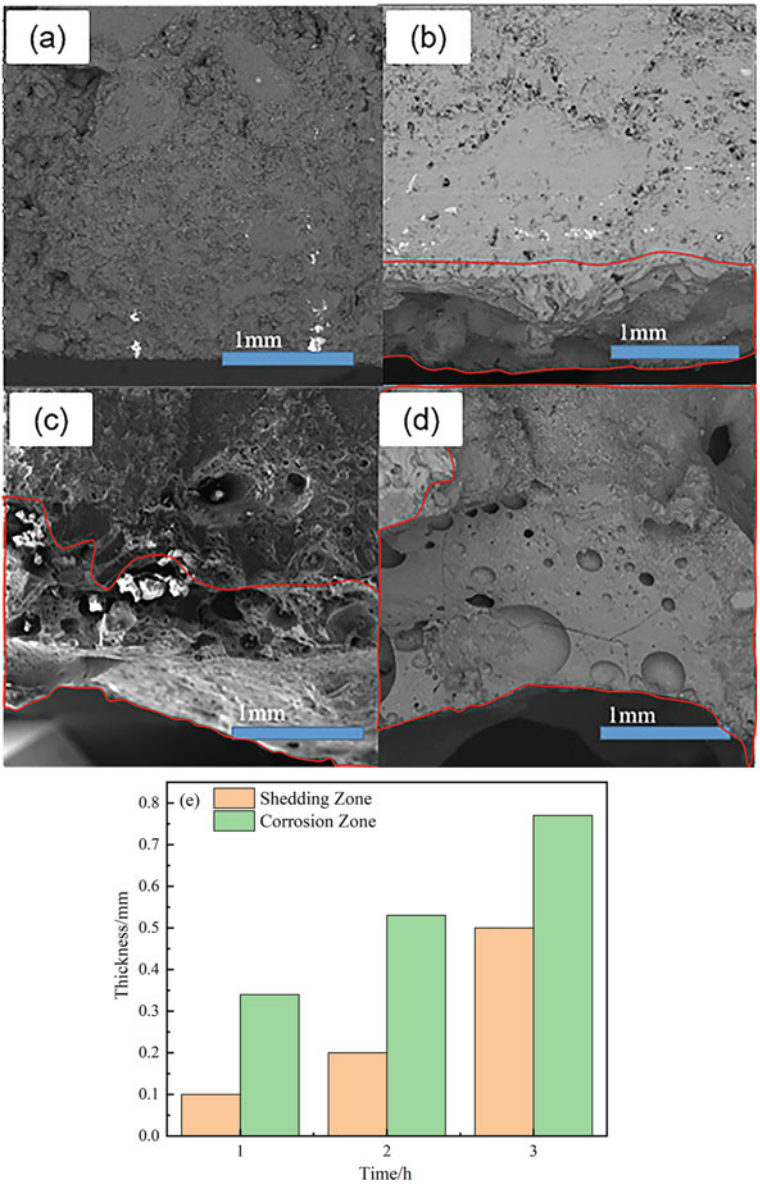

Fig. 1 Spalling layer and corrosion zone of SiC-Si_3N_4 composite brick corroded by Na_2CO_3 **a** original sample, **b** 1 h, **c** 2 h, **d** 3 h

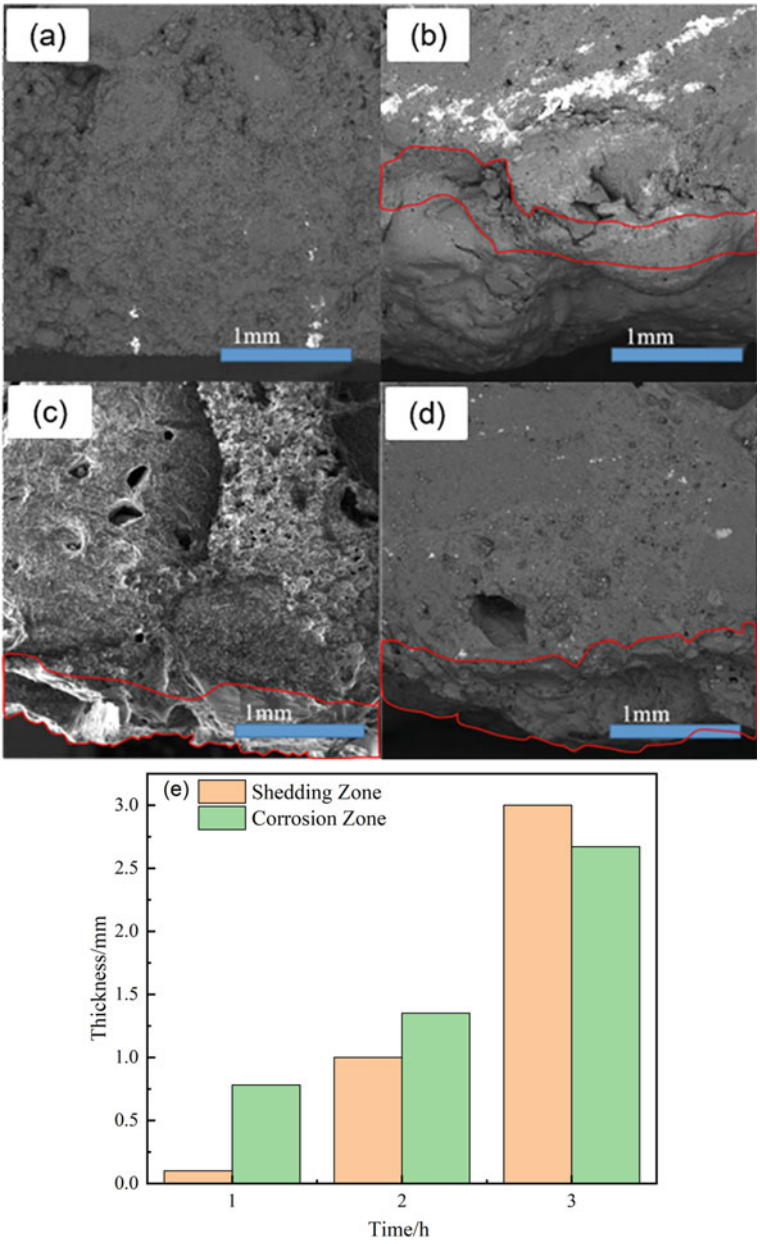

Fig. 2 Vertical interface section of SiC-Si_3N_4 composite brick corroded by K_2CO_3 **a** original sample, **b** 1 h, **c** 2 h, **d** 3 h

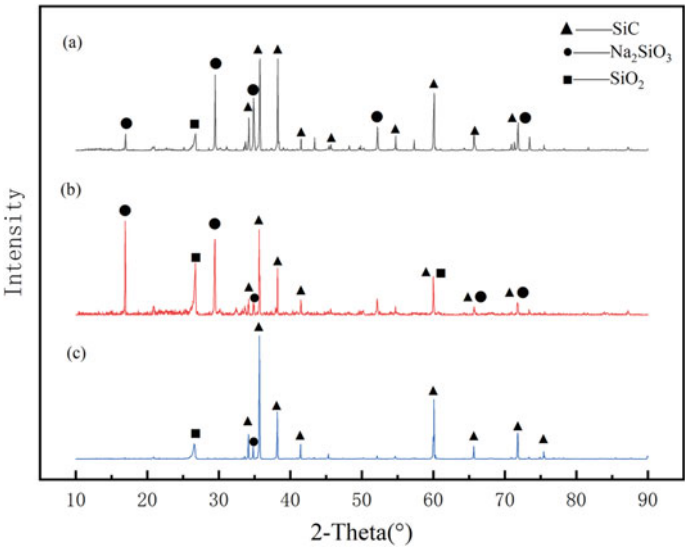

Fig. 3 XRD patterns of SiC-Si_3N_4 composite brick corroded by Na_2CO_3 for 3 h **a** spalling zone, **b** obvious corrosion zone, **c** slight corrosion zone

agent. The main phases in the corrosion zone are SiC, Na_2SiO_3, and SiO_2. Compared with the SiC-Si_3N_4 composite brick before corrosion, Si_3N_4 phase disappears and new phases Na_2SiO_3 and SiO_2 appear. It indicates that Si_3N_4 is easier to react with Na_2CO_3 than SiC. Based on the above experimental results, it is speculated that when K_2CO_3 is used as corrosion agent, the corrosion effect is worse than that of Na_2CO_3, the amount of SiC involved in the reaction is less, and the silicon mostly exists in the form of SiC or SiO_2.

Discussion

In order to further clarify the phase evolution of SiC-Si_3N_4 composite brick during alkali metal corrosion, the Equilib module of FactSage was used to calculate the phase equilibrium. K_2CO_3 or Na_2CO_3 was selected to react with SiC or Si_3N_4, respectively. The reaction temperatures were set at 200–1400 °C. According to the composition of refractory in this study, the total mass of each group of reactants is 100 g, the mass ratio of carbonate to SiC is 50:50, and the mass ratio of carbonate to Si_3N_4 is 70:30. The phases that occur during the reaction can be divided into gas phase, liquid phase, and solid phase. Solid phase includes carbonate, silicate, C, SiC, and Si_3N_4. Liquid phase including slag phase. The gas phase includes N_2, CO, CO_2, and alkali metal vapors.

As shown in Fig. 4, K_2CO_3 reacts with SiC at low temperature to form K_2SiO_3 and C. At about 1000 °C, K_2SiO_3 transforms into slag phase, i.e. K_2O (slag) and SiO_2 (slag). K (g) gas is formed at 1150 °C. In addition, there is a small amount of CO. The mass is less than 1 g, which is not shown in the figure. At the same time, the mass of K_2O (Slag) and SiC decreases, while the mass of SiO_2 (Slag) and C increases slightly. The possible reactions are as follows:

T < 1000 °C

$$SiC + K_2CO_3 = K_2SiO_3 + 2C \quad \Delta G^{\theta} = -477789 - 193.065T \tag{1}$$

1000–1150 °C

$$K_2SiO_3 = K_2O(slag) + SiO_2(slag) \tag{2}$$

T > 1150 °C

$$2K_2O + SiC = SiO_2 + C + 4K(g) \quad \Delta G^{\theta} = 34371.6 - 330.726T \tag{3}$$

$$3K_2O + SiC = SiO_2 + CO + 6K(g) \quad \Delta G^{\theta} = 297418 - 658.25T \tag{4}$$

When K_2CO_3 is used as an aggressive agent to attack refractory, the initial temperature of corrosion reaction is lower than Na_2CO_3. And there is a very small amount of $K_2Si_2O_5$, which is not shown in the figure because it is less than 0.1 g. Compared with SiC, the amount of Si_3N_4 remaining after reaction is less. Nitrogen mainly exists in the form of N_2. At 780 °C, K_2SiO_3 begins to transform into K_2O (slag) and SiO_2 (slag), until it was completely consumed at 975 °C. After that, K_2O is reduced to potassium vapor and the amount of SiO_2 increases. With the increase of temperature, Si_3N_4 is consumed until 1345 °C. The mass of C remains unchanged, only decreases slightly after 975 °C. The mass change of potassium vapor mainly occurs after 975 °C. The mass of CO increases after 1150 °C. It is speculated that the reactions involved are as follows (Fig. 5):

T < 780 °C

$$3K_2CO_3 + Si_3N_4 = 3K_2SiO_3 + 3C + 2N_2 \quad \Delta G^{\theta} = 89{,}806 - 245.0T \tag{5}$$

780–975 °C

$$K_2SiO_3 = K_2O(slag) + SiO_2(slag) \tag{6}$$

T > 975 °C

$$2K_2O + C = CO + 4K(g) \quad \Delta G^{\theta} = 26{,}3850 - 328.5T \tag{7}$$

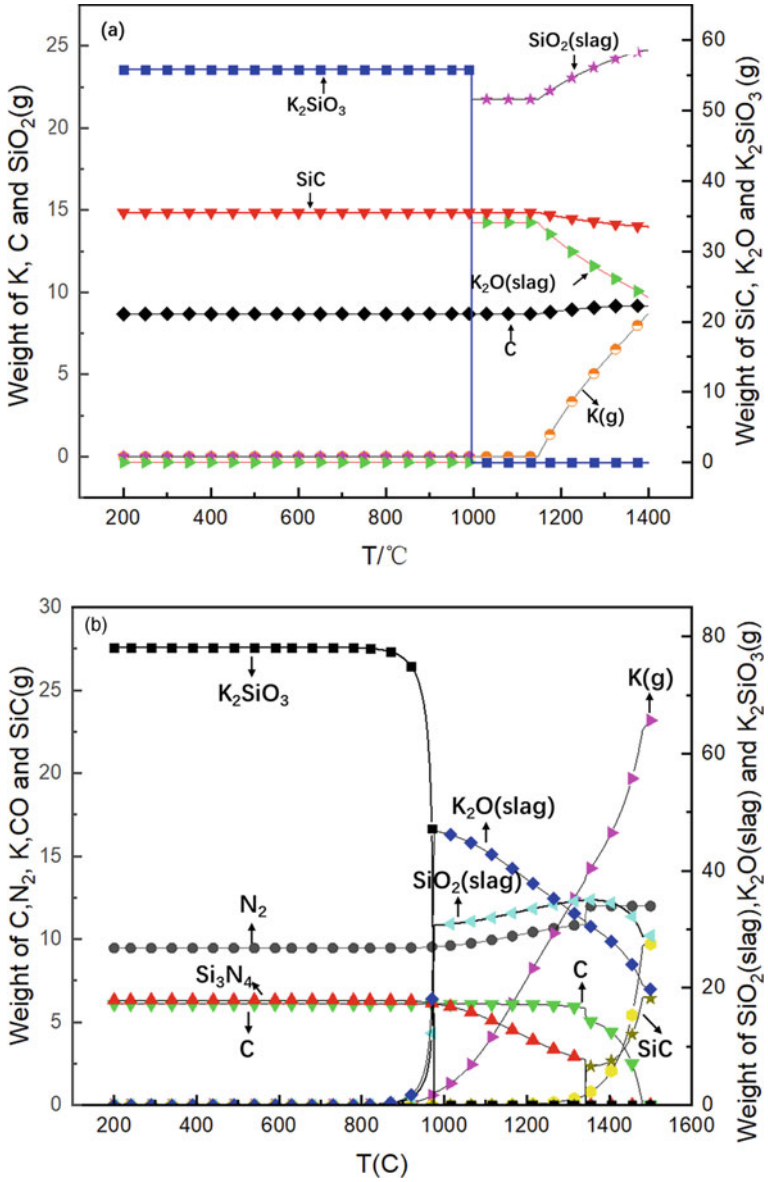

Fig. 4 Equilibrium phase of K_2CO_3 reacting with SiC and Si_3N_4 **a** SiC; **b** Si_3N_4

$$6K_2O + Si_3N_4 = 3SiO_2 + 2N_2 + 12K(g) \quad \Delta G^{\theta} = 485{,}5581 - 1269T \qquad (8)$$

When Na_2CO_3 reacts with SiC or Si_3N_4, a large amount of Na_2SiO_3 is formed at low temperature. When SiC is corroded by Na_2CO_3, it is accompanied by the formation of C. At 1090 °C, Na_2SiO_3 transforms into Na_2O (slag) and SiO_2 (slag), but C remains unchanged. After 1245 °C, the mass of SiC, C, and Na_2O decreases,

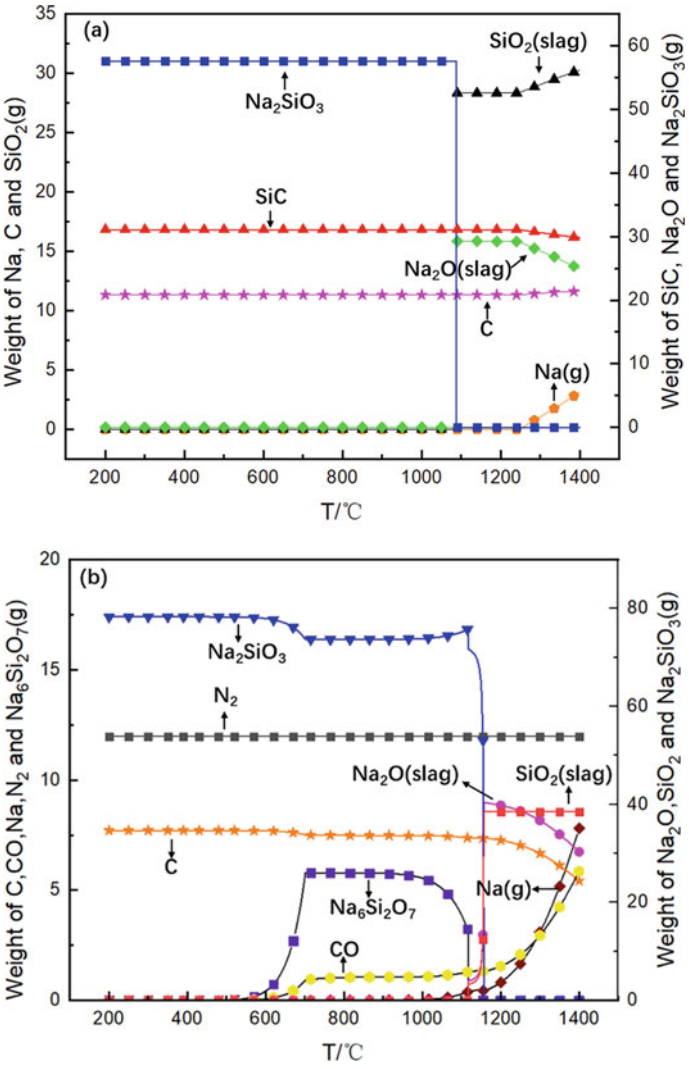

Fig. 5 Equilibrium phase of Na_2CO_3 reacting with SiC and Si_3N_4 **a** SiC; **b** Si_3N_4

while SiO_2 increases. At the same time, gas phase is formed, mainly CO and Na(g). The possible reactions are as follows:

T < 1090 °C

$$SiC + Na_2CO_3 = Na_2SiO_3 + 2C \quad \Delta G^{\theta} = -38{,}6770 - 88.06T \tag{9}$$

1090–1245 °C

$$Na_2SiO_3 = SiO_2(slag) + Na_2O(slag) \tag{10}$$

T > 1245 °C

$$2Na_2O + SiC = SiO_2 + C + 4Na(g) \quad \Delta G^{\theta} = 148{,}443 - 322.1T \tag{11}$$

$$3Na_2O + SiC = SiO_2 + CO + 6Na(g) \quad \Delta G^{\theta} = 474{,}559 - 649.5T \tag{12}$$

At low temperature, Na_2CO_3 reacts with Si_3N_4 to form C, N_2, and Na_2SiO_3. At 400 °C, part of Na_2SiO_3 is converted to $Na_6Si_2O_7$. The CO content increases obviously after 480 °C and becomes stable after 700 °C. At 1120 °C, silicate begins to transform into Na_2O (slag) and SiO_2 (slag), and disappears completely at 1160 °C. After that, the mass of CO increases obviously, while C and Na_2O decrease. It shows that Na_2O is reduced to Na(g). Different from K_2CO_3, Na_2CO_3 was not completely consumed at the beginning, and about 2 g remained. It was not consumed until 700 °C. Si_3N_4 is completely consumed. N exists in the form of N_2, and its mass remains unchanged during the reaction. It is speculated that the reactions involved are as follows:

T < 400 °C

$$3Na_2CO_3 + Si_3N_4 = 3Na_2SiO_3 + 3C + 2N_2 \quad \Delta G^{\theta} = -754{,}987 - 22.708T \tag{13}$$

400–1120 °C

$$Na_2CO_3 + Na_2SiO_3 + C = Na_6Si_2O_7 + 2CO \quad \Delta G^{\theta} = -231{,}530.4 - 277.55T \tag{14}$$

1120–1160 °C

$$Na_2SiO_3 = SiO_2(slag) + Na_2O(slag) \tag{15}$$

$$Na_6Si_2O_7 = 2SiO_2(slag) + 3Na_2O(slag) \tag{16}$$

T > 1160 °C

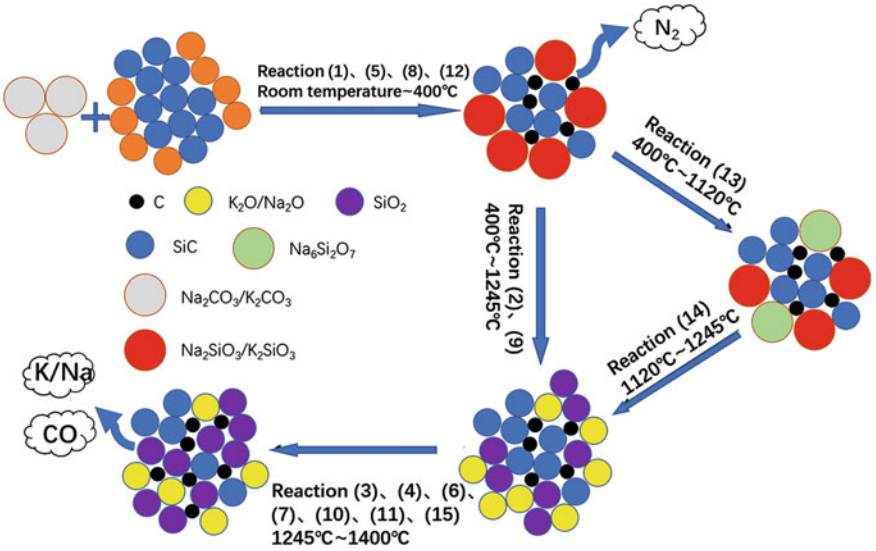

Fig. 6 Schematic diagram of corrosion process of SiC-Si_3N_4 composite brick by alkali metal

$$Na_2O + CO = CO + Na(g) \quad \Delta G^{\theta} = 321{,}868.7 - 324.09T \tag{17}$$

Through the above analysis, it is found that with the increase of temperature, the corrosion of SiC-Si_3N_4 composite brick by alkali carbonate can be roughly divided into three stages: (1) carbonate corrodes composite brick to form silicates, (2) silicates transform into slag phases, and (3) some alkali metal oxides are reduced. Schematic diagram of corrosion process of SiC-Si_3N_4 composite brick is shown in Fig. 6. Si_3N_4 in SiC-Si_3N_4 composite brick is columnar or reticular structure, interweaved into three-dimensional space network, which can wrap small particles of SiC and combine large particles of SiC to play a strengthening role [11–13]. With the consumption of Si_3N_4, the brick structure of the composite brick is destroyed, the strength of the brick decreases, and micropores appear. As the corrosion reaction continues, part of SiC is consumed and silicate is formed, and the reaction products are peeled off from the brick.

Conclusions

In this paper, sodium carbonate and potassium carbonate were used as corrosion reagents to carry out high-temperature corrosion experiments on SiC-Si_3N_4 composite refractories. When sodium carbonate is used as corrosion agent, the corrosion layer and spalling layer of composite brick are obviously wider. The thicknesses of spalling zone and corrosion zone are 3.0 mm and 2.67 mm, respectively, after

sodium carbonate corrodes refractory for 3 h. However, the thickness of spalling zone and corrosion layer after 3 h potassium carbonate corrosion are only 0.5 mm and 0.77 mm, respectively. The results show that the corrosion ability of sodium carbonate is greater than that of potassium carbonate. According to the theoretical analysis, when the temperature is lower than 400 °C, the corrosion agent will react with Si_3N_4 in the composite brick to form silicate and N_2. As Si_3N_4 is consumed, the strength of the refractory is reduced, and the subsequent corrosion reagents react with SiC to form silicate and C. At this time, the structure of the refractory is destroyed, which is the reason of micropore and spalling on the surface of the refractory. When the temperature rises to 1100–1250 °C, the silicate formed is heated and transformed into slag phase. At 1100 °C, K_2O(slag) is reduced by SiC and C to K(g) and C or CO. The reduction temperature of Na_2O(slag) is relatively high, about 1250 °C. If there is residual Si_3N_4, alkali metal oxides are preferentially reduced by Si_3N_4. To sum up, the damage of sodium carbonate to SiC-Si_3N_4 composite brick is greater in the pusher kiln environment. Reducing the content of sodium salt in vanadium oxide raw material can effectively reduce the corrosion of refractories in the kiln.

Acknowledgements This work was supported by the National Natural Science Foundation of China (No. 51974047), the Natural Science Foundation of Chongqing, China (cstc2022ycjh-bgzxm0003), and the Large Instrument Foundation of Chongqing University (No. 202303150268).

Funding Information National Natural Science Foundation of China, Grant/Award Number: 51974047; Natural Science Foundation of Chongqing, China, Grant/Award Number: cstc2020jcyj-msxmX0043; Fundamental Research Funds for the Central Universities, Grant/Award Number: 2020CDJ-LHZZ-084.

References

1. Sun LY, Ke XT, Jiang YH (2005) Application and prospect of vanadium nitrogen alloys. Sichuan Metall 27(4):12–17
2. Staśko R, Adrian H, Adrian A (2005) Effect of nitrogen and vanadium on austenite grain growth kinetics of a low alloy steel. Mater Charact 56(4–5):340–347
3. Ali IHM, Moustafa IM, Farid AM, Glodowski RJ (2005) Improvement of low carbon steel properties through V-N microalloying. Mater Sci Forum MSF 500–501:503–510. https://doi.org/10.4028/www.scientific.net/msf.500-501.503
4. Zhang ZX, Lin G, Jiang LZ, Xu Z (2008) Beneficial effects of nitrogen on austenite antibacterial stainless steels. Mater Chem and Phys 111(2):238–243
5. Wong QQ (2015) Analysis of domestic production of vanadium nitride. Sichuan Metall 37(2):1–4
6. Ma RF, Zhou GH, Lu ML, Wan H (2014) Reason for scaling in vanadium nitride push board kiln. Hebei Metallurgy 5:16–19
7. Klemm H (2010) Silicon nitride for high-temperature applications. J AM Ceram Soc 93:1501–1522
8. Jack KH (1976) Sialons and related nitrogen ceramics. J Mater Sci 11(6):1135–1158
9. Reddy NK (2002) Reaction-bonded silicon carbide refractories. Mater Chem and Phys 76(1):78–81
10. Popper P (1994) Applications of silicon nitride. Key Eng Mat 89–91:719–724

11. Yang L, Xie Z, Li S, Song M (2014) Progress in research and application of gas-pressure-sintered silicon nitride ceramics. J Ceram 35(5):457–464
12. Zou C, Zhang C, Li B, Wang S, Feng C (2013) Microstructure and properties of porous silicon nitride ceramics prepared by gel-casting and gas pressure sintering. Mater and Design 44:114–118
13. Bocanegra-Bernal MH, Matovic B (2009) Mechanical properties of silicon nitride-based ceramics and its use in structural applications at high temperatures. Mat Sci Eng A 527(6):1314–1338

Author Index

© The Minerals, Metals & Materials Society 2024

G. Alvear et al. (eds.), *Advances in Pyrometallurgy*, The Minerals, Metals & Materials Series, https://doi.org/10.1007/978-3-031-50176-0

Subject Index

© The Minerals, Metals & Materials Society 2024

G. Alvear et al. (eds.), *Advances in Pyrometallurgy*, The Minerals, Metals & Materials Series, https://doi.org/10.1007/978-3-031-50176-0